UNIVERSITY OF SALERNO

DEPARTMENT OF PHYSICS "E. R. CAIANIELLO"

UNIVERSITY OF CAMPANIA "LUIGI VANVITELLI"

DEPARTMENT OF MATHEMATICS AND PHYSICS

DOCTORAL COURSE IN "MATHEMATICS, PHYSICS AND APPLICATIONS"

XXIX CYCLE

CURRICULUM: PHYSICS

DOCTORAL THESIS

Measurement of Λ_c Baryon production in the decay channel $\Lambda_c \to pK^0_S$ in proton-proton and proton-lead collisions with ALICE detector at LHC

Candidate:
Elisa Meninno

Supervisor:
Prof. Salvatore DE PASQUALE

PhD Coordinator:
Prof. Sandro PACE

University of Salerno
University of Campania "Luigi Vanvitelli"

Abstract

Measurement of Λ_c Baryon production in the decay channel $\Lambda_c \to p\mathrm{K}^0_\mathrm{S}$ in proton-proton and proton-lead collisions with ALICE detector at LHC

by Elisa MENINNO

This thesis describes the study of the production of the charmed baryon Λ_c in proton-proton and proton-Lead collisions with the ALICE experiment, operating at the Large Hadron Collider (LHC) at CERN.
ALICE was build to study hadronic collisions (pp and A-A) and, in particular, aims to investigate the *Quark-Gluon Plasma* (QGP), state of the matter during the first instants of life of the universe. When two ultra-relativistic heavy nucleus collide, the extreme conditions of temperature and pressure, necessary for the QGP formation, can be created. In particular, heavy quarks (charm and beauty) are produced in hard scattering processes during the first stages of the hadronic collision.
The measurement of hadrons with heavy quarks, in pp collisions at the LHC energies, is a powerful test for perturbative quantum cromodynamics (pQCD) in this energy domains. Moreover, this studies are the necessary reference for studying the production of heavy quarks in nucleus-nucleus collisions: here, the heavy quarks primarily produced, propagate through the hot medium created in the collision and interact with its constituents, bringing information about all the medium evolution. Studying the Λ_c production in p-Pb collisions, in addition, allows for the investigation of *cold nuclear matter* (CNM) effects, not due to the formation of the medium.
The thesis describes the analysis strategy developed and used to measure the Λ_c, through the reconstruction of the decay channels $\Lambda_c^+ \to pK^0_\mathrm{S}$, using invariant mass studies. The analysis has been performed using two data sample: $\sim 3 \times 10^8$ events in pp collisions at $\sqrt{s}$ = 7 TeV and $\sim 10^8$ events in p-Pb collisions at $\sqrt{s_{NN}}$ = 5.02 TeV, collected respectively in 2010 and 2013 with the ALICE detector.
All the relevant results are shown, from the Λ_c signal extraction in several intervals of transverse momentum, to the measurement of the cross section of production of Λ_c *prompt* (i.e. from direct hadronization of quark charm). The results are compared with those obtained with other analyses performed with the ALICE experiment, using different analysis strategies and different Λ_c decay channels, in both pp and p-Pb sample. Also a first comparison with predictions from Monte Carlo simulation is shown.
The results presented in this thesis have been recently approved by the ALICE Collaboration, and some of them already presented at several national and international conferences. A publication, including all the Λ_c analyses performed in ALICE, is at the first step of review by the Collaboration.

University of Salerno
University of Campania "Luigi Vanvitelli"

Abstract

Measurement of Λ_c Baryon production in the decay channel $\Lambda_c \to pK^0_S$ in proton-proton and proton-lead collisions with ALICE detector at LHC

by Elisa MENINNO

Nella tesi è descritto lo studio della produzione del barione con *charm* Λ_c in collisioni protone-protone e protone-Piombo con l'esperimento *ALICE* (*A Large Ion Collider Experiment*), che opera presso il potente acceleratore *LHC* (*Large Hadron Collider*).
ALICE è stato costruito per studiare collisioni adroniche (pp e nuclei pesanti, A-A) e, in particolare, è ottimizzato per investigare il *Quark-Gluon Plasma* (*QGP*), stato in cui doveva trovarsi la materia nei primi istanti di vita dell'Universo. Quando due nuclei pesanti si avvicinano a velocità prossime a quella della luce per poi collidere, possono ricrearsi le condizioni estreme di temperatura e densità necessarie alla formazione del *QGP*. I quark pesanti (*charm* e *beauty*) sono prodotti in processi di *hard scattering* tra partoni durante le primissime fasi di una collisione adronica.
La misura di adroni contenenti quark pesanti in collisioni pp alle energie di *LHC* è un utile test per la cromodinamica quantistica perturbativa ($pQCD$) in questo nuovo dominio di energia. Inoltre, tali misure costituiscono il termine di confronto per gli studi di produzione di quark pesanti in collisioni tra nuclei. Qui, i quark pesanti primariamente prodotti, infatti, si propagano attraverso il mezzo caldo e denso, formatosi nella collisione, interagendo con i suoi costituenti. Questo li rende sonde sensibili all'intera evoluzione del mezzo caldo creato. Dal confronto delle misure di barioni e mesoni con *charm* (Λ_c è il barione più leggero contenente *charm*), è possibile recuperare preziose informazioni circa il tipo di mezzo formatosi in una collisione tra ioni pesanti.
Studiare la produzione di Λ_c, in collisioni p-Pb, inoltre, permette di studiare effetti di materia nucleare fredda, non dovuti alla formazione del *QGP*.
In questa tesi viene descritta la strategia di analisi sviluppata e utilizzata per misurare il barione Λ_c , attraverso la ricostruzione del canale di decadimento $\Lambda_c^+ \to pK^0_S$ basata su studi di massa invariante. L'analisi è stata eseguita su due campioni di dati: circa 3×10^8 eventi in collisioni pp a $\sqrt{s}$ = 7 TeV e circa 10^8 eventi in collisioni p-Pb a $\sqrt{s_{NN}}$ = 5.02 TeV, raccolti rispettivamente nel 2010 e nel 2013 con il rivelatore *ALICE*. Sono presentati i risultati ottenuti, dall'estrazione del segnale per la Λ_c in diversi intervalli di impulso trasverso, fino alla misura della sezione d'urto di produzione di Λ_c *prompt* (da adronizzazione diretta del quark *charm*). I risultati sono inoltre confrontati con quelli ottenuti con altre analisi, realizzate sempre con l'esperimento *ALICE* e usando entrambi i campioni dati pp e p-Pb , ma studiando diversi canali di decadimento e utilizzando diverse strategie di analisi.
Una pubblicazione su questa analisi è attualmente il fase di *review* da parte della Collaborazione ALICE.

Ringraziamenti

Voglio cominciare questa pagina ringraziando la mia splendida famiglia: grazie i miei genitori Angela e Tonino, che sin da bambina mi hanno fatto capire l'importanza dello studio, e mi hanno dato la possibilità di inseguire i miei sogni, incoraggiandomi sempre. Grazie a loro, ai miei fratelli e a mia sorella, non mi sono mai sentita sola in questi lunghi anni di studio, e, forte del loro amore, sono arrivata alla fine di questo percorso.
I miei più sentiti ringraziamenti vanno al mio tutor, il Professore Salvatore De Pasquale, per avermi introdotta in un ambiente di lavoro tanto stimolante. Qualche anno fa, non avrei mai immaginato di poter passare tanto tempo al CERN, partecipare alla presa dati ad LHC passando giorni e notti nella Control Room di ALICE, collaborare con fisici da tutto il mondo, parlare del mio lavoro a conferenze internazionli.. Grazie per aver sempre avuto fiducia nelle mie capacità, dandomi la possibilità di fare tutte queste esperienze.
Il lavoro presentato in questa tesi non sarebbe mai arrivato a conclusione senza le mie collaboratrici di sempre: grazie in particolare alla Dott.ssa Annalisa De Caro, mia guida dai tempi della laurea magistrale, fonte inesauribile di idee e di motivazione. Grazie a lei e alla Dott.ssa Paola Pagano per avermi fatto dono della loro esperienza, per la pazienza, i consigli, per avermi mostrato quanta passione e dedizione richiede la ricerca, stimolando in me sempre maggiore entusiasmo per questo lavoro.
Ringrazio il gruppo ALICE TOF, in cui, partendo dai miei turni QA, ho imparato tantissimo.
Ringrazio anche i coordinatori del gruppo di lavoro "D2H" per aver saputo coordinare al meglio la mia analisi e quella di altri fino ad arrivare alla tanto agognata pubblicazione dei nostri risultati.
Grazie ai miei amici di Salerno e Grottaminarda, ai miei colleghi fisici, coristi e ciclisti, le mie dolci conquiline e grazie ai miei amici a Ginevra. Tutti loro hanno impreziosito questi tre anni della mia vita, regalandomi tanti momenti felici.
Merci beaucoup Martine et Alexandra, une nouvelle famille pour moi à Gènevé.
Infine, un grazie infinto va a Daniel. Sapere che ci sei sempre tu al mio fianco rende tutto più semplice e bello. Ich liebe dich…

Contents

List of Figures

List of Tables

List of Abbreviations

ACM	**A**uxiliary **C**ontrol **M**odule
ACORDE	**A**LICE **CO**smic **R**ay **DE**tector
AD	**A**LICE **D**iffractive detector
AGS	**A**lternating **G**radient **S**ynchrotron
ALICE	**A** **L**arge **I**on **C**ollider **E**xperiment
AMORE	**A**utomatic **MO**nitoRing **E**nvironment
AOD	**A**nalysis **O**bject **D**ata
ATLAS	**A** **T**oroidal **L**HC **A**pparatu**S**
Bevatron	**B**illions of **eV** Synchro**tron**
BNL	**B**rookhaven **N**ational **L**aboratory
CERN	**C**onseil **E**uropéen pour la **R**echerche **N**ucléaire
CM	**C**enter of **M**ass
CMS	**C**ompact **M**uon **S**olenoid
CNM	**C**old **N**uclear **M**atter
CPDMC	**C**lock and **P**ulser **D**istribution **M**odule
CTP	**C**entral **T**rigger **P**rocessor
CTTM	**C**osmic and **T**opology **T**rigger **M**odule
DA	**D**etector **A**lgorithm
DAQ	**D**ata **Acq**uisition
D-RORC	**D**AQ **Read**out **R**eceiver **C**ard
DAs	**D**etector **A**lgoritms
DATE	**D**ata **A**cquisition and **T**est **E**nvironment
DCA	**D**istance of **C**losest **A**pproach
DCAL	**D**i-jet **CAL**orimeter
DCS	**D**etector **C**ontrol **S**ystem
DDL	**D**etector **D**ata **L**inks
DRM	**D**ata **R**eadout **M**odule
DQM	**D**ata **Q**uality **M**onitoring
ECS	**E**xperiment **C**ontrol **S**ystem
EMCAL	**E**lectroMagnetic **CAL**orimeter
ESD	**E**vent **S**ummary **D**ata
FEA	**F**ront-**E**nd **A**nalogue
FEE	**F**ront-**E**nd **E**lectronics
FEP	**F**ront-**E**nd **P**rocessor
FMD	**F**orward **M**ultiplicity **D**etector
FPGA	**F**ully **P**rogrammable **G**ate **A**rray
FXS	**F**ile **E**xchange **S**erver
GDC	**G**lobal **D**ata **C**ollector
GUI	**G**raphical **U**ser **I**nterface
HF	**H**igh **V**oltage
HLT	**H**igh **L**evel **T**rigger
HMPID	**H**igh-**M**omentum **P**article **I**dentification **D**etector
HPTDC	**H**igh **P**erformance **T**ime To **D**igital **C**onverter

ITS	**I**nner **T**racking **S**ystem
LDC	**L**ocal **D**ata **C**oncentrator
LEIR	**L**ow **E**nergy **I**on **R**ing
LHC	**L**arge **H**adron **C**ollider
LHCb	**L**arge **H**adron **C**ollider **b**eauty
LTM	**L**ocal **T**rigger **M**odule
LTU	**L**ocal **T**rigger **U**nit
IP	**I**nteraction **P**oint
ME	**M**atching **E**fficiency
MO	**M**onitor **O**bjects
MPI	**M**ulti-**P**arton **I**nteraction
MRPC	**M**ultigap **R**esistive **P**lat **C**hambers
MVA	**M**ulti**V**ariate **A**nalysis technique
MW	**M**atching **W**indow
OCDB	**O**ffline **C**ondition **D**ataBase
OO	**O**bject **O**riented
PCB	**P**rinted **C**ircuit **B**oard
PDS	**P**ermanent **D**ata **S**torage
PHOS	**PHO**ton **S**pectrometer
PID	**P**article **I**dentification
PMD	**P**hoton **M**ultiplicity **D**etector
pQCD	**Q**uantum **C**romo**D**ynamics
PS	**P**roton **S**ynchrotron
PSB	**P**roton **S**ynchrotron **B**ooster
QED	**Q**uantum **E**lectro-**D**ynamics
QGP	**Q**uark-**G**luon **P**lasma
RHIC	**R**elativistic **H**eavy **I**on **C**ollider
RPC	**R**esistive **P**lat **C**hambers
SDD	**S**ilicon **D**rift **D**etector
SPD	**S**ilicon **P**ixel **D**etector
SPS	**S**uper **P**roton **S**ynchroton
SSD	**S**ilicon **S**trip **D**etector
TDC	**T**ime To **D**igital **C**onverter
TDS	**T**ransient **D**ata **S**torage
TOF	**T**ime **O**f **F**light
TPC	**T**ime **P**rojection **C**hamber
TRD	**T**ransition **R**adiation **D**etector
TRM	**T**DC **R**eadout **M**odule
ZDC	**Z**ero-**D**egree **C**alorimeter

.

Dedicated to my family…

Introduction

The study of the behavior of heavy (*charm* and *beauty flavoured*) quarks is a unique tool to investigate the medium formed in heavy-ion collisions, called *Quark-Gluon Plasma* (QGP). As part of this program, the investigation of thermalization and hadronization of heavy quarks in the medium can be studied via the baryon/meson ratio for charm (Λ_c /D) and for beauty (Λ_b/B). It has been predicted [1] that if [ud] di-quark exist in the QGP formed in heavy ions collisions, this would lead to a significant enhancement of Λ_c $/D^0$ (and Λ_b $/D^0$). Indeed, in the presence of di-quarks [ud], the Λ_c (Λ_b) can be formed from two-body collisions between c (b) quarks and [ud] quarks. Compared to the usual three-body collisions among c(b), u and d, the two-body collisions have a larger phase space than the three-body collisions. In Fig. 1 the yield of Λ_c , estimated in a quark coalescence model, is plotted as a function of the temperature of QGP. The dashed line corresponds to the case without di-quark mass, the two solid lines are instead for the cases with di-quark mass $m_{[ud]}$ of $450MeV$ (bold solid line) and 600 MeV (thin solid line)

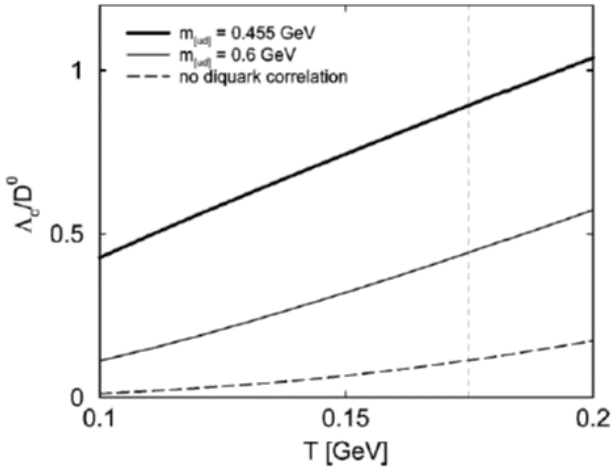

FIGURE 1: Λ_c yield in function of the temperature of the QGP, estimated in a coalescence model.

The Λ_c analysis described in this thesis is performed with the ALICE (*A Large Ion Collider Experiment*) experiment at the LHC (*Large Hadron Collider*). A subset of the central barrel detectors of ALICE is essential for the analysis: the *Inner Tracking System* (ITS) for vertex reconstruction and tracking, the *Time Projection Chamber* (TPC) for tracking and Particle Identification (PID) and the *Time of Flight* (TOF) detector for PID.
The measurement of Λ_c in Pb-Pb collisions is challenging with the resolution on the impact parameter of the current *Inner Tracking System* (ITS) detector [2]. However, it's really important to study heavy baryon production also in elementary systems, i.e pp and p-Pb collisions.

- pp collisions:

It is necessary for ALICE to establish a firm baseline measurement in pp collisions measuring Λ_c production through different channels. It is also worthwhile to note that Λ_c production has been measured mainly at electron-positron colliders at SLAC [3], elsewhere before [4, 5] and at HERA in ep collisions [6]. Existing Λ_c cross-section measurements at hadron colliders are back to ISR [7] in a completely different energy regime. At Tevatron collider D mesons have been extensively measured, in terms of cross section too [8], while no-$prompt$ Λ_c s have been reconstructed as decay products of b-hadrons [9]. Several decay modes of Λ_c^+ have been measured by FOCUS [10] with a fixed-target experiment at FNAL, (but not the channel object of this analysis). At LHC the LHCb experiment reported a measurement of $prompt$ Λ_c^+ production at forward rapidity [11], (our analysis will be done at midrapidity and employing the reconstruction of a different decay channel).

- p-Pb collisions:
  a complete understanding of the Pb-Pb results requires an understanding of cold nuclear matter effects in the initial and final state, which can be accessed by studying p-Pb collisions assuming that the QGP is not formed in these collisions. In the initial state, the nuclear environment affects the quark and gluon distributions, which are modified in bound nucleons depending on the parton fractional momentum x and the atomic mass number A [12] [13]. At LHC energies, the most relevant effect is shadowing: a reduction of the parton densities at low x, which becomes stronger when Q^2 decreases and the nucleus mass number A increases. This effect, induced by the high phase-space density of small-x partons, can be described, within the collinear factorization framework, by means of phenomenological parameterizations of the modification of the PDFs (denoted as nPDFs). If the parton phase-space reaches saturation, PDF evolution equations are not applicable and the most appropriate theoretical description is the Colour Glass Condensate effective theory (CGC) [14]. Furthermore, the multiple scattering of partons in the nucleus before and/or after the hard scattering can modify the kinematic distribution of the produced hadrons: partons can lose energy in the initial stages of the collision via initial-state radiation [15], or experience multiple soft collisions before the heavy-quark pair is produced [16]. In addition to the initial-state effects, also final-state effects may be responsible for a modification of heavy-flavour hadron yields and momentum distributions. The presence of significant final-state effects in high-multiplicity p–Pb collisions is suggested by different observations, e.g. the presence of long-range correlations of charged hadrons [17] [18], the evolution with multiplicity of the identified-hadron transverse-momentum distributions [19], and the suppression of the Ψ(2S) production with respect to the J/Ψ one [20].

We study the channel $\Lambda_c^+ \rightarrow p\bar{K^0}$ exploiting the ALICE PID and tracking capabilities (in particular using V0 topology reconstruction to reduce combinatorial background) and it extends, with respect to the golden channel, i.e. $\Lambda_c^+ \rightarrow pK^-\pi^+$, the $p_{\rm T}$ range of the measurement at higher momenta. The present thesis is organized as described in the following:
After the introduction, the first chapter (1) will be focused on the hadron matter phase transition, from ordinary strong matter to a new phase (the QGP), and on the QGP studies possible nowadays trough experiments with heavy-ion collisions.
Among the different ways we have to test the QGP formed, a very important role is played by the heavy flavour (charm and beuty) quarks production. The main results

obtained in different facilities, until the most recent results at the LHC at CERN, are summarized in 2.
The chapter 3 instead will be focused on the ALICE experiment with the LHC at CERN, describing in detail all its components and focusing in particular on those that are crucial for the Λ_c analysis, subject of this thesis.
The TOF detector will be carefully presented in chapter 4.
The Λ_c analysis, through the reconstruction of that particular decay channel, will be explained in the section 5: The Data Sample and Monte Carlo productions used are first introduced, as well as the software implemented. Successively the analysis strategy, with raw yield extraction, efficiency and acceptance estimate, feed-down correction, are carefully described.
In the last chapter, 6, results are finally shown, in terms of Λ_c cross section in pp and p-Pb collisions, with all the studies done to determine the systematic uncertainties for this analysis . Since the unexpected results from the theoretical point of view, a long list of additional checks have been performed to validate the results. Our Λ_c cross section measurement and Λ_c /D^0ratio measurement will be compared with other Λ_c measurements performed both with ALICE and LHCb experiment, as well as the comparison with previous measurements performed with other experiment in different experimental conditions.
After that, conclusions and discussion of results are reported.

Chapter 1

The Quark-Gluon Plasma

In this chapter, the essentials of the Quark-Gluon Plasma (QGP) will be illustrated, as well as the tools we have to study the QGP through heavy-ion collisions.

1.1 Asymptotic freedom and confinement in QCD

The interaction between protons and neutrons inside the nucleus has been studied since the discovery of the atomic structure. Protons were postulated to be held together by an interaction stronger than the electromagnetic one. The introduction of quarks as elementary constituents of protons, neutrons and all the other hadrons opened new possibilities to understand the basis of nuclear force.
The Quantum Electro-Dynamics (QED) has been the first local gauge theory that explained the interaction between electrons and photons through the electric charge current, introduced by an Abelian group U(1) [21].
For the strong force, the interpretation of the quark-gluon interaction as a gauge field theory has been the main theoretical development in order to describe the deep nature of this interaction. Only with the introduction of the quark colour charge and the local gauge symmetry SU(3) colour , it was possibile to define the Quantum Chromo-Dynamics (QCD) [22] [23], the most important theory that allows to explain parton interactions within hadrons.
QCD provides us with two important characteristics of quarks and gluons dynamics:

- Asymptotic freedom
- Break-up of chiral symmetry

Asymptotic freedom Lets consider a quark represented by a triplet ψ. Similarly to the QED case, it is possible to apply the formalism of the Yang-Mills theories at the group SU(3) colour and obtain the QCD Lagrangian:

$$\mathcal{L} = \sum_{i=1}^{N_f} \bar{\psi}_i (i\gamma^\mu D_\mu - m_i)\psi_i - \frac{1}{4}\sum_{a=1}^{8}(F^a_{\mu\nu}F^{a\mu\nu}) \tag{1.1}$$

The first term of the 1.1 sums over the number of flavours, the second one instead is a sum over the number of gauge bosons foreseen in the theory. Since gluons are colour charged, they can interact with each other, showing an opposite behaviour with respect to photons that are not charged. QCD is a non-abelian theory and the evolution term of the gauge fields is defined as:

$$F_{\mu\nu} = \partial_\mu G_\nu - \partial_\nu G_\mu + g f_{abc} G^b_\mu G^c_\nu \tag{1.2}$$

The last term of 1.2 shows that gluons can interact with each other with the same coupling g, as quarks do.

In Fig. 1.1 the strong coupling constant in QCD, $\alpha_s = \frac{g^2}{4\pi}$ is shown, with the anti-screening feature. As the typical length scale decreases (or equivalently the transfert momentum Q of the interaction increases), the coupling strength decreases in QCD, and this is related to the anti-screening of the color charge, in sharp contrast to the screening for the QED. For interactions at high transverse momentum, the coupling decreases and it reaches a fixed ultraviolet point

$$\lim_{q^2 \to \infty} \alpha_s(q^2) = 0 \tag{1.3}$$

This phenomenon is called *asymptotic freedom* of QCD, and its discovery was awarded with the Nobel Prize in 2004 [1].

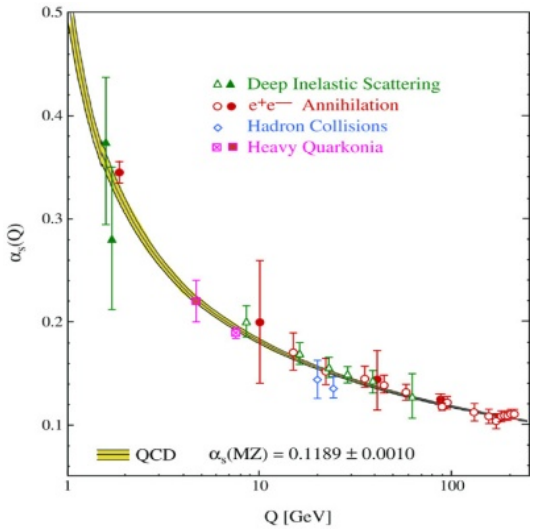

FIGURE 1.1: Coupling coefficient α_s for QCD, as a function of transfert momentum Q, measured with different colliding systems.

Quarks interaction, in this situation, can be studied through the parton model, where the fundamental particles for the strong interaction can be considered as free within hadrons.
On the other side, the coupling increases when the exchanged momentum between coloured objects decreases, and it reaches a potential wall when the distances between quarks are of the order of the fermi (hadrons size). This is a signature of the *confinement* of the color. Due to this effect, quarks and gluons are confined within hadrons and they cannot be "seen" one-by-one. Beyond a critical distance, the potential becomes high enough such that a new quark-antiquark pair pops up from the vacuum. In this way, the original quark-anti-quark pair splits in two pairs. So, quarks are always confined inside hadrons and we can never isolate them in QCD.

α_s has been measured via many different physics channels and the current word average value is 0.1184 $\pm$ 0.0007 [24]. So, perturbative QCD calculations are fully valid to describe the strong interaction at high energies, and this is one of the major successes of the QCD. The description of i) the evolution of parton distribution functions at low Bjorkien x values, ii) the production of jets in elementary collisions, the properties of bottomonium boud states, represent beautiful examples of the success of the QCD predictions in its perturbative domain.

[1] http://www.nobelprize.org/nobel_prizes/physics/laureates/2004/

Since the QCD coupling strength becomes large at long distances, instead, in this case we cannot adopt a perturbative method anymore. So, many effective models have been developed in the domain of hadronic and nuclear physics. Wilson's lattice gauge theory may be used. It treats four-dimensional space-time not as a continuum, but as a lattice with a finite number of points, in analogy with crystals, in which quarks occupy lattice points while the gauge fields occupy the lattice links. Within this lattice discretization, on may solve QCD using Monte Carlo numerical simulations. Lattice calculations for gauge theories is the most promising non-perturbative technique to solve QCD equations. Nowadays, computing facilities for lattice QCD calculations are a crucial component for the scientific research. They allow us to compute the α_s constant, extract the mass of quarks and most of the hadrons, and study the hadronic matter phase diagram.

Chiral symmetry breaking in QCD
A simplified Lagrangian of three quark flavors $f(u, d, s)$ can be written as 1.4:

$$\mathcal{L} = \sum_{f}^{N_f} \bar{\psi_f}(i\not{D} - m_f)\psi_f - \frac{1}{4}G^a_{\mu\nu}G^a_{\mu\nu} \tag{1.4}$$

with $N_f = 3$, the coupling gluon field tensor is defined as

$$G^a_{\mu\nu} = \partial_\mu A^a_\nu - \partial_\nu A^a_\mu + g f^{abc} A^b_\mu A^c_\nu \tag{1.5}$$

and the covariante derivate of the quark field is

$$i\not{D}\psi = \gamma^\mu(i\partial_\mu \quad + g A^a_\mu \frac{\lambda^a}{2})\psi \tag{1.6}$$

The gauge covariant derivative relates the coupling of the interaction between the fundamental constituent g and the gauge fields, bearer of the colour interaction, the gluons.

For massless quarks, this QCD Lagrangian exhibits a chiral [2] symmetry. This means that one can decompose the quark files in left-handed and right-handed:

$$\psi_{L,R} = \frac{1}{2}(1 \pm \gamma_5)\psi \tag{1.7}$$

and the QCD Lagrangian 1.4 will be invariant under helicity and flavour transformations. This symmetry is represented as the $SU(3)_L \times SU(3)_R$ symmetry of QCD. A consequence is that the associated parameter, the vacuum expectation value or condensate $< \bar{q}q >$, should be equal to zero.
However, the condensate $< \bar{q}q >$ is not zero, (the existence of the pion is a confirmation of that [25]) and this is what is called *spontaneous breaking of the chiral symmetry*. The worlds *spontaneous* reminds that the chiral symmetry is respected by the QCD Lagrangian, but broken by the states at low energies. This spontaneous breaking of the chiral symmetry is one of the predictions of the QCD and it allows to predict the existence of the Goldstone bosons. The symmetry should be again restored at high energies and a restoration of symmetry represents a valid condition for the existence of a phase transition. An analogy with the ferromagnetic transition, for metallic superconductors, related to the spontaneous breaking of the isotropy symmetry, can be made.

[2] "Chiral" derives form "hands" in Greek.

In quantum filed theories, the symmetries of the Lagrangian can be spontaneously broken at low energies or temperatures. In the QCD in particular, at low energies there is a spontaneous breaking of the chiral symmetry. The restoration of this symmetry at high temperatures becomes a good condition for the existence of a phase transition.
It should be noticed that the initial assumption for the Lagrangian (1.4) was consider quarks u, d and s without mass. Clearly their mass is not zero, anyways that is a good approximation, since tje masses of the light quarks are small compared to Λ_{QCD}.

1.2 QCD phase transition

On the basis of thermodynamical considerations and QCD calculations, strongly interacting matter is expected to exist in different states. Its behaviour can change for different conditions of temperature and baryonic chemical potential μ_B. μ_B is defined as the energy E needed to increase of one unity the total number of baryons and anti-baryons:

$$\mu_B = \frac{\partial E}{\partial N_B} \tag{1.8}$$

In Fig. 1.2 the phase diagram for hadronic matter[3] is presented, for non vanishing μ_B and in the pressure versus temperature plane.

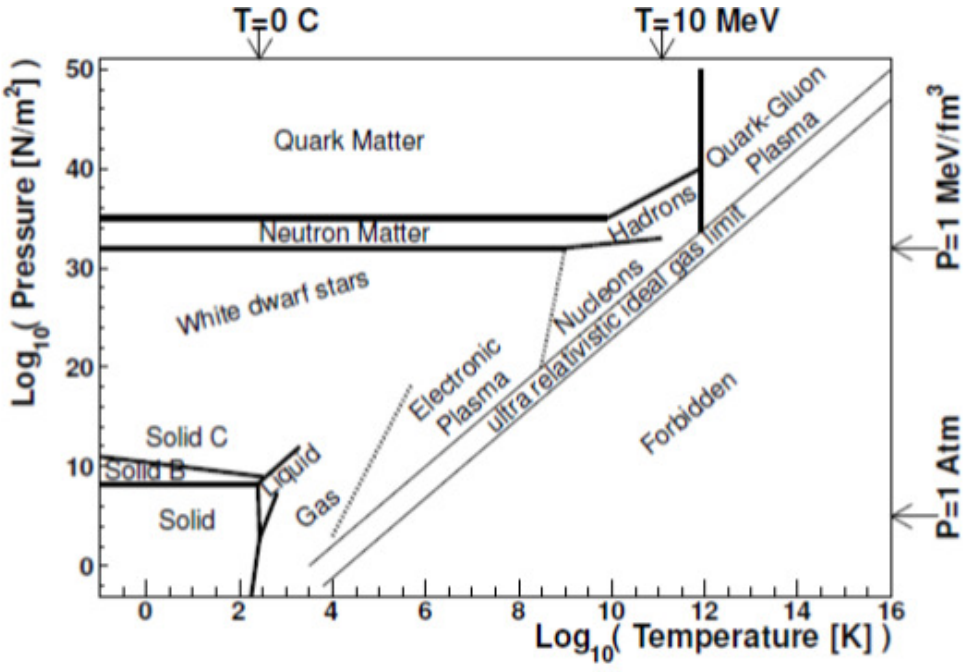

FIGURE 1.2: Phase diagram of hadronic matter in the pressure versus temperature plane for non vanishing baryonic potential.

We can immediately distinguish two regions, one for temperatures below $10^{19}K$ and pressure below $10^{30}Pa$, where the electromagnetic interaction between atoms or ions provides the proper degrees of freedom, and one for temperatures and/or

[3]matter in which the strong interaction is the main interaction between its elementary constituents

pressures higher, where the strong interaction is dominant.
More in details, at temperatures above $10^9 K$ (1 MeV and/or pressures above $10^{32} Pa$ ($1 MeV/fm^3$)), the strong interaction is expected to be dominant. At lower temperatures but pressures above 1 MeV/fm^3, the matter can be described as a degenerated gas of neutrons. Such a state should exist in the neutron stars. For higher pressures, above $10^{35} Pa$ (1 GeV/fm^3), the matter is expected to become a low temperature gas of quarks, not anymore confined inside hadrons. On the other hand, the neutron matter is expected to evaporate in a gas of nucleons when increasing the temperature of several MeV, like the liquid-gas phase transition in ordinary matter.
At very high temperatures and pressures, the strength of the strong interaction decreases and the nucleon gas could go through a transition to a deconfined state of matter, expected due to the vacuum polarization at the origin of the asymptotic freedom. In analogy with the electromagnetic plasma where ions and electrons are dissociated, this new and deconfined state of matter has been called *Quark-Gluon Plasma* (QGP) (this name was proposed in the 80's by the Professor E. Shuryak [26]). The transition to the QGP take place at temperatures $\sim$ 200 MeV ($\sim 2{\times}10^{12} K$), with quarks and gluons not confined anymore in colorless particles.
Finally, at temperatures higher than $10^{16} K$, it is really hard to understand very well what would be the structure of matter. Some scientists have speculated about new phenomena, like the formation of microscopic black holes, unification of interactions, formation of superstring gas, ecc..

Fig. 1.3 shows another illustration of the phase diagram of nuclear matter, varying its temperature and baryo-chemical potential.

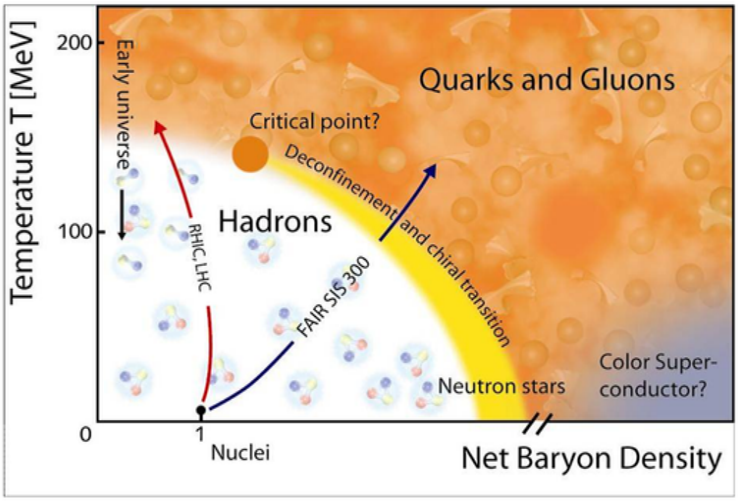

FIGURE 1.3: Phase diagram of hadronic matter in the temperature versus baryonic potential plane.

At low temperatures and for $\mu_B \simeq m_p \simeq$ 940 MeV, the nuclear matter is in its standard conditions (atomic nuclei). Increasing the energy density of the system, "heating" the nuclear matter or increasing μ_B, an hadronic gas phase is reached. In this state nucleons interact and form pions, excited states of the protons and neutrons (Δ resonances) and other hadrons. If the energy density is further increased, a deconfined QGP phase is predicted, with still interacting partons, but not confined within hadrons anymore. For extreme values of baryo-chemical density, nuclear matter should be in conditions of quark colour superconductivity. There are several

"paths" on the phase diagram, that the phase transition can follow, varying the temperature and the baryo-chemical potential, and these transitions can be reproduced only by particular experimental setups. In the early Universe for example, the transition from a QGP phase to hadron matter took place for $\mu_B \sim 0$, as a consequence of the Universe expansion and the decrease of its temperature. In that case the transition phase evolved from a deconfined state of partons to hadronic matter. This transition corresponds to the area on the QCD phase diagram accessible by LHC and RHIC.

The first prediction of a critical transition for the hadron matter at high temperatures was done by Hagedorn in the 60's, before the formulation of the QCD and the discovery of partons [27]. Studying the number of the hadron species (today more than 2000 hadron species have been discovered) he found an exponential trend of the hadron species density ρ with the hadron mass m. He found that his experimental data could be described with the following function:

$$\rho(\mathrm{m}) = \frac{\mathrm{A}}{\mathrm{m}^2 + [500\mathrm{MeV}^2]\exp(\mathrm{m}/\mathrm{T_H})} \tag{1.9}$$

In the 1.9, $\rho(m)$ is the hadron species density per mass unity. The parameter T_H was found, from the experimental data, close to the mass of the pion $\sim 180\ MeV$. It was found out that such a dependence of $\rho(m)$ induces a divergence for the function describing the statistical properties of a hadron gas when the temperature of matter goes above the Hagedorn parameter T_H. Hence, T_H was interpreted as a limiting temperature of matter.

Since the hadron density increases with the temperature[4], at a certain point hadrons overlap with each other and can not be considered anymore as point-like particles, as was instead assumed by Hagedorn. So, in order to understand what happens when $T > T_H$, one first has to understand the internal structure of hadrons and which are the degrees of freedom of the system, and this can be understood thanks to the QCD.

After the first studies made by Hagedorn and after the discovery of the asymptotic freedom [28] [29], the existence of new phase of matter, with deconfined quarks and gluons, was predicted, and a first pioneer phase diagram of hadronic matter was drawn [30], shown in Fig. 1.4.

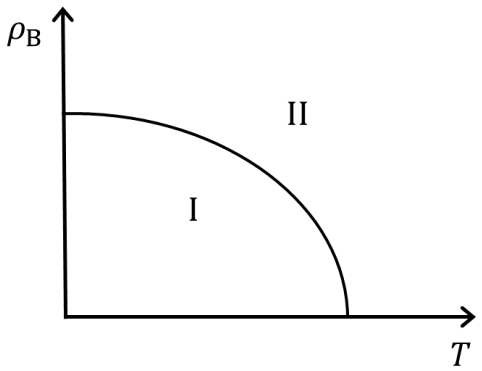

FIGURE 1.4: First phase diagram of hadronic matter [30]: ρ_B is the baryonic density, T is the temperature, I the confined phase and II the deconfined phase.

[4]The energy density of an ideal utra-relativistic gas increases as T^4.

To answer the question if the QGP phase transition really exists or not, the QCD and in particular the intrinsic symmetries of the QCD can help. The dynamical breaking of chiral symmetry is an important aspect of QCD due to the large coupling at low energies that can predicts the occurring of a phase transition at high temperatures.

We have seen that a spontaneous breaking of the chiral symmetry proves that there should be a phase transition of the hadronic matter. One can now wonder if this transformation is related to the deconfinement of quarks and gluons leading to the QGP, or it's just a different phase transformation. Nowadays, lattice QCD calculations are the only way to answer this question.

1.3 Results from lattice QCD calculations

In the last years, many progresses were achieved on algorithms and computing performances, so today lattice QCD allows for non-perturbative QCD calculations with high reliability. Lattice QCD allows to study the interacting potential of quark-antiquark pairs as a function of the radius of the hadrons, varying the temperature of the system. The potential, as shown in Fig. 1.5, seems to decrease till zero values with an increase of the temperature, allowing a deconfined phase where partons are interacting but not constraint within hadrons anymore [31].

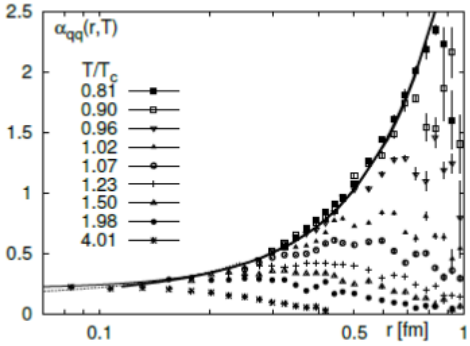

FIGURE 1.5: Coupling of the strong interaction as a function of the distance between two partons, varying the critical temperature of the system. Increasing the temperature, the coupling tends to vanishing and opens the possibility to a deconfined phase.

For massless quarks, lattice pQCD calculations show a phase transition at vanishing baryonic potential, $\mu_B = 0$, as expected from the spontaneous breaking of chiral symmetry. Before the transition, the system should be described with hadrons, while after it, partons become the main characters of the system, with their many more degrees of freedom. We can consider a gas made of quarks and gluons, where the energy density is proportional to the fourth power of the temperature (ϵ/T^4), with a constant ϵ related to the number of degrees of freedom of the system. Results of ϵ/T^4 versus temperature are shown in Fig. 1.6) [32] for 2 or 3 light quarks taken into account in the calculation, or with two lights and one heavies (strange) quark. The observed "jump" in this plot is a signal for the increase of the degrees of freedom of the system, going from the hadronic phase to the deconfined phase. The critical temperature was found to be $T = 173 \pm 15 MeV$ and the critical energy density $\epsilon = 0.7 \pm 0.3 GeV/fm^3$ [33]. It was also observed that, above the critical temperature, the energy density is proportional to T^4, as for an ideal ultra-relativistic

gas, although the corresponded proportionality factor (Stefan-Boltzmann constant) is about 20% smaller than the value for an ideal gas of gluons and u,d and s quarks without mass.

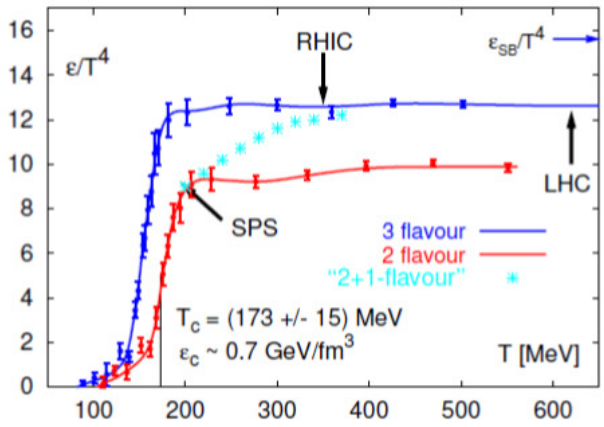

FIGURE 1.6: Energy density in function of the temperature for the hadronic matter at μ_B=0, according to lattice QCD calculations, performed for i) two massless quarks, ii) three massless quarks and iii) two massless quark and one (s) with its real mass. A transition at a temperature of $\sim$ 173 MeV and energy density of $\sim$ 0.7 GeV/fm^3 is observed.

Lattice QCD calculations showed also that for massive quarks (quark s in the Fig. 1.6), there could be a cross-over without criticalness, instead of a phase transition. So, the criticalness of the transition has been studied as a function of the quark masses, as can be seen in Fig. 1.7, assuming $\mu_B = 0$, quarks u and d with same mass and quark s with mass m_s [34]. It can be observed that for both low and large masses for u and d, a first order phase transition is predicted. The cross-over instead occurs for intermediate quark masses. A second order phase transition occurs in the border line between first order and cross-over regions.
Lattice QCD calculations with physical quark masses have determined a critical temperatures between 150-200 MeV. Today there is still some confusion about the exact critical temperature of the transition, depending on the method used for its determination.

Finally, lattice QCD calculations have studied also the order parameters of the chiral and the deconfinement transitions. As it can be seen in Fig. 1.8, both transitions take place at the same critical temperature and, most probably, they are indeed the same transition.

Calculations at $\mu_B \neq 0$, performed in the last years, show that there would be a critical point at $\mu_B \sim 0.75 M_N$ (M_N is the nucleon mass) where the cross-over becomes a second order phase transition. Beyond this critical point the transition would becomes a first order phase transition between the gas of hadrons and the quark-gluon plasma [35](see Fig. 1.9). In addition, other calculations predict a transition to a colour superconductor matter at higher values of μ_B .

1.4 QCD in laboratory: Heavy Ion collisions

The heavy ion collisions allow us to study in detail the hot and dense medium under controlled environments, as beam energy and colliding nuclei can be changed

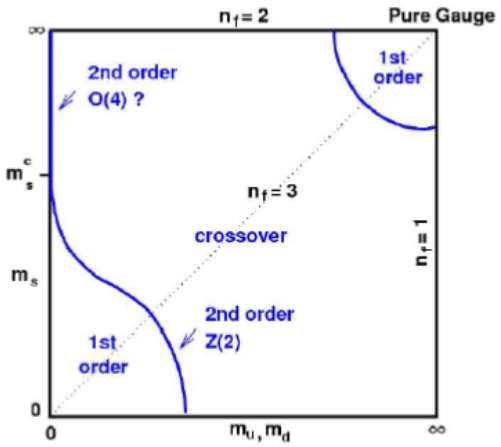

FIGURE 1.7: Lattice QCD calculations of the criticalness of the hadronic matter phase transition for $\mu_B = 0$ and for three quark flavours assuming the mass of u and d identical and a strange quark mass with mass m_s [34].

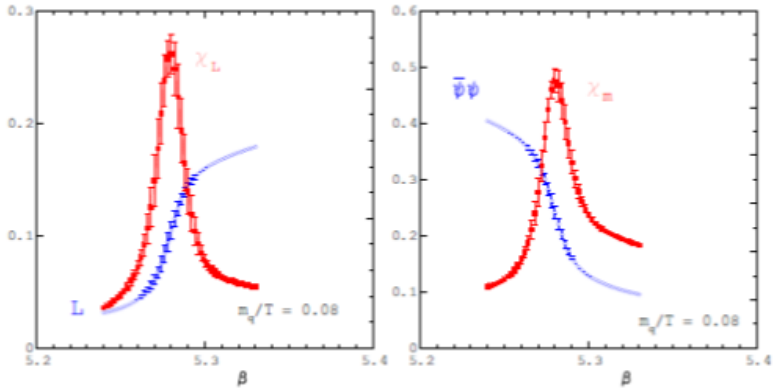

FIGURE 1.8: Critical behavior for massless quarks and for μ_B=0 of the order parameters of the deconfinement transition (on the left) and chiral transition (on the right), predicted by lattice QCD. The order parameters are the *Polyakov susceptibility* χ_L and the *chiral susceptibility* χ_m. The conclusion is that the two transitions would actually be the same transition, or at least they would take place at the same critical temperature.

to explore wider regions in the phase diagran of QGP [36]. Moreover the collider experiments have been providing the possibility to develop realistic theories of the many-body systems of quarks ad gluons including the quark-gluon plasma.

1.4.1 Past achievements until LHC

The energy content available in the nuclear collision is the main factor in which experimental facilities differ from each other [37]. One of the earliest experiments of heavy ion collisions dates back to **Bevalac** at the Lawrence Berkeley National Laboratory, U.S, in 1971, when the proton synchrotron **Bevatron** (**B**illions of **eV** Synchro**tron**) was joined to the SuperHILAC linear accelerator as an injector for heavy ions. It could accelerate a wide range of stable nuclei up to an energy of 2.6 GeV/nucleon [38].
Heavy ion collisions with more higher energies were carried out in the Alternating

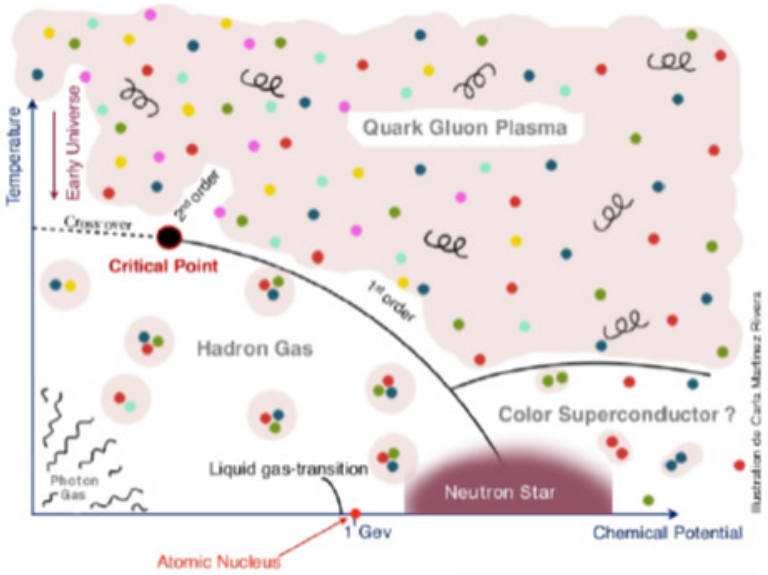

FIGURE 1.9: Hadronic matter phase diagram, according the most recent lattice QCD results and hypothesis.

Gradient Synchrotron (AGS) at the Brookhaven National Laboratory (BNL) for Au nuclei at $\sqrt{s_{NN}}$ = 5GeV and the Super Proton Synchrotron (SPS) at European Organization for Nuclear Research (CERN) for Pb nuclei at $\sqrt{s_{NN}}$=17GeV.
Those were fixed-target experiments. The energy was not sufficient to fully produce the QGP, however their results indicated the existence of a collective behavior in heavy nuclear collisions. The observation at SPS of the J/Ψ suppression, which is possible due to the color screening, also suggested the emergence of primordial medium effects.
One of the biggest achievements of the heavy ion experiments was the discovery of the QGP in the Relativistic Heavy Ion Collider (RHIC) [39–42] at BLN, started in 2000, performing *Cu-Cu* and *Au-Au* at $\sqrt{s_{NN}}$ = 130 GeV and $\sqrt{s_{NN}}$ = 200 GeV. AGS is used as an early-stage accelerator and injector for RHIC. Medium effects are observed in comparison to the results of proton-proton collisions, indicating the existence of the hot and dense matter. One example is the jet quenching, where a small bunch of high momentum hadrons called mini-jet gets suppressed when it travels trough the bulk medium due to the strong interaction with the medium.
On of the greatest achievements at RHIC was finding the QGP as a nearly-perfect relativistic fluid in the vicinity of the quark-hadron cross-over, instead of a gas, as many had speculated before, because of the asymptotic freedom of the QGP. This can be seen comparing the anisotropy in momentum space with that in coordinate space. The QGP has an elliptic shape in the transverse place, for non-central collisions. What happens is that, if the interaction among the constituents is weak, the system is gas-like and the momentum anisotropy is not produced; if, on the contrary, the interaction is strong, the system is liquid-like and momentum distribution would reflect the spatial azimuthal anisotropy. The experimental data [43] [44] show the existence of this anisotropy in momentum space, that reaches the hydrodunamic limit at $\sqrt{s_{NN}}$=200 GeV. The ratio of the azimuthal ellipticity in momentum space ν_2 to that in coordinate space ε over the charged particle yield, per rapidity unity, shown in Fig. 1.10, increases as the collision energy does, for AGS (E877), SPS (NA49) and RHIC (STAR) experiments compared with hydrodynamic expectations.
Experiments at RHIC also give insight into various high-energy phenomena, such as

gluon saturation in the cold nuclear matter (matter at high energy without the effects of the medium). Color glass condensate picture indeed gives a good description of both *d-Au* and *Au-Au* collisions at RHIC (the medium would be produced only in the latter environment). RHIC also has started to explore the system dependence of the hot matter, performing $U-U$ collisions at $\sqrt{s_{NN}}$=193 GeV and $Au-Cu$ collisions $\sqrt{s_{NN}}$=200 GeV.

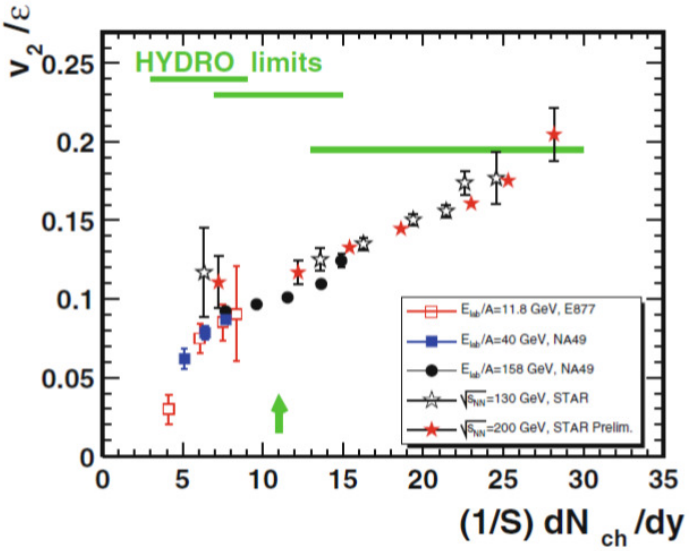

FIGURE 1.10: Ratio of azimuthal ellipticity in momentum space ν_2 to that in coordinate space ε over the charged particle yield per transverse unit area.

With the beginning of the heavy-ion program at the LHC in CERN in 2010, heavy-ion physics entered a new energy regime. LHC run Pb-Pb collisions at $\sqrt{s_{NN}}$=2.76 TeV, during the RunII (the first period of data taking) and its data already has provided valuable information for the quark matter. The analysis of the azimuthal anisotropy at LHC has shown that the medium still behaves like a fluid with small viscosity, and this is an important information, since it was naïvely expected that the QGP become slightly more weakly-coupled with the increase of energy, due to the QCD asymptotic freedom. The energy density at LHC is estimated to be $\sim 15GeV/fm^3$, about three times larger that at RHIC.
During the RunII, started in 2015, LHC run Pb-Pb collisions at $\sqrt{s_{NN}}$=5.5 TeV

1.4.2 Reaction energy and collision geometry

The collision geometry (see Fig. 1.11), for the short-range hadronic interactions, clearly determines the amount of matter participating in the nuclear collision, so it's a very important and carefully explored subject [45–48]. The experimental heavy-ion results from the beginning have confirmed that role of the simple geometric picture of nuclear-collision reaction dynamics [37]: the reaction radius (defined as the squared root of the reaction cross section) rises linearly with the geometric size of the colliding nuclei, described by the sum of their radius, which is proportional to $A^{1/3}$. This means that the colliding nuclei need to "touch" each other for a local deposit of energy and baryon number.
The two nuclei collide nearly at the speed of light in high-energy heavy ion collisions. Thus, they are squeezed in the direction of the beam axis, due to the Lorentz

contraction in the laboratory frame. For example, at LHC energy of $\sqrt{s_{NN}}$ = 2.76 TeV, Lorentz dilatation factor is $\gamma \sim 1500$ for the projectile nucleus, which means that the nucleus of diameter $\sim$ 14 fm is reduced to $\sim$ 0.01 fm (0.1 fm at RHIC corresponding to an energy of $\sqrt{s_{NN}}$ = 200 GeV. The hot and dense medium would be create in the overlapping area between the two passing nuclei.

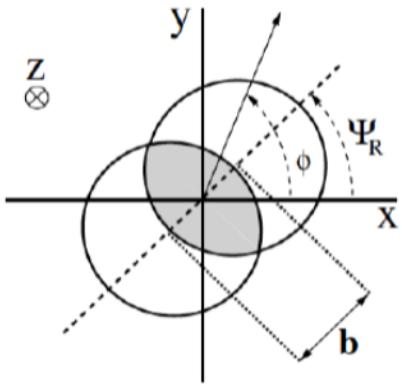

FIGURE 1.11: Geometry of a nucleus-nucleus collision. the vector $\vec{b}$ is the impact parameter for the collisions; Ψ_R is the reaction (or event) plane.

Centrality:
The collision axis is conventionally chosen as *z-axis* and often referred as the longitudinal direction, opposed to the transverse plane, which is perpendicular to the collision axis. It is really important to assure that the collision is as central as possible, in order to minimize the number of spectator (non-interacting or partially interacting nucleons) and maximize the number of participants (nucleons which collide). However, only in quite rare cases, when the impact parameter is very small, we truly can benefit of the largest possible region of interaction and do not encounter complications due to spectators "polluting" the experimental data. The non-centrality of collisions is characterized by the impact parameter *b*, that is the distance between the centers of the two colliding nuclei on the transverse plane. The centrality is defined by groups of events, related to the number of participants. The groups are ordered from the most to the less central events. 0-20% of centrality means, for example, that the most central collisions are selected up to 20% of the total events.
Energy:
A quantity of considerable importance is the **energy content** of the colliding system, that will be, in virtue of the conservation of energy, the energy content of the final-state many-body system. From the energies and the momenta of the colliding projectile (*p*) and target (*t*), we can form the Lorentz invariant quantity(1.10):

$$\sqrt{s_{pt}} \equiv \sqrt{(E_p + E_t)^2 - (\vec{p}_p + \vec{p}_t)^2} \tag{1.10}$$

In the CM frame where $\vec{p}_p + \vec{p}_t = 0$, $\sqrt{(s_{pt})}$ will be the energy content of the projectile-target reaction. Clearly this can be generalized to any number of particles:

$$\sqrt{s^n} \equiv \sqrt{(\sum_{i=1}^{n} E_i)^2 - (\sum_{i=1}^{n} \vec{p_i})^2} \tag{1.11}$$

This will be the final-state energy delivered by the initial colliding nuclei, and it is also the invariant intrinsic rest energy of the fireball of dense matter measured in terms of the energy and momentum of the colliding nuclei.

Rapidity:

The longitudinal momentum of a particle is an inconvenient variable, since it depends on the velocity of the CM frame with reference to the laboratory frame. For the analysis and understanding of the experimental results, it is necessary to be able to view the physical results from the CM frame. The introduction of the *rapidity* y defined as in 1.12:

$$y = \frac{1}{2}\ln(\frac{1+v_z}{1-v_z}) = \frac{1}{2}\ln(\frac{E+p_z}{E-p_z}) = \ln(\frac{E+p_z}{m_\perp}) \tag{1.12}$$

with $m_\perp = \sqrt{(E)^2-(p_z)^2}$ transverse mass, replacing p_z, allows us to change the reference system, being additive under successive Lorentz transformations along the same direction (Lorentz "boost"):

$$y' = y + y_c \tag{1.13}$$

where $y^{'}$ is the rapidity seen in the laboratory system (which moves with velocity v_c with respect to the CM frame of reference and is given in terms of the CM rapidity y and y_c, the rapidity of the transformation.

Pseudorapidity:

In analogy with the definition of rapidity, we can introduce a simpler variable, called *pseudorapidity* η, defined as:

$$\eta = \frac{1}{2}\ln(\frac{p+p_z}{p-p_z}) = \frac{1}{2}\ln(\frac{1+\cos\theta}{1-\cos\theta}) = \ln(\cot\frac{\theta}{2}) \tag{1.14}$$

Where θ is the particle-emission angle relative to the beam axis. In Fig. 1.12 we can see how the angle θ varies with the pseudorapidity. A massless particle emitted transversely at $\eta = y = 0$, for example, has $\theta = \pi/2$.

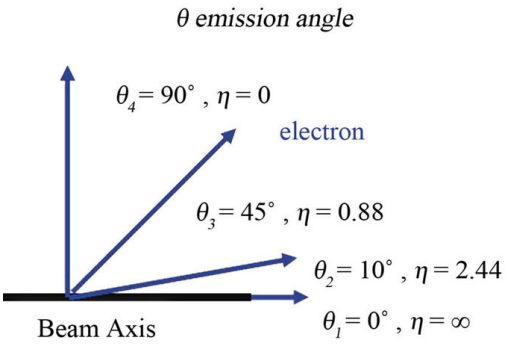

FIGURE 1.12: Relation between the emission angle θ and the pseudorapidity η.

From the relation between pseudorapidity and rapidity, given b

$$m_\perp \sinh y = p_\perp \sinh\eta, E\tanh y = p\tanh\eta \tag{1.15}$$

one can see that that the pseudorapidity is always greater than the rapidity. In collider physics, transverse momentum $p_T = \sqrt{(m_T)^2 - (m)^2}$ and pseudorapidity are very useful, since independent of mass and thus particle species. At relativistic energies they are also close to the transverse mass and the rapidity, respectively, and become identical in relativistic mass-less limit.

1.4.3 Stages and evolution of dense matter

Local equilibrium conditions can be approached in experiments involving heavy ions.
The local average energy of each particle characterizes the local temperature *T*.
Local chemical potentials μ_i are introduced in order to regulate the average particle and/or quark-flavour density.
These parameters express different equilibration processes in the fireball.
Termal equilibrium: In order to establish thermal equilibrium, equipartition of energy among the different particles has to occur in the collision processes. Local thermal equilibrium can be achieved only by elastic scattering, and one can call the time scale on which these processes occur as τ_{th}. The use of the temperature *T* as paramter presupposes that thermal equilibrium has been established.
Chemical equilibrium: This equilibrium requires reactions that change number of particles, and it is more difficult and thus slower to be established. Using the chemical potential μ_i presupposes that, in general, the particular relative chemical equilibrium is being considering, involving reactions that distribute a certain already existent element/property among different accessible compounds. One can call the relevant time scale τ^{re}_{chem}. In relativistic reactions, particles can be made as energy is converted into matter. Therefore one can expect to reach (more slowly) the absolute chemical equilibrium. The relevant time scale can be called as τ^{abs}_{chem} and one can characterize the approach to the absolute chemical equilibrium by the *fugacity factor* γ_i for particle *i*. Often the evolution of γ_i in the collision as a function of time is studied, since the absolute chemical equilibrium cannot generally be assumed to occur.
The following relation exists between the relaxation times:

$$10^{-22}s > \tau^{exp} \simeq \tau^{abs}_{chem} > \tau^{rel}_{chem} > \tau_{th} \tag{1.16}$$

where τ^{exp} is the life expanding fireball of dense matter, of the same magnitude as the time light needs to traverse the largest nuclei.
To understand the difference between absolute and chemical equilibrium, one can consider the **baryon number**, the globally conserved property of dense hadronic matter. Locally, the global conservation implies a balance of inflow against outflow, that means no sources of sinks of baryon number. The chemical potential μ_b controls the difference in number of all baryons and anti-baryons. A change in the energy of the system, according to the first law of thermodynamics, is then given by

$$dE = -PdV + TdS + \mu_b db \tag{1.17}$$

However, the addition of a baryon-anti-baryon pair will not be noted in 1.17, since baryonic number *b* remains unchanged.
Writing the 1.17, it's implicitly assumed that the absolute chemical equilibrium is reached, i.e. we are assuming that there is a bath of baryon number in which our system is immersed, and hence a full phase-space occupancy of all available phase-space cells, without extra space for other pairs. By changing the chemical potential

μ_b we can regulate the difference in number of baryons and anti-baryons, the relative chemical equilibrium controls the relative number of particle by virtue of the value of the chemical potential, while densities of baryons and anti-baryons move together.
The chemical equilibrium and hence the chemical composition of the fireball, evolve along with the temperature of the fireball created in heavy-ion collisions. The following stages occur(see Fig. 1.13):

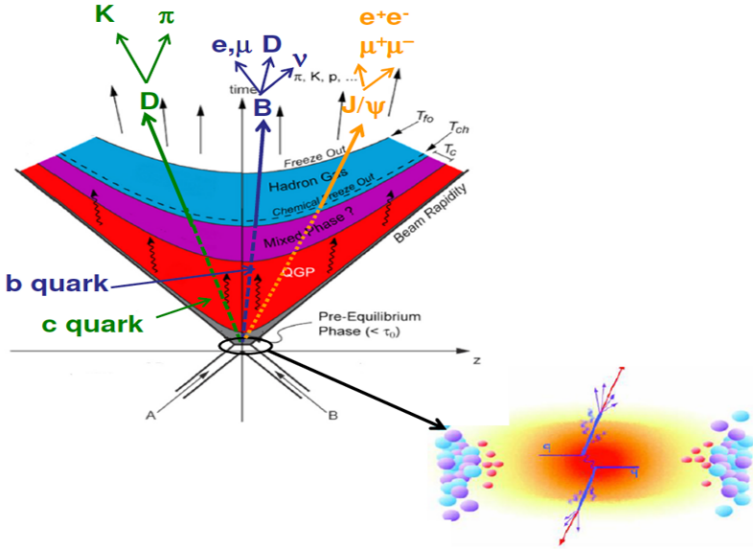

FIGURE 1.13: Different stages of the evolution of the fireball with the temperature.

- The **formation of a thermalized state** within τ_{th} (still subject today to theoretical investigation). We assume that the thermal state of a particle (quark, gluon)–momentum distribution is reached instantaneously, compared with the time scales for the chemical equilibrium. In this way, we can avoid questions about the very first moments of the heavy-ion interactions, and we explore mainly what happens after $\tau_0 \equiv \tau_{th} \simeq 0.25 - 1 fm/c$.

- The subsequent **chemical equilibrium** time. During interaction lasting not less than $\sim$ 1.5 fm/c, different particle-production reactions occur, allowing the approach of the chemical equilibrium for light not-strange quarks. The energy is redistributed among an increasing number of degrees of freedom, so that the temperature drops rapidly.

- **Strangeness chemical equilibrium**: Up to $\sim$ 5 fm/c, the production and then the chemical equilibrium of strange quarks take place. The temperature continues to drop, mainly due to the expansion flow, but also the excitation of the strange quark degree of freedom introduces a non-negligible effect.

- **Hadronization/freeze-out**:The fireball of dense matter expands and decomposes into the final-state hadrons. The dynamics is strongly dependent on the size of the initial state and on the nature of the equations of state.

In the meantime, the local temperature evolves in time to accommodate changes in the internal structure, as expected for an isolated system. So we have a temperature evolution that passes through these series of stages:

- T_{th} temperature associated with the initial thermal equilibrium,
  $\downarrow$ evolution dominated mainly by production of q and $\dot{q}$;
- T_{ch} chemical equilibrium of non-strange quarks and gluons,
  $\downarrow$ evolution dominated by expansion and production of s and $\dot{s}$;
- T_s chemical equilibrium of u, d and s quark flavors,
  $\downarrow$ expansion, dissociation by particle radiation;
- T_f temperature at hadron-abundance freeze-out,
  $\downarrow$
  hadron rescattering and reequilibration;
- T_{tf} temperature at the thermal freeze-out, $T = T(\tau^{exp})$.

1.5 Probing the Quark-Gluon Plasma

We found that at sufficienty high temperatures and/or densities, strongly interacting matter will be in a new state, consisting of deconfined quarks and gluons, the QGP. There are a number of methods we can use to probe the properties of this state [49]:

- hadron radiation
- electromagnetic radiation
- dissociation of a passing quarkonium beam
- energy loss of a passing hard jet

Hadron radiation: Hadron particle yield is an essential observable, since hadrons constitute the bulk part of the produced medium, i.e., most of the initial energy is carried by hadrons. We can get a lot of information analyzing hadron radiation dependence on transverse momentum, rapidity, centrality, beam energy, particle species.
The emission of hadrons consisting of light (u, d, s) quarks has been studied; their size is given by the typical hadronic scale of about 1 fm $\simeq 1/(200MeV)$. Due to the strong interactions with the medium,the particle spectra are expected to contain information about the latest stage of heavy-ion collisions. Since they can't exist inside a deconfined medium, they are formed at the transition surface between QGP and physical vacuum. The physics of this surface is independent on the interior (e.g. how hot is the QGP), so studying soft hadron production in high energy collisions provides information about the hadronization transition, but not about the hot QGP. At the hadronization point, in the case of static thermal radiation, all the information about the earlier stages of the medium is lost. However, if the early medium has a very high energy density and can expand freely, this expansion will lead to a global hydronamic flow, giving ad additional overall boost in momentum to the produced hadrons; they will experience a **radial flow** depending on the initial energy density. Moreover, if the initial condition were not spherically symmetric, as e.g. for the peripheral heavy-ion collisions, the difference in pressure in different spatial directions will lead to a further **directed** or **elliptic** flow. Since both forms of flow depend on the initial condition, these studies can in principle provide information about the very early pre-hadronic stages.
The rapidity distribution dN/dy, or the pseudo-rapidity distribution $dN/d\eta_p$, is a basic observable to quantify the particle production in the system.

The charged particle multiplicities at mid-rapidity are ~ 650 at RHIC $\sqrt{s_{NN}}$ = 17GeV, and $\sim$ 1600 at LHC, as can be seen in Fig. 1.14 (left figure). The transverse momentum distribution, shown in the right panel of Fig. 1.14, is also very informative. Indeed, we can write the particle spectrum in terms of Fouries series expansion of p_{T} spectrum (1.18):

$$\frac{dN}{d\phi_p p_T dp_T dy} = \frac{1}{2\pi}\frac{dN}{p_T dp_T dy}[1 + 2\sum_n \nu_n(p_T, y)cos(n\phi_p - n\Psi)] \tag{1.18}$$

Ψ is the reaction plane, $\nu_n(p_T, y)$ are the Fourier armonics and are they are given by (1.19)

$$\nu_{\mathrm{n}}(\mathrm{p_T}, \mathrm{y}) = \int \mathrm{d}\phi_{\mathrm{p}}\mathrm{cos}(\mathrm{n}\phi_{\mathrm{p}} - \mathrm{n}\Psi)\frac{\mathrm{dN}}{\mathrm{d}\phi_{\mathrm{p}}\mathrm{p_T}\mathrm{dp_T}\mathrm{dy}} / \int \mathrm{d}\phi_{\mathrm{p}}\frac{\mathrm{dN}}{\mathrm{d}\phi_{\mathrm{p}}\mathrm{p_T}\mathrm{dp_T}\mathrm{dy}} \tag{1.19}$$

The second order harmonics ν_2, called *elliptic flow*, is expected to be larger than other harmonics for non-central heavy-ion collisions, due to the space-time azimuthal anisotropy in the hot medium. The large ν_2 observed is well quantified by hydrodynamics models, supporting the fact that the QGP is a strongly-coupled medium. It's known to be roughly proportional to the spatial anisotropy ϵ at RHIC and LHC. Moreover it's known to be very sensitive to the viscosity in the hydrodynamic phase, as deviation from equilibrium would lead to a less strongly-coupled medium. The particle spectrum in high-p_{T} regions ($p_{\mathrm{T}} \geq 5$ GeV) shows non-hydrodynamic behavior. At peripheral collisions the spectrum exhibits power low behavior, expected from the QCD (see plot on the right in the Fig. 1.14). At central collisions, it is clearly less than the scaled reference in pp collisions, since the medium effects become more prominent. The deviation is quantified by the *nuclear modification factor* R_{AA}, defined as (1.20)

$$R_{AA}(p_T, y) = \frac{dN}{p_T dp_T dy} \Big/ < N_{coll} > \frac{dN_{pp}}{p_T dp_T dy} \tag{1.20}$$

where $< N_{coll} >$ is the average number of binary collisions (AA denotes a nucleus-nucleus collision and pp a proton-proton collision reference).

Electromagnetic radiation: the unknown hot medium emits also photons and dileptons (e^+e^- or $\mu^+\mu^-$ pairs), electromagnetically charged particles with no color, formed either by the interaction of quarks and/or gluons, or by quark-antiquark annihilation. The experimental data indicate that the quark-gluon plasma is a very opaque medium with respect to the color charge and that is, on the other hand, reasonably transparent in terms of electromagnetic interactions. So, once photons and di-leptons are formed, since they interact only electromagnetically, they can leave the medium without any further modification. Hence their spectra provide information about the state of the medium at the place or the time they were formed, so they constitute a possible probe of the QGP. Photons created at the time of the collision are called *prompt photons*, as a heavy-ion analogy with the cosmic microwave background in the early universe. Photons emitted from the QGP are called *thermal photons*, in analogy with the black body radiation, and are very useful for the estimation of the medium temperature. Finally, photons produced when hadrons decay in later stages are called *decay photons*: they are the majority ($\sim 90\%$) of the inclusive photons for $1 < p_{\mathrm{T}} < 3$ GeV, after that thermal photons become important. Prompt and thermal photons are called *direct photons*.
Direct photon spectra for $Au-Au$ and pp collisions along with next-to-leading order

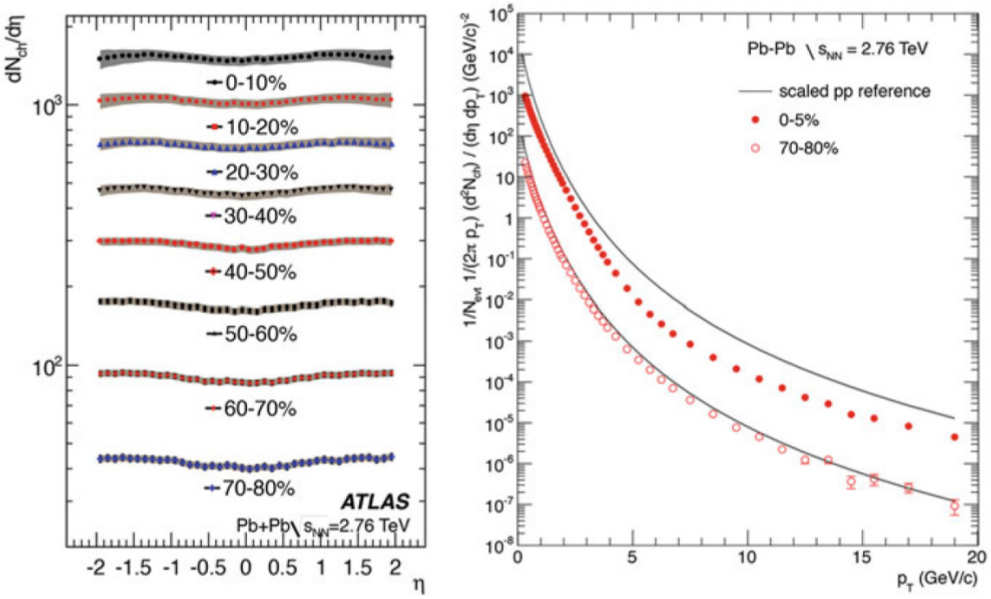

FIGURE 1.14: Left: Pseudo-rapidity distributions of charged particles for different centrality ranges, in Pb-Pb collisions at $\sqrt{s_{NN}}$=17GeV by ATLAS Collaboration. Right: p_{T} spectra of charged particles for central and peripheral collisions at the same energy by ALICE Collaboration.

pQCD calculations are shown in Fig. 1.15 [50], in which a clear enhancement of photon yield for the $Au - Au$ data can be immediately observed. Moreover, fitting with an exponential function, for the medium emitting thermal photons in the central 0-20% collisions the value found for the slope parameter-or effective temperature-is 221 $\pm$ 38 MeV. Since this is the average over time evolution, the initial temperature T_{init} should be larger. Hydrodynamics model calculations suggest $T_{init} \sim$ 300-600 MeV for the thermalization time $\tau_0 \sim 0 - 6 - 0.15 fm/c$, well beyond the crossover temperatuce $T_c \sim 170\ MeV$, suggesting hence that the hot medium is the QGP, instead of just hadronic matter. The enhancement is not observed for d-Au collisions. Experiments at LHC suggest a slightly higher slope parameter of 304 MeV, for the thermal photon production on time average. [51]

One can also consider the elliptic flow of photons in analogy with the hadronic case. The elliptic flow ν_2 of direct photons reflects the termalization time of the QGP, indeed prompt photons don't have ν_2, since the momentum anisotropy has not developed yet at time zero [52]. Finally, the production of W and Z bosons in Pb-Pb collisions at LHC [53] [54]follows very well that of pp collisions scaled by the number of participants. This suggests that they are created at the time of the collision and don't interact with the medium. Same trends can be found for large momentum photons at RHIC and LHC.
Both electromagnetic and hadronic radiations are emitted by the medium itself. Another approach is to test the medium with outside probes, and here we have two successful examples, quarkonia and jet quenching.

Jet quenching: Another possible probe for QGP is to shoot an energetic parton (quark or gluon), into the medium. The quantity on energy loses when it comes out, will tell us something about the medium density. In nucleus-nucleus collisions, a pair of streaks of partons at high momentum, called (mini-)*jet*, are produced. They

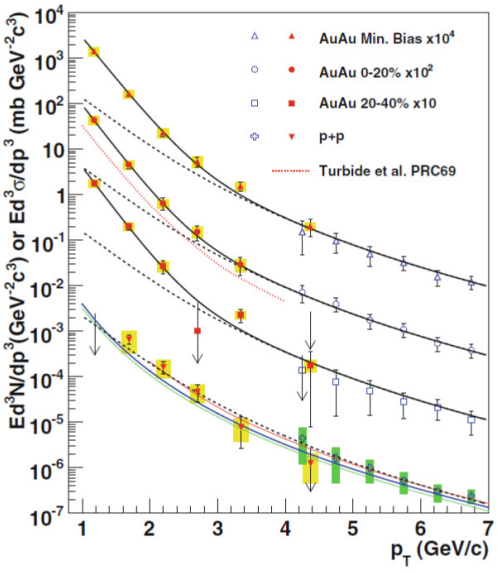

FIGURE 1.15: Transverse momentum dependence of direct photon particle spectra in $Au-Au$ minimum bias collisions at RHIC in 0-20% and 20-40% centrality classes, shown together with pp results [50]. The dashed lines are the scaled pp data; the three lines on the pp results are next-to-leading order pQCD calculations. The dotted line on the $Au-Au$ results is also a result from theoretical calculations.

are not thermalized and are considered to be dominant in hadronic particle spectra at high-p_{T} . The trigger event is called *near-side* jet, the other is the *away-side* jet. For proton-proton binary collisions and deuteron-gold collisions, the two steaks are clearly observed [55]. On the other hand, in heavy-ion collisions, the away-side jet is, at least partially, absorbed [56]. These results are summarized in Fig. 1.16. The phenomenon is called jet quenching and is considered a strong evidence of the formation of a hot and dense medium. In particular, the density increases in the course of the deconfinement transition, and so the energy loss by a fast passing colour charge is expected to increase with the density. Moreover, for quarks, the amount of jet quenching is predicted to depend on the mass of the quarks.

Quarkonia: quarkonia are a special kind of hadrons, bound states of heavy (c or b) quark and antiquark, that are expected to be able to survive in the QGP. Indeed, according to lattice QCD calculations, the ground states of charmonium $J/\Psi(1S)$ and bottomonium Υ have binding energies around, respectively, 0.6 and 1.2 GeV, much larger than the typical hadronic scale $\Lambda_{QCD} \sim 0.2$ GeV; as a consequence, they are smaller, with radii of about 0.1 and 0.2 fm. The higher excited quarkonium states are less tightly bound and hence larger, although their binding energy are in general still larger, so their radii still smaller than those of the usual light quark hadrons, as χ_c(1P) (about 0.3 fm) and Ψ'(2S) (about 0.4 fm). On the other hand, the crucial quantity for dissociation of a bound state is the relation between binding and color screening radius. Because of the color screening effect, the quarkonia melt as the temperature becomes higher, and the phenomenon is called sequential melting. Hence we expect that the different charmonium states have different *melting temperatures*, since for example the higher excited states are lee tightly bound and this easier to melt when the temperature increases. So, analyzing the in-medium quarkonia dissociation, we should have a thermometer for the created QGP. The experimental data show a clear evidence of the suppression of the J/Ψ [57] at SPS,RHIC and LHC.

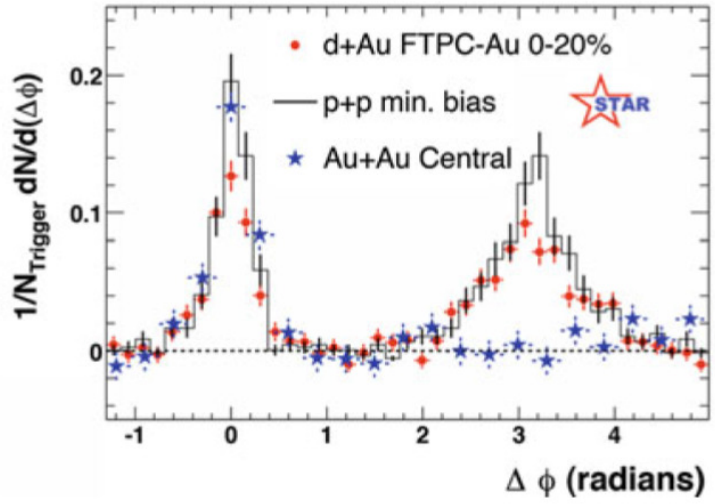

FIGURE 1.16: Correlation of near-side and away-side jets (p_{T} in [4-6] GeV) [56]. It is clearly visible for pp and $d-Au$ collisions, whereas it is lost for $Au-Au$ collisions ($\sqrt{s_{NN}} = 200GeV$

.

It has to be noticed that also J/Ψ regeneration processes in later stages may be important. At LHC it also has been observed a Υ suppression, where the excited state is more suppresses than the ground state, as it can be seen in Fig. 1.17 [58]. It is also interesting to note that the J/Ψ suppression in the Au-Cu collisions [59] at RHIC shows stronger suppression for the Cu-going side whereas it remains the same for the Au-going side compared with the Au-Au collisions.

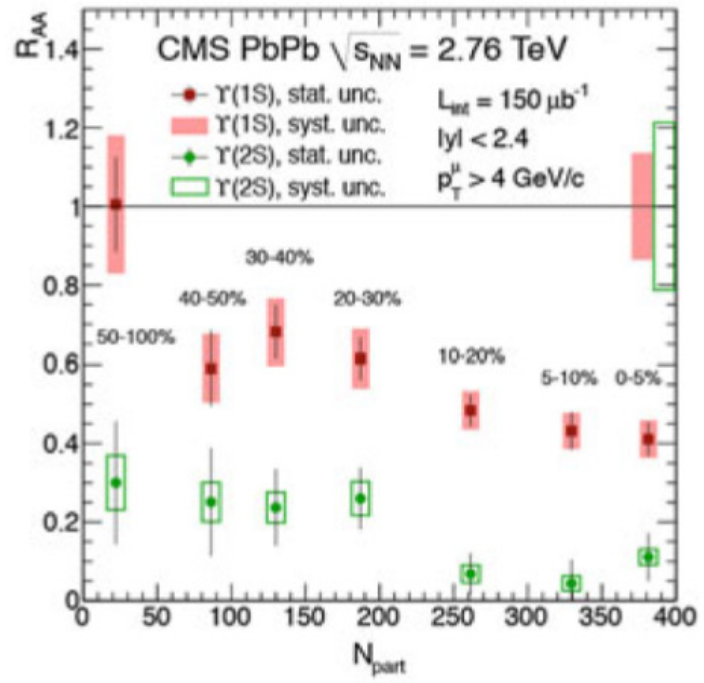

FIGURE 1.17: R_{AA} for $J/\Psi(1S)$ and $\Upsilon(2S)$ as a function of the number of participants in Pb-Pb collisions from the CMS Collaboration at LHC [58].

Quarkonia and jets (as well as open charm/beauty) are called *hard probes*: They are produced at the very early stages of the collisions, before the medium is created.

Chapter 2

Heavy Flavours as powerful probes for the QGP

This chapter is focused on the study of heavy-flavour production in proton-proton, proton-nucleus and nucleus-nucleus collisions. A review [60] of the main results reached at RHIC and LHC will be presented.

2.1 Introduction

Open and hidden heavy-flavour production in nucleus-nucleus collisions is a powerful probe of the QGP. Indeed, charm and beauty are produced in hard parton scattering processes occurring in the early stages of the collision, on a time scale generally shorter than the QGP thermalization time. So they can traverse the QCD medium, interact with its constituents and experience the whole evolution of the medium.
QCD energy loss occurs via both inelastic (energy loss, medium-induced gluon radiation) and elastic (collisional energy loss) processes. So charm and beauty quarks allow for the investigation of the energy-loss mechanisms, in addition to the QGP properties. Furthermore, through their interaction with the medium, low-p_{T} heavy quarks could participate to the collective expansion of the system and possibly reach the thermal equilibrium with its constituents.
Theoretical calculations based on Quantum Chromo-Dynamics (QCD) predict a dependence of the energy loss on the colour charge and on the mass of the parton traversing the medium. This results in an expected hierarchy of the parton energy loss, with beauty quarks losing less energy than charm quarks, and charm quarks losing less energy than light quarks and gluons.
One of the observables that are sensitive to the interaction of hard partons with the medium is the nuclear modification factor R_{AA}, defined as the ratio of the particle yield measured in Pb-Pb collisions and the cross section in pp collisions, scaled with the nuclear overlap integral. R_{AA} is expected to be equal to unity in the absence of medium effects. The expected hierarchy of the energy loss described above can be probed comparing the R_{AA} of different particle species, namely B-, D- and light-hadron R_{AA}.
Further knowledge of the properties of the medium created in heavy-ion collisions can be gained from the study of the azimuthal anisotropy of open heavy flavours: the initial spatial asymmetry of non-central collisions is transformed into an asymmetry in momentum via hydrodynamic expansion of the medium. This is quantified in terms of the second coefficient ν_2 in a Fourier expansion of the D-meson azimuthal distribution, called "elliptic flow". ν_2 brings information on the medium transport properties, on the question if heavy quarks take part in the collective expansion of

the medium, and on the path-length dependence of energy loss.
Quarkonia production in nucleus-nucleus collisions is expected to be significantly suppressed with respect to pp collisions [61]: when the temperature reaches a certain value, the color screening melts the bounded states $c\bar{c}$ or $b\bar{b}$. This suppression should occur sequentially, according to the energy binding of each state. Hence the in-medium dissociation can provide an estimate of the initial temperature reached in the collision. In addition, increasing the collision energy, the $c\bar{c}$ and $b\bar{b}$ pairs multiplicity increases, and this could lead to a new charmonium production via recombination of these quarks [62].
Heavy-flavour production in pp collisions provides important tests of our understanding of many aspects of QCD, both perturbative and non-perturbative. Indeed, while the partonic hard-scattering processes can be calculated in the framework of pQCD, down to low p_{T} , the process of quarkonia bound state formation from heavy-quark pairs is not perturbative, since it involves long distances and soft momentum scales.
Moreover, the study of p-Pb collisions is crucial to access *cold nuclear matter* (CNM) effects in the initial and final state, such as modification of the Parton Distribution Functions in nuclei (nPDF) [63] [64], gluon saturation at low Bjorken-x [65], k_T broadening, assuming that an extended, long-lived QGP is not formed in these collisions.
First systematic heavy-ion measurements in nucleus-nucleus collisions were performed at the RHIC . These studies were continued and extended with higher collision energies at RHIC and LHC. The first run at the LHC, from 2009 to 2013 (*Run I*), has provided a considerable quantity of measurements in pp collisions, at the unprecedented center-of-mass energies $\sqrt{s}$ from 2.76 (reference for Pb-Pb) to 8 TeV, in p-Pb collisions at $\sqrt{s_{NN}}$ = 5.02 TeV and in Pb-Pb collisions at $\sqrt{s_{NN}}$ = 2.76 TeV.
The energy values reached during the secon run (*Run II*) were even bigger: pp collisions at $\sqrt{s}$ = 13 TeV, p-Pb and Pb-Pb collisions at$\sqrt{s_{NN}}$ = 5.02 TeV. With respect to SPS and RHIC, LHC has extended by more than one order of magnitude the range of explored collision energies and has largely enriched the studies of heavy-flavour production with a multitude of new observables and new precision. This was possible thanks to the energy increase, on one hand, and thanks to the excellent performance of the LHC and of the different experiments, on the other hand.

2.2 Heavy-flavour production in proton-proton collisions

The production of open-heavy flavour particles, due to their short lifetime, is studied through their decay products, using different techniques:

- Fully reconstruction of particle decays (the decay channel $\Lambda_{\mathrm{c}} \rightarrow \mathrm{pK}\pi$, used for the analysis described in this thesis, is an example).
- Selection of specific inclusive decays. For example, in order to study the beauty production, one can study a specific particle, like the J/Ψ, imposing that it points to a secondary vertex dislocated a few hundred of μm from the primary vertex. These displaced (or *not-prompt*) mesons are hence supposed to come from beauty decays only.
- Detection of leptons from semi-leptonic hadron decays.
- Reconstruction of c- and b-jets.

A method instead of another one can be used in a specific contest, according to, for example, the trigger strategy, the available statistic, the required precision, ecc.
Hidden heavy-flavours are also investigated analyzing their decay products. For example, the triplet S-waves (J/Ψ, Ψ(2S), Υ(1S), Υ(2S), Υ(3S)) are the most studied, since they decay quite often in di-leptons. The triplet P-waves, such as χ_c and χ_b, are usually reconstructed via their radiative decays into triplet S-waves. Studies of other states, such as the singlet S-wave, are even more complex.
The LHC Run 1 provided a big quantity of measurements in the charm and beauty sector in pp collisions at $\sqrt{s}$ = 2.76, t and 8 TeV:
Heavy-flavour decay leptons The first open-heavy-flavour measurements using heavy-flavour decay electrons were performed at RHIC by PHENIX and STAR in pp and A-A collisions [66] [67], followed by ATLAS [68] and ALICE [69] [70] at the LHC. In Fig. 2.1 a selection of p_{T} -differential cross section measurements in pp collisions are shown, together with theoretical calculations. The p_{T} -differential cross sections are well described by pQCD calculations within uncertainties.

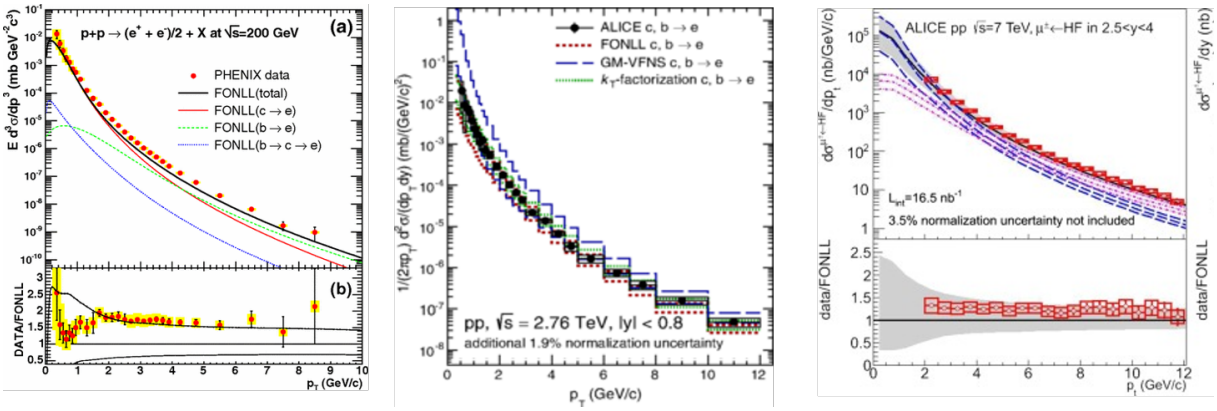

FIGURE 2.1: Heavy-flavour decay electron cross sections in pp collisions. a) Electrons at mid-rapidity for $\sqrt{s_{NN}}$ = 200 GeV from PHENIX [66]; b) electrons at mid-rapidity for $\sqrt{s_{NN}}$ = 2.76 TeV from ALICE [69]; c) muons at forward-rapidity for $\sqrt{s_{NN}}$ = 2.76 TeV from ALICE [70]. FONLL [71], GM-VFNS [72] and k_T-factorization calculation [73] are superimposed.

Open charm D meson production was studied in pp collisions at RHIC, Tevatron and LHC. D mesons are reconstructed via their hadronic decays channels :

- $\mathrm{D}^0 \rightarrow K^-\pi^+$, c$\tau$ = 123 μm, branching ratio (BR) = (3.88 $\pm$ 0.05)%
- $\mathrm{D}^+ \rightarrow K^-\pi^+\pi^+$, c$\tau$ = 312 μm, BR = (9.13 $\pm$ 0.19)%
- $\mathrm{D}^{*+} \rightarrow D^0\pi^+$, strong decay, BR = (67.7 $\pm$ 0.5)%
- $\mathrm{D}_\mathrm{s}^+ \rightarrow \phi\,(\rightarrow K^-K^+)\pi^+$, c$\tau$ = 312 μm, BR = (2.28 $\pm$ 0.12)%

D-meson selection is based on the reconstruction of decay vertices displaced by a few hundred μm from the interaction vertex, exploiting the detector particle identification abilities to reduce the combinatorial background. Raw D-meson yields are obtained from an invariant mass analysis of the pairs/triplets of candidates. The results at RHIC report on inclusive D-meson yield, i.e. those from both c and b quark fragmentation [74]. The former are called "prompt", the last "secondary" D mesons. At Tevatron and LHC, instead prompt D-meson yield are reported. In this case, the contribution from B-meson decay feed-down is subtracted. This is done

in ALICE using pQCD calculations and based on data-driven approach, in order to obtain the prompt D-meson yields. Production cross section measurements of prompt D mesons were performed with ALICE in pp collisions at $\sqrt{s}$ = 7 TeV and 2.76 TeV [75] [76] and found well described by perturbative QCD calculations. The p_{T} -differential cross sections for $\mathrm{D}^0\mathrm{D}^{*+}$and D_s^+ at $\sqrt{s}$ = 7 TeV, as example, are shown in Fig. 2.2, together with FONLL [71], GM-VFNS [72] and k_T-factorization calculation [73]. Within uncertainties, theoretical predictions and measurements agree with each other although the measurements tend to be higher than the central value of the FONLL predictions, as it was observed at lower collision energies, at RHIC and at Tevatron [66]. For GM-VFNS, instead, the data lie on the lower side of the predictions.

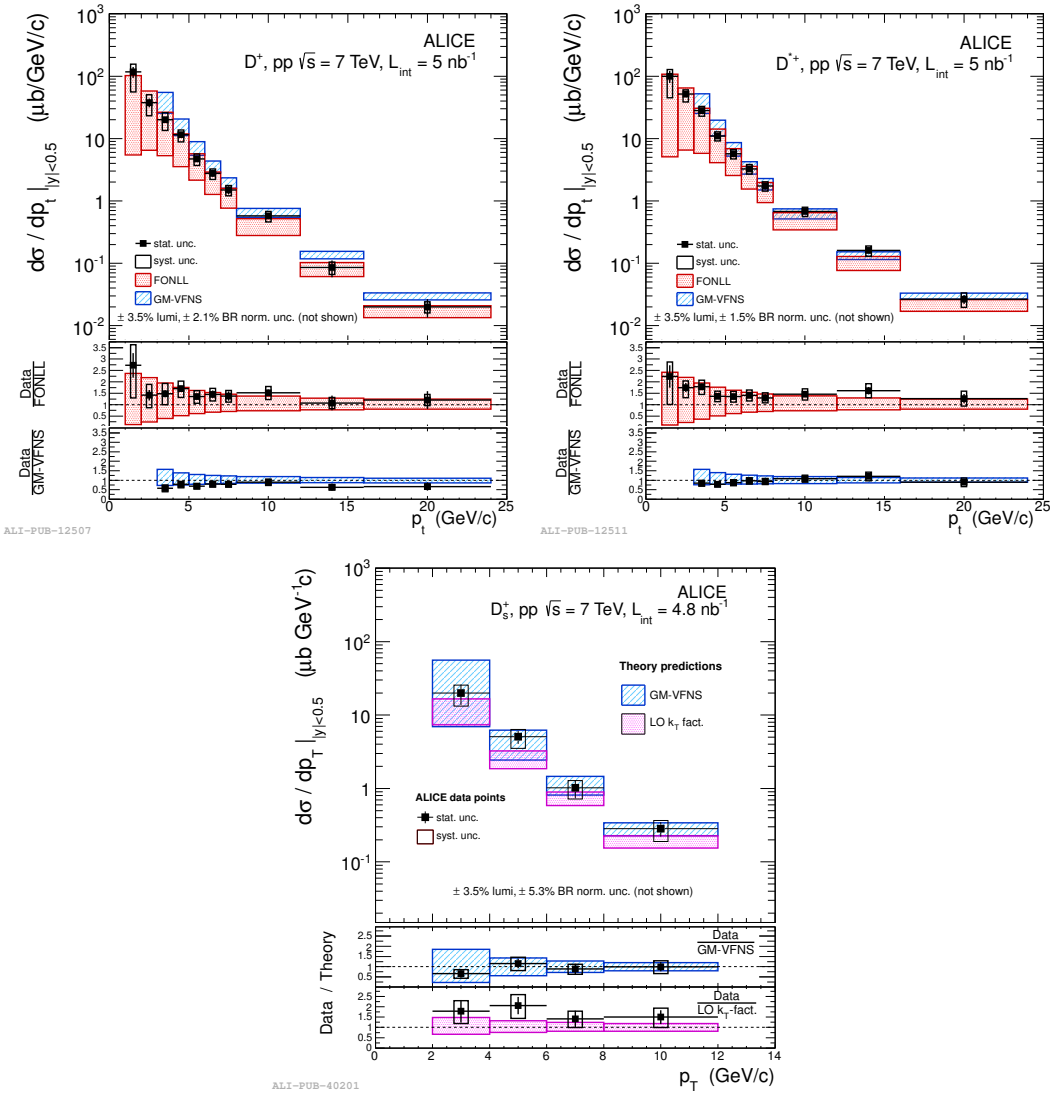

FIGURE 2.2: p_{T} -differential inclusive cross sections for prompt D^0, D^{*+} [75] and D_s^+ [76]in pp collisions at $\sqrt{s}$ = 7 TeV compared with FONLL, GM-VFNS and k_T-factorization theoretical predictions.

In order to extend the D^0 measurement down to p_{T} = 0, where the decay-vertex selection becomes very inefficient, a different analysis technique based on PID and

background subtraction was recently developed [77]. The cross section measurement for prompt D^0 in pp collisions, using this analysis technique, denoted as *without decay-vertex reconstruction* in shown in the Fig. 2.3, together with the results obtained using selection on the secondary vertex. The results with the two different analysis techniques are in good agreement with each other.

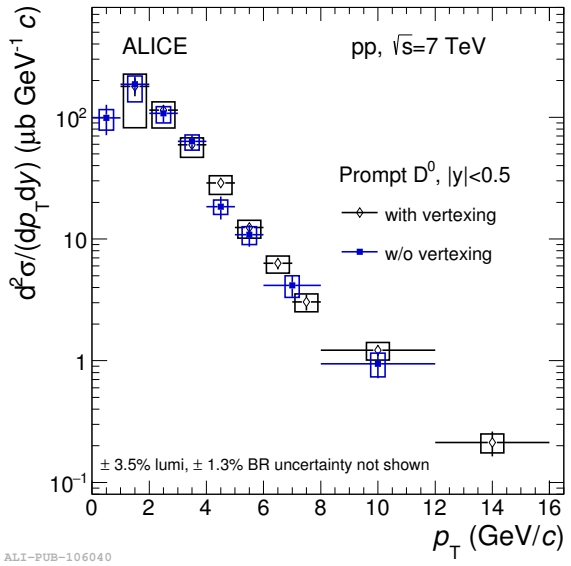

FIGURE 2.3: p_{T} -differential production cross section of D^0 mesons with $|y| < 0.5$ in pp collisions at $\sqrt{s}$ = 7 TeV [77]. The comparison between the prompt D^0 cross sections measured with and without decay-vertex reconstruction is shown.

Multiplicity dependence of D-meson yields The self-normalized yields of D^0, $D^+$and D^{*+} were evaluated as a function of the charged-particle multiplicity normalized by their average in multiplicity-integrated events, for different p_{T} ranges of the D mesons [78] [79]. The average D-meson self-normalized yields in pp collisions are shown in the left panel of Fig. 2.4 for different D-meson p_{T} ranges from 1 to 20 GeV/c. A faster-than-linear increase with the multiplicity can be observed, with a trend that is independent of the D-meson p_{T} within uncertainties.
In the right panel of the same figure, the self-normalized yields are compared with predictions from a percolation model [80], [81], EPOS 3 [82] and PYTHIA [83], all of which include a contribution from MPI to particle production. A qualitative agreement with data is observed for all the models, though at high multiplicities PYTHIA 8 and EPOS 3 without hydrodynamical evolution of the collision seem to underestimate the increasing trend with multiplicity observed in data.
As we will see in the next, a similar increase of charmed-meson yield with the multiplicity is observed in p-Pb collisions [79] (see Fig. 2.9, left plot).

Charmed baryon production measurements in hadron colliders until now are poor. The Λ_{c} analysis discussed here is indeed the first measurement of Λ_{c} in mid-rapidity ($|\eta| < 0.9$) at the LHC energies. Until now Λ_{c} production has been measured mainly at electron-positron colliders at SLAC [3], at CLEO [4], ARGUS [5] and at HERA in electron-proton collisions [6]. Existing Λ_{c} cross-section measurements at hadron colliders in pp collisions are back to ISR [7], at significantly lower energies ($\sqrt{s}$ = 62 GeV). At Tevatron collider, D mesons were extensively measured [8], and non-$prompt$ Λ_{c} were reconstructed as decay products of b-hadrons [9, 84, 85]. At LHC the LHCb experiment reported the measurement of non-$prompt$ Λ_{c} production

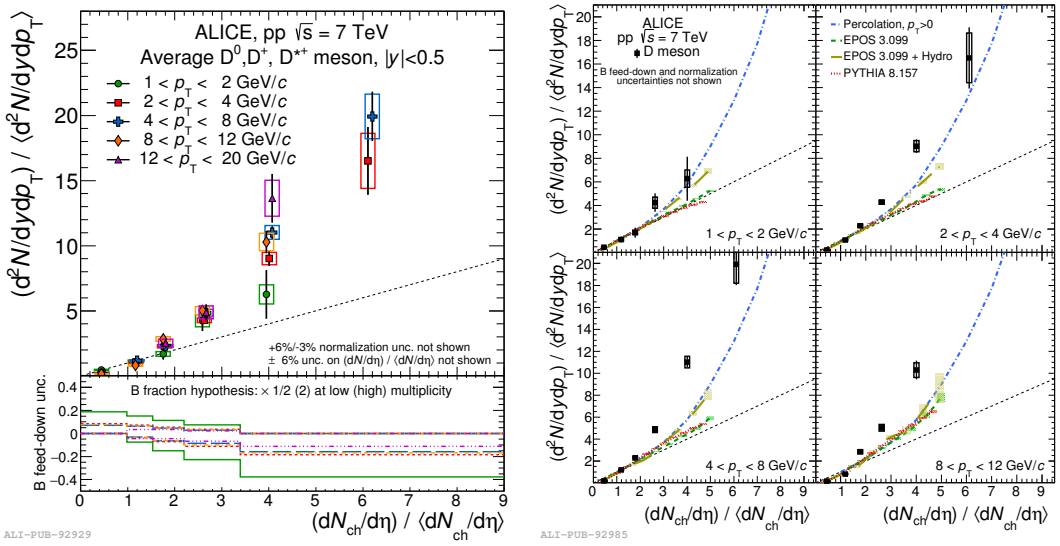

FIGURE 2.4: D-meson yields in pp collisions vs multiplicity.
Left: Average of D^0, $D^+$and D^{*+}relative yields in pp collisions at $\sqrt{s}$ = 7 TeV, as a function of the relative charged-particle multiplicity at central rapidity in several $p_{\rm T}$ intervals. The results are presented with their statistical (vertical bars) and systematic (boxes) uncertainties, except for the feed-down fraction uncertainty that is drawn separately in the bottom panels. **Right**: Results compared with calculations of several event generators with hard and soft components. The position of the points on the abscissa is the average value of $(dN_{\rm ch}/d\eta)$.

in pp collisions at $\sqrt{s}$ = 7 TeV at forward rapidity [11](see FIg. 2.5). No dedicated FONLL calculation is available for $\Lambda_{\rm c}$, due to the poor knowledge of the fragmentation function. GMVFNS predictions, which are compared with the results from LHCb, include the fragmentation function resulting from a fit to e^+e^- collider data, in which prompt and secondary contributions are considered together.
There are not existing measurements of $\Lambda_{\rm c}$ in p-Pb collisions.

Open beauty Open beauty production is usually measured studying b-jets or beauty hadrons via their hadronic decays (in analogy with what done for the D-mesons). They have been studied in the past in e^+e^- colliders. With hadron colliders, the higher collision energy increases their production cross-section but, on the other hand, makes the B-hadrons reconstruction more difficult, due to the very high combinatorics.
Measurements of B cross section via displaced charmonium, have been performed at Tevatron and LHC [88–90], where charmonia from beauty decays are selected by a fit of the decay length distribution of the charmonium candidate. The $p_{\rm T}$ -differential cross sections of charmonia from beauty decay (non-prompt J/Ψ, $\Psi(2S)$, η_c,χ_{c1}, χ_{c2}), showed in Fig. 2.6 at low and intermediate $p_{\rm T}$, are well described by pQCD calculations. At high $p_{\rm T}$, instead, the predictions tend to overestimate the data.

At LHC, ATLAS and CMS also performed measurements of b-jet cross section [91]. Again, the measurements are reproduced quite well by theoretical calculations.

Hence, open charm and beauty differential cross sections in pp are globally well described by the pQCD, even if the theoretical uncertainties are quite large.
Quarkonium production mechanisms are instead still a puzzle and the comparison with models is still not reliable, due to the large theoretical uncertainties.

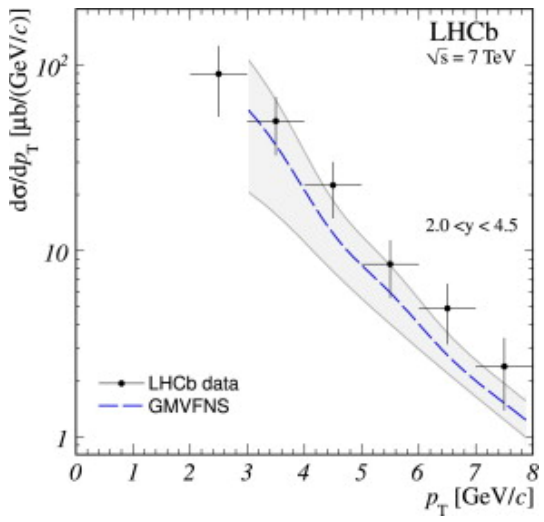

FIGURE 2.5: p_{T} -differential cross sections for charmed baryon Λ_{c}^{+} in pp collisions at $\sqrt{s}$= 7 TeV, measured by LHCb [11], compared with GM-VFNS calculations [86] [87].

In addition to p_{T} - and y-differential cross sections, LHC during Run I has also made first measurements of heavy-flavour production versus charged-particle multiplicity, azimuthal correlations to charged-particles or heavy-flavour hadrons, or measurements of associated heavy-flavour production, allowing for a better and deeper understanding of the production mechanisms.
The analysis of the Run 2 data (taken from 2016) will provide more precise and more differential cross section measurements at the center-of-mass energy of $\sqrt{s}$ = 13 TeV, allowing for, as consequence, strong constraints to the theoretical calculations and better understanding of the production mechanisms.

2.3 Heavy-flavour production in proton-nucleus collisions: study of CNM effects

CNM effects are not due to QGP formation, but to the fact that the colliding particles are nuclei: for example, as far as heavy flavour production is concerned, PDFs in nuclei differ from those in free nucleons, and influence the heavy quark production kinematic. These effects are visible and can be studied in can be studied in p–A collisions. Some of these CNM effects are:

- modification of the effective partonic luminosity in colliding nuclei, with respect to colliding protons, expressed in therms of nuclear-modified PDFs (nPDF) or within the *Colour Glass Condensate* (CGC) theoretical framework at low$x$;
- multiple scattering of partons in the nucleus before and/or after the hard scattering, leading to parton energy loss and transverse momentum broadening;
- in addition to genuine CNM effects, the large set of particles (partons or hadrons) produced, may be responsible for a modification of open heavy flavour and quarkonia production. It's still an open point if this set of particles could form a "medium" with some degree of collectivity [92].

A way to quantify CNM effects is to measure the nuclear modification factor R_{pA}, defined as the ratio between the production yield N_{pA} in p-A collisions, in a given

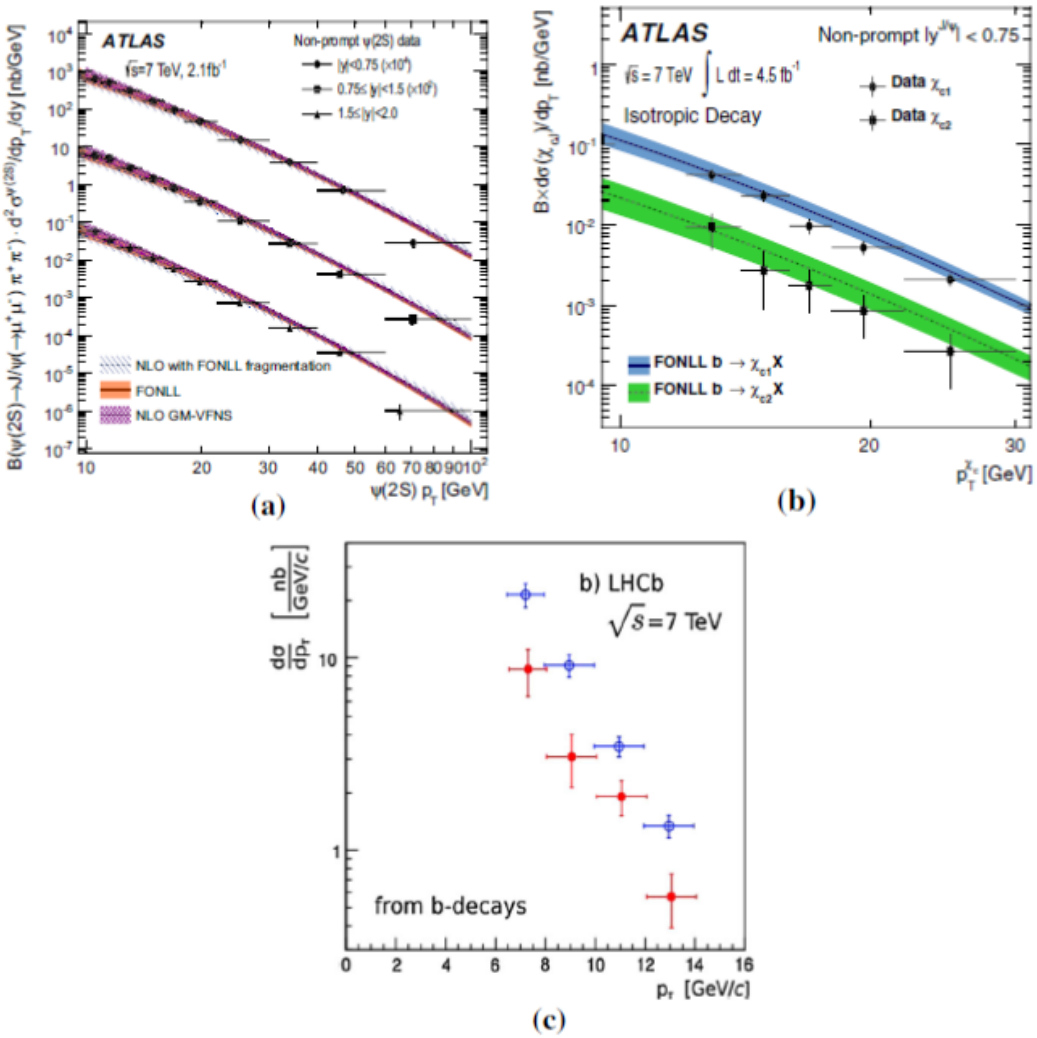

FIGURE 2.6: p_{T} -differential cross sections for non-prompt charmonia (assumed to come from beauty decays: a) $\Psi(2S)$ by ATLAS [89], compared with FONLL [71] and GM-VFNS [86] [87]; b) χ_{c1} and χ_{c2} by ATLAS [90], compared with FONLL [71]; c) J/Ψ and η_c by LHCb [88].

centrality class, and the pp production cross section at the same energy, scaled by the average nuclear overlap function $< T_{\mathrm{pA}} >$, obtained with the Glauber model [93]

$$R^{C}_{\mathrm{pA}} = \frac{N^{C}_{\mathrm{pA}}}{< T_{\mathrm{pA}} >_{C} \sigma_{\mathrm{pp}}} \tag{2.1}$$

In minimum-bias collisions, i.e. without selection on centrality, R^{C}_{pA} becomes

$$R_{\mathrm{pA}} = \frac{\sigma_{\mathrm{pA}}}{A\sigma_{\mathrm{pp}}} \tag{2.2}$$

where A is the mass number. R_{pA} = 1 is expected to be $\sim$ 1, assuming that no medium is created in p-Pb collisions.
In the next, some of the most important and recent results at RHIC and LHC about CNM effects on open and hidden heavy flavour production will be described.

Heavy-flavour decay leptons The production of leptons from charm and beauty decays was studied at RHIC and LHC in d-Au and p-Pb collisions at $\sqrt{s_{\mathrm{NN}}}$ = 200

GeV and 5.02 TeV respectively. The heavy-flavour decay spectrum is determined by extracting the non-heavy-flavour contribution to the inclusive lepton distribution. Beauty decay-electron spectra, in particolar, are extracted from the heavy-flavour decay-electron spectra by a cut or fit of the lepton impact-parameter distribution or taking into account the lepton azimuthal correlation to heavy flavours or charged hadrons.
Heavy-flavour decay lepton $R_{\rm dAu}$ measurements versus transverse momentum, by PHENIX experiment [94], are shown in Fig. 2.7. At mid-rapidity there is a mild dependence on the multiplicity. Results at forward and backward rapidity are similar for peripheral collisions, for most central events instead they show a strong deviation from unity. Preliminary results with ALICE at LHC show a multiplicity-integrated $R_{\rm pA}$ close to unity and a rapidity dependence similar to what observed at RHIC [95]. Within larger uncertainties, first preliminary measurements of the beauty-hadron decay-electrons $R_{\rm pPb}$ at mid-rapidity by ALICE are also consistent with unity [95].
The similar behavior of RHIC and LHC heavy-flavour decay lepton $R^{C}_{\rm pA}$, within the large uncertainties, despite the different x-Bjorken ranges covered, suggests that nPDFs might not be the dominant effect in heavy-flavour production. Additional mechanisms like $k_{\rm T}$-broadening, initial- or final-state energy loss could be at play.

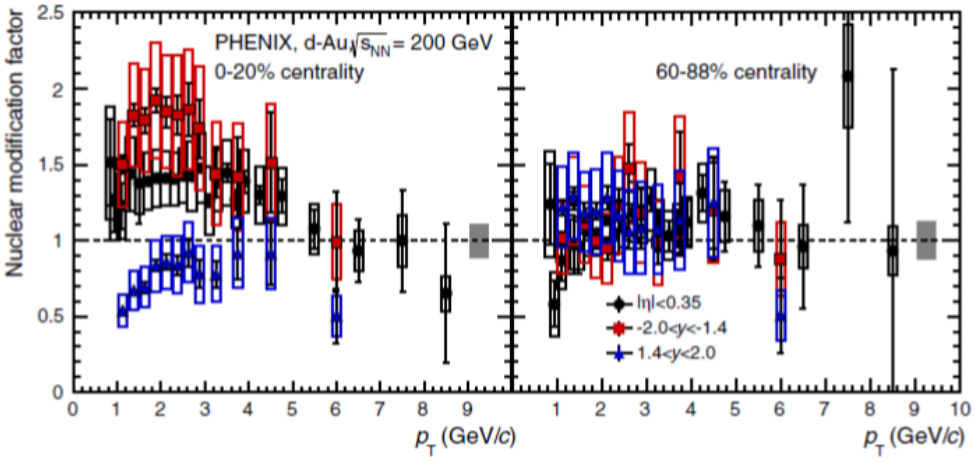

FIGURE 2.7: Nuclear modification factor of leptons from heavy-flavour decays in d-Au collisions. Measurement performed with the PHENIX detector at $\sqrt{s_{\rm NN}}$ = 200 GeV, as a function of $p_{\rm T}$ in two different centrality classes [94].

D mesons The $p_{\rm T}$ -differential cross sections of $\rm D^0$, $\rm D^+$, $\rm D^{*+}$and $\rm D_s^+$ were measured by ALICE in minimum bias p-Pb collisions at $\sqrt{s_{NN}}$ = 5.02 TeV [96], using the same analysis strategy used for the pp data sample. D mesons are reconstructed in different $p_{\rm T}$ intervals in 1 < $p_{\rm T}$ < 24 GeV/c. No significant variations of $R_{\rm pPb}$ among the different D meson-species are observed.
Recently, the nuclear modification factor of prompt $\rm D^0$mesons in the interval 0 < $p_{\rm T}$ < 12 GeV/c was computed using the cross sections in pp and p-Pb collisions resulting from the analysis without decay vertex reconstruction [77]. Figure 2.8 shows the combined measurement of the nuclear modification factor of prompt (non strange) D mesons, obtained by using the $\rm D^0$measurement without decay-vertex reconstruction for the interval 0 < $p_{\rm T}$ < 1 GeV/c and the average of the measurements

for D^0, $D^+$and D^{*+}mesons in the interval $1 < p_T < 24$ GeV/c. In this figure, the combined R_{pPb} from data is compared with theoretical results: on the left the comparison is made with models including CNM effects[63, 97–99], describing quite well the experimental results within uncertainties. On the right, the comparison is also done with the transport model calculations Duke and POWLANG [100], which assume that a Quark-Gluon Plasma is formed in p-Pb collisions. The current precision of the measurement does not allow to discriminate between the two scenarios, with only CNM effects or also with QGP formed, even though the data seem to disfavor a suppression larger than 15-20% in the p_T interval $5 < p_T < 10$ GeV/c.

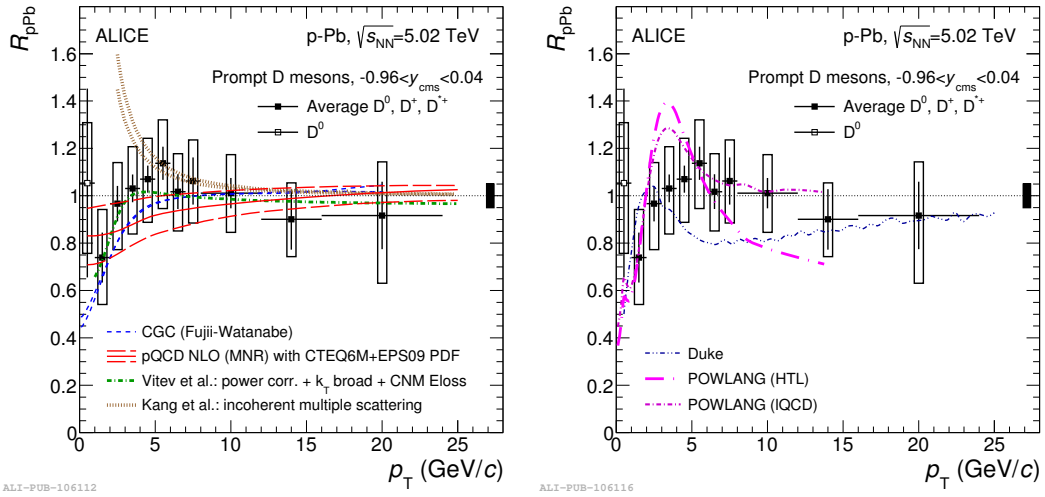

FIGURE 2.8: Nuclear modification factor R_{pPb} of prompt D mesons in p-Pb collisions at $\sqrt{s_{NN}}$ = 5.02 TeV. **Left**: Nuclear modification factor R_{pPb} of prompt D mesons in p-Pb collisions at $\sqrt{s_{NN}}$ = 5.02 TeV: average R_{pPb} of D^0, $D^+$and D^{*+}mesons in the interval $1 < p_T < 24$ GeV/c [96], shown together with the D^0 R_{pPb} in $0 < p_T < 1$ GeV/c [77].The data are compared with results of theoretical calculations including only CNM effects, NLO pQCD with EPS09 nPDFs, a LO pQCD calculation with CNM effects and a calculation based on incoherent multiple scatterings. **Right**: Same data as on the left. Here the results are compared to the results of the Duke and POWLANG transport models.

D meson production was also studied as a function of the charged-particle multiplicity [78] [79]. An enhancement of the D-meson yields, similar to what observed in pp collisions at $\sqrt{s}$ = 7 TeV is observed (see Fig. 2.9, left plot). However, in p-Pb collisions in addition to the contribution by the MPI, also CNM effects and the contribution of the multiple binary nucleon collisions should be taken into account.

Open beauty measurements First measurements of the beauty production cross section in p-A collisions were performed by LHCb in p-Pb collisions at $\sqrt{s_{NN}}$ = 5.02 TeV at large rapidity ($2 < y_{lab} < 4.5$), via the analysis of non-prompt J/Ψ mesons, reconstructed from an invariant mass analysis of opposite sign muon pairs, using a fit to the decay time of the J/Ψ along the beam direction to select the J/Ψ coming from beauty decays [101]. The p_T -integrated R_{pPb}, is close to unity at backward-rapidity, and shows a modest suppression at forward-rapidity, as shown in Fig. 2.10.
CMS performed preliminary measurements of B mesons B^0, $B^+$and B_s^0, in p-Pb collisions at $\sqrt{s_{NN}}$ = 5.02 TeV [102]. B mesons were reconstructed via their decays to J/Ψ + K or ϕ at mid-rapidity in $10 < p_T < 60$ GeV/c. The results seem to suggest that B-hadron production is not affected, or is only mildly affected, by CNM effects. To

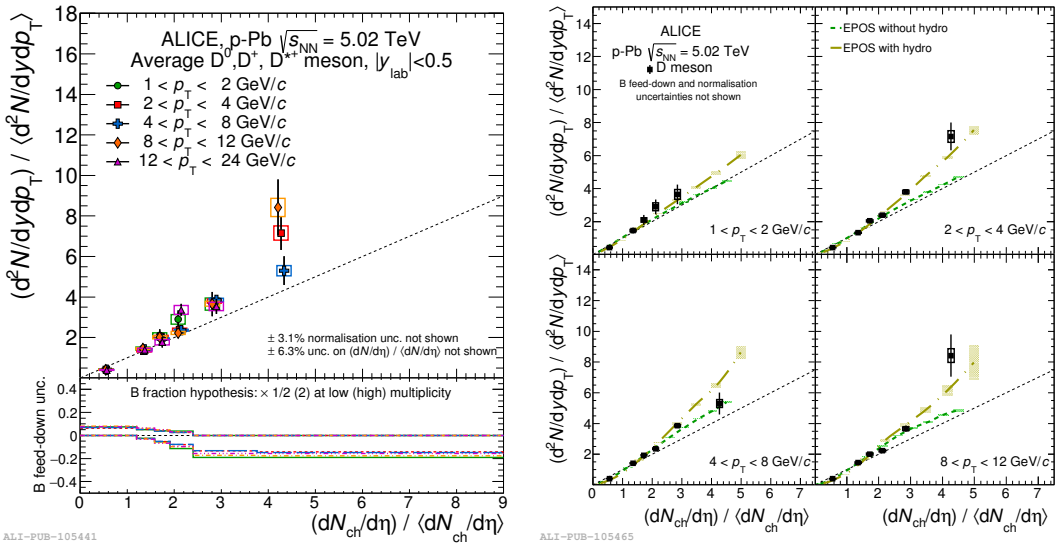

FIGURE 2.9: D-mesons yields vs multiplicity in p-Pb collisions with ALICE. **Left**: Average of D^0, $D^+$and D^{*+}relative yields in p-Pb collisions at $\sqrt{s_{NN}}$ = 5.02 TeV, as a function of the relative charged-particle multiplicity at central rapidity in several p_T intervals. **Right**: Average D-meson per-event yields vs relative charged-particle multiplicity at central rapidity, compared with EPOS 3 [82].

summarize, a rapidity dependence of J/Ψ production was measured at RHIC and LHC. The suppression is more pronounced at forward than mid-rapidity.

2.4 Heavy-flavour production in nucleus-nucleus collisions

Inclusive measurements with leptons

The key points of the measurements of the semi-leptonic decay channels are lepton identification and background subtraction. STAR [104] and PHENIX [105] [106] Collaborations measured the electronic yield at various center-of-mass energies and in various colliding systems. The p_T dependence of the nuclear modification factor in the 10% most central Au-Au collisions at $\sqrt{s_{NN}}$= 200 GeV is shown in Fig. 2.11 [107]. A suppression for the nuclear modification factor was observed, increasing with the transverse momentum and reaching a factor 4 for $p_T > 4$ GeV/c. From the comparison with the measurements in d-Au [108] and Cu-Cu [109] collisions at $\sqrt{s_{NN}}$ = 200 GeV, also shown in the figure, a clear dependence on the colliding system was found. In particular, the observation that the nuclear modification factor is consistent or larger than unity in d–Au collisions demonstrates that the high-p_T suppression in nucleus–nucleus collisions is induced by the presence of the hot and dense medium. A clear dependence of the suppression on the centrality was also observed [105].

At LHC, heavy-flavour production was measured in the leptonic decay channel in Pb-Pb collisions at $\sqrt{s_{NN}}$ = 2.76 TeV. ALICE [110] observed a suppression for the nuclear modification factor of muons from heavy-flavour decays that increases from peripheral to central collisions, up to a factor three in central collisions. Fig. 2.12 shows the nuclear modification factors of muons from heavy-flavour decays in 2.5 < y < 4 as a function of p_T in the 10% most central collisions (left panel) and as a function of centrality in 6 < p_T < 10 GeV/c (right panel). The observed suppression increases from peripheral to central collisions, up to a factor of three in central

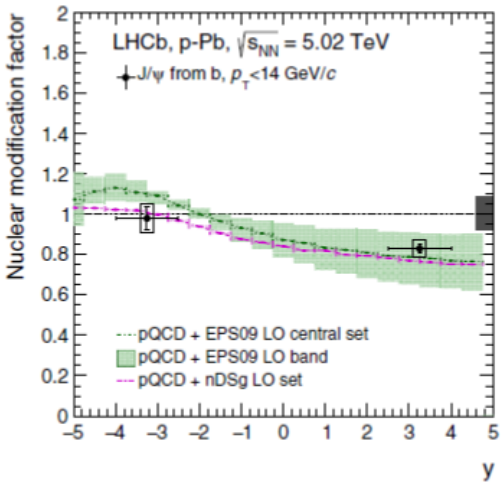

FIGURE 2.10: LHCb measurements of non-prompt J/Ψ in p-Pb collisions [101]: the nuclear modification factor is shown as a function of the rapidity and compared to nPDF-based calculations calculations [103].

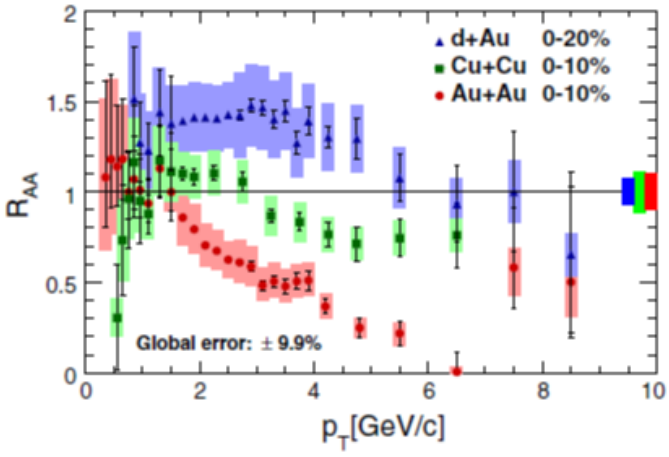

FIGURE 2.11: Transverse momentum dependence of the $R_{\rm AA}$ of heavy-flavour decay electrons at mid-rapidity measured in central d-Au [108], Cu-Cu [109] and Au-Au [107] collisions.

collisions. The results are consistent with preliminary results for electrons at mid-rapidity by ALICE [111] and also with preliminary measurements performed by ATLAS [112].

D meson measurements

The differential charm production cross section is determined from measurements of open charm mesons, by STAR and ALICE. $R_{\rm AA}$ for D^0mesons in the most central Au-Au collisions, measured by the STAR experiment [113] (left plot of Fig. 2.13 is enhanced at around 1.5 GeV/c and shows a strong suppression at $p_{\rm T}$ > 3 GeV/c. The ALICE experiment measured the production of D^0, $D^+$and D^{*+}in Pb-Pb collisions at $\sqrt{s_{NN}}$ = 2.76 TeV [114]. The average $R_{\rm AA}$ of D mesons, for two centrality classes, is shown on the right panel of Fig. 2.13. The high-$p_{\rm T}$ D-meson yield for the most central events is strongly suppressed, by a factor four at 10 GeV/c. The

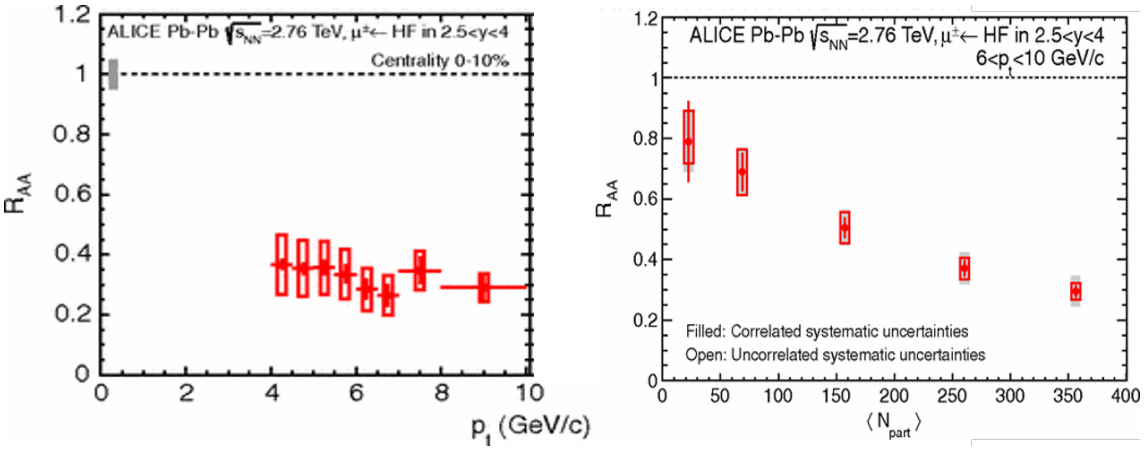

FIGURE 2.12: Nuclear modification factor $R_{\rm AA}$ of heavy-flavour decay muons with 2.5 < y < 4 measured by ALICE in Pb–Pb collisions at $\sqrt{s_{NN}}$= 2.76 TeV as a function of $p_{\rm T}$ in the 10% most central collisions (left panel) and as a function of the mean number of participating nucleons (righ panel) [110].

analysis of the Pb-Pb 2011 data allowed to extend the measurements to higher momenta, observing a similar suppression patter up to 30 GeV/c [115]. In addition, the $\rm D_s^+$meson, consisting of a charm and an anti-strange quark, was measured for the first time in Pb-Pb collisions [116](see Fig. 2.14). The observed central value for the $R_{\rm AA}\rm D_s^+$is larger than that of $\rm D^0$, $\rm D^+$and $\rm D^{*+}$, although the large statistical and systematic uncertainties don't allow to draw any final conclusion. The low-$p_{\rm T}$ $R_{\rm AA}$for $\rm D_s^+$is well described by the TAMU model [117] [118] based on heavy-quark diffusion and hadronization via recombination.

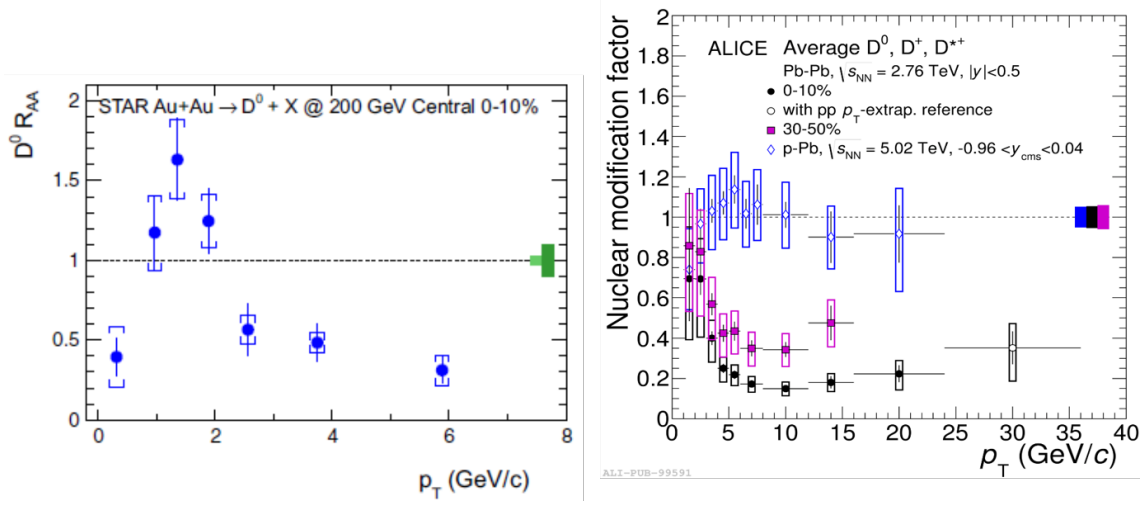

FIGURE 2.13: Left:Transverse momentum dependence of the nuclear modification factor $R_{\rm AA}$ of $\rm D^0$mesons in the 10% most central Au-Au collisions at $\sqrt{s_{NN}}$= 200 GeV [113]. Right: $R_{\rm AA}$ of prompt D mesons (average of $\rm D^0$, $\rm D^+$and $\rm D^{*+}$) versus $p_{\rm T}$ for 0-10% and 30-50% centrality classes in Pb-Pb collisions at $\sqrt{s_{NN}}$= 2.76 TeV [114] and p-Pb collisions at $\sqrt{s_{NN}}$= 5.02 TeV [96]. Theoretical calculations for $\rm D_s^+$mesons, using the TAMU model [117] [118] are superimposed.

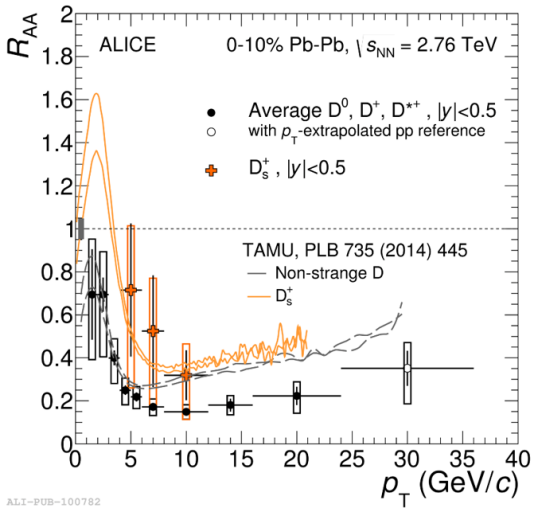

FIGURE 2.14: Nuclear modification factor R_{AA} of $\mathrm{D_s^+}$mesons [115], compared with the averaged R_{AA} for $\mathrm{D^0}$, $\mathrm{D^+}$and $\mathrm{D^{*+}}$ [114], measured by ALICE.

Beauty production measurements

The detection and identification of beauty hadrons usually exploits their long life times, with cτ values about 500 μm. Precise charged particle tracking and vertexing are of crucial importance, with a required resolution on the track impact parameter in the transverse plane being of the order of 100 μm. Most decay channels proceed as b$\rightarrow$c, giving rise to a topology that contains both a secondary and a tertiary decay vertex. Lepton identification is often used in beauty measurements, as the semi-leptonic branching ratio is about 20%, taking into account both decay vertices. As we have seen in pp collisions, the beauty contribution is extracted from semi-electronic decays of heavy flavours through a fit of the impact-parameter distribution. Preliminary results from the ALICE Collaboration in Pb-Pb collisions [119], using the same strategy, indicate R_{AA}values below unity for electron p_{T} larger than 5 GeV/c. Beauty measurements are achieved also using the B$\rightarrow$J/Ψ+X decay mode, decomposing the J/Ψ yield into its prompt and non-prompt components, using a fit to the lifetime distribution. A first measurement using this technique was performed by CMS Collaboration [120], measuring the $R_{\mathrm{AA}}$of non-prompt J/Ψ in 6.5 < p_{T} < 30 GeV/c and $|y| < 2.4$. This measurement is shown in Fig. 2.15. A recent measurement from the ALICE Collaboration [121], also shown in Fig. 2.15, shows similar values for $R_{\mathrm{AA}}$for close kinematic ranges (4.5 < p_{T} < 10 GeV/c and $|y| < 0.8$).

Comparison of R_{AA} for charm, beauty and light-flavour hadrons

The expected dependence of in-medium energy loss on the parton colour charge and mass can be investigated by comparing the nuclear modification factor of charged hadrons, mostly originated from gluon fragmentation at the LHC energies, with that of hadrons with charm and beauty. Open heavy-flavour hadron production is expected to be sensitive to the energy density of the system through the mechanism of in-medium energy loss of heavy quarks. Figure 2.16(left panel) shows the D-meson R_{AA} measured by ALICE [122] as a function of the average number of nucleons participating in the interaction, compared to the one of J/Ψ from beauty-hadron decays measured by CMS [123]. The D-meson p_{T} range was chosen in order to obtain a significant overlap with the p_{T} distribution of B mesons decaying to J/Ψ with 6.5 < p_{T} < 30 GeV/c, thus allowing a consistent comparison. A similar trend as a function of centrality is observed, but the D-meson $R_{\mathrm{AA}}$is systematically lower than the

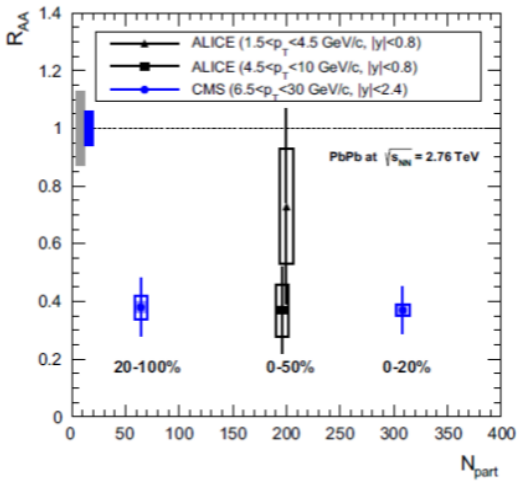

FIGURE 2.15: Non-prompt J/Ψ R_{AA} measured in two centrality bins from CMS [120] and in one centrality bin for two p_{T} ranges from ALICE [121]. The ALICE points are slightly shifted horizontally for better visibility. The correlated uncertainties are shown as filled box at $R_{\mathrm{AA}} = 1$.

one of J/Ψ from B decays in central collisions. This is consistent with the expectation from the predicted energy loss hierarchy, with a smaller in-medium energy loss for beauty than for charm. Calculations including mass-dependent radiative and collisional energy-loss [124] predict a difference between the R_{AA} of D mesons and non-prompt J/Ψ similar to the measurement. Figure 2.16 (right panel) also shows the comparison of the D-meson R_{AA} with that of charged hadrons and pions [125], measured again by ALICE: a similar suppression is observed within uncertainties. More in details, the R_{AA} of D mesons and light-flavour hadrons are consistent for $p_{\mathrm{T}} > 6$ GeV/c. For $p_{\mathrm{T}} < 6$ GeV/c, the R_{AA} of D mesons tends to be slightly higher than that of pions, even if more data are needed to study the effect of charm quark mass at low p_{T} .

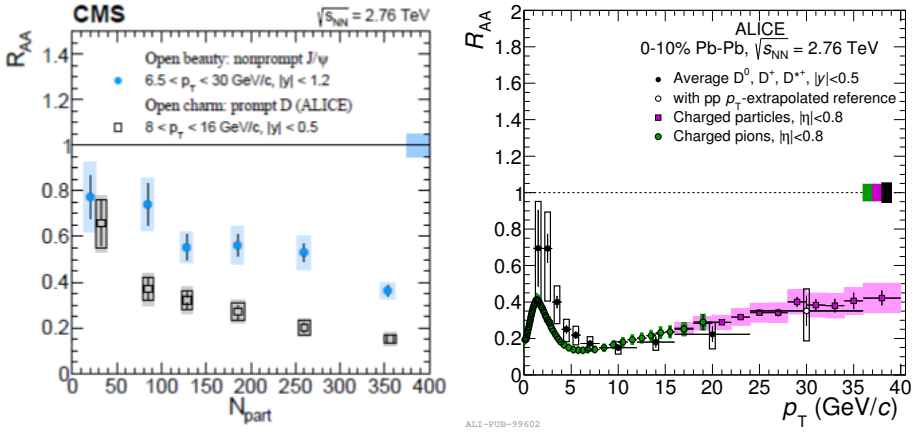

FIGURE 2.16: Comparison of R_{AA} for charm, beauty and light-flavour. Left: R_{AA} of D mesons in $8 < p_{\mathrm{T}} < 16$ GeV/c from ALICE [122] and preliminary non-prompt J/Ψ mesons from CMS in $6.5 < p_{\mathrm{T}} < 30$ GeV/c [123]; Right: Prompt D-meson R_{AA} (average of D^0, $\mathrm{D}^+$and D^{*+}) as a function of p_{T} compared to the nuclear modification factor of pions and charged particles in the 0-10% centrality range [125].

Azimuthal anisotropy measurements

The elleptic flow is measured in general using three methods: event plane (EP) [126], scalar product (SP) [127] and multi-particle cumulants [128]. In the following an overview of the elliptic flow measurements at RHIC, using heavy-flavour decay electrons, and LHC, using D mesons, will be presented.

electrons

The starting point in order to determine the heavy-flavour decay-electron ν_2 is the measurement of ν_2 for inclusive electrons, which include photonic or background electrons (from photon conversion in the detector material and internal conversions on the Dalitz decays of light mesons), contamination from hadrons and heavy-flavour decay electrons. The heavy-flavour decay-electron $\nu_2$is obtained from the inclusive electron ν_2, weighted by the corresponding contributions to the inclusive yield. The PHENIX Collaboration measured the heavy-flavour decay-electron $\nu_2$in Au-Au collisions at $\sqrt{s_{NN}}$ = 62.4 and 200 GeV using the event-plane method [129]. ν_2, showed in Fig. 2.17, for minimum-bias events, is larger than zero in 0.5 < p_{T} < 2.5 GeV/c. At larger p_{T} it shows a decreasing trend, however the statistical uncertainties is not enough for a firm conclusion, as well as to give any conclusion on the energy dependence of ν_2. Measurements performed by STAR at $\sqrt{s_{NN}}$ = 200 GeV show a ν_2 larger than zero for p_{T} > 0.3 GeV/c compatible with the PHENIX results in the same centrality class [130].

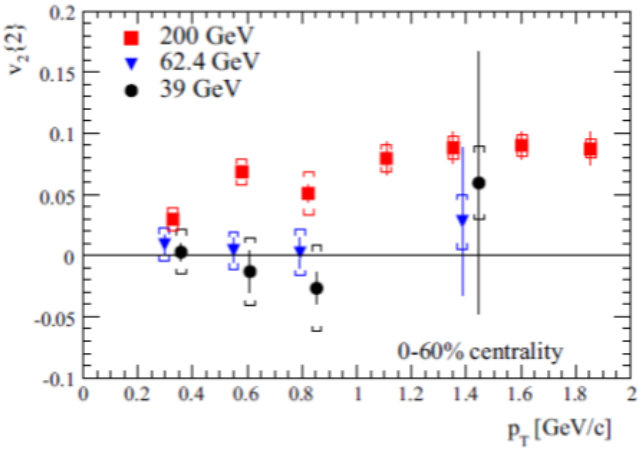

FIGURE 2.17: D-mesons ν_2 measured by the PHENIX Collaboration in Au-Au collisions at RHIC [129]. Measurement performed at $\sqrt{s_{NN}}$ = 200 GeV as a function of p_{T} .

D mesons

The ALICE Collaboration measured the ν_2 of prompt D mesons in Pb-Pb collisions at $\sqrt{s_{NN}}$ = 2.76 TeV [131]. The D mesons (D^0, $\mathrm{D}^+$and D^{*+}) were measured in 2 < p_{T} < 16 GeV/c at mid-rapidity using their hadronic decay channels and exploiting the separation (few hundred μm) of the decay vertex from the interaction point to reduce the combinatorial background. The measurement of the ν_2 for D-mesons was performed using the three methods described above. The D-meson ν_2 measured in different centrality classes in Pb-Pb collisions [132], shown in Fig. 2.18, is larger than zero with a significance $\sim$ 6 in the interval 2 < p_{T} < 6 GeV/c and comparable in magnitude to the one of charged hadrons, dominated by light-flavour hadrons [111] [133]. These results indicate that at low p_{T} charm quarks participate in the collective motion of the system. ν_2 results at high p_{T} could give insight into

the path-length dependence of the in-medium energy loss, but the present statistics does not allow to give a conclusion on this.

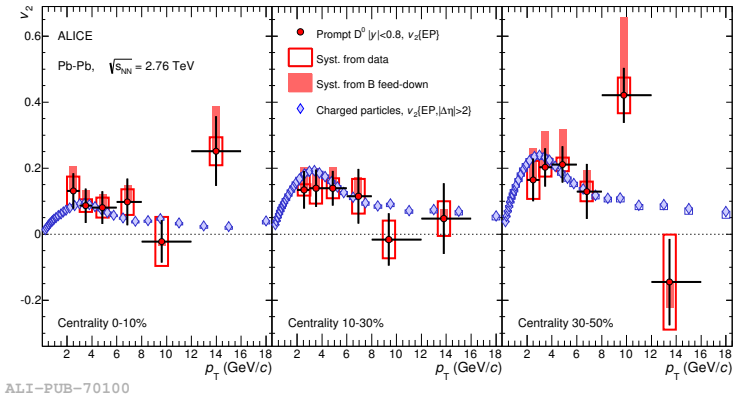

FIGURE 2.18: D-mesons ν_2 measured by the ALICE Collaboration [132] [134]. Comparison of prompt D^0 meson and charged-particle ν_2 measured by ALICE Collaboration [111] [133] in three centrality classes as a function of p_T .

An increasing trend of ν_2 towards more peripheral collisions is observed, as shown in Fig. 2.19 for the D^0meson [134].
ν_2 results at high p_T could give insight into the path-length dependence of the in-medium energy loss, but the present statistics does not allow to give a conclusion on this.

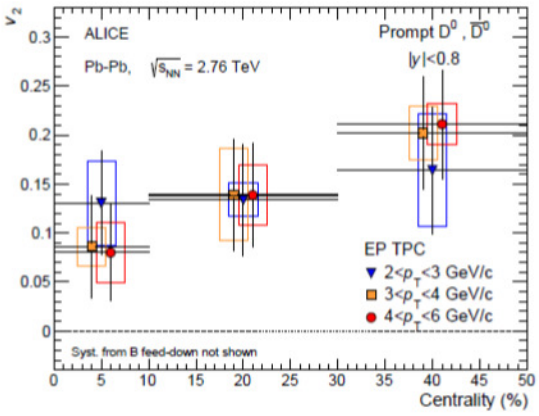

FIGURE 2.19: Centrality dependence of the D^0meson ν_2 measured by ALICE for three different p_T intervals [134].

Chapter 3

ALICE detector

Introduzione al capitolo su ALICE

3.1 LHC

The Large Hadron Collider (LHC) [135] is the world's largest and powerful particle accelerator and collider. It is installed in the 26.7 km long tunnel, previously build to host the Large Electron-Positron (LEP) Collider [136]. Along its circumference, four main experiments are located in four different interaction points.
A Toroidal LHC ApparatuS (ATLAS) and *Compact Muon Solenoid* (CMS), the biggest, are multi-purpose detectors, aimed to discover the Higgs boson and study physics beyond the Standard Model (SM). *Large Hadron Collider beauty* (LHCb) experiment is focused on the flavour physics, in particular on the study of the CP-symmetry violation using beauty-hadron decays. *A Large Ion Collider Experiment* (ALICE) is aimed to the study of Quark-Gluon Plasma produced in heavy-ion collisions, but also a shorter physics program with pp and p-Pb collisions is carried on. We will come back to ALICE in the next paragraph.
LHC was designed to run protons at the maximum collision energy $\sqrt{s}$ of 14 TeV for pp collisions and $\sqrt{s_{NN}}$ of 5.5 TeV for Pb-Pb collisions. However, after a technical incident in 2008, in 2010 and 2011 LHC run at half of the nominal energy, proving Pb-Pb collisions at $\sqrt{s_{NN}}$ = 2.76 TeV and pp collisions at $\sqrt{s}$ = 7 TeV. In 2012, due to the excellent performance of the machine, it was decided to increase $\sqrt{s}$ to 8 Tev for pp collisions. The p-Pb run of 2013 completed this first three years long period of data taking, referred as *Run I*.
After two years of maintenance and upgrading, LHC restarted physics in 2015 (*Run II*) with pp collisions at $\sqrt{s}$ = 13 TeV, the highest energy even reached by a particle accelerator and, by the end of the year, with Pb-Pb collisions at the unprecedented energy of $\sqrt{s_{NN}}$ = 5.02 TeV. The collection of these data marks a new chapter in the precision studies of the properties of the hot and dense hadronic matter. Run II continued in 2016 with the second pp run and with the p-Pb run, at $\sqrt{s_{NN}}$ = 5.02 and 8.16 TeV. The lower energy of 5.02 TeV was chosen identical to 2013 p-Pb and equivalent to Pb-pb 2015, with the aim of compare different colliding species.
Another important accelerator parameter, beside the collision energy, is the instantaneous luminosity L. This is the proportionality factor between the event rate (R) and the interaction cross section (σ_{int}) of the process under study:

$$R = L\sigma_{int} \tag{3.1}$$

The instantaneous luminosity can be determined as

$$L = \frac{N_b^2 n_b f \gamma}{4\pi\epsilon_n \beta^*} F \tag{3.2}$$

where N_b is the number of particles per bunch, n_b the number of bunches per beam, f the revolution frequency, γ the Lorentz factor, ϵ_n the normalized transverse emittance,β^* the amplitude function in the interaction point, F the geometric reduction factor due to the beams crossing at a certain angle.
The transverse emittance tells us if the process of packing protons into bunches was successful: a low emittance particle beam means that the particles have more or less the same momentum and they are confined to a small distance. The β functions depends on the accelerator magnet configuration. in order to have the highest luminosity at the interaction point, according to the 3.1, it's needed to keep the emittance low and the β^* the lowest possible. Since the emittance changes as a function of the beam momentum, usually the normalized emittance, defined as $\epsilon_n = \gamma\beta\epsilon$, is considered. ϵ_n does not vary during the beam acceleration. The F factor can be expressed int terms of the crossing angle at the interaction point θ_c as

$$F = \left[1 + \left(\frac{\theta_c \sigma_z}{2\sigma_{xy}^*}\right)^2\right]^{-1/2} \tag{3.3}$$

assuming that in each bunch the particles are distributed in the three spatial directions according to Gaussian distributions, with σ_{xy} and σ_z being the sizes in the transverse and longitudinal direction respectively. The bunch transverse and longitudinal sizes are the same for the two beams, as the number of particle per bunch. This number has an upper limit due to the non-linear beam-beam interaction that affects each particle, when two bunches collide. The number of bunches per beam, instead, changes according to the different filling schemes. The beams parameters in particular change in order to have the requested luminosity in the different interaction points (corresponding to the different experiments)).

3.1.1 The injection chain

The accelerator complex [137], shown in Fig. 3.1 is composed by machines that in succession accelerate particles to higher energies. These machines are pre-existing CERN accelerators, upgraded to meet the demanding needs of LHC: many high intensity bunches (25 ns spacing), small transverse emittance and very well defined longitudinal emittance. The proton source is simply a hydrogen tank, from where protons are extracted (an electric field is used to strip the atoms of their electrons) and injected in the*Linear Accelerator 2* (Linac2) increasing the energy up to 50 MeV. The protons are then injected in the *Proton Synchrotron Booster* (PSB) and accelerated to 1.4 GeV. The accelerations continues in the *Proton Synchrotron* (PS) reaching the energy of 25 GeV and finally in the *Super Proton Synchrotron* (SPS). Here protons reach the energy of 450 GeV and are finally transferred to the two beam pipes of the LHC, both in a clockwise and anticlockwise direction, and they are accelerated to their nominal energy.
Lead ions instead are produced from a highly purified lead sample heated to a temperature of about $500°$C. The lead vapour is ionized by an electron current. many different charge states are produced with a maximum around Pb29+. These ions are selected and accelerated to 4.2 MeV (energy per nucleon) before passing through a carbon foil, which strips most of them to Pb54+. The created Pb54+ beam is then accelerated to 72 MeV per nucleon in the *Low Energy Ion Ring* (LEIR) and transferred

successively to the PS. Here the beam is accelerated to 5.9 GeV/nucleon, stripped to Pb82+ passing through a second foil and sent to the SPS. The SPS accelerates the beam to 177 GeV/nucleon and sends it to the LHC.

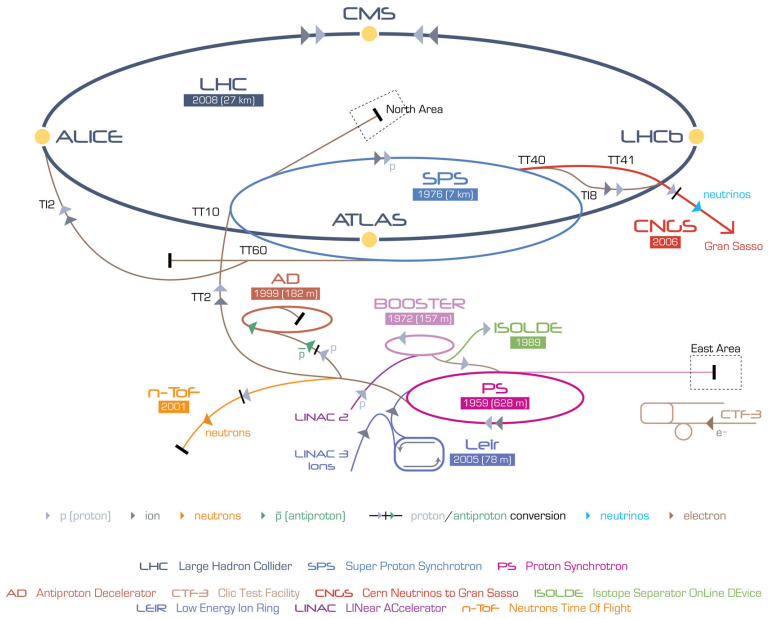

FIGURE 3.1: Schema of the LHC injection chain

3.1.2 LHC operations

The total number of collisions is usually expressed in therms of *integrated luminosity* $L_{int} = \int dtL$ in unities of inverse cross section and reported in function of time and period. In Figs. 3.2 and 3.3 the total integrated luminosity recorded for pp and p-Pb collisions is shown.

In Fig. 3.4 is reported the integrated luminosity registered by the different experiments during Run I and run II Pb-Pb collisions. During the data taking of 2010, ATLAS, ALICE and CMS registered an integrated luminosity of about 10 μb^{-1}, about 100 μb^{-1} in 2011, for Pb-Pb collisions at $\sqrt{s_{NN}}$ = 2.76 TeV. In November 2015 the fist Pb-Pb collisions of the Run Ii data taking, with the energy $\sqrt{s_{NN}}$ of 5.02 TeV started. In this occasion, ALICE registered an integrated luminosity of 360 μb^{-1}.

3.2 ALICE

The ALICE experiment at the LHC [138] is mainly aimed to the study of hadronic matter under extreme conditions of temperature and energy density, as those reached in heavy ion collisions, in particular to verify the QCD predictions about the existence of a phase transition from the common hadronic matter to the QGP, with quarks and gluon not confined into hadrons. In addition to Pb-Pb collisions, ALICE is also interested in pp and p-Pb collisions, for a comparison with Pb-Pb collisions. The ALICE detector (Fig. 3.6) has dimensions 16×16×26 m^3 and a total weight of about 10000 t. With respect to the other experiments at the LHC, ALICE can benefit of an excellent Particle Identification (PID), optimized to work in high track density environment, like Pb-Pb collisions. This is obtained combined different techniques from different detectors.These can be briefly summarized in three main groups:

- **Detectors of the *central barrel***: These detectors, shown in Fig. 3.5 are mainly dedicated to the vertex reconstruction, tracking and particle identification. They are host inside the magnet (B_z = 0.5 T) used in the past for the L3 experiment at LEP, and cover the pseudo-rapidity range -0.9 $\leq \eta \leq$ 0.9 (corresponding to the polar acceptance $\pi/4 \leq \theta \leq 3\pi/4$) and the total azimuthal acceptance (0 $\leq \phi \leq 2\pi$). Moving from the interaction point to the board, the central barrel consists of
  - *Inner Tracking System* (ITS), detectors at high resolution for tracking;
  - *The Time Projection Chamber* (TPC), for tracking and particle identification using energy loss measurements;
  - *Transition Radiation Detector* (TRD)
  - *Time Of Flight* (TOF) for particle identification using time-of-flights measurements;
  - *High-Momentum Particle Identification Detector* (HMPID);
  - *ElectroMagnetic CALorimeter* (EMCAL);
  - *Di-jet CALorimeter* (DCAL);
  - *PHOton Spectrometer* (PHOS),

- **Forwards detectors**: These detectors are collocated in high pseudo-rapidity regions (corresponding to small angles with respect the beam line) and are generally used for trigger and/or for event characterization. They are:
  - V0;
  - *Zero-Degree Calorimeter* (ZDC);
  - *Forward Multiplicity Detector* (FMD);
  - *Photon Multiplicity Detector* (PMD);
  - *ALICE Diffractive detector* (AD);
  - Muon spectrometer.

  - **Detectors for cosmic rays**: ALICE is also provided with an array of scintillators for cosmic ray detection, collocated in the upper region of the L3 magnet, the ALICE COsmic Ray DEtector (ACORDE). The detected cosmic rays can be used for triggering purposes.

In the following of the chapter, an overview of the main features for each mentioned detector will be given. One can find a more exhaustive description of all of them in [138]. In the following chapter will be focused instead on the TOF detector.

3.2.1 Central barrel detectors

ITS
This detector [2] is the closest one to the interaction point. It consists in six concentric cylindrical layers of three different kinds of detectors: *Silicon Pixel Detector* (SPD) for the two intern layers, *Silicon Drift Detector* (SDD) for the two intermediate ones and *Silicon Strip Detector* (SSD) for the two most external layers. The internal ray is only 4 cm (the minimum possible due to the beam

pipe with a ray of 2.9 cm), the external one is 43.9 cm. The layout of the ITS was chosen taking into account the high density of particles produced in Pb-Pb collisions (up to 50 particles/cm^2). The material budget was reduced to the minimum in order to reduce multiple scattering that affects mainly particles with low momentum.

The ITS plays a crucial rule in the ALICE physics program. it is fundamental to determine the primary vertex of the interaction, with a resolution better than 20 μm in central Pb-Pb collisions, and the impact parameter of the tracks, with resolution better than 65 μm in Pb-Pb collisions for transverse momentum (p_{T}) > 1 GeV/c. Moreover, the ITS allows for the identification of particles with momenta less than 100 MeV/c (hence, in the momentum region not accessible by the TPC), through measurements of specific energy loss (dE/dx) in the SDD and SSD. As can be seen in Fig. 3.8, ITS dE/dx measurements allow for a good separation of kaons from protons for p < 1 GeV/c, and pions from kaons for p < 450 MeV/c.

TPC

It's the main detector for tracking in ALICE [141], optimized to provide, together with the other central barrel detectors, charged-particle momentum measurements with a good two-track separation, particle identification and vertex determination. It covers the pseudorapidity range $\mid \eta \mid \leq 0.9$ and the full azimuthal angle. Its layout was optimized in order to have excellent tracking in a very high tracks multiplicity environment, reduce the material budget in order to minimize multiple scattering and the production of secondary particles, to limit the detector occupancy but still guarantee a good momentum resolution for high-p_{T} particles . The TPC has a cylindrical shape centered on the interaction point, with an internal radius of 85 cm, an external one of 250 cm and a total length of 500 cm, along the beam direction, for a total active volume of almost 90 m^3. It is filled with a mixture of Ne, CO_2 and N_2, in the proportions 90/10/5. A central cathodic plane divides the TPC in two regions. After ionization by a charged particle, the electrons drift toward the readout planes on the two edges (MWPC), with a maximum drift time of 88 μs, setting in this way a limit on the sustainable event rate of the TPC. At high interaction rates, pile up becomes relevant. This effect can be rejected using the fact that tracks from pileup point to a different primary vertex. The readout planes are divided in 18 sectors, where the MWPC are hosted. The TPC tracking efficiency is very high, > 90 % for p_{T} > 100 MeV/c, until about 100 GeV/c. measuring the tracks deflection in the magnetic filed, ITS and TPC are able to determine the momentum of charged particles with a resolution better than 1% at low p_{T} and better than 20 % for $p_{\mathrm{T}} \sim$ 100 GeV/c (See Fig. 3.9).

An example of particle dE/dx in the TPC is shown in Fig. 3.10, where the energy loss distributions for the different species are fitted with the Bethe-Bloch formula. The bands for pions, kaons and protons are well separated for p < 1 GeV/c. Deutons are well separated from protons until $\sim p$ < 2 GeV/c.

TRD

The main purpose of the TRD is to provide electron identification for p_{T} > 1 GeV/c. Below this value, electrons can be identified measuring their dE/dx with the TPC. Above 1 GeV/c instead, the transition radiation (TR) from electrons passing a radiator (interface of two media with different dielectric constants) combined with the specific energy loss in a particular gas mixture provides a good pion rejection capability. Using also information from ITS and

TPC, TRD allows for the study D- and B-mesons through their semi-leptonic decays and the production of vector meson resonances (like J/ψ, Υ, Υ, ...) through their lepton decay channel e^+e^-. The TRD is segmented along the azimuthal angle in 18 sectors. Each sector contains 30 modules arranged in five sections along z and six radial layers. Each detector element consists of a radiator 0f 4.8 cm thickness, a drift section of 30 mm thickness and a multiware proportional chamber (MWPC) with pad readout. During the Run I, only 10 of the 18 sectors or the TRD had been installed. All the other were installed before the start of Run II.

TOF
This detector will be extensively described in the following chapter

HMPID
The purpose of this detector with limited acceptance (-0.6 $\leq \eta \leq$ 0.6) is identify charged hadrons at p_{T} > 1 GeV/c, extending the momentum range over which ALICE can perform PID through dE/dx and time-of-flight measurements. The detector is composed by Ring Imaging Cherenkov (RHIC) counters collocated 4.5 m far from the beam line and divided in 7 modules, each of them with dimensions 1.5×1.5m^2. The radiator is a 15 mm tick layer of C_6F_14 liquid with a refraction index n = 1.2989 at $lambda$ = 175 nm, corresponding to a momentum threshold of p_{th} = 1.21 m, where m is the particle mass. Cherenkov photons, emitted by a fast charged particle traversing the radiator, are detected by a photon counter with a thin layer of CsI deposited on the pad cathod of a MultiWire Pad chamber (MWPC).

EMCAL, DCAL
The EMCAL is a large Pb-scintillator sampling calorimeter, mainly used to measure *jet*, as trigger for photons and electrons at high momenta. The detector element is composed by 1.44 mm tick Pb layers and 1.76 tick layers of scintillator, with longitudinal wavelength-shifting fibers readout via avalanche photo diodes. The EMCAL covers the pseudorapidity range $\mid \eta \mid \leq$ 0.7, with a polar angle coverage of $\Delta\phi$ = 107°, on opposite position in azimuth with respect to the PHOS detector, about 430 cm far from the interaction point.
The DCAl [140] was installed during the Long Shutdown I of LHC, and it has the same structure of the EMCAL, but collocated in the opposite position. Together with the EMCAL, the DCAL can provide bigger acceptance for measurements of back-to-back correlations of jets and hadrons.

PHOS
The PHOS is a high-resolution electromagnetic spectrometer, covering a limited acceptance ($\mid \eta \mid \leq$ 0.12 and polar angle coverage of $\Delta\phi$ = 100°) at central rapidity, situated almost 5 meters under the interaction region, in the opposite (azimuthal) direction with respect to the EMCAL. It is composed by scintillator crystals of $PbWO_4$. This detector is dedicated to low p_{T} direct photon measurements and study of high-p_{T} π^0 and υ-jet correlations.

3.2.2 Forward detectors

V0, ZDC and T0
The **V0** detector [142] is a small angle detector. It consists of two arrays of scintillators, *V0-A* and *V0-C*, which cover the pseudorapidity ranges 2.8 < η < 5.1

and -3.7 < η < -1.7 for collisions at the IP (z = 0). V0-A is located 329 cm far from the IP, on the side opposite to the muon spectrometer (see Fig. **??**). V0-C is located on the front face of the hadronic absorber. Both arrays are segmented in four rings in the radial direction, and each ring is divided in eight sections in the azimuthal direction. This detector, together with the SPD, provides the minimum bias (MB) trigger for the central barrel detectors, for pp and Pb-Pb collisions. It is also used to remove the *beam-gas* background, due to particles of the beam interacting with residual particles in the beam-pipe. V0 detector also provides the estimate of the centrality, from the measurement of the multiplicity of particles reaching the scintillators [143](See Fig. 3.12), interpolated with the Glauber model [93].
The centrality of the collision can be estimated also in an alternative way, detecting the spectator nucleons that keep their trajectory in forward direction along the beam line. Aimed at that, two **ZDC** are places at 115 m away from the IP on both sides, exactly along the beam line. These calorimeters are also used to estimate the reaction plane in nuclear collisions. Each ZDC is composed by two calorimeters, one for the spectator neutrons (ZN), the other one for the spectator protons (ZP) placed externally. In particular the ZDCs are "spaghetti" calorimeters made by a stack of heavy metal (tungsten) plates allocating a matrix of quartz fibres. Since in Ultra Peripheral Collisions (UPC) the spectators stay in the beam pipe, the ZDCs collect a samll amount of energy both for central and UP events. To distinguish the two classes of events, tho additional electromagnetic calorimeters (ZEM) are used, places at 7 m away from the IP on both sides of the beam pipe and opposite to the muon arm.
The **T0** detector consists of two arrays (T0A and T0C) of Cherenkov counters (12 counters for array), located at the sides opposite to the collisions zone, at 370 cm and 70 cm away from the IP. Each array is composed by a 12 cylindrical Cherenkov counters, equipped with a quartz radiator and a photomultiplier tube. The T0's main purpose is to determinate the start time of the collision t_0.

FMD,PMD and AD
The **FMD** provides the measurement of the charged-particle multiplicity in the pseudorapidity range -3.4 < η < -1.7 and 1.7 < η < 5.0, extending the pseudorapidity region covered by the SPD. It consists of silicon strip detectors located at three different positions along the beam pipe: FMD1 is located at 320 cm from the IP on the C side of ALICE. FMD2 and FMD3 are places on both sides of the ITS, about 75 cm away from the IP.
The **PMD** measures the spatial distribution of photons produced in forward direction, in the region 2.3 < η < 3.7, providing an estimate of the transverse electromagnetic energy and of the reaction plane of the collision. It is made of two planes of gas proportional counters preceded by two converter plates.
The **AD** [139] detector was installed in the ALICE cavern during the first long Shutdown of LHC. It consists of four stations of scintillator pads located at 18 m on side A (ADA) and 20 m on side C (ADC) from the IP. Its main goal is to extend the current rapidity coverage, in order to have more sensitivity to tag rapidity gaps related to diffractive processes

Muon spectrometer
The muon spectrometer [144](see Fig. 3.13 was designed with the aim to study the open heavy flavour production and the quarkonia production (J/ψ, ψ', $\Upsilon(1S)$, $\Upsilon(2S)$ and $\Upsilon(3S)$) via the muonic decay channel $\mu^+\mu^-$. Quarkonia states in particular exhibit invariant mass peaks very close to each other, hence

requiring a very good mass resolution of the detector. For this purpose, a dipole magnet was installed at about 7 m from the IP, proving a nominal magnetic filed of 0.7 T along the z axis (perpendicular to the beam axis). The invariant mass resolution is about 70 MeV in the J/ψ and about 100 MeV close to the $\Upsilon(1S)$. In this way all the five different resonance states can be resolved and measured. The spectrometer is located externally to the central barrel and covers the pseudorapidity region -4.0 $\leq \eta \leq$ -2.5. A front absorber, made of carbon and concrete, suppresses all the primary and secondary particles coming from the IP, except muons. A high-granularity tracking system is provided with 10 chambers arranged in 5 stations of 2 chambers each, perpendicular to the beam axis and with cathodic planes for the signal's readout. The reached spatial resolution is better then 100 μm. Two of the 5 chamber stations are placed between the L3 magnet and the dipole magnet. These chambers are highly segmented (more than one million channels) in order to keep the occupation rate within 5%. One of the stations is hosted in the dipole magnet, instead the last two are outside the dipole. The trigger system (MTRG) is designed to select only heavy quark resonance decays. It is composed by 4 planes of Resistive Plate Chambers (RPCs) arranged in two stations and positioned after a muon filter made of 1.2 m thick iron, that allows only muons with p > 4 GeV/c to reach the trigger chambers. Finally, an inner beam shield, made of tungsten, lead and stainless steel, protects the spectrometers from background arising from primary particles emitted in the collisions and from their showers produced in the beam pipe and in the shield itself.

3.2.3 Cosmic rays detectors

ACORDE
The detector ACORDE consists of sixty scintillator modules, located on the top part of the ALICE's magnet L3. It is used during cosmic ray data taking sessions, providing a fast *trigger* signal useful to calibrate and align the central barrel detectors and also to performance particular physics studies with cosmic rays.

3.3 ALICE online operations

The data taking activities are controlled by five central online systems [138] [145]: the Data Acquisition (**DAQ**) system, responsible for the configuration of the different detectors during the data taking, interfaced with the Central Trigger Processor (**CTP**) and the High-Level Trigger (**HLT**) system; the Detector Control System (**DCS**) allows for the monitoring of the detector hardware from a central interface. All these operations are coordinated by the Experiment Control System (ECS). The detectors can operate individually, in "standalone" mode, to perform calibration, commissioning and debug activities. During the physics data taking (with beam or just cosmic rays), detectors are grouped in "partitions", that can work in parallel and independently, after having received trigger inputs. The ECS monitors the DCS status, interacts with the DAQ and the HLT processes, links the partition with the Central Trigger Processor (CTP), in case of global partitions, or with the Local Trigger Unit (LTU), in case of standalone mode.

The ALICE physics program includes the study of a large variety of physical observables, with very different beam conditions. To digest all the resulting information, ALICE had to create a data acquisition system able to operate in two different running modes: very frequent but small events, with few produced particles in pp mode and the relatively rare, but extremely large events, with thousands pf new particles produced in ion operation mode. Moreover, the ALICE DAQ system needs to balance its capacity to record the regular stream of very large events resulting from central collisions, with the ability to select and record rare processes at the same time. These requirements result in an event building bandwidth of up to 2.5 GByte/s and a storage capability of up to 1.25 GByte/s, providing a total of more than 1 PByte of data every year.
The ALICE DAQ system flow is schematically shown in Fig. 3.14. For every bunch crossing in the LHC machine during the data taking, the Central Trigger Processor (CTP) decides, within less than one μs, if to collect the data resulting from a collision. The trigger decision is sent to the front-end electronics (FEE) of each detector, via the Local Trigger Unit (LTU) that is interfaced with an optical broadcast system, the Trigger and Timing Control (TTC) system. After the reception of a positive decision, the data collected by each detector are sent to the DAQ Readout Receiver Card (D-RORC), via 400 optical Detector Data Links (DDL). The D-RORD interface the DDLs with 300 individual computer, the Local Data Concentrator (LDC) with Front-End Processors (FEP). The data are sent is several hundred of fragments (corresponding to the information from one single event) from DDLs to LCDs, where they are checked, processed and assembled into sub events. These sub events are then sent to the 40 Global Data Collector (GDC) computers to build the full events in the format of ROOT files. These event are first stored locally, in the Transient Data Storage (TDS), and finally exported in the CERN Computer Centre and recorder in the Permanent Data Storage (PDS), becoming available for the offline analysis.
The framework of the ALICE DAQ is the Data Acquisition and Test Environment (DATE) software. DATE is a distributed process-oriented system. It was designed to run on several machines with the Scientific Linux CERN operating system and it consists of a collection of packages performing different function:

- collecting of the event fragments in the LDC, transferred into its memory by the DDL, reassembling of these fragments into sub-events;
- building of the full events, putting together all the sub-events related to the same physics events, through the GDC;
- data storage;
- synchronization of all the processes;
- management of the configuration states, errors and log messages reports, monitoring.

Finally, the DAQ system [146] also includes a special framework to perform calibration online, in order to allow a faster data analysis offline. Two types of processes, called Detector Algoritms (DAs) are running in the DAQ machines. If the calibration is performed on a standalone run, the data are collected locally on the LCDs and analyzed at the end of the run. In case of a regular physics run, the data are analyzed online through the DATE monitoring functionality. The produced DA output is then transfer from the DAQ system to the File Exchange Server (FXS) interface. From there, data can be archived in the offline data base (Offline Condition DataBase - OCDB) using the so-called

SHUTTLE framework. Hence, SHUTTLE acts like an interface between the online systems and the offline resources. Here the data go through a second level of processing called preprocessing, converted in ROOT format and finally the OCDB and the DCS DataBase are updated. From the OCDB on GRID data can be successively recovered and used for data reconstruction or analysis offline.

3.3.1 Data Quality Monitoring online

Data Quality Monitoring (DQM) [147] [148] is an important aspect of the experiments at the LHC, since the used detectors are extremely sophisticated devices and given the variety of running condition. DQM is part of the ALICE DAQ (see Fig. 3.14) and involves the online collection of the data, their analysis using defined algorithms and storage and visualization of the produced monitoring information. The DQM software runs of dedicated servers connected to the event building network. In particular, the data feeding the DQM nodes, come from the LDCs if the data to be monitored are coming from a specific detector, of from QDC if the interest is on global observables related to the whole event.

The AMORE software

The DQM framework for ALICE is the Automatic MOnitoRing Environment (AMORE) software. It is a flexible and modular software, used to analyze data samples and produce and visualize monitoring results. It is based on the data analysis framework ROOT [151] and the DATE monitoring libraries (see Fig. 3.15). In case the same analysis is needed online and offline, the ALICE Off-line framework (AliRoot) for simulation, reconstruction and analysis, can be used at the level of the modules.

AMORE is based on a publisher-subscriber paradigm where a large number of processes, called “agents”, execute detector-specific decoding and analysis on raw data samples and publish their results in a pool (see Fig. 3.16). Then clients can connect to the pool and visualize the monitoring results, through a dedicated interface. The Data samples are subevents coming from LCDs, GDCs or raw data flies. The monitoring results are encapsulated in“Monitor Objects” (MO), that contain additional information allowing their proper handling by the framework.

For each detector, “modules” are built into dynamic libraries, loaded at runtime only if and when it is needed. Modules are typically split in two main parts, corresponding to the publishing and the subscribing sides of the framework (See Fig. 3.17).A module’s publisher can be instantiated many times, in order to collect more statistics, and each instance corresponds to an agent. The publishers analyze the raw data and publish them in the pool. The client consists of a ROOT-based Graphical User Interface (GUI), where the MOs are dispayed (you can see an example of MOs in Fig. 3.18).

The pool is implement as a MySQL database (the open-source MySQL was chosen as it is a reliable, performant and light-weight system). This database keeps the data published by the agents. Moreover it contains important information about the agents, such as the machine where they can run, which detector they belong to, and configuration files. The pool is implemented as

a database. The open-source MySQL system was chosen as it proved to be reliable, performant and light-weight. Figure 4 shows a rough schema of the database and the detailed description of the tables follows. The database is used not only to keep the data published by the agents, but also to store the configuration of AMORE as a system. This includes information about the agents such as the machine where they can run and to which detector they belong (agents table) as well as the optional configuration files. When a new agent is created in the system, a row is added to agents table. The table where published data will be stored is created or recreated when the agent is started. Most of the detector use the AMORE Quality Assurance (QA) module, that is based on the AliRoot QA framework. In this case, four event species are defined: Calibration, Low Multiplicity, High Multiplicity and Cosmic. The species are computed online according to the beam type, the trigger condition, the event type. The plots are duplicated four times, but only those belonging to the particular species are filled. In the QA framework, moreover, a QA checker class is used, to decide on the quality of an object by the comparison with reference distributions or thresholds. As a consequence, a species quality flag is displayed in the GUI, together with info boxes, messages or alarms for the DQM operator during the data taking.
During the data taking monitor cycles (in general 50s for each) sample the events. The data collected at the end of each cycle are analyzed by the agents, and DQM MOs histograms are visualized on the GUI, to be monitored by operators (DQM shifters or DQM experts). Those histrograms are periodically saved and archived in the ALICE Logbook, where they can stay for a week before being deleted, unless they are marked as permanent. In this way, thy can checked by the experts anytime after the data taking.
Since its start in 2008, the AMORE framework has been successfully used to monitor all the data taking. Thanks to the continuous interaction between users and framework developers, the system is continuously updated and upgraded with new tools, according to the needs.

3.4 ALICE offline operations

AliRoot is the ALICE offline framework for simulation, reconstruction and analysis [149] [150]. It uses the ROOT [151] system as base on which the framework and all the applications are built, and it is complemented by AliEn [152] interface, giving access to the Grid. This framework is based almost entirely on the Object-Oriented (OO) programming paradigm, and it's written in C++. The huge and unprecedented amount of collected data at LHC require processing and storage resources that cannot be concentrated in a single computing center. It's more natural and efficient that these resources are distributed among the facilities of all the institutes and universities participating in the experiment. The existence of a worldwide distributed computing system, the Grid, is the ideal way to host this effort. The AliCE Environment (AliEn) [152] framework was developed with the aim of offering to the ALICE users a transparent access to the worldwide distributed computing resources through the Grid.

The functionality of hte AliRoor framework is schematically shown in Fig. 3.19. The left side of the figure represents the simulation, the right part the reconstruction, where real data or simulated data are reconstructed in order to have information about the cinematic of the event. Monte Carlo event generators create simulated data. The generated data are transported through the detector via detector simulation packages. These packages generate a detailed simulated energy deposition in the detector, called *hit*. Hits are then converted into the format that will be output by the electronics of the detectors, called *raw data*, after an intermediate stage (*digits*). From this point, the processing of real or simulated data is indistinguishable. The data produced by event generators contains all the information about the generated particles, like momentum and Particle identification (PID). As these events are processed through the simulation chain, this information is disintegrated and converted in the information generated by real particles crossing a specific detector. Then the reconstruction algorithms collect all the information contained in the raw data and from there they can identify the particles. Finally, the reconstructed information about particles is compared with the information taken directly from the used Monte Carlo generato. As shown in Fig. 3.19, in the AliRoot framework also fast simulation algorithms are implemented: fast simulations, used for special studies, skips several step in the simulation/reconstruction chain, increasing the speed of the simulation but at the expense of details in the results.

3.4.1 Simulation

The simulation of physics events is extremely important for any analysis and for evaluating the efficiency of the algorithms used to reconstruct and analyze data. In heavy-ion collisions a very large number of particles in the final state is produced. This is a challenge for the reconstruction and analysis algorithms, which require a precise simulation of the detectors response. Many effects, like the material absorption, the acceptance, detector configuration, .. have to be taken into account.
Several event generators are available, providing particle generation for the simulated collision, like HIJING, or PYTHIA, or others. All the information about the generated particles, like particle species, momentum, decay products, are organized in *trees*, stored as ROOT files. The generated particles are then propagated through the sensitive region of the detector, where they loose energy, decay, interact with the material inside the detector. All the information about the interaction of the particles with the detector are collected as hints. Many Monte Carlo generators, like GEANT3, GEANT4 or FLUKA, are used to reproduce the detector layout. By combining the detector and the electronic response, to each hit a digital output is associated, and stored as summable digit. Finally digits are converted into the raw data format, ready to be the input for the tracking reconstruction procedure.

3.4.2 Track reconstruction

A charged particle passing through the detectors leaves a number of discrete signals that measure the positions in the space where it had passed. These points are reconstructed using a *cluster-finding* procedure, specific for each detector. For each space point, also the uncertainty on the position is estimated.

The space points together with the uncertainties are then passed to the track reconstruction algorithms. If the detector is also able to measure the produced ionization, this additional information can be used for the particle identification.
Offline track reconstruction for the detectors in the ALICE central barrel (ITS, TPC, TRD, TOF) is based on the Kalman filter approach [153], extensively used in high-energy physics experiments. Each track candidate is represented as a state vector, whom evolution betwenn two points is given by a deterministic component, namely a linear equation of motion, and by a stochastic component, to account for multiple scattering.
The ALICE track reconstruction is based on a limited number of steps:

- Determination of the position of the primary vertex, needed to build the "track seeds" (used as starting point for the kalman filter) using the cluster in the two ITS inner layers.
- Track reconstruction in the TPC. The track finding in the TPC proceeds from the outer to the inner part. The clusters on the outermost pads and the primary vertex position determined in the previous step are used as seeds.
- Matching of the TPC tracks with the points on the ITS, from the SSD layer to the innermost SPD layer.
- Back propagation and second fit of the tracks, from SPD up to the outer radius of the TPC.
- Extrapolation and track matching with TRO, followed by the propagation to the outer detectors (TOF, HMPID, EMCAL, DCAL, PHOS), for the particle identification.
- Back track propagation and refitting up to the primary vertex. Track parameters are evaluated in proximity of the vertex.
- Recalculation of the primary vertex position, using the reconstructed tracks to obtain the optimal resolution.

The output of this procedure is the Event Summary Data (ESD), which contains all the information about the event, both at track and event level. The ESD is a tree with objects of type AliESDEvent saved in the .root format. The most important information are then extracted from the ESDs and saved in Analysis Object Data (AOD), in order to make easier and more efficient the analysis of these data. For each data sample, the respective files containing EODs and AODs are saved and available for the users on the Grid.
Performance of the track reconstruction
The track reconstruction efficiency is defined as the ration between the number of the reconstructed *good* tracks and the number of the generated tracks. In Fig.? the track prolongation effecincy between TPC and ITS is shown, as a function of the transverse momentum, in Pb-Pb collisions. The efficiency is more than 90% in all the considered p_{T} -interval, when at least two hits in the ITS are required, while it goes down to the 75% when only one point is required. In the figure, it is also shown the good agreement (within 2%) between data and simulations.

3.4.3 Data Quality assurance offline

The QA framework [154] provides an automatic way to asses the quality of the data, at various level of Monte Carlo simulation and Monte Carlo and real data reconstruction. The QA is performed in two steps:

- Creation of QA objects, for a given level and a given detector. These objected are produced as ROOT histograms and saved in ROOF files.
- Checking of the QA objects, by comparing them with either defined values or defined references, and giving a final quality statement.

The result of the checking is represented per detector, at a certain level or simulation or reconstruction, it is stored and can be accessed at any stage of the data processing, to verify the QA of the previous steps.

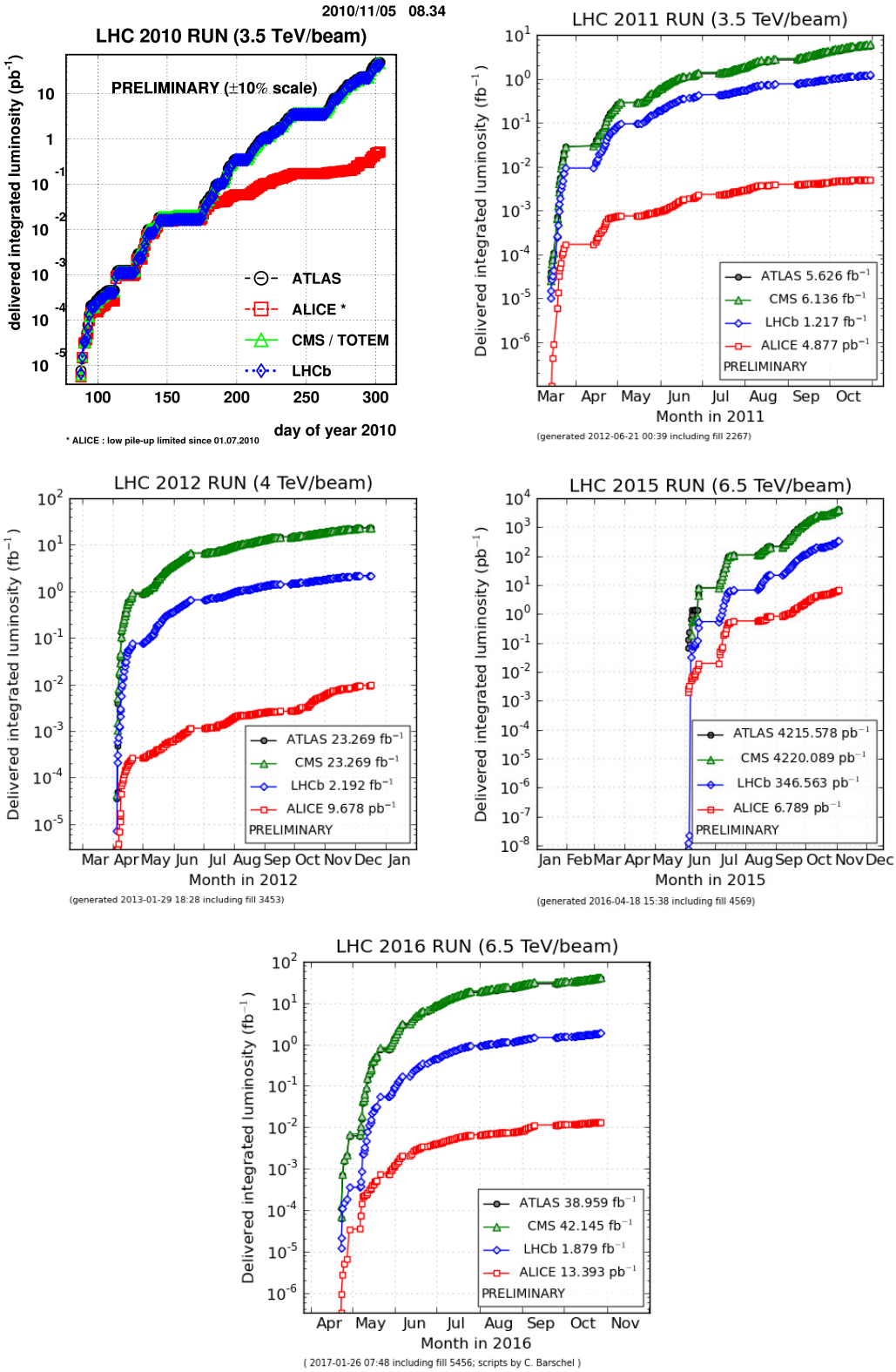

FIGURE 3.2: Total integrated luminosity recorded by LHC during 2010, 2011, 2012, 2015 and 2016 pp collisions.

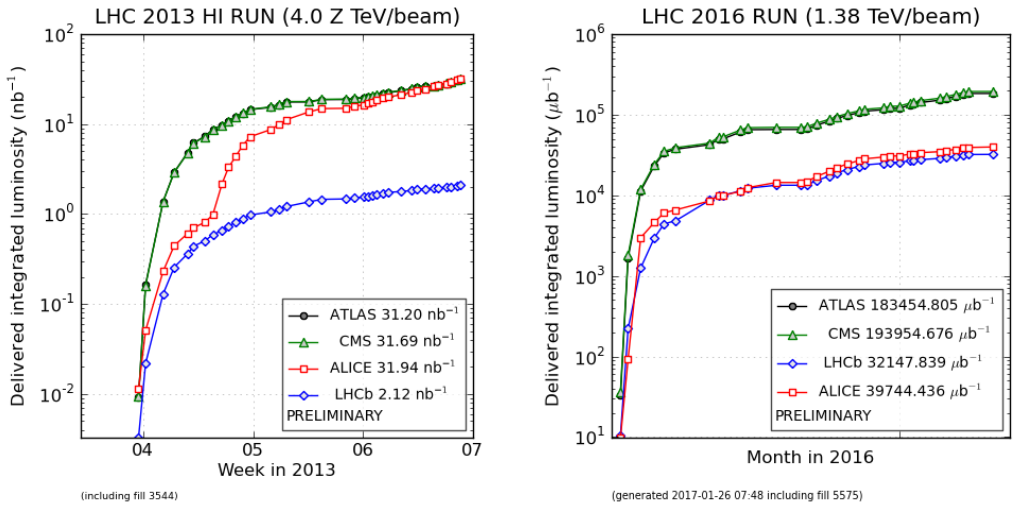

FIGURE 3.3: Total integrated luminosity recorded by LHC during 2013 and 2016 p-Pb collisions.

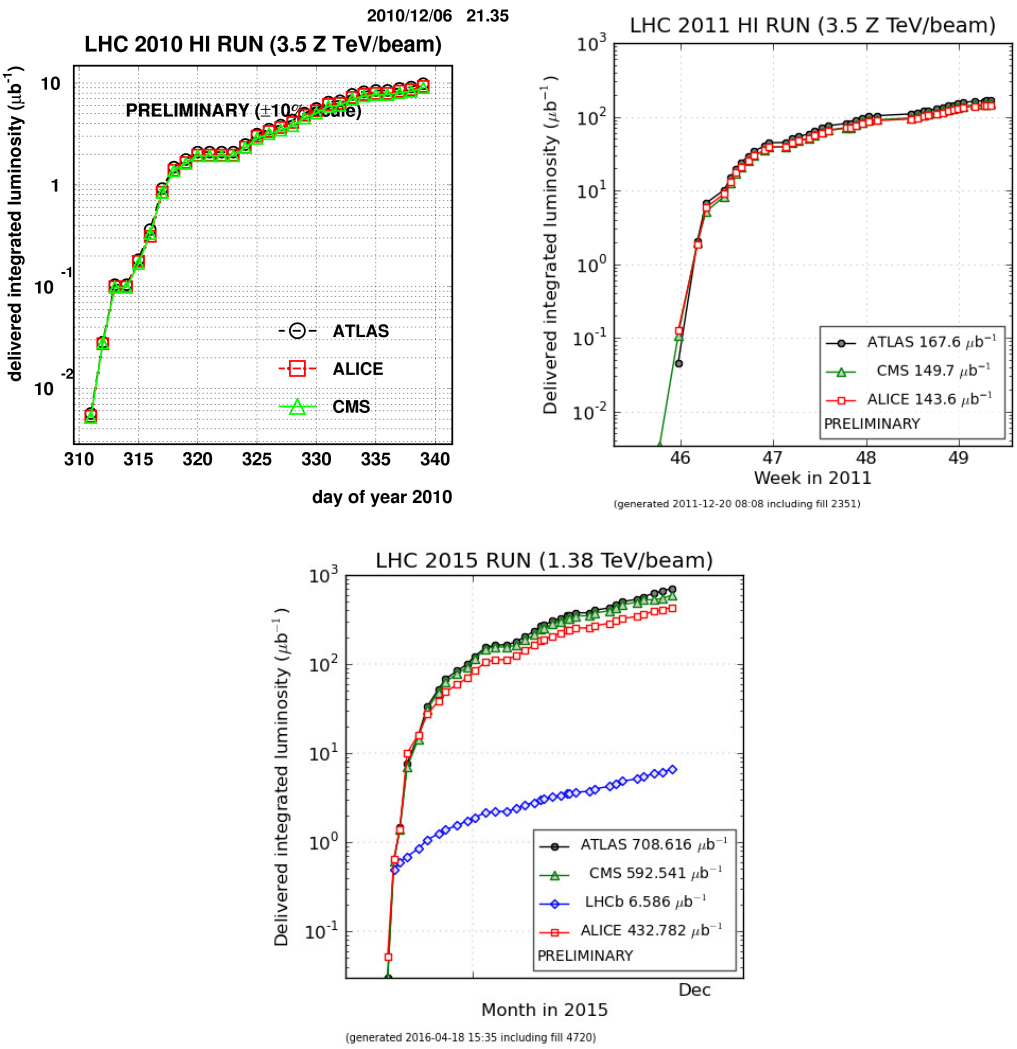

FIGURE 3.4: Total integrated luminosity recorded by LHC during 2010, 2011 and 2015 Pb-Pb collisions.

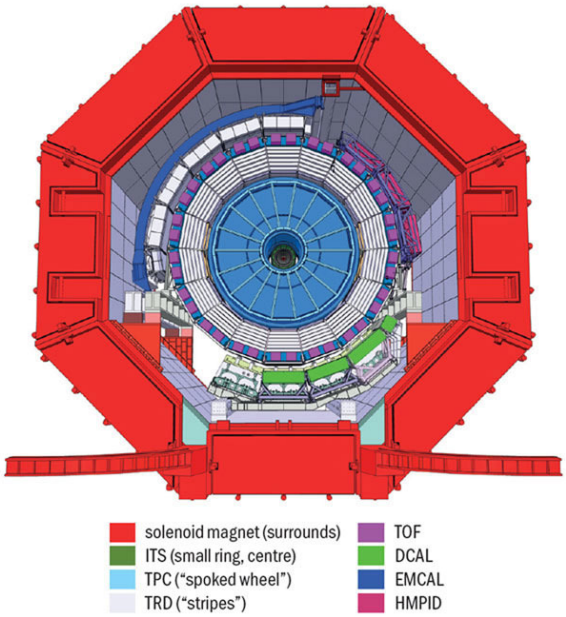

FIGURE 3.5: Schematic traversal view of the ALICE central barrel detectors. The five PHOS modules are not visible.

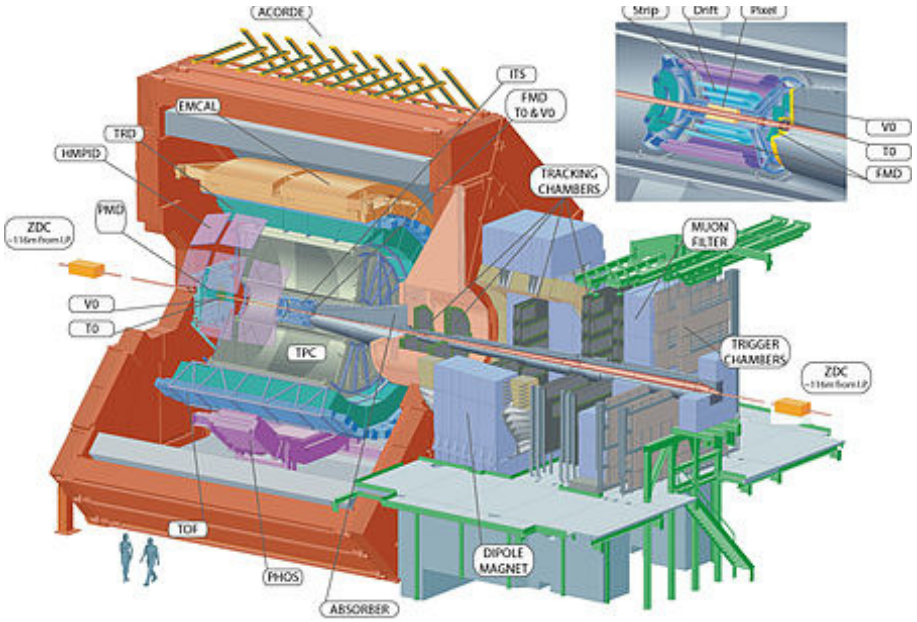

FIGURE 3.6: Schematic view of the ALICE detector. Here AD [139] and DCAL [140] are not visible, since they were added only recently, during the Long Shutdown 1 of LHC.

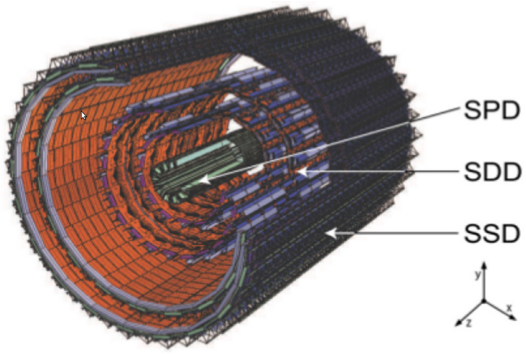

FIGURE 3.7: Schematic view of the ITS detector.

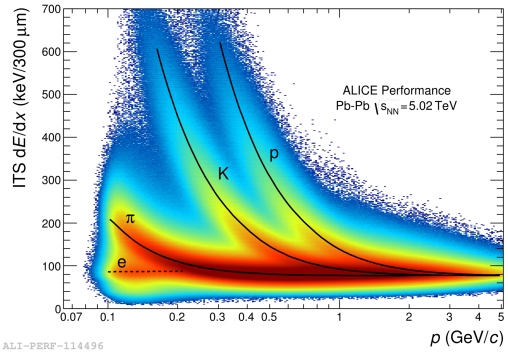

FIGURE 3.8: Distribution of dE/dx for charged particles in function of particle momentum, measured by the ITS in Pb-Pb collisions. The overlapped black lines are dE/dx parametrizations, based on the Bethe-Bloch formula.

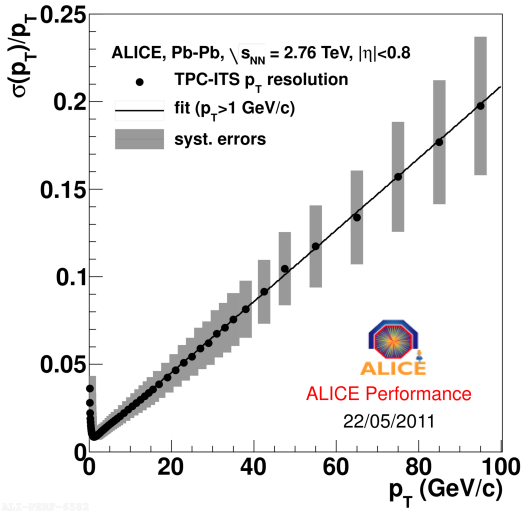

FIGURE 3.9: TPC tracks momentum resolutions.

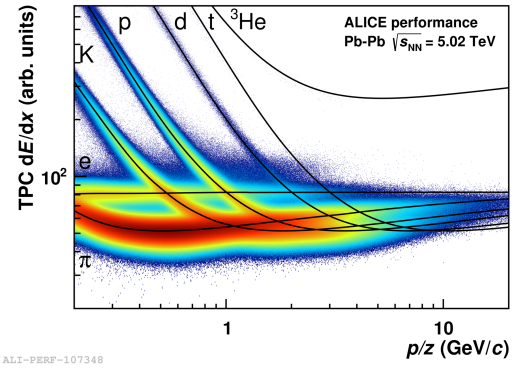

FIGURE 3.10: Distribution of dE/dx for charged particles in function of particle momentum, measured by the TPC in Pb-Pb collisions. The overlapped black lines are dE/dx parametrizations, based on the Bethe-Bloch formula.

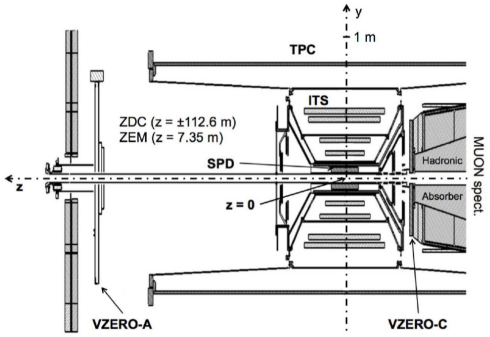

FIGURE 3.11: Position of the two VZERO arrays within the general layout of the ALICE experiment.

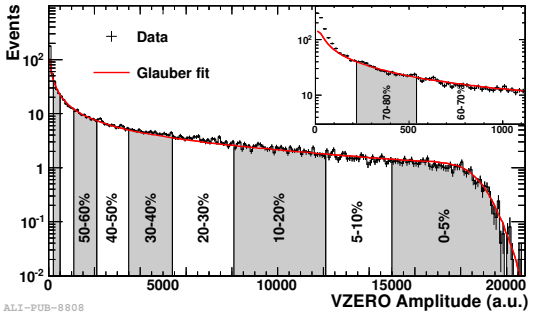

FIGURE 3.12: Distribution of the summed amplitudes in the VZERO scintillators. The inset shows the low amplitude part of the distribution. The curve shows the result of the Glauber model fit to the measurement. The vertical lines separate the centrality classes used in the analysis.

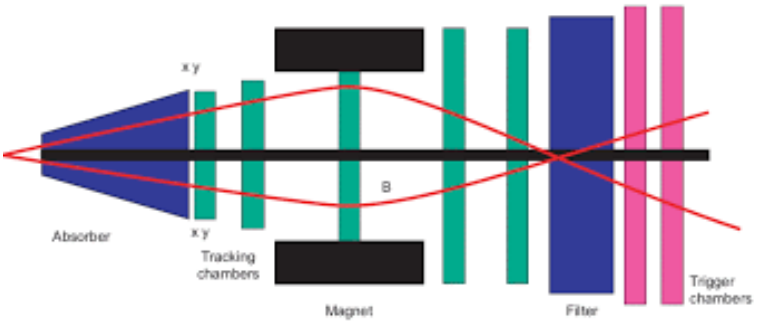

FIGURE 3.13: Layout of the ALICE dimuon spectrometer: an absorber to filter the background, a set of tracking chamber, inside and after the magnet, and a set of trigger chamber.

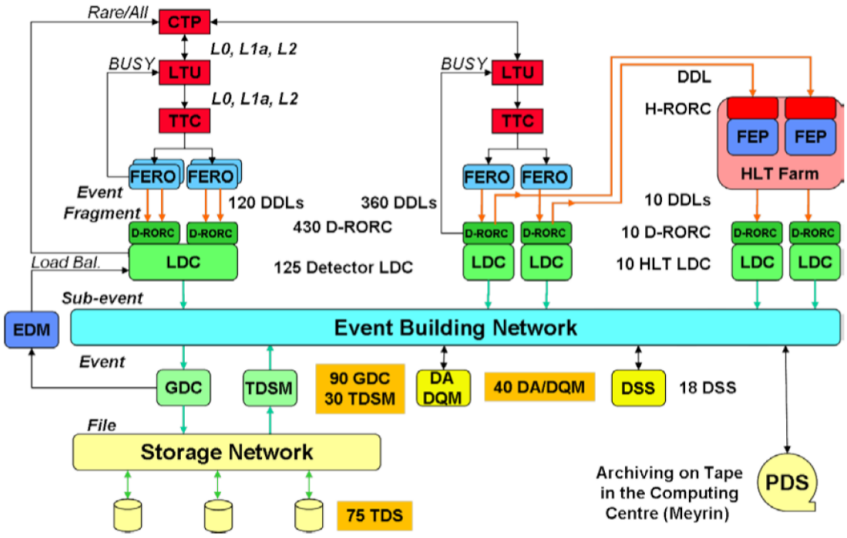

FIGURE 3.14: The ALICE DAQ architecture

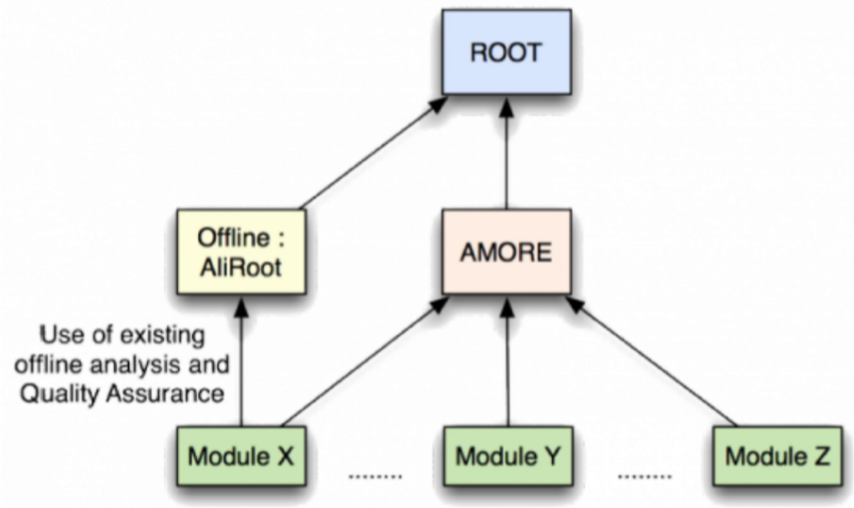

FIGURE 3.15: Schema of the main dependencies of AMORE.

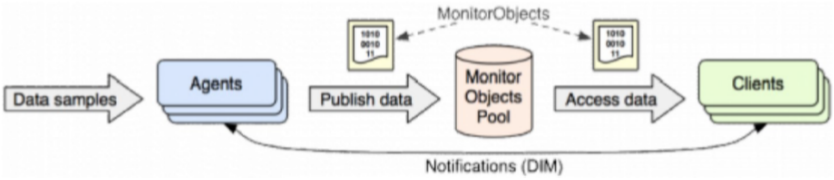

FIGURE 3.16: The publisher-subscriber paradigm of AMORE.

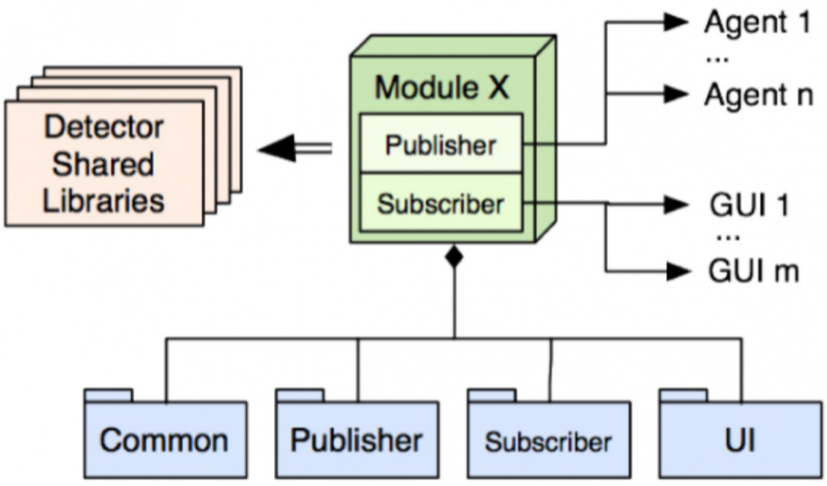

FIGURE 3.17: Description of an AMORE module.

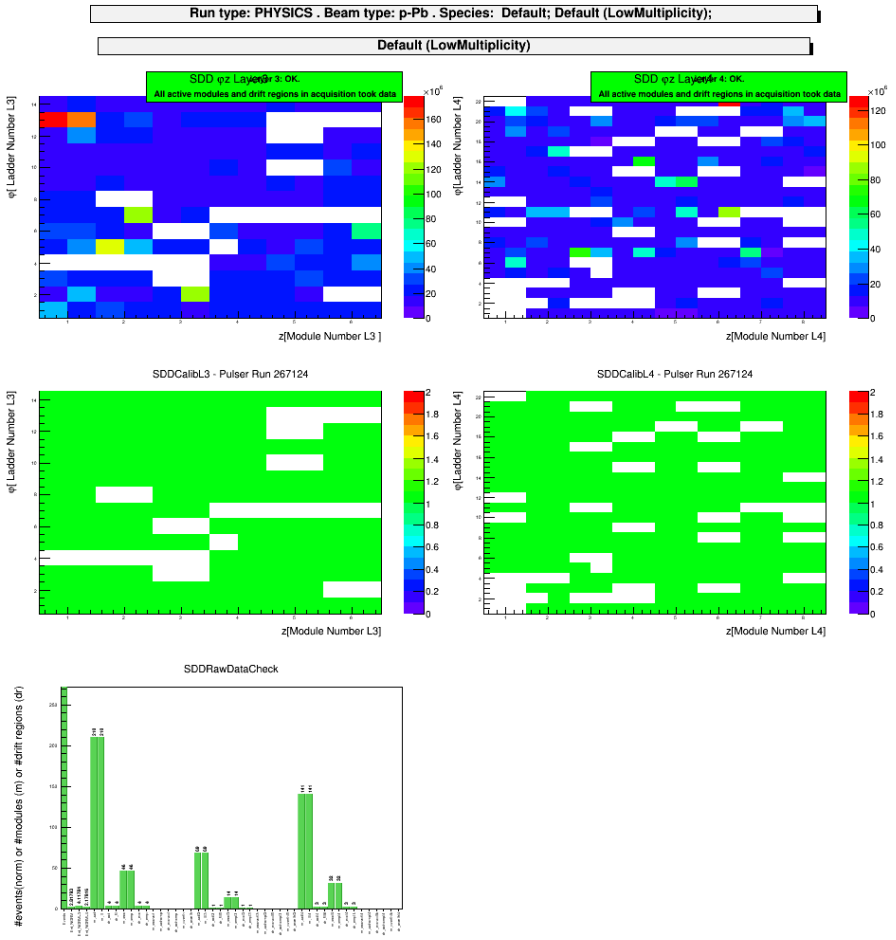

FIGURE 3.18: Example of Monitor Objects displayed on the AMORE GUI.

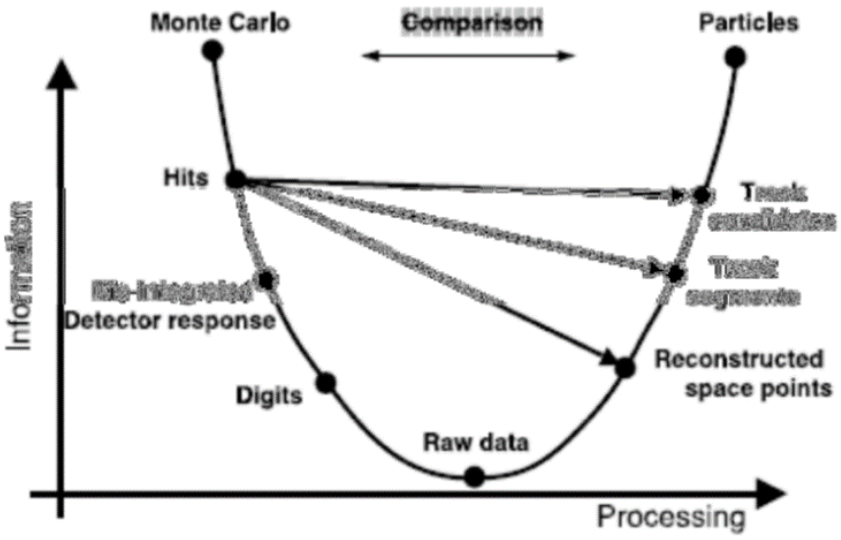

FIGURE 3.19: Aliroot data processing framework.

Chapter 4

The ALICE Time-Of-Flight detector

The Time Of Flight (TOF) [155] is one of the main detectors of the ALICE central barrel, with a fundamental role in the particle identification. The measurement performed with TOF, together with momentum and track length measured by the tracking detectors, is used to calculate the particle mass. In this way, charged particles in the intermediate momentum range are identified in ALICE, providing a separation π/K up to 2.5 GeV/c and K/p up to 4 GeV/c in 3σ.
Multigap Resistive Plat Chambers (MRPC) are the elementary TOF units, proving the required time resolution.
The Salerno group, of which the PhD candidate is a member, together with the Bologna group has the full responsibility for the design, construction, testing and commissioning of TOF detector. In particular, together with the research activity object of this thesis, the PhD candidate has worked on different tasks related to the TOF data quality monitoring (DQM) offline and TOF data quality assurance (QA).
In this chapter, the design of the detector will be discussed in detail, as well as the TOF performance and the TOF PID capabilities. The operations of data quality monitoring (online) and data quality assurance (offline) for the data taken with the TOF detector will be also illustrated.

4.1 Time-of-fligh technique

The TOF detector [155–157] measures the time t_{TOF} needed for a particles coming from the interaction point to reach the sensitive surface of the detector. Combining this information with that of the particle momentum p, provided by the tracking detectors, it is possible determine the mass m as:

$$m = \frac{p}{\beta\gamma} = p\sqrt{\frac{ct_{TOF}{}^2}{L} - 1} \tag{4.1}$$

where L is the measured track length and $\beta = v/c$ the Lorentz factor. The TOF detector is situated about 3.7 m far from the IP. With a magnetic filed of B_z = 0.5 T, and taking into account the detector material, it turns out that the minimum momentum threshold for pions is about 300 MeV/c, 350 MeV/c for kaons and 450 MeV/c for protons.

In order to distinguish two particles with the same track length, same momentum but different masses m_1 and m_2, it is necessary that the difference Δt between the two times of flight is greater than the correspondent mass resolution. Indeed, from the 4.6, in the hypothesis of $p >> mc$:

$$\Delta t \simeq \frac{Lc}{2}\frac{({m_1}^2 - {m_2}^2)}{p^2} \tag{4.2}$$

The capability of distinguish the two particle, can be expressed in terms if the TOF time resolution σ_{TOF} as:

$$n_{1/2} = \frac{\Delta t}{\sigma_{TOF}} \simeq \frac{L}{2c}\frac{({m_1}^2 - {m_2}^2)}{p^2\sigma_{TOF}} \tag{4.3}$$

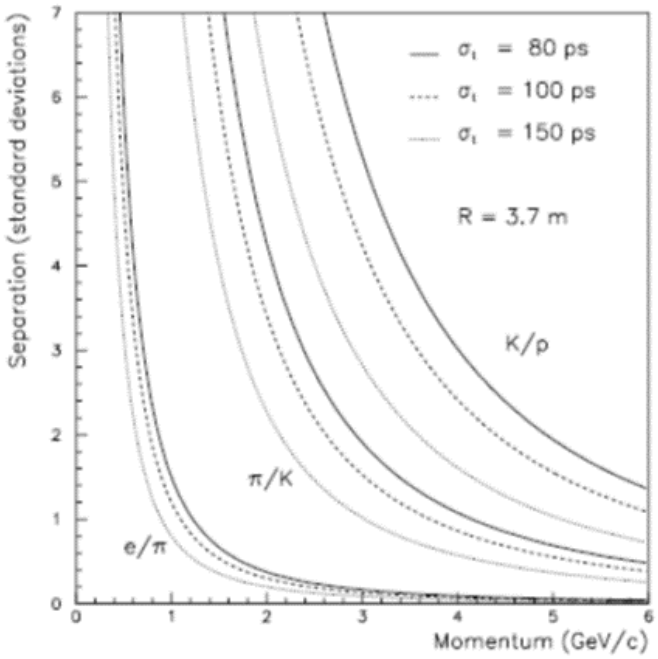

FIGURE 4.1: Predicted separation of particles emitted at $\theta = 90°$ for TOF. Separation shown in correspondence of three different TOF resolutions.

So, the TOF performance for the particle identification depends on the reached TOF resolution. Fig. 4.2 shows different expected separations assuming respectively a TOF resolution of 80 ps, 100 ps and 150n ps. σ_{TOF} is given by several contributes:

$$(\sigma_{TOF})^2 = (\sigma_{MRPC})^2 + (\sigma_{TDC})^2 + (\sigma_{Clock})^2 + (\sigma_{FEE})^2 + (\sigma_{Cal})^2 + (\sigma_{t_0})^2 \tag{4.4}$$

where $\sigma_{MRPC} \simeq 50$ ps is the intrinsic resolution of the MRPCs; $\sigma_{TDC} \simeq 20$ ps the intrinsic resolution of the readout card, due to the signal digitization; $\sigma_{Clock} \simeq 20$ ps the resolution related to the fluctuations of the *clock* signal and his distribution to the electronics; $\sigma_{FEE} \simeq 10$ ps the resolution related to the

jitter of front-end electronics; σ_{Cal} summerises the uncertainties on the calibration parameters, such as cable lengths and paths on the readout boards; σ_{Cal} the resolution on the measurement of the interaction point.

4.2 The TOF detector

The TOF detector is a large area detector with cylindrical shape, covering a pseudorapidity range $|\eta| < 0.9$ (polar angles between 45 and 135 degrees) and the full azimuth, with a surface of 141 m^2 and an inner radius of 3.7 m (see Fig. 4.2).

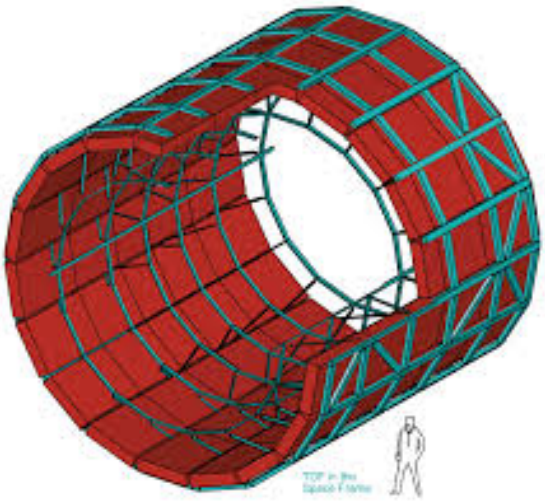

FIGURE 4.2: Time Of Flight layout.

It has a modular structure with 18 sectors (supermodules - SM)(see Fig. 4.3 in ϕ and 5 modules along the beam line for each sector, with a total of more than 10^5 readout channel. Each modules covers approximately 20 degrees of azimuthal angle, in correspondence with each TRD module.
A detector operating efficiently, with an excellent intrinsic resolution and a low occupancy, not exceeding the 10% at the highest predicted charged-particle density of $dN/d\eta = 8000$ was required to satisfy the ALICE performance requirements [158]. This led to the current design, with more than 10^5 independent TOF channels. Several types of gaseous detector were taken into account, in the framework of the LAA project at CERN. At the end, the Multigap Resistive Plate Chamber (MRPC) was chosen as the best option [159], in order to achieve a time resolution $\sim$ 100 ps, while operating in a high-track multiplicity environment, potentially with high detector occupancy in Pb-Pb collisions. The MRPC are an evolution of the Resistive Plate Chamber (RPC).

4.2.1 RPC and MRPC

RPC are gaseous parallel detectors, which electrodes made of materials with high resistivity (instead of metallic plates used in the PPCs), providing an uniform electric field, filled with a proper gas mixture. When a charged particle

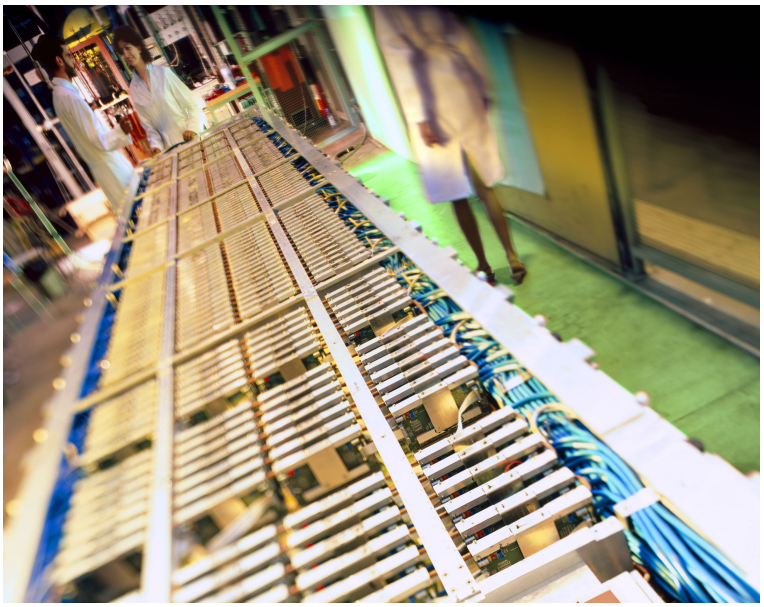

FIGURE 4.3: A supermodule of the TOF detector after assembly.

traverses the area between the plates, by ionization it produces ion and electron pairs. Thanks to the strong electric field, the electron migrating toward to the anode can generate avalanches in the gas. The avalanches can degenerate in *streamer*, propagating at even faster velocities. The movement of the charges in the electric filed gives a signal read by the electronics (*pads* on anode and cathode). This technology already presents advantages with respect to the traditional wire chamber with a radial electric field ($E \sim 1/r$): since the electric field is uniform, the primary electrons don't need to reach a point in which the electric field is strong enough to produce avalanches. In this ways, the time uncertainty on the primary ionization point is totally removed. This point affects the amount of produced charges, so it affects strongly the detection efficiency. On the other hand, the avalanches formation (so, the signal formation) is affected by two components: first, the fluctuations on the produced amount of charges needed to produce a signal above a certain threshold, depending on the gap width and on the intensity of the electric field; second, the fluctuation on the poissonian distribution of primary ion-electron pairs, affected by the chosen gas.
After a few years of studies, it turned out that the traditional RPC are not suitable to bear too high streamers of particles, like those during Pb-Pb collisions. In that situation indeed, the huge amount of charged collected at the electrodes would reduce the intensity of the electric field, badly affecting the efficiency. It was found out that the use of MRPC allowed to operate with intense particles streams, maintaining high efficiency and time resolution.

A MRPC [159] is a RPC in which the initial gap is divided in many smaller gaps (see Fig. 4.4), through resistive plates electrically floating, parallel to the two original electrodes, made of the same material. With respect to the RPC, in case of High Voltage (HV) applied, so high electric field inside each gap, the dimension of the avalanche and the amount of charges collected are limited by the small dimensions of the gaps. The resistive internal gaps are transparent to the fast signals generated by the avalanches inside each gap. So the induced signal on the external electrodes is the sum of the signals induced by the single

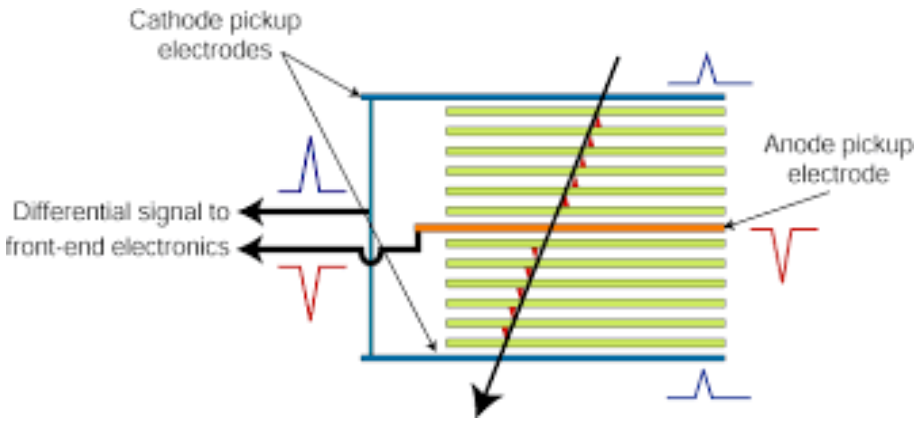

FIGURE 4.4: Schematic view of a MRPC.

avalanches in the single gaps.

Many gaps allow for the achievement of high efficiency, the small size of each gap is aimed to achieved a good time resolution.
The detector element of the ALICE TOF is a *double-stack* MRPC. As shown in Fig. 4.5 [160], it essentially consists of two MRPCs, built on each side of the anode plane. What it is measured hence is the sum of the signals from the two stacks. In this way, with respect to a single-stack MRPC, the collected signal is the same, while the applied voltage is lower of a factor two. The MRPC strip is 122 cm long and 13 cm large, with an active area of 7.4 x 120 cm^2, subdivided into two rods of 48 readout pads of 2.5 x 3.4 cm^2. It consists of two stacks of glass, each with five gaps of 250 μm. Spacers made of nylon fishing line keep the distance between the fixed glass plates. The resistive plates are made of "soda-lime" glass, the internal ones are μm thick while the external ones are 550 μm thick and resistivity of 2-25 $M\Omega$. The High Voltage is applied through the electrodes connected to the external surface of the resistive plates. The Printed Circuit Boards (PCB) with the readout pads are collocated externally and are hold together with honeycomb panels maintaining the rigidity of the system. The strips are filled with a non-flammable gas mixture of 93% freon $C_2H_2F_4$ and 7% SF_6, allowing to reach high ionisation density, absorb photons from recombination of primary ion pars and electron emitted by the cathode, avoiding the production of secondary avalanches.
The MRPCs performance was tested with beam test[161] at PS of CERN, together with all readout electronics, taking into account a sample of strips, randomly chosen from a two years long mass-production. Results are shown in Fig. 4.6 for the efficiency and the time resolution, in function of the voltage applied at the electrodes. It was demonstrated an efficiency close to 100% and an intrinsic time resolution better then 50 ps (which includes also the contribution from the full electronic chain, measured to be about 38 ps).
Extensive test were performed at CERN PS and Gamma Irradiation Facility (GIF) [162] also to study possible gas mixtures, ageing effects and rate capability. No ageing effect was observed with a dose up to 3.5 bigger than the foreseen dose, for the standard running scenario for the first 10 years of LHC operations; the rate capability was found larger than the maximum expected of 50 Hf/cm^3.

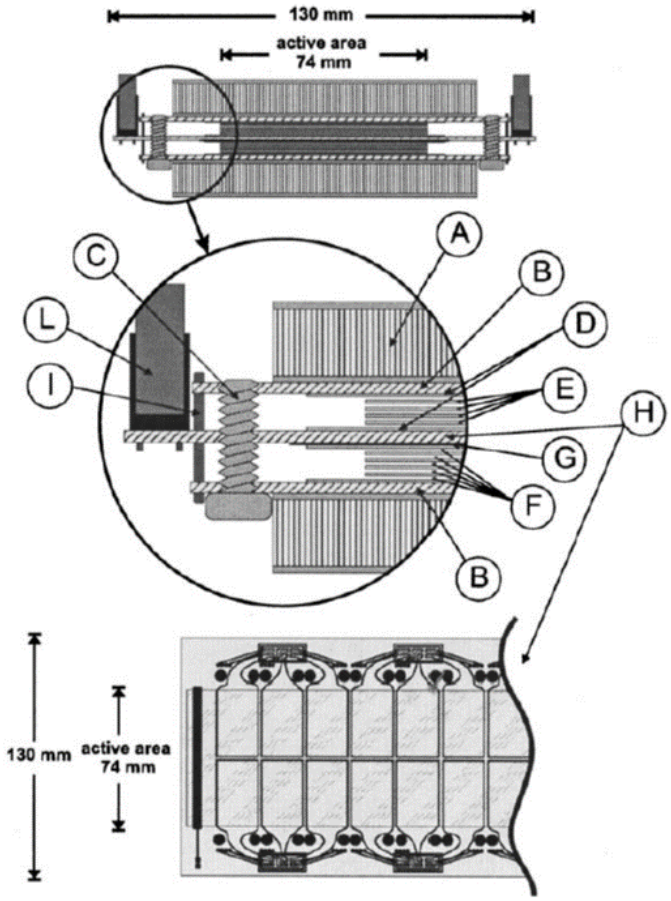

FIGURE 4.5: Schematic cross section of a double-stack MRPC. (A) honeycomb panel; (B) PCB with the cathodic pads; (C) plexiglass screw to hold the fishing-line spacer; (D) external glass plates; (E) four internal glass plates; (F) five gas gaps; (G) 250 μm mylar film; (H) PCB with anode pickup pads; (I) connector (pin) to bring the cathode signal to the central PCB; (L) flat cable connector for the MRPC-signal transmission to the interface card.

4.2.2 MRPCs performance

The performance of the MRPCs was very stable during the first three years (2009-2012) of data taking. The typical behavior during collisions is shown in Fig. 4.7: the current from a few nA (current without beam) quickly increases when the HV is switched on and then quickly decreases to a stable value, depending on the beam conditions and luminosity.

The current of the MRPCs was observed to increase linearly with the luminosity (see Fig. 4.8, left), without showing any deviations related to abnormal noise.

From the interaction rate at ALICE and the TOF hit multiplicity per event, it is possible to estimate the average rate of particles in the TOF detector as a function of the TOF current, and this result is shown in the right of Fig. 4.8. From these two plots, it is possible to extrapolate the TOF rate for the luminosity of 5000 Hz/barn foreseen in the ALICE upgrade in 2018 [2]. The expected rate is 60 Hz/cm^2 and this, compared with results from test beam [162] indicates that

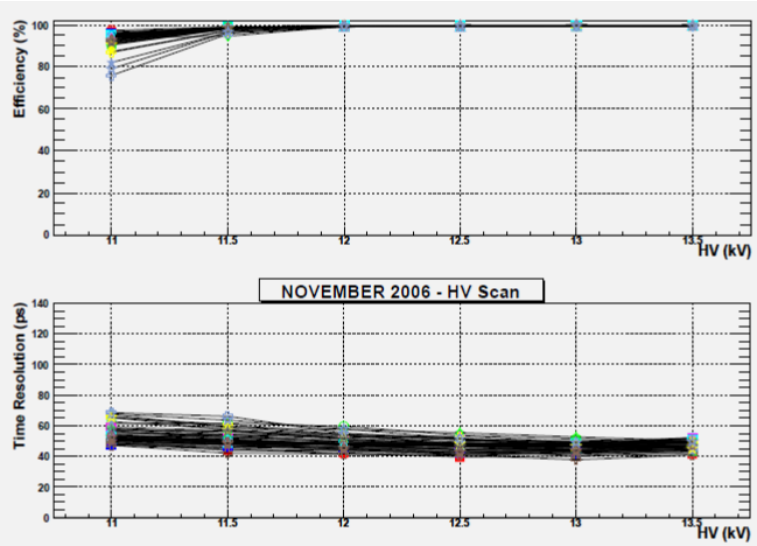

FIGURE 4.6: Efficiency and time resolution as a function of high voltage for a sample of mass-production MRPC strips. The operating voltage is 13 kV.

also in the period of maximum luminosity of LHC, the MRPCs are expected to operate without significant loss in performance.

4.2.3 TOF modules

These strips are located inside gas-tight modules (see Fig. 4.9), and positioned transversely to the beam direction. Five modules along the z direction are needed to cover the full cylinder. They have all the same structure and width of 128 cm, but different length. Dimensions and layout were designed in order to have the boarder areas of the modules aligned with the dead areas of the other detectors, thus minimizing disturbance for the external detectors. The overall TOF barrel length, considering the active region, is 741 cm.
Inside each module, the angle of the strips with respect to the axis of the cylinder is progressively increasing from $0°$ in the central part of the detector (θ = 900°) to $45°$ in the extreme part of the external module (θ = 450°). In this way the median zone of each strip is perpendicular to radii coming from the IP, hence minimizing the angle of incoming particles with respect to the normal direction. Moreover, adjacent strips were overlapped of about 2 mm, in order to avoid dead areas. Also the modules were designer in order to avoid any loss of sensitive area, along the z-axis. The only unavoidable dead area is due to the presence of the supporting structure.
15 strips are placed in the central module, 19 in the intermediate and in the external ones, inside a box sealing the gas volume and supporting the external front-end electronics. Externally, PCBs have on one side connectors for cables from the strips and, on the other side, connectors to the Front-End Analogue (FEA) electronic cards. Finally the volume containing the electronic cards, cables for input/output, water cooling and gas pipes are covered by a 0.15 cm aluminium cover. The TOF detector consists in total of 90 modules. It was decided to not install three central modules, in front the PHOS, in order to reduce the amount of material for this high resolution electromagnetic calorimeter.

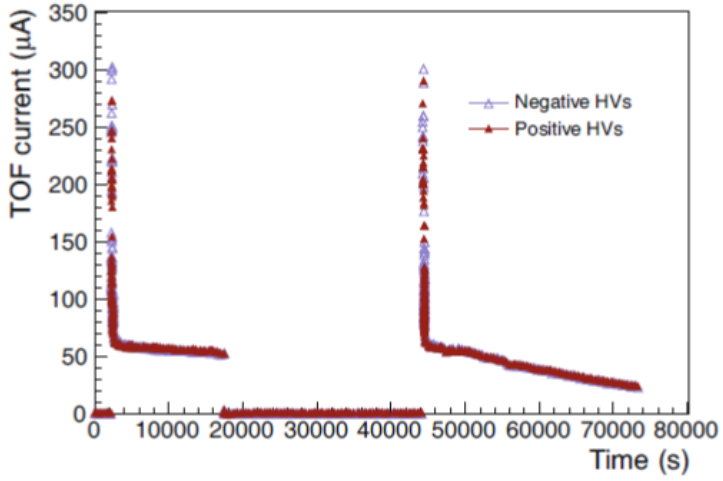

FIGURE 4.7: TOF current for positive and negative HV in function of time during pp collisions. Two different fills are shown.

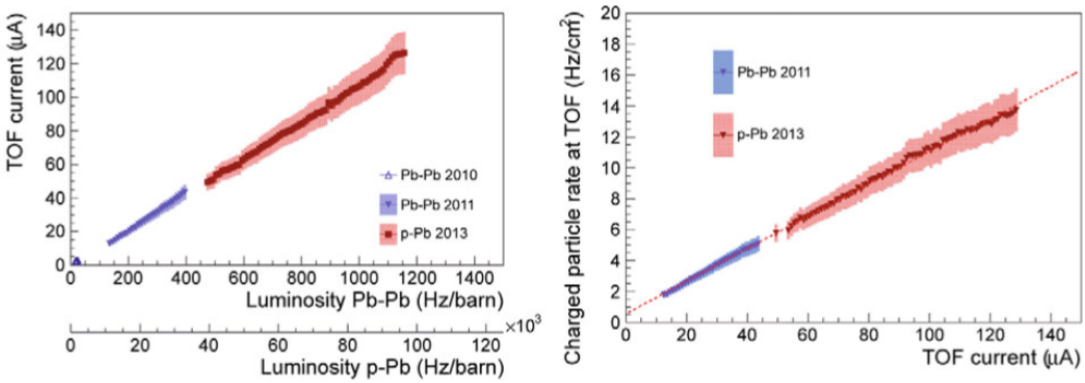

FIGURE 4.8: TOF current and TOF estimated particle rate. Left: TOF current in function of luminosity in Pb-Pb and p-Pb collisions. Right: TOF estimated particles rate versus HV current. In both the figures, points and bands indicate average and spread of the measurements, respectively. The dashed line is the linear fit to the 2013 data.

4.2.4 Front-End and readout electronics

The signal from the MRPC must be amplified and discriminated and the time measured with an accuracy matching the intrinsic time resolution of the detector. A schematic view of the TOF electronics of front-end and readout is shown in Fig. 4.10.

Each strip has connectors for the transport of the different signal from the cathodic pads to the FEA cards. Each FEA card contains three chips NINO ASIC (amplification Specific Integrated Circuit), that are 8 channels amplifier/discriminators devices, with a common threshold regulation. It was decided to adopter this technology during the R & D Research & Development) phase of the TOF detector. NINO ASIC chips were developed in 2002 and tested at PS in 2003 with excellent results [163]. The width of the output signal is called Time over Threshold (ToT), since it refers to the charge released

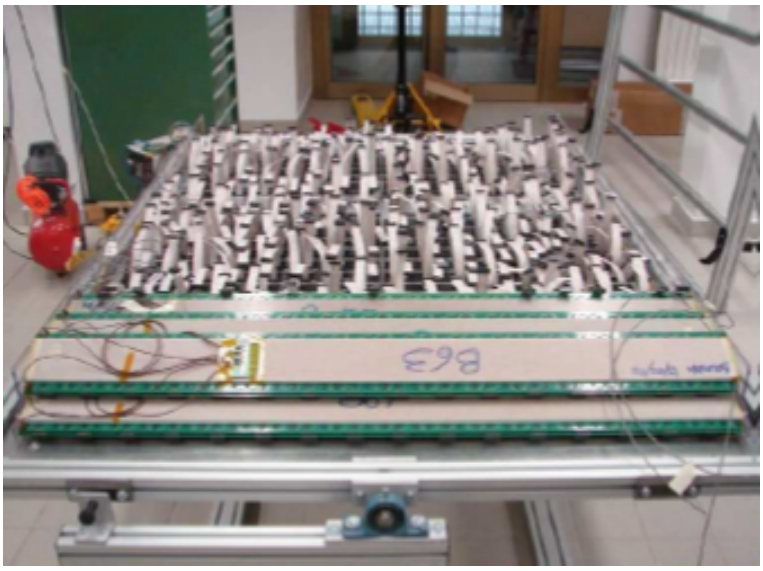

FIGURE 4.9: Photographs of a TOF module during assembly, with strips installed inside the gas volume.

during the interval in which the signal is above the threshold [1]. The minimum value of the ToT is 6 ns, and this information on the charge is important in order to correct the *time-slewing* effect: when two analogue signals with different amplitudes arrive at the same time and are digitalised, the output values are different, because their leading edge reaches the threshold at different times; there is hence a dependence on the amplitude of the signal. Each FEA reads 24 pads, displaced in two rows, corresponding to 8 channels $\times$ 3 NINO chips, so that one strip is read by four FEAs. The discriminated signal is sent, for the time measurement, to the readout component of the system, the Time To Digital Converter (TDC) Readout Module (TRM). TRMs are installed inside *crates*, at the collocated at the edges of the supermodules (two crate for each side of each supermodule).
Moreover, the OR signal from a couple of neighboring FEAs is sent to a card called FEAC, still locate inside the SM. Each FEAC supplies a group of 10 or 12 FEA, with a voltage of 2.5 V, monitors their temperature through a set of systems and collects the OR signals thanks to a Fully Programmable Gate Array (FPGA) card.
The FEAC output is sent to a card called Local Trigger Module (LTM). According to this configuration, a *trigger* signal is defined if at least one *hit* has been recorded by any one of the 96 pads of two ha-f-strips (the group of half-strips connected to the FEAC is also referred as *maxi-pad*. This TOF trigger signal is used as trigger for cosmic rays (useful for physics purposes and for the calibration of central barrel detectors) and contributes, as Level 0 (L0) trigger, to the physics selection (for minimum bias events in pp collisions and ultra peripheral events in p-Pb and Pb-Pb collisions).
As said, each side of the SM contains two crates, which contain four types of cards: the TDC Readout Module (TRM), the Local Trigger Module (LTM), the

[1]The Front-End ASICs (NINO)amplifies and discriminates the MRPC signal, with an output width correlated to the charge of the input signal.The time when the signal becomes larger than the threshold, defining in this way the *leading edge*, give the time-of-fligh measurement. The time when the signal becomes smaller than the threshold defines instead the *trailing edge*.The ToT, correlated to the MRPC charge, corresponds to the time difference between the leading and the trailing edges

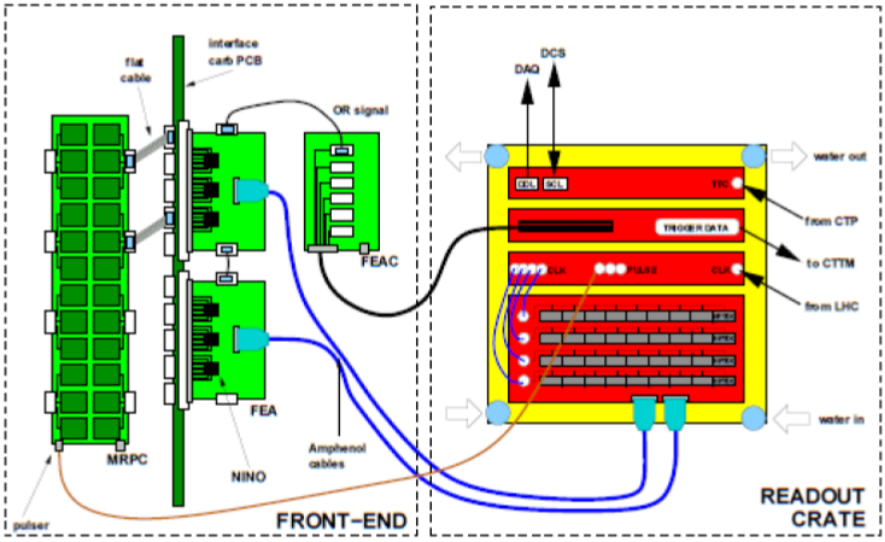

FIGURE 4.10: Schematic view of the TOF front end and readout electronics.

Clock and Pulser Distribution Module (CPDM) and the Data Readout Module (DRM).

TRM

The TRMs (9 or 10 TRMs are installed in each crate) control the readout operations. Each TRM card hosts up to High Performance TDC (HPTDC) 8-channel chips, i.e. 240 channels, corresponding to the readout pads of 2.5 MRPC strips. The HPTDC determines the difference between the signal from the FEA and the trigger input: Only the hits that fall in a valid matching window, starting a $t_{latency}$ before the trigger arrival are transferred to the HPTDC. Both $t_{latency}$ and matching windows are programmable. Moreover, TRM manages HPTDC configuration, HPTDC hits readout, transfer of the data in temporary internal buffer and successive transfer to DRMs.

LTM

The LTM is in charge of receiving the output from the FEAC and transferring it to a bigger card, the Cosmic and Topology Trigger Module (CTTM). This card, located under the muon spectrometer platform, receives the LTM signals, defines the L0 and L1 triggers and sends them, in 800 ns after the collision, to the CTP of the experiment. In addition, the LTM allows for setting and monitoring of the FEAC low voltages and their temperature inside the electronic volume of the module.

CPDM

The CPDM receives the LHC *clock* via an optical fiber and distributes it to the TRD, DRM and LTM cards of a crate pair with a very low *jitter* (17 ps) and a pulser signal for calibration and monitoring purposes to the MRPC strips.

DRM

The DRM is the interface between the TOF readout system and the ALICE DAQ. In particular, as we have seen before, it is interfaced to the DAQ system via the 72 DDLs of the TOF.
The DRM receives and decodes trigger signals and messages from the TTC and propagates to all the cards of the crate the L1 and L2 trigger signals.
It hosts a computer with which is possible to reprogram the firmware for all the FPGAs present on the crate.
The DRM also monitors the general condition of the readout and sets a *busy* signal to the Auxiliary Control Module (ACM), that can inhibit further triggers from being generated by the CTP.

4.3 TOF Data Quality monitoring online

During data taking, the TOF data have to be monitored online by a DQM operator, who checks the shape of the signal,the detector and electronics configuration, the hit occupancy. The TOF DQM monitoring tools are based on the AMORE framework and AliRoot QA framework (see section 3.3.1). A big vantage of the TOF DQM system is that results obtained online can also be checked offline, being hence a fundamental resource for detector experts that could want to investigate some issues spotted by DQM operators.

4.3.1 Monitoring the TOF signal - TOF raw time

The TOF signal is provided by the HPTDC and encoded by the TRMs in raw data format. When a HPTDC receives a trigger signal, it searches for hits falling in the TOF time matching windows (MW) (see sec. 4.2.4), that is set at 600 ns. The raw time is measured in TDC bin units (N_{tdc}) from the beginning of the MW. N_{tdc} is then multiplied for the time bin width of the TDC, to have the time in ps.
The TOF raw time is monitored online, by the DQM operator, in the full TOF MW. The two histograms on the left side of Fig. 4.11 are the time spectrum for the hits at TOF during physical events, considering all the event integrated (top plot) or a particular trigger selection (bottom plot). The box on the top right of the plot is a *quality flag*: it will provide an alarm (warning/yellow or error/red) is the peak is shifted from the expected position, otherwise a green (as in the showed figures) box will inform that everything is under control. For physics runs (pp, p-Pb and Pb-Pb) taken during the Run 2 data taking, the main peak is observed within 150 and 220 ns. PHYSICS (e.g. pp, p-Pb, Pb-Pb) runs: the main peak has to be within 150 and 225 ns, followed by a tail due to slower particles with a later arrival time. Since the TOF matching window is 600 ns, if the bunch spacing is small enough, a double peak structure can be observed, since not only hits coming from the trigger bunch crossings are recorded, but also from the following bunch crossing. This secondary peak is then discarded during the reconstruction phase.
The histogram on the right of Fig. 4.11 represents the number of TOF hits per

physical event. The distribution is approximately Poissonian. The number of entries indicates the number of physical events processed, The mean value is a rough estimate of the average hit multiplicity.

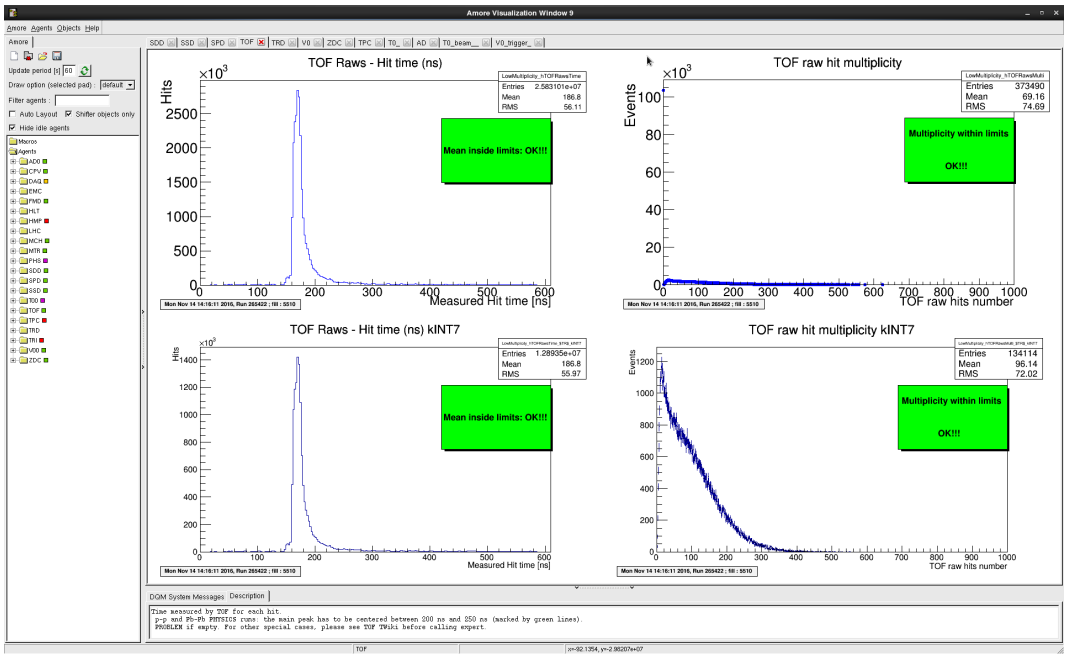

FIGURE 4.11: TOF Raws Hit time and TOF raw hit multiplicity. On the left: time spectrum for hits on TOF during physical events for all the integrated events (top plot) and after kINT7 trigger selection (bottom plot). On the right: number of TOF hits per physical event for all the integrated events (top plot) and after kINT7 trigger selection (bottom plot).

The TOF DQM summary image in the logbook contains more details and shows additional histograms that are meant for the TOF experts and that can be monitored offline at any time.

4.3.2 Monitoring the TOF readout status

Having a good readout efficiency is a necessary ingredient in order to be able to reproduce the detector response in MC simulation. Moreover, at reconstruction level, it's important to remove noise and spot possible issues at the TRM levels. So, TOF channels that are flagged as "bad", at hardware level, or "noisy" or "inefficient", are *masked* at reconstruction level, i.e. hits coming from those bad channels are discarded. These bad channels are identified by comparing the map of the recorder hits with some reference map.
In Fig. 4.12 an example of enabled channel maps is reported, for a physic run taken during Pb-Pb collisions in 2015 (Run 2). On the horizontal axis, the numbering is referring to the supermodule index, while on the vertical axis to the strip index for each supermodule.

Each bin corresponds to a FEA card and the bin content to the number of enabled FEA channels (24 in total, channels can also be disabled by the monitor process). Empty bins in the map of the enable channels can be due to different kinds of issue. Some white spaces correspond to disabled TRMs. A given of

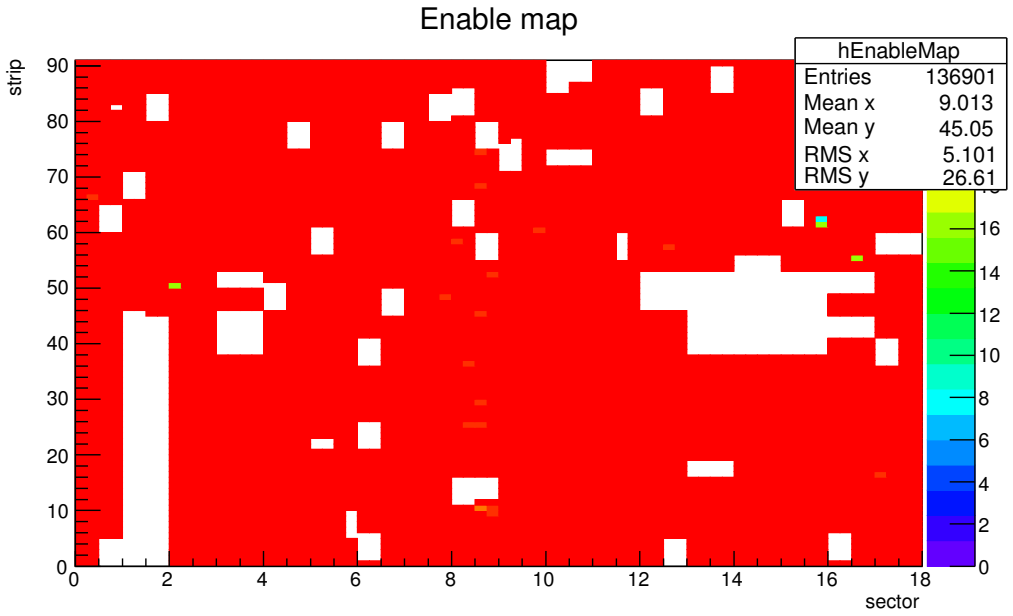

FIGURE 4.12: Map of the enabled TOF readout channels, during a Pb-Pb run, 245731, taken in 2015. The channels to be masked during the reconstruction, because inefficient, are not yet removed from the map.

channels may not receive data because the corresponding strips or front-end cards are not powered, due to issues with high or low voltage power supplies. The central modules of sectors 13, 14 and 15 were installed, due to the presence of the PHOS, so the correspondent white space are do not indicate any issue.
The TOF DCS sends to the TOF Detector Algorithm (DA) all the information about the hardware status of the detector (HV, FEE, ecc.). From this information, the DA is able to produce *maps* of the readout configuration, saving the status of each channel in a OCDB object, the transferred to the Grid OCDB. This is done at least two times per run, at the beginning (Start Of Run - SOR) and the end (End Or Run -EOR) of the run. The most recent version of this object can be retrieved from AliEn during the data reconstruction. The hit map, relative to the same run, is shown in Fig. 4.13. The channels marked as bad, noisy or inefficient from the OCDB are masked.
The reference map for this run is shown in Fig. 4.14. The latter is the one to be used during data reconstruction, to discard hits coming from bad channels, and during the simulation of *anchored* [2] runs, to take into account the effective TOF readout efficiency.
Any possible difference between the hit map and the reference map suggests possible undetected changes in the readout or DAQ configuration or a problem in the propagation of the channel status to the CDB. In any case, it triggers checks by the TOF experts.

The noisy channels are flagged during dedicated "noise scan" runs, performed before the stable beam, in particular during the beam energy rump-up of each LHC *fill* (injection of protons or ions), when the TOF strips are supplied with

[2]The Monte Carlo event samples to be analyzed for efficiency studies are simulated taking into account the same running condition of the real data taking: beam properties, trigger, detector configuration and calibration, ecc. The simulated runs are called "anchored" runs.

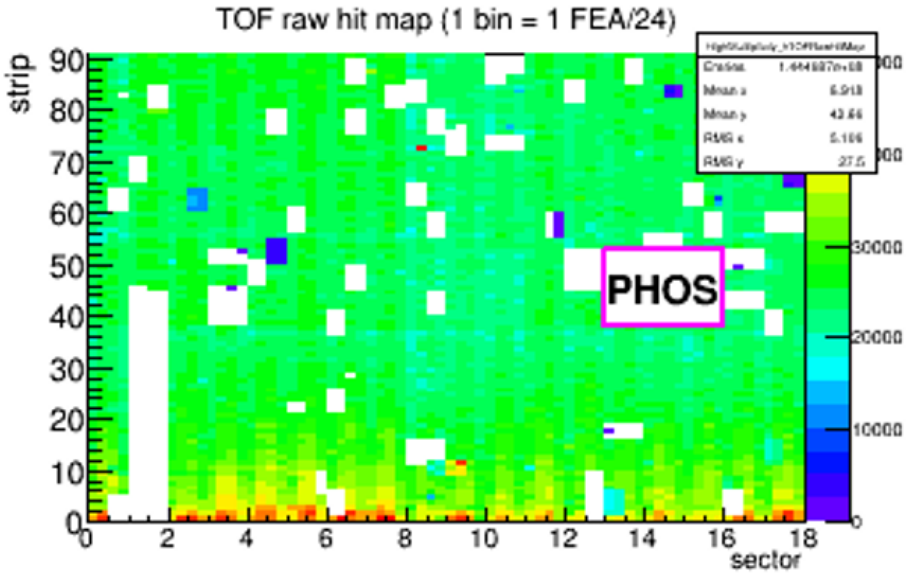

FIGURE 4.13: Hit mao relative to a sample of events from the physics Pb-Pb run 245731 taken in 2015.

only 0.5 kV power, much lower than the nominal HV of 13 kV. A 1 kHz trigger is sent to all the readout elements. The hits recorded in this condition are considered as noise. The TOF DA processes the data searching for these noisy channels, and flag them as noise in the OCDB object, from which the map in Fig. 4.15 is obtained. When, for example, a channel is flagged as noisy in more than 50% of the noise scan runs taken in a certain period, it is considered pathologically noisy and disabled from the data acquisition.

4.4 TOF data Quality Assurance offline and performance

The following ingredients are of fundamental importance for the TOF performance:

- TOF matching efficiency,
- TOF signal calibration,
- knowledge of the interaction time ($t_{\rm ev}$) for each event, with the best possible resolution.

These three points will be discussed in detail in the following. In particular, the TOF detector performance and PID will be discussed using QA histograms.
The ALICE Calibration is procedure performed in multiple steps. A first partial reconstruction of a sub-sample of high-multiplicity minimum bias events, devoted for the calibration, is carried out during the *pass0* (the name stands for "calibration pass 0") period. The output of the calibration routines determines the calibration parameters to be stored in the OCDB objects (these objects are updated, if pre-existing, or just created for the actual run). At the next calibration step, called *cpass1*, the same sub-sample of events is reconstructed, by using the updated version of the OCDB objects. This calibration procedure is

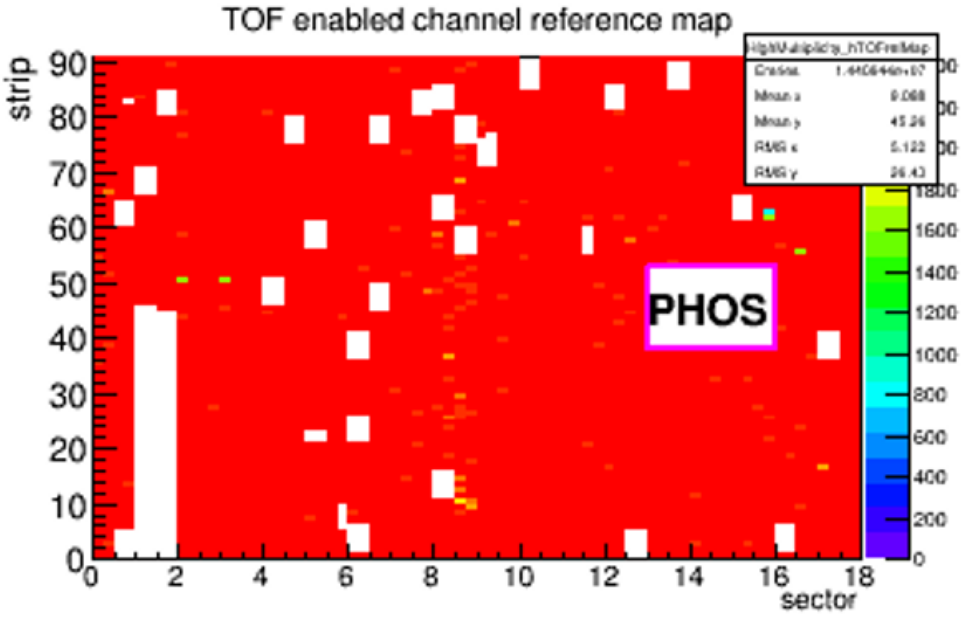

FIGURE 4.14: Refernce TOF readout channels map of the physics Pb-Pb run 245731 taken in 2015. The map shows the enable channels, efficienct and not noisy.

run in parallel with QA checks on the cpass1 ESDs. The output of cpass1 calibration triggers a second update of the OCDB. The full reconstruction (*pass1*) starts only wgen the calibration is completed and satisfactory for all the detectors.
QA can run equally after simulation or reconstruction.

4.4.1 TOF matching efficiency

After the propagation through TPC and TRD, tracks are extrapolated to the sensitive layer. The tracking algorithm searches for TOF clusters within a geometric matching window (3 cm for Pb-Pb collisions, 10 cm for pp collisions)[3] and if any cluster is found, the closest hit to the crossing point is associated to the track.
The quality of the tracking processes is checked in the TOF QA analysis, looking at the distance (called also *residual*) between the extrapolated point of the track and the center of the track containing the matched hit. The residuals along the z direction, D_z is shown in Fig. 4.16 as a function of the strip index. Distributions are centered at zero, without big differences between pp and p-Pb case, except for the fact that the tracks populate the relative geometrical matching window and except for the different track multiplicity.

The TOF matching efficiency is defined as ratio between the tracks reconstructed at TOF and those reconstructed using the ALICE tracking detectors, i.e. ITS, TPC and TRD. It is affected by many factors: MRPC detection efficiency, TOF

[3]The geometrical matching window is opened around the intercept of the extrapolated track and the TOF sensitive surface.

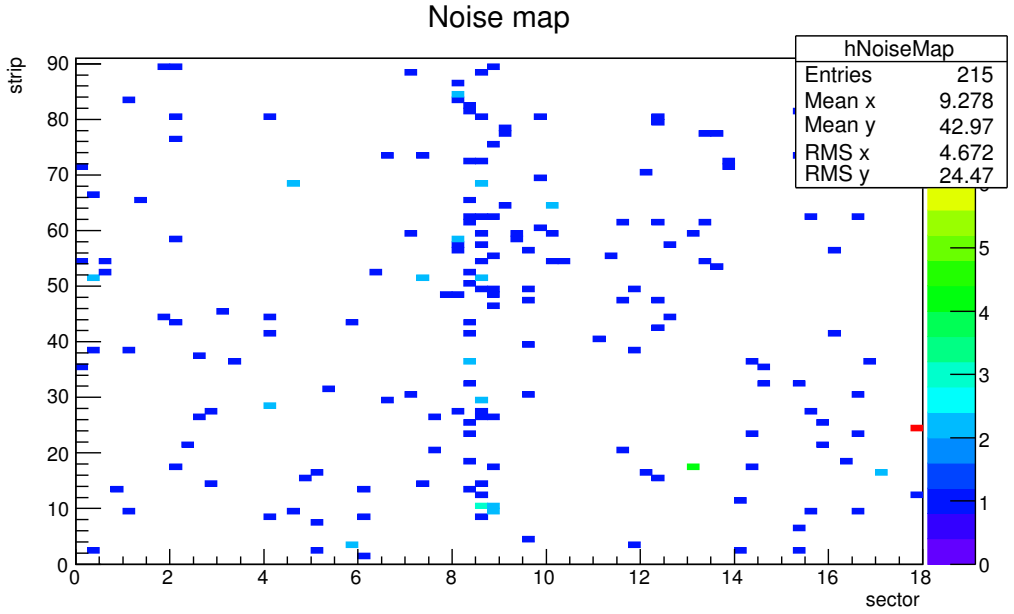

FIGURE 4.15: Map of noisy TOF channels for the physics Pb-Pb run 245731 taken in 2015.

geometrical acceptance, uncertainties in the track extrapolation, material located in front of the TOF and track-TOF matching algorithm efficiency. Tracks with $p_{\mathrm{T}} < 0.3$ GeV/c don't reach the detector, due to the curvature of the trajectory in the magnetic field. For tracks with $p_{\mathrm{T}} > 0.3$ GeV/c, the matching efficiency rapidly increases and it reaches a more or less constant value for $p_{\mathrm{T}} > 1$ GeV/c. A typical behavior versus p_{T} is shown in Fig. 4.17

In Fig. 4.18 the matching efficiency is also compared with what obtained using simulated Monte Carlo (MC) productions. Tracking and matching algorithms are common to both data and simulations. The response of the MRPC detector has been carefully simulated in the Monte Carlo, taking into account beam test results. The MRPC efficiency in the center of a paid is taken as $\sim$ 99.5 %. However, due to the readout structure of the MRPC, a particle crossing the MRPC close to a pad boundary induces a charge on the pad itself and a smaller charge also on the neighboring pads. So, the boarded between two pads is defined as a 13mm wide region, where the pad efficiency decreases from 99.5% to 0, going towards the next pad, while the efficiency of the nearby pad increases from 0 to 99.5%. This effect concerns three sides of each pad, while along the fourth side, which has no neighbouring pads, there is only a 4 mm wide region where the pad efficiency decreases, until 88.3% at the pad extremity. All those effects are included in the Monte Carlo simulations. In this way, the overall simulated MRPC efficiency is reduced to $\sim$ 98.5 %. The very good agreement (few percent of difference) between data and MC simulations, proves the reliability of the current MRPC simulation.

In order to compare the matching efficiency for different runs, one needs to take into account only the active good channels. This is done normalizing the efficiency for the fraction of TOF good channels, taking this information from the OCDB reference maps. In this way, the trending plot of the average matching efficiency from tracks with $p_{\mathrm{T}} > 1$ GeV/c, for a different set of runs, can be produced. An example is shown in Fig. 4.19, where the efficiencies before

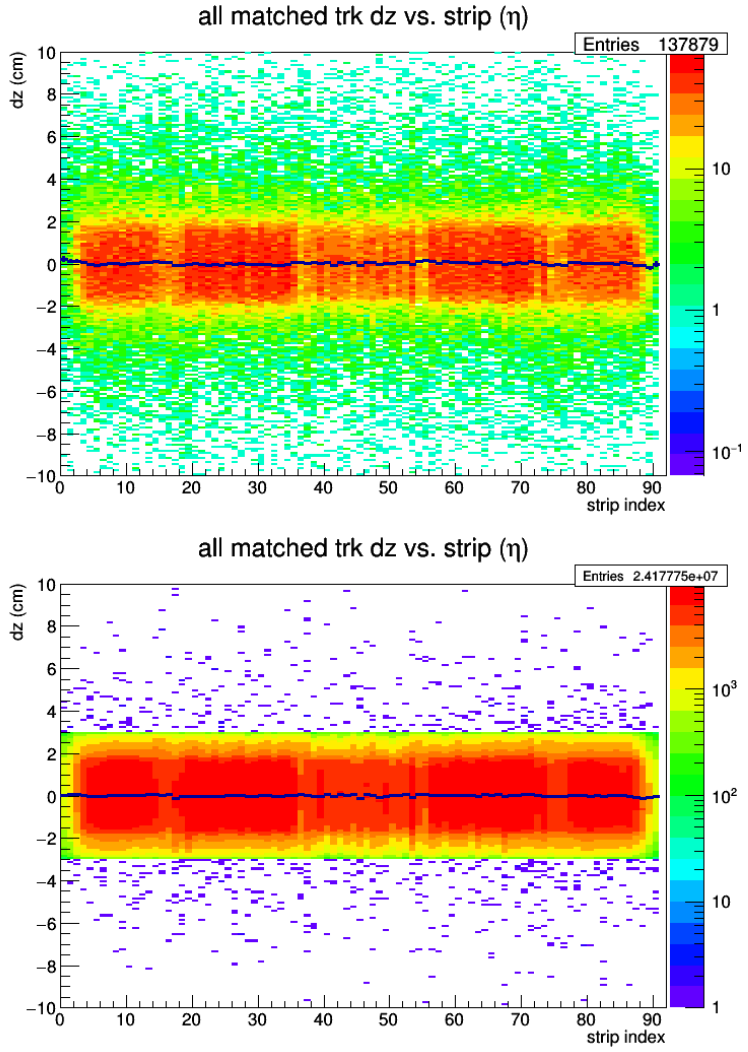

FIGURE 4.16: TOF matching residuals along the z direction, vs the strip number. Top: plot obtained for one run of pp collisions at $\sqrt{s}$= 13 TeV taken 2016. Bottom: same plot obtained for Pb-Pb collisions taken in 2015.

and after normalization are overlapped. One can observe that the normalization minimizes the differences between the runs. Any discrepancy from this roughly flat trend can be due to several issues and it is investigated by experts.

4.4.2 Timing calibration

If the TOF were an ideal detector, the difference between the time measured by TOF and the expected time, calculated during reconstruction for a given particle species, ($t_{\rm TOF}$- $t_{\rm exp}$) would be centered at zero. The TOF time calibration is based on the determination of three components: i) a global *offset*, common to all the channels; ii) second channel-dependent offset; iii) time-slewing (already mentioned in section 4.2.4) correction at channel level. All the three components require full track reconstruction in the ALICE detector, so they are strongly dependent on the calibration of the TPC (section 3.2.1), that is the main tracking detector in ALICE.

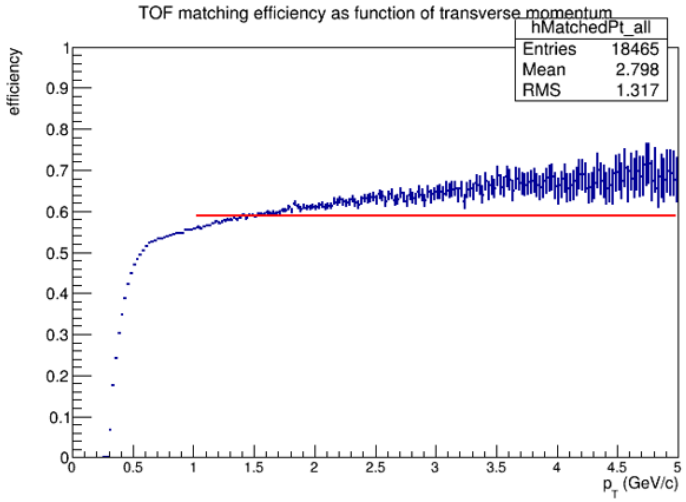

FIGURE 4.17: TOF matching efficiency versus reconstructed p_{T} for tracks with η in -0.8, 0.8. The data sample refers to pp 2016 collisions.

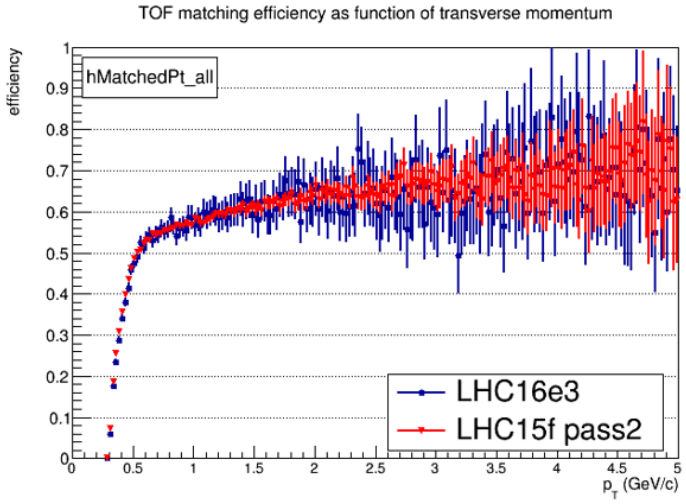

FIGURE 4.18: TOF matching efficiency versus reconstructed p_{T} for tracks with η in -0.8, 0.8. Data are compared with simulations.

The need to determine the global offset comes from the observation of a time shift in LHC clock phase, resulting in a non constant offset in the measured time of flight, due to the temperature dependence of the fiber refractive index. For a sample of particles with reconstructed momentum $p > 0.5$ GeV/c (in order to assure a good tracking performance), the measured arrival time-of-flight is compared with the expected time in the pion mass hypothesis [4]. The distribution of the time differences, sampled in time (10 minute samples), is fitted with a Gaussian function, whose mean is the global channel offset for the considered time interval. This contribution to the calibration is estimated during the *cpass0* calibration step.

The channel-by-channel offset comes from the delays introduced in the measured time-of-flight by the cable lengths and by the electronics. Such calibration is performed as done for the global offset, but in this case the distribution

[4]The choice to use pions as mass reference was driven by the fact that pions are the most abundant species produced in the collisions and they dominate the time distribution.

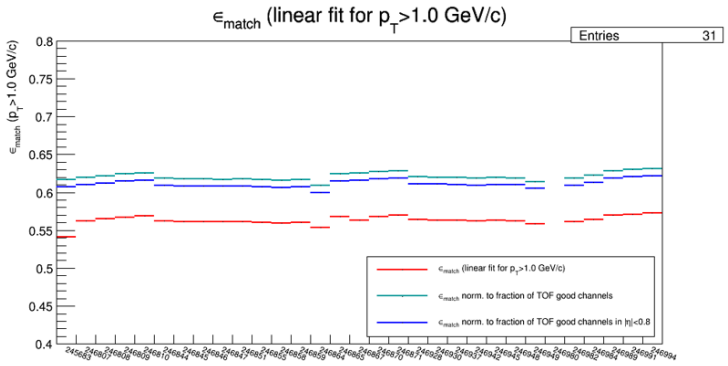

FIGURE 4.19: Trending distribution for the TOF matching efficiency versus run number.

of the time differences is evaluated for each channel. The mean of the fit of the distribution gives us the channel-by-channel offset. A much larger statistics is needed for this calibration: several million events for pp collisions, collected over several days of data taking; much less for events taking during p-Pb and Pb-Pb collisions, due to the very high average number of particles per event
Finally, the time-slewing effect correction is applied, making use of the correlation between the measured time and the signal width (ToT), fitted with a 5th-order polynomial. This calibration is performed channel-by-channel, using data collected overy long periods (several months).

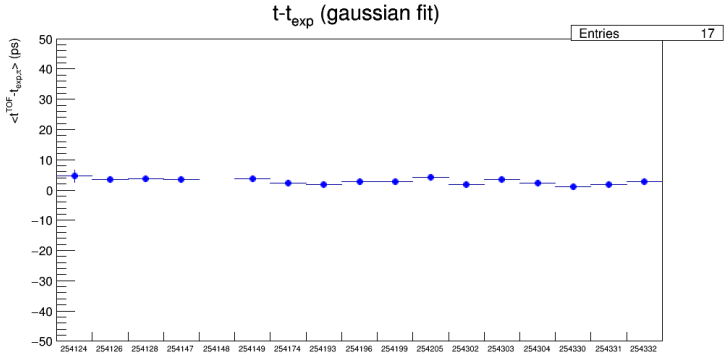

FIGURE 4.20: Trending distribution of the ($t_{\rm TOF}$- $t_{\rm exp}$) alignment for a set of 2016 pp runs at $\sqrt{s}$= 13 TeV is shown, obtained by the QA offline analysis. Each value per run is the mean value from the gaussian fit of the ($t_{\rm TOF}$- $t_{\rm exp}$) distribution.

In Fig. 4.20, the ($t_{\rm TOF}$- $t_{\rm exp}$) alignment for a set of 2016 pp runs at $\sqrt{s}$= 13 TeV is shown, for the cpass1 reconstruction. The average difference stays close to 0, with on offset per run not greater than 10 ps (an offset up to $\pm$ ps is tolerated in the QA analysis).
After the above three calibration, it is possible to evaluate the TOF performance in terms of time resolution. For tracks with a momentum in the range 0.95 < p < 1.05 GeV/c, the difference between the measured time of flight and the pion time expectation is evaluated. The distribution is fitted then with a Gaussian function, whose width is given by $\sigma^2_{\rm TOT} = \sigma^2_{\rm TOF} + \sigma^2_{t_{\rm ev}}$, where $\sigma_{t_{\rm ev}}$ is the resolution on the event time. Since the TOF t_{ev} resolution is expected to scale with

the square root of the number of tracks used, $\sigma_{t_{ev}} = A/\sqrt{n_{\text{tracks}}}$, the measured σ_{TOT} can be plotted as a function of n_{tracks} and fitted according this expression. The Fig. 4.21 shows the result of this fit for p-Pb collisions (Run I), indicating that for $n_{\text{tracks}} \longrightarrow \infty$ $\sigma_{\text{TOF}} \sim 80$ ps.

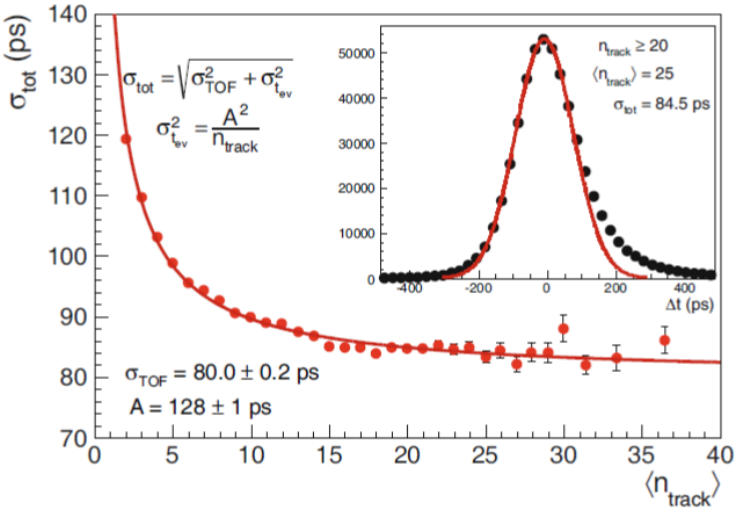

FIGURE 4.21: TOF total time resolution versus number of tracks per event.

4.4.3 Event time determination with the TOF

The T0 detector (section 3.2.2) is dedicated to the event time (t_{ev}, when the collision happens) determination. However, due to the limited acceptance of the detector, the detector efficiency is limited and no signals are observed by the T0, so the event time estimation is not available, for a fraction of the events. This negatively affects the total time-of-flight resolution for the TOF detector, σ_{TOT}. In order to reduce this uncertainties, an alternative method for the t_{ev}determination was developed: the TOF detector can also provide an estimate of t_{ev}, when at least three tracks have an associate TOF signal. A combinatorial algorithm compares the measured TOF times and the expected times, assuming a common t_{ev}, obtained from a χ-minimization procedure. In particular, for a given track j, the event time is estimated using all the other tracks in the event, considering all the possible mass combinations (m_{i}, where $i = \pi, \text{K}, \text{p}$):

$$\chi^2 = \sum_{n_{\text{tracks}}} \frac{[(t_{\text{TOF}} - t_{\text{ev}}) - t_{\text{exp}}(m_{\text{i}})]^2}{\sigma^2_{\text{TOF}} + \sigma^2_{t_{\text{exp}}}} \tag{4.5}$$

The sum in the 4.5 is over all the tracks matched at TOF except for j, $t_{\text{TOF}}$the measured time and $t_{\text{exp}}$the expected time with the mass hypothesis i. $\sigma_{\text{TOF}}$and $\sigma_{\text{exp}}$are the corresponding errors. The combination minimizing the χ^2 is used to derive t_{ev}, which is then subtracted from the TOF time associated to the track j. This procedure is repeated for each track, making the determination of t_{ev}independent of the TOF measured time of the track. A check on the χ^2 vale of each used track and of the final t_{ev}, is also performed in order to reject mismatched tracks. In Fig. 4.22 the efficiency of the TOF event time algorithm is reported as a function of the number of TOF-matched tracks available. The

contribution to the total time resolution due to the $t_{\rm ev}$calculated with the TOF detector, becomes negligible when the number of tracks is high: $\sim$ 25 ps for $n_{\rm tracks}$ = 30, even lower for high-multiplicity Pb-Pb collisions with an average of 600 particles on TOF for most central events.
In the physics analysis, the event time is determined combining the $t_{\rm ev}$estimates by TOF and T0 detectors, weighted by the respective resolutions.

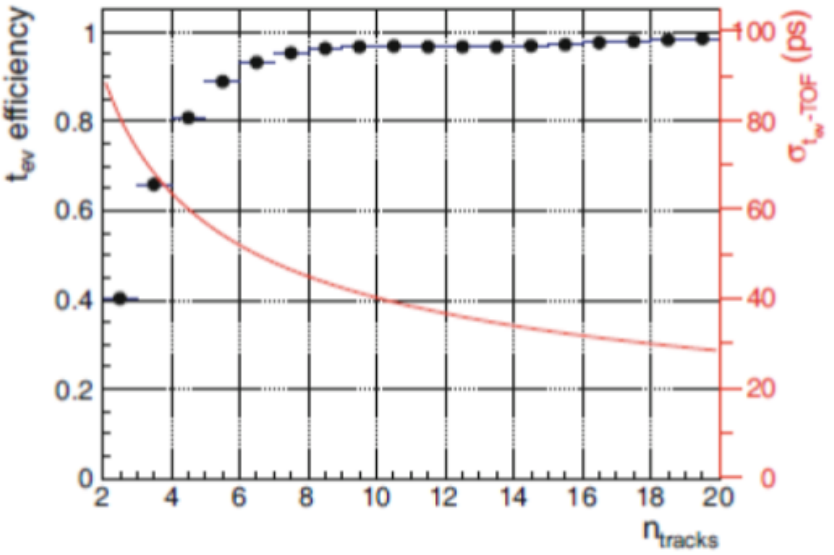

FIGURE 4.22: Distribution of β as measured by the TOF detector as a function of momentum for particles reaching the TOF in Pb-Pb interactions.

4.4.4 Particle identification with TOF

In Fig. 4.23 the distribution of the measured velocity $\beta = L/tc$ for tracks matched at TOF is shown in function of their momentum. Pions, kaons and proton are clearly well separated in the intermediate $p_{\rm T}$ range. Points not corresponding to physical values are due to mismatched tracks at TOF.

TOF detector is the simplest PID estimator. The TOF PID strategy is based on the time difference between the arrival time, measured by the TOF, and the event time $t_{\rm ev}$, for a given mass hypothesis m_i (i = e, μ, π, K, p, d). This difference can be quantify in terms of the $n\sigma$ quantity:

$$n_\sigma = \frac{\Delta t_i}{\sigma_{\rm TOT}} = \frac{t_{\rm TOF} - t_{\rm ev} - t_{\rm exp}(m_i, p, L)}{\sigma_{\rm TOT}(p, m_i, t_{\rm ev})} \tag{4.6}$$

where $t_{\rm TOF}$is the hit time measured by TOF, $t_{\rm ev}$the event time, $t_{\rm exp}$the expected time for a particle of mass mi, momentum p and track lenght L. $\sigma_{\rm TOT}$(p,m_i,$t_{\rm ev}$) takes into account, summing in quadrature, $\sigma_{\rm TOF}$($\sim$ 80 ps), the uncertainty on $t_{\rm ev}$(which depends on the method used, as seen before) and the uncertainty due to tracking and reconstruction, studied using Monte Carlo simulations.
The $n\sigma$ variable is used implementing 2 or 3 σ cuts, depending on the peculiarities of each single analysis. The good understanding of the detector response and the good parametrization of its resolution is confirmed by looking at the

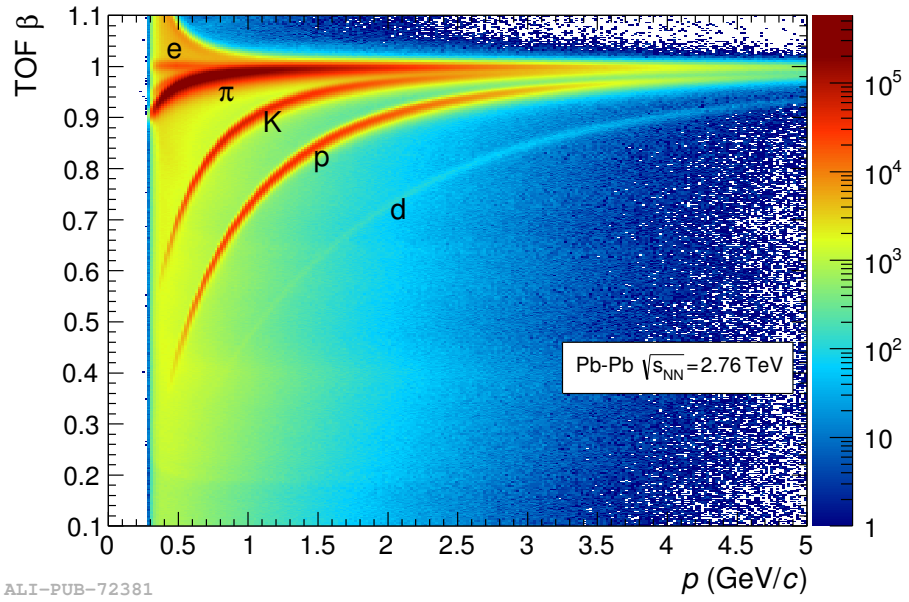

FIGURE 4.23: Efficiency and resolution of the algorithm for TOF $t_{\rm ev}$, as function of the number pf TOF-matching tracks.

average values (expected around zero) and pulls (expected around one) of the distribution of this variable. As example, in Fig. 4.24 the distribution of the $n\sigma$ as a function of the momentum, for the kaon, proton and pion hypothesis is shown. For kaons for example, pions and protons are also visible, as well as the region where pions start to affect the purity of a selected kaon sample. Each momentum slice has been fitted with a gaussian fit , in the [-2,+2] range, and the resulting mean and pull (width of the distribution) are plotted in black and red, respectively. In the region where there are no contamination from other particles, mean and pull are in good agreement with the expected vales (represented by dashed lines). At low $p_{\rm T}$, the presence of mismatched tracks alter the distribution, but this contributed is easily removed using the TPC PID information. This approach has been used for PID in several analysis, as well as in the analysis object of this thesis, where the TOF PID information is combined with the TPC PID information.

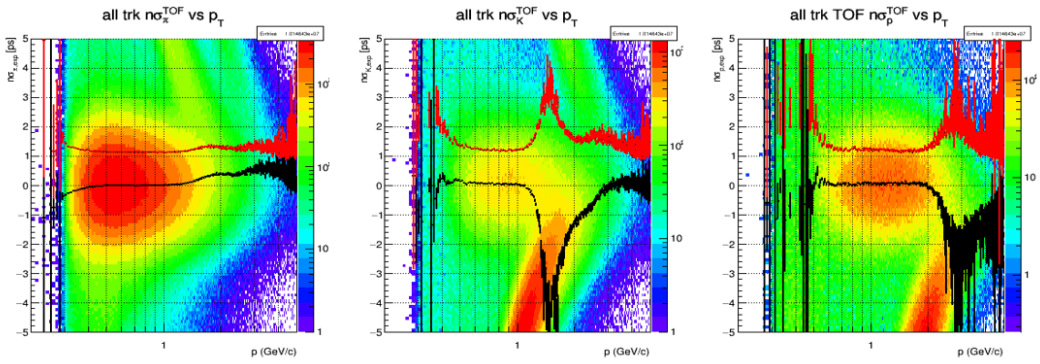

FIGURE 4.24: $n\sigma$ plots for pions, kaons and protons.

An other complementary approach is to use the $n\sigma$ variable to construct a probability of identification for a given mass hypothesis i, in the following way:

$$P_i^{\mathrm{TOF}} = \frac{e^{(n\sigma)^2}}{\sqrt{2\pi\sigma_{\mathrm{TOT}}}} \tag{4.7}$$

This quantity can be used to select tracks above a given identification probability threshold, similarly to what can is done by applying a $n\sigma$ cut, in the Bayesian approach.

4.4.5 TOF trigger for cosmics anc collisions

Thanks to its large coverage, high granularity and fast signals, the TOF has been used also as trigger detector during ALICE commissioning and data taking activities. The TOF trigger [164] consists of 1690 trigger channels, each covering 888 cm^2. The information from the front-end electronics is send to the LTM, used as interface between the fron-end cards and the CTTM (see also section 4.2.4). The CTTM processes the signals and sends the results to the CTP, providing a level-zero fro the experiment.
For what concerns cosmic event, a trigger signal starts when there is a back-to-back (opposite directions) coincidence between two tracks in two different sectors [5].
The TOF trigger has been also successfully used to select resonances decays in UPC during p-Pb and Pb-Pb collisions. These events are characterized by the presence of only a few tracks coming from resonance decays (ρ, ϕ, J/Ψ) and almost no other tracks in ALICE. TOF trigger in this case has to select such topologies requiring that only few tracks reached to detector. It is also possible, thanks to the high segmentation, to require a small number of fired TOF pads with an additional azimuthal topological cut, i.e. at least two opposite hits with $150° < \Delta\phi < 180°$.

[5] In order to increase the acceptance for low-momentum muons, this condition is slightly released, allowing a trigger signal also if one of the three sectors adjacent to the lower one has fired.

Chapter 5

Λ_c analysis

5.1 Data Sample

The analysis presented here has been performed on the following data samples:

- $\sim 3 \times 10^8$ pp events collected in 2010 during the runs at $\sqrt{s}$ = 7 TeV, with minimum bias (MB) trigger [1].
- $\sim 1 \times 10^8$ p-Pb events collected in 2013 during the runs at $\sqrt{s}_{NN}$ = 5.02 TeV, with MB trigger.

The list of 'good' runs in the ALICE Run Condition Table was used as first selection criteria. We then used for this analysis the following list of runs, separated by period:
pp **data sample:**

- LHC10b (31 runs): 117222, 117220, 117116, 117112, 117109, 117099, 117092, 117086, 117077, 117065, 117063, 117060, 117059, 117054, 117053, 117052, 117050, 117048, 116645, 116643, 116574, 116571, 116562, 116403, 116288, 116102, 115401, 115393, 115193, 115186, 114931;
- LHC10c (36 runs): 120829, 120825, 120824, 120823, 120822, 120821, 120820, 120758, 120750, 120741, 120671, 120617, 120616, 120505, 120504, 120503, 120244, 120079, 120076, 120073, 120072, 120069, 120067, 119862, 119859, 119856, 119853, 119849, 119846, 119845, 119844, 119842, 119841, 119163, 119161, 119159
- LHC10d (53 runs): 126437, 126432, 126425, 126424, 126422, 126409, 126408, 126407, 126406, 126405, 126404, 126403, 126359, 126352, 126351, 126285, 126284, 126283, 126168, 126160, 126158, 126097, 126090, 126088, 126082, 126081, 126078, 126073, 126008, 126007, 126004, 125855, 125851, 125850, 125849, 125848, 125847, 125844, 125843, 125842, 125633, 125632, 125630, 125296, 125134, 125101, 125100, 125097, 125085, 125023, 124751, 122375, 122374
- LHC10e (115 runs): 130848, 130847, 130844, 130842, 130840, 130834, 130799, 130798, 130795, 130793, 130704, 130696, 130608, 130601, 130520, 130519, 130517, 130480, 130375, 130356, 130354, 130343, 130342, 130179, 130178, 130172, 130158, 130157, 130149, 129983, 129961, 129960, 129959, 129744, 129742, 129738, 129736, 129735, 129729, 129726, 129725, 129723, 129667,

[1] at least one hit registered in the V0 detector

129666, 129659, 129654, 129653, 129652, 129650, 129647, 129641, 129639, 129599, 129587, 129586, 129540, 129528, 129527, 129523, 129520, 129514, 129513, 129512, 128913, 128855, 128853, 128850, 128843, 128836, 128835, 128833, 128824, 128823, 128820, 128778, 128777, 128678, 128677, 128621, 128615, 128611, 128609, 128605, 128582, 128507, 128505, 128504, 128503, 128498, 128495, 128494, 128486, 128483, 128452, 128366, 128263, 128260, 128192, 128191, 128189, 128186, 128185, 127942, 127941, 127940, 127937, 127936, 127935, 127933, 127931, 127822, 127719, 127718, 127714, 127712

p-Pb **data sample:**

- LHC13b, pass3, AOD (11 runs): 195344, 195346, 195351, 195389, 195391, 195478, 195479, 195480, 195481, 195482, 195483;
- LHC13c, pass2, AOD (14 runs): 195529, 195531, 195566, 195567, 195568, 195592, 195593, 195596, 195633, 195635, 195644, 195673, 195675, 19567749;

The Monte Carlo productions used to estimate efficiency for the first data sample are LHC10f7a and LHC11b2; they are respectively 2.55×10^7 and 6.28×10^6 Pythia simulated events of pp collisions at $\sqrt{s}$=7 TeV anchored to 'good' 2010 runs for LHC10b/c/d/e periods. By construction, in the Monte Carlo production LHC11b2 there are more Λ_c than in LHC10f7a and, in particular, more Λ_c^+ than Λ_c^- .
For the p-Pb case, the Monte Carlo production used to estimate efficiency is LHC13d3, corrisponding to $\sim 4.2 \times 10^7$ Pythia simulated events of $p-Pb$ collisions at $\sqrt{s_{NN}}$=5.02 TeV anchored to 'good' 2013 runs for LHC13b/c periods. In both cases, each event contains a charm or beauty pair; one of the quark hadronizes in charmed hadrons in the central rapidity ($|y| < 1.5$). The Λ_c baryons are forced to decay only in the following channels: $pK^-\pi^+$, $p\bar{K^0}$, $\pi^+\Lambda$ and their charged conjugates; the D mesons are forced to decay in the following decay channels: $D^0 \to \pi^+K^-$, $D^+ \to \pi^+\pi^+K^-$ and $D_s^+ \to \pi^+K^+K^-$ and charge conjugates. In the Tab. 5.1 the branching ratios used in these MC productions are reported. In particular, $\bar{K^0}$ and Λ decay naturally, i.e. $\bar{K^0} \to K_S^0$ in 50% of cases and $K_S^0 \to \pi^+\pi^-$ in $(69.20 \pm 0.05)\%$ of cases and $\Lambda \to p\pi^-$ in $(63.9 \pm 0.5)\%$ of cases.

	BR in PDG (2014) [%]	BR in these MC [%]
$\Lambda_c \to pK^-\pi^+$	5.0±1.3	5.0/(5.0+2.3+1.07)=60
$\Lambda_c \to pK^0$	2.3±0.6	2.3/(5.0+2.3+1.07)=27
$\Lambda_c \to \pi^+\Lambda$	1.07±0.28	1.07/(5.0+2.3+1.07)=13
$D^0 \to \pi^+K^-$	3.89±0.05	3.89/3.89=100
$D^+ \to \pi^+\pi^+K^-$	9.4±0.4	9.4/9.4=100
$D_s^+ \to \pi^+K^+K^-$	5.50±0.27	5.50/5.50=100

TABLE 5.1: Branching ratios for charmed hadrons.

In order to compute the acceptance corrections, the following minimum bias Monte Carlo productions have been used, for both pp and p-Pb data samples [2]:

[2]Since the acceptance is simply a geometric factor, it can be estimated in the same way for both pp and p-Pb data samples

LHC10d1, LHC10d4 and LHC10f6a respectively anchored to LHC10b, LHC10c and LHC10d data taking periods.

The analysis has been performed with the following AOD productions:

- AOD099/135-7 for 2010 pp data, i.e. LHC10b, c, d, e periods, at pass2 step of reconstruction;
- AOD100/136/136a for c-enriched and b-enriched Monte Carlo productions LHC10f7a and LHC11b2, anchored to pp data;
- AOD041 for minimum bias Monte Carlo production LHC10f6a;
- AOD056 for minimum bias Monte Carlo production LHC10d1 and LHC10d4;
- AOD for for 2013 p-Pb data, i.e. LHC13b pass3 and LHC13c pass2;
- AOD for minimum bias Monte production LHC13d3 anchored to p-Pb data.

A toy Monte Carlo simulation has been used to study possible contamination of the p-$K^0_{\rm S}$ invariant mass plots due to D meson reflections (see appendix A); in this simulation the D^+ and D^+_s mesons (and their c.c) can decay in the following ways: $D^+ \rightarrow \pi^+ K^0_{\rm S}$, $B.R. = (1.47 \pm 0.07)\%$, and $D^+_s \rightarrow K^+ K^0_{\rm S}$, $B.R. = (1.48 \pm 0.08)\%$.

5.2 Software

The analysis was performed using AliROOT code. The list of the main classes with their corresponding task is summarized in the following:

- `AliAODRecoCascadeHF`: this is an object that contains all relevant informations about the V0+bachelor candidates.
- `AliRDHFCutsLctoV0`: this is an object devoted to the definition of the candidate selection criteria (cut object). For this analysis the variables used to select candidates are the following ones: (π^+, π^-), (p, π^-), $(\bar{p}, \pi^+)$ and (p, K^0_S), (π, Λ) invariant masses, transverse momentum of V0 daughters, bachelor and V0, transverse impact parameter of bachelor and V0, distance of closest approach (DCA) of V0 daughters and DCA of bachelor and V0, cosine of pointing angle of V0 and bachelor-V0 candidate with respect to the primary vertex.
- `AliAnalysisTaskVertexingHF`: this is a task that runs at ESD-to-AOD filtering level. It creates, in particular, the doublets bachelor-V0 by combining a single reconstructed track (AliAODTrack) with a V0 object (AliAODv0) according to single-track and V0 selection criteria as well as loose topological cuts on Λ_c $\rightarrow$V0+bachelor candidate variables. The output file `AOD.VertexingHF.root` stores then the V0-bachelor doublets.
- `AliAnalysisTaskSELc2V0bachelor`: this is the main analysis task developed to perform this analysis. This task is equipped to perform the analysis in two ways:

  tree fill: we fill a variable tree with candidates that survive to the following selection: only offline V0s, $|m_{inv}(\pi^+, \pi^-) - m(K^0_{\rm S})| < 50 MeV/c^2$, a 3 sigma proton compatibility cut using TPC PID information (to speed up the cut optimization procedure, if required) and, optionally, the $p_T(\Lambda_{\rm c})$ range;

invariant mass histogram fill: only selected candidates according to the cut values defined in the AliRDHFCutsLctoV0 object passed to this class.

- `AliCFVertexingHFLctoV0bachelor`: this is a task to estimate efficiency and acceptance via multidimensional histograms fill.
- `AliHFMassFitter`: this is a task to to fit invariant mass histograms.

5.3 Analysis strategy and selection cuts

For the event selection the following cuts have been used:

- physics selection is used and trigger mask required to `AliVEvent::kAnyINT` for data, kAnyINT or kMB for the anchored Monte Carlo production;
- trigger class is set to CINT1;
- `MinVtxType` set to 3 and `MaxVtxZ` to 10 cm.

A candidate is determined by the combination of a track (the bachelor) with other two (different) tracks, opposite charge, associated with a V0 candidate[3]. The analysis is performed constructing the combinatorics of the V0 candidate with the bachelor track candidate. Each bachelor-V0 candidate has therefore three prongs in total.

At filtering level the candidates have been constructed by taking into account:

- the quality selections on single bachelor-tracks and V0 candidates defined in the Tabs. 5.2 and 5.3, respectively;
- and bachelor+V0 candidate selection cuts reported in Tab. 5.4.

Quantity	Cut
`kITSrefit`	`kTRUE`
$\mid d_0 \mid$	$<$3 cm
p_{T}	$>$0.3 GeV/c
`minNTPCclusters`	70
`accept kink`	`kFALSE`
$\mid \eta \mid$	$<$0.9

TABLE 5.2: Cuts applied for the selection of the bachelor candidates at ESD-to-AOD filtering level. d_0 is the transverse impact parameter of the bachelor with respect to the primary vertex.

To reduce combinatorial background, a 'four layers' analysis strategy has been developed, starting from tighter track quality cuts and basic topological cuts to improve the bachelor track and V0 candidate selection, then making tighter requests on the identified V0 (see sections 5.3.1 and 5.3.2) and their combination with the bachelor track based on PID selection (see section 5.4) Finally, cut optimization procedure (see section 5.5).

[3]The same track can not contribute at the same time as bachelor and V0-daughter for a defined $\Lambda_c \rightarrow$bachelor-V0 candidate. This is avoided at candidate construction level by checking the reconstructed track labels.

Quantity	Cut
p_{T} (daugthers)	>0.1 GeV/c
$\mid d_0 \mid$ (daughters)	>500 μm
DCA between V0-daughters	<1.5cm
ρ	[2 mm; 2 m]
cosine pointing angle	>0.99

TABLE 5.3: Cuts applied for the selection of the V0 candidates at ESD-to-AOD filtering level. ρ is the fiducial volume radius of the V0 candidates.

Quantity	Cut
$m_{inv}(p, K^0_S) - m(\Lambda_c)$	$< 1GeV/c^2$
$m_{inv}(\pi^+, \pi^-) - m(K^0_S)$	$< 50MeV/c^2$
DCA between bachelor and V0	$< 1000cm$

TABLE 5.4: Cuts applied to $\Lambda_{\mathrm{c}} \rightarrow pK^0_{\mathrm{S}}$ candidates at filtering level.

5.3.1 Bachelor track and V0 candidate quality selection

Additional track quality cuts applied to the bachelor track and V0-daughter tracks at analysis level are reported in Tabs. 5.5 and 5.6, respectively.

Quantity	Cut
$\mid \eta \mid$	<0.8

TABLE 5.5: Additional track quality cuts applied for the selection of the bachelor candidates at analysis level.

A fiducial acceptance cut on Λ_{c} candidates (black lines in Fig. 5.1), $\mid y \mid < y_{fiducial}(p_T)$, has been applied, where:

$$y_{fiducial}(p_T) = \begin{cases} -\frac{0.2}{15}p_{\mathrm{T}}^2 + \frac{1.9}{15}p_{\mathrm{T}} + 0.5 \text{ if } p_{\mathrm{T}} < 5 \text{ GeV}/c \\ -0.8 \text{ if } p_{\mathrm{T}} \geq 5 \text{ GeV}/c \end{cases}$$

5.3.2 Bachelor and V0 combined selection

Additional topological cuts on the V0-bachelor candidate have been actively checked without success. As example, a cut on the distance of closest approach (DCA) between the V0 and the bachelor doesn't seem helpful to discriminate between signal and background, as shown in Fig. 5.2. The same can be concluded for the Λ_{c} candidate decay length and its $c\tau$, see Fig. 5.3, reflecting ALICE vertexing resolution [165], shown in Fig. 5.5 in terms of track impact parameter (d_0) resolution in the transverse plane ($r\phi$ direction) as a function of p_{T} . Remembering that the proper decay length ($c\tau$) of Λ_{c} is $\sim 60\mu m$, we cannot apply selection on vertex displacement for V0-bachelor candidates.

Quantity	Cut
kTPCrefit	kTRUE
accept kink	kFALSE
$\mid \eta \mid$	<0.8
V0 kind	offline

TABLE 5.6: Additional track quality cuts applied for the selection of the V0 daughters and V0 candidates at analysis level.

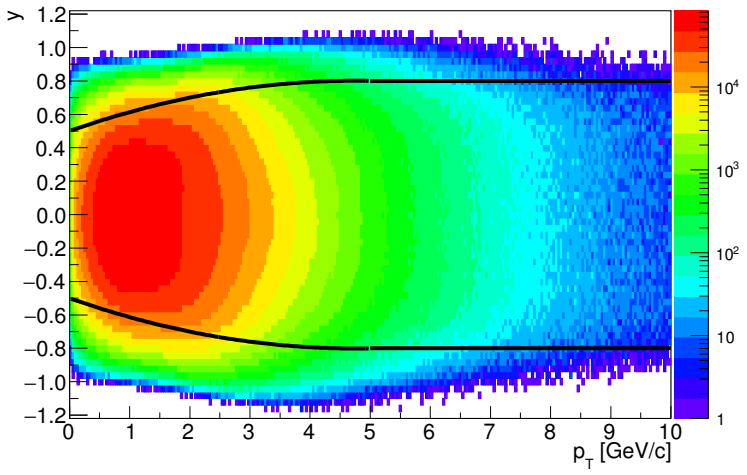

FIGURE 5.1: p_{T} vs rapidity distribution for all Λ_c candidates. The superimposed black lines are the applied cuts.

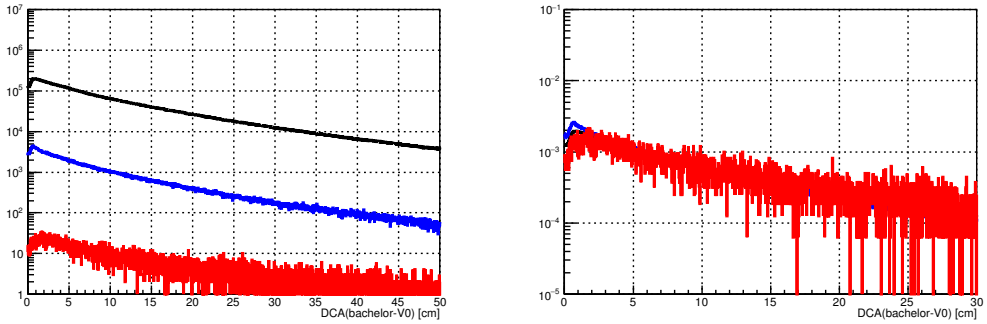

FIGURE 5.2: DCA between V0 and bachelor for signal (red), background (blue) and real data (black). On right plot the same normalization is used.

Since not good signal-to-background separation in these variables, we decide to not take into account secondary-vertex variables (topological cuts) to improve signal-over-backrgound ratio.

We also checked other bachelor-V0 candidate variables, some inspired by D mesons and Λ_c in three prongs analysis and other by the past papers. In Fig. 5.4 we reported the checked variable $d_0(bachelor) \times d_0(V0)$. It is clear that it is not possible to separate signal from background in this variable.

The only variables used to improve the signal extraction are geometrical ($d_0(bachelor)$,

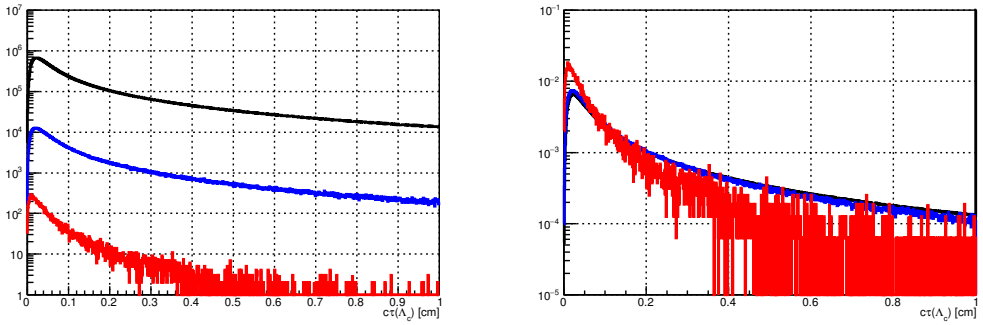

FIGURE 5.3: Λ_c candidate decay length distributions for signal (red), background (blue) and real data (black). On right plot the same normalization is used.

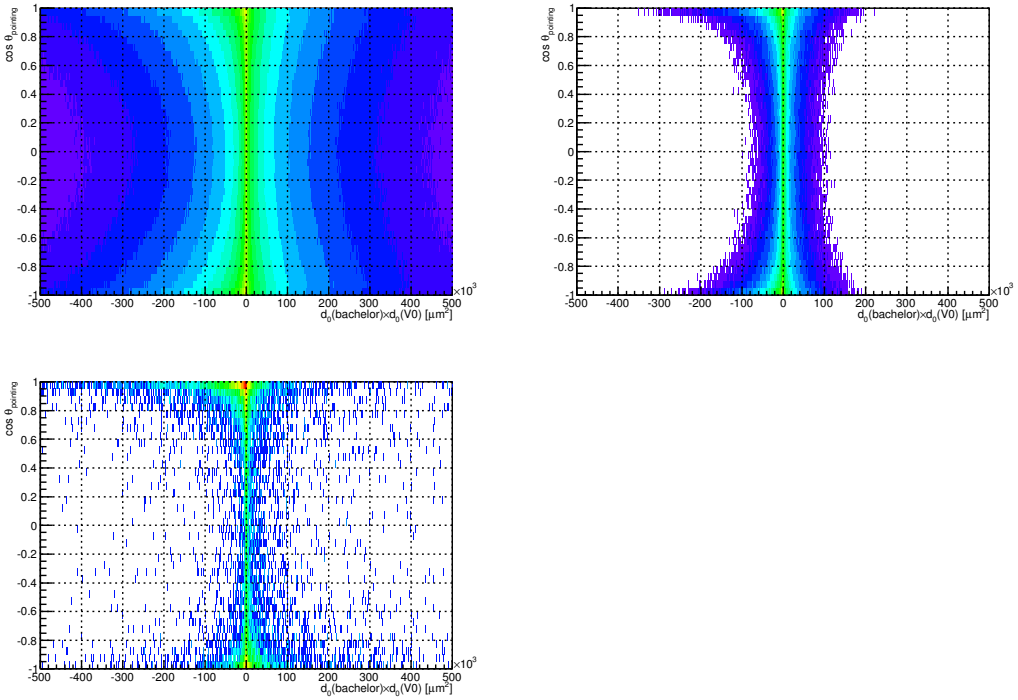

FIGURE 5.4: $d_0(bachelor) \times d_0(V0)$ *vs* cosine of Λ_c pointing angle. On the top left: data; on the top right: MC background; on the bottom left, MC signal.

$d_0(V0)$) and kinematics ($p_T(bachelor)$, $p_T(V0)$, $p_T(V0-daughters)$). Then, for this analysis we can benefit of a good K^0_S signal extraction by $\pi^+\pi^-$ invariant mass distributions (see fig. 5.6) and a very good bachelor identification via energy-loss and time-of-flight measurements.

5.4 PID strategy

The PID strategy has been developed taking into account the need to reduce the background for this channel. Since the V0 identification is essentially set by the $\pi^+ - \pi^-$ invariant-mass cut, the PID has been focused on the bachelor.

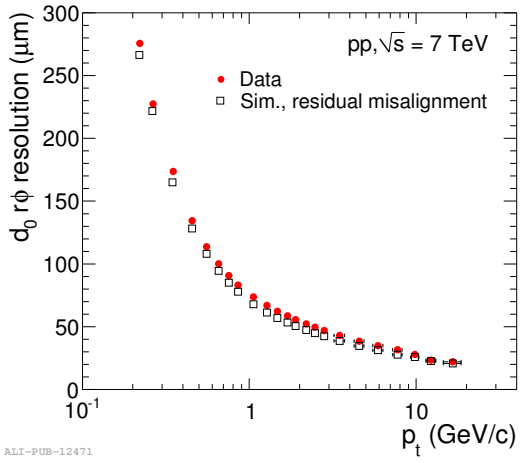

FIGURE 5.5: Track impact parameter (d_0) resolution in the transverse plane ($r\phi$ direction) as a function of p_{T} , comparing data and simulation. This resolution includes the uncertainty in the primary vertex position, which is reconstructed excluding the track being probed.

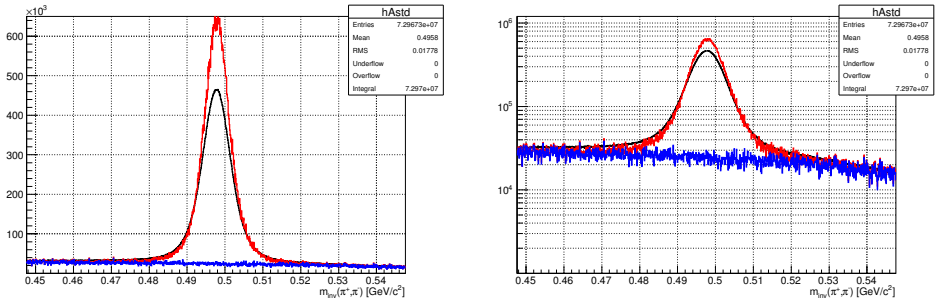

FIGURE 5.6: $\pi^+ - \pi^-$ invariant mass distributions for true (red) and fake (blue) K^0_{S} . superimposed in black the same distribution for data. Left: linear scale; right: logarithmic scale.

We use a *number-of-sigma* cut strategy (a more conservative approach than the combined or bayesian ones) to identify proton and we used TPC and TOF informations. For the pp data sample, we took into account of the presence of a fake TRD geometry in LHC10d reconstructed data at pass2: this alters proton matching efficiency at TOF below 1 GeV/c momentum in a way which is difficult to be simulated. So, the TOF information has not been used at all for tracks with p<1 GeV/c in all data (not only for period LHC10d).

For p<1 GeV/c a 2 sigma proton-compatibility cut using TPC PID information is requested.

Above this value, the TOF is mandatory requested, i.e. the candidate is discarded if TOF information is not available. Further the track has to be compatible with a proton hypothesis within 3 sigmas for TOF and 3 sigmas for TPC (this last request only for the p-Pb data sample). As explained in next section, this cut has been further tightened to further reduce background, paired with an additional cut on the p_{T} of the V0. In the Figs. 5.7 and 5.8we report the TOF

and TPC proton identification performance on data expressed in terms of number of sigmas [4] as a function of bachelor momentum and the same for the MC productions (LHC11b2 and LHC10f7a MC productions for the pp data sample in Figs. 5.9 and 5.10, LHC13d3 for p-Pb in Fig. 5.11). We also tried to recover signal by using TPC when TOF is not available for bachelor with p≥1 GeV/c but unfortunately we have not been successful since the background increases more than the signal because of high pion (mainly) and kaon contamination in the momentum region where all energy-loss bands overlap together (see left plots in Figs. from 5.7 to 5.11).

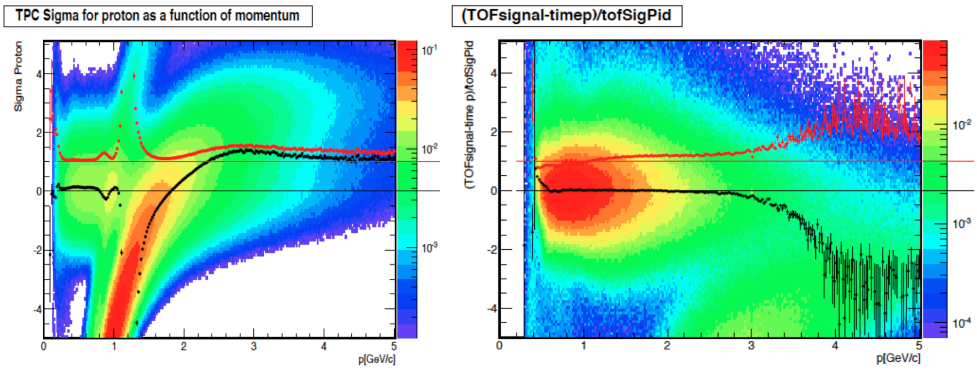

FIGURE 5.7: pp data: proton identification performance with TPC, on the left, and TOF, on the right. Mean (black points) and pull (red points) are shown in both cases. Superimposed reference lines for expected mean (black) and pull (red) values.

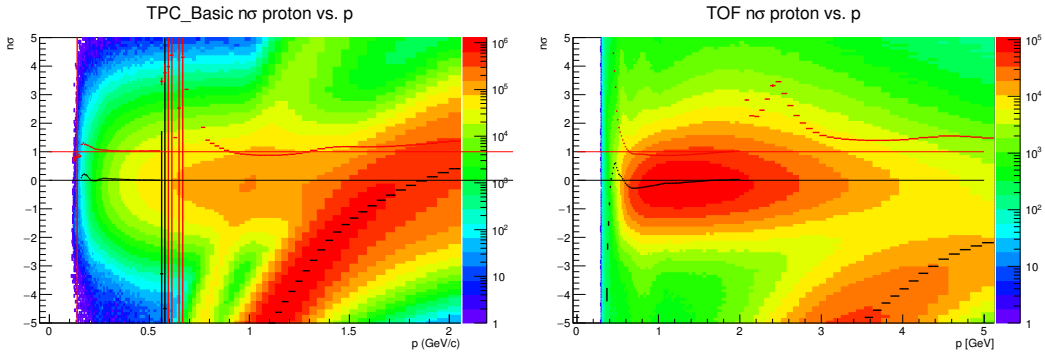

FIGURE 5.8: Data: proton identification performance with TPC, on the left, and TOF, on the right. Mean (black points) and pull (red points) are shown in both cases. Superimposed reference lines for expected mean (black) and pull (red) values.

5.5 Cut optimization

The $\Lambda_c \to pK^0_S$ baryons are successfully reconstructed in $2-12 GeV/c\, p_T$ region, in several p_T intervals, for both of the used data samples. Once the $\Lambda_c \to pK^0_S$ candidate is reconstructed, a p_T -dependent kinematic and geometrical selections are applied on the final decay products. The cuts were optimized to

[4] The number of sigmas is the ratio of the difference between the measured and the expected values and the detector resolution.

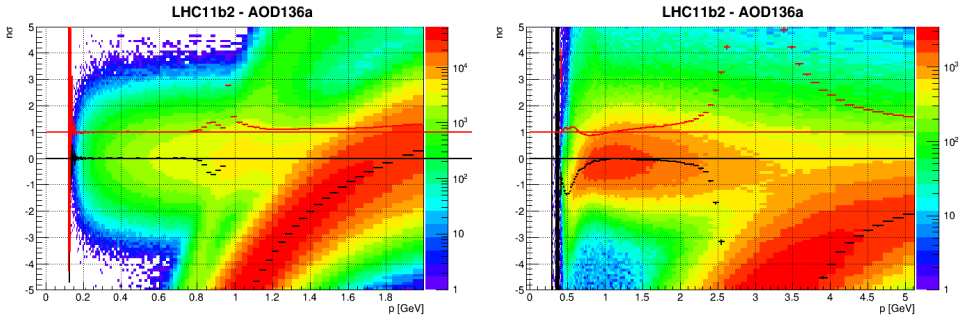

FIGURE 5.9: Monte Carlo LHC11b2: proton identification performance with TPC, on the left, and TOF, on the right. Mean (black points) and pull (red points) are shown in both cases. Superimposed reference lines for expected mean (black) and pull (red) values.

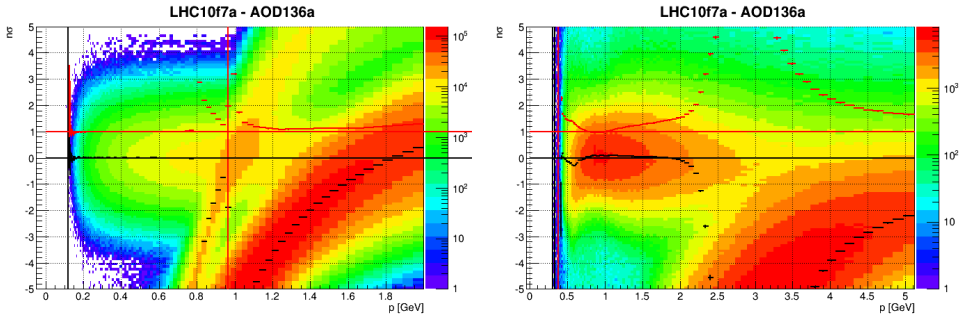

FIGURE 5.10: Monte Carlo LHC10f7a: proton identification performance with TPC, on the left, and TOF, on the right. Mean (black points) and pull (red points) are shown in both cases. Superimposed reference lines for expected mean (black) and pull (red) values.

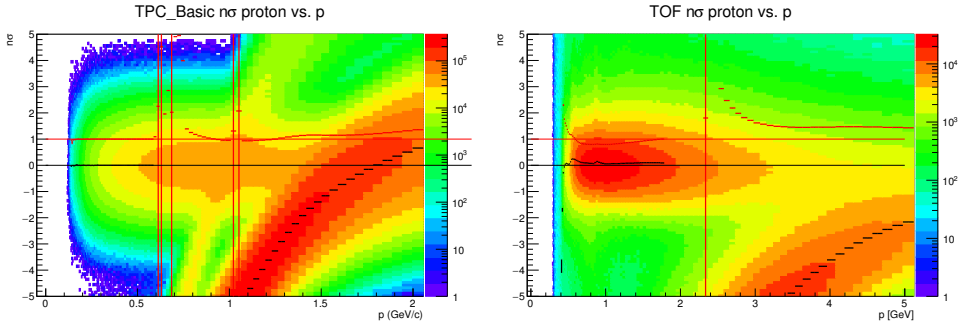

FIGURE 5.11: Monte Carlo LHC13d3: proton identification performance with TPC, on the left, and TOF, on the right. Mean (black points) and pull (red points) are shown in both cases. Superimposed reference lines for expected mean (black) and pull (red) values.

obtain the highest signal-over-background ratio and significance, $\frac{signal}{\sqrt{signal+background}}$, by using a maximum likelihood criterion with the signal extracted on the anchored MC productions, in terms of mean and width of the signal peak.

For the p-Pb data sample, we tried first to extract Λ_c signal in six p_T intervals, as we did in the past for the analysis on the pp data, but at the end we decided to take into account the interval $4-6GeV/c$, because it gives better results than considering the smaller intervals of $4-5GeV/c$ and $5-6GeV/c$. For the cuts

p_{T} (Λ_{c}) $[GeV/c]$	$\lvert m(\pi^+,\pi^-) - m(K^0_S)\rvert$ [MeV/c^2]	$\lvert m(\pi^+,\bar{p}) - m(\bar{\Lambda})\rvert$ $\lvert m(p,\pi^-) - m(\Lambda)\rvert$ [MeV/c^2]	$m(e^+,e^-)$ [MeV/c^2]
2-3	<5.0	>5	>100
3-4	<8.1	>5	>100
4-5	<8.6	>5	>300
5-6	<9.0	>5	>300
6-8	<10	>5	>300
8-12	<10	>5	>300

TABLE 5.7: Cuts applied for the selection of the V0 candidates for the pp data sample.

p_{T} (Λ_{c}) $[GeV/c]$	$\lvert m(\pi^+,\pi^-) - m(K^0_S)\rvert$ [MeV/c^2]	$\lvert m(\pi^+,\bar{p}) - m(\bar{\Lambda})\rvert$ $\lvert m(p,\pi^-) - m(\Lambda)\rvert$ [MeV/c^2]	$m(e^+,e^-)$ [MeV/c^2]
2-3	<6.0	>5	>100
3-4	<7.0	>5	>100
4-6	<8.5	>5	>100
6-8	<10	>5	>100
8-12	<11	>5	>100

TABLE 5.8: Cuts applied for the selection of the V0 candidates for the p-Pb data sample.

optimization in the $4-6GeV/c$ p_{T} region, we choose intermediate values from a previous optimization on $4-5GeV/c$ and $5-6GeV/c$ The three additional cuts on $p-\pi^-$, $\pi^+-\bar{p}$ and e^+-e^- invariant masses, reported in the Tab. 5.7 5.8, help to remove some residual background especially in the low p_{T} region and then the corresponding signal extracted, as shown in Fig. 5.12 for the pp data sample.

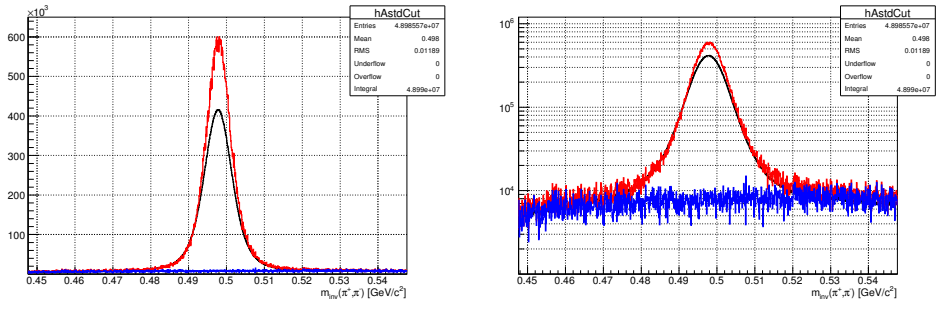

FIGURE 5.12: $\pi^+-\pi^-$ invariant mass distributions for true (red) and fake (blue) K^0_S ; superimposed in black the same distribution for data with the additional selections on $p-\pi^-$, $\pi^+-\bar{p}$ and e^+-e^- invariant masses. Left: linear scale; right: logarithmic scale.

In addition to the cuts discussed in the previous section, a kinematical cut on the p_{T} of the V0 has been applied, exploiting at the same time a stronger cut on PID. The TOF PID strategy applied is a 3σ compatibility cut for intermediate

momenta (1≤p<3GeV/c) and an asymmetric compatibility cut (-2<σ<3) for high momenta (p≥3GeV/c).

The reason of this set of cuts is shown on Fig. 5.13, where the number of sigmas as a function of bachelor momentum are shown for TOF, on the left, and TPC on the right. A larger cut on V0 $p_{\rm T}$ allows to reduce the contamination of kaons and pions in the selected proton sample. The drawback of this is that the sample is significantly reduced at high momentum making problematic a signal extraction in the highest $p_{\rm T}$ bins. The relaxation of the cut on V0 $p_{\rm T}$, paired with a stronger selection of TOF PID (asymmetrically), allows to improve significance and retain statistics at higher momentum.

Finally, we found some kinematical (transverse momenta) and geometrical (transverse impact parameters) variables useful for an optimal signal extrapolation: in Tab. 5.9 we report the value chosen.

$p_{\rm T}$ ($\Lambda_{\rm c}$) $[GeV/c]$	$p_{\rm T}$ (p) $[GeV/c]$	$p_{\rm T}$ ($\pi^{\pm}$) $[GeV/c]$	$p_{\rm T}$ ($K^0_{\rm S}$) $[GeV/c]$	$\lvert d_0(p)\rvert$ $[cm]$	$\lvert d_0(K^0_S)\rvert$ $[cm]$
2-3	>0.6	>0.2	>0.5	<0.05	<0.05
3-4	>0.6	>0.2	>0.6	<0.05	<0.05
4-5	>0.7	>0.2	>0.7	<0.1	<0.09
5-6	>0.7	>0.2	>1.0	<0.1	<0.09
6-8	>0.9	>0.2	>1.1	<0.1	$< \infty$
8-12	>1.1	>0.3	>1.2	<0.1	$< \infty$

TABLE 5.9: Cut variables to be optimized for the pp data sample.

$p_{\rm T}$ ($\Lambda_{\rm c}$) $[GeV/c]$	$p_{\rm T}$ (p) $[GeV/c]$	$p_{\rm T}$ ($\pi^{\pm}$) $[GeV/c]$	$p_{\rm T}$ ($K^0_{\rm S}$) $[GeV/c]$	$\lvert d_0(p)\rvert$ $[cm]$	$\lvert d_0(K^0_S)\rvert$ $[cm]$
2-3	>0.5	>0.2	>0.8	<0.05	$< \infty$
3-4	>0.6	>0.2	>0.8	<0.05	$< \infty$
4-6	>0.8	>0.2	>1.0	<0.08	$< \infty$
6-8	>0.9	>0.2	>1.0	<0.1	$< \infty$
8-12	>0.9	>0.3	>1.2	<0.1	$< \infty$

TABLE 5.10: Cut variables to be optimized for the p-Pb data sample.

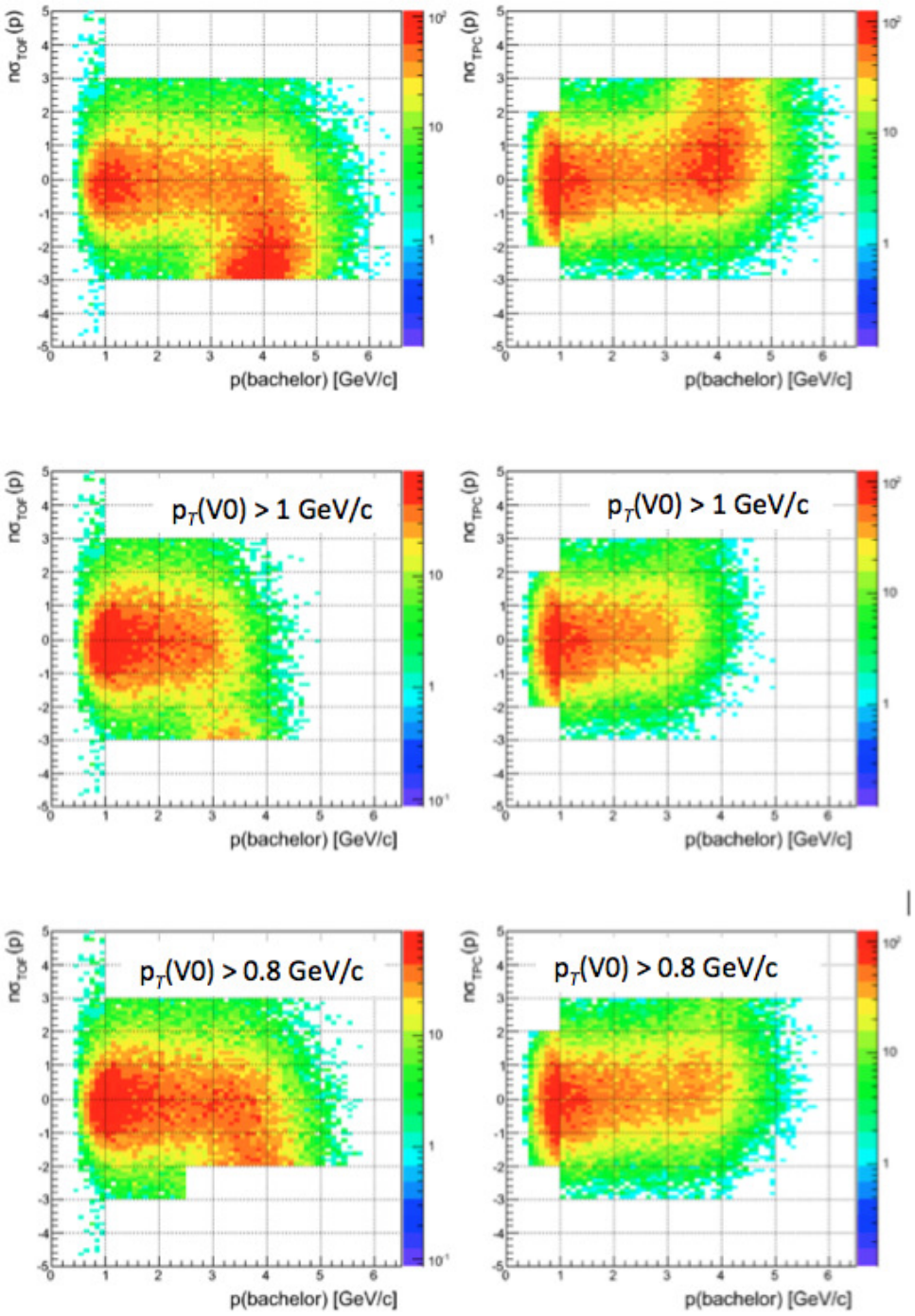

FIGURE 5.13: Effects of different PID cuts on TOF (left) and TPC (right) variables for the bachelor track in the bin $4<p_{\mathrm{T}}<5$ GeV/c bin with different cuts on V0 p_{T} . Top: no cut on V0 p_{T} applied and contamination from pions and kaons visible; middle: strong cut on V0 p_{T} but reduction of statistics at larger momentum; bottom: relaxation of the cut on V0 p_{T} and strengthening of the cut on TOF PID.

Chapter 6

Λ_c results in pp and p-Pb collisions

6.1 Raw yield extraction

In this section the raw yield extraction results is described. The invariant mass spectra and raw yield signal extracted, respectively in pp and p-Pb collisions, in $|y| < y_{fiducial}(p_T)$ and in five p_T (Λ_c) bins are showed in the Figs. 6.1 and 6.2. The fit function used to reproduce these invariant mass distributions is the sum of a Gaussian for the Λ_c peak and a second order polynomial for the background. The fit is performed in two steps using the Minuit package, the first gives a rough estimation of the background function parameters using the side bands, while the second includes also the signal range and gives the final estimation of all parameters. The amount of signal is then extracted by subtraction of the background fit (in red in the pictures) from the total fit (in blue). Despite the high background, a significance larger than 3σ in all bins is obtained, with a signal/background ratio greater than 1% also in the lowest p_T bin.

In Fig. 6.3 and 6.4 we reported the mean and width values obtained respectively in pp an p-Pb collisions on real data superimposed to the ones obtained on MC productions: within the errors they are in agreement.

In the Tabs. 6.1 and 6.2 we reported the raw yield values and their statistical uncertainties for the two data samples.

	p_T (Λ_c) $[GeV/c]$				
	2-3	3-4	4-6	6-8	8-12
Raw yield	540	370	345	140	110
Statistical uncertainty	170 (30%)	110 (30%)	90 (26%)	60 (43%)	40 (36%)

TABLE 6.1: pp data: summary of the raw yield values and their statistical uncertainties.

6.2 Acceptance and efficiencies

For the acceptance estimate we used the indicated minimum bias production, for both the data sample. The acceptance is defined as the ratio between the Λ_c produced in the fiducial acceptance, i.e. $\mid y \mid < y_{fiducial}(p_T)$, where $y_{fiducial}$

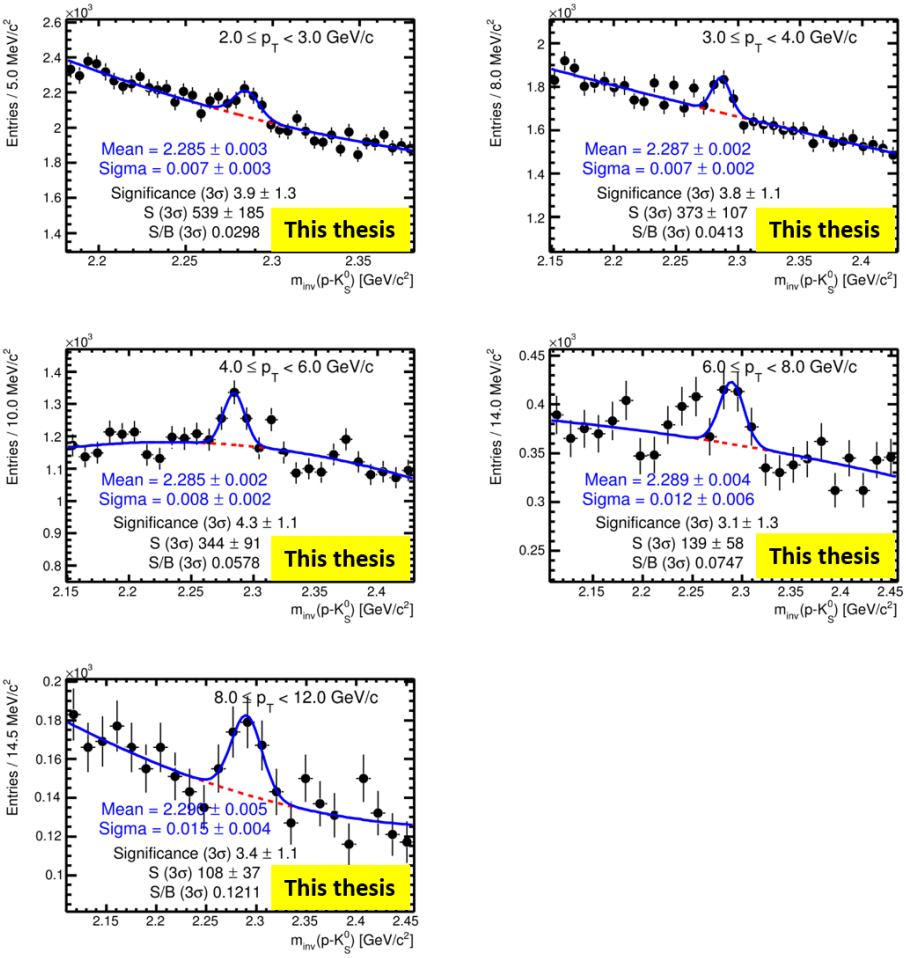

FIGURE 6.1: Raw yield extraction in five different $p_{\rm T}$ bins in [2;12[GeV/c in pp collisions at $\sqrt{s}$= 7 TeV.

	$p_{\rm T}$ (Λ_c) $[GeV/c]$				
	2-3	3-4	4-6	6-8	8-12
Raw yield	1086	923	683	311	134
Statistical uncertainty	428 (40%)	216 (23%)	211 (30%)	81 (26%)	48 (36%)

TABLE 6.2: p-Pb data: summary of the raw yield values and their statistical uncertainties.

smoothly increasing from 0.5 to 0.8 in $0 < p_T < 5GeV/c$ and $y_{fiducial} = 0.8$ above $5GeV/c$ (see black lines in Fig 5.1), and the Λ_c generated in $|y| < 0.5$. The result is shown in Fig. 6.5 and 6.6 respectively for Λ_c from b and from c.

As expected the value grows above unity at large $p_{\rm T}$ and saturates. Similar results have been obtained for D mesons and the Λ_c decay in three prongs also studied in ALICE. Moreover, we separated the Λ_c prompt from the Λ_c originated from b-quarks (feed-down). As expected, due to the absence of cuts on the primary-secondary vertex displacement, the result is very similar for both cases.

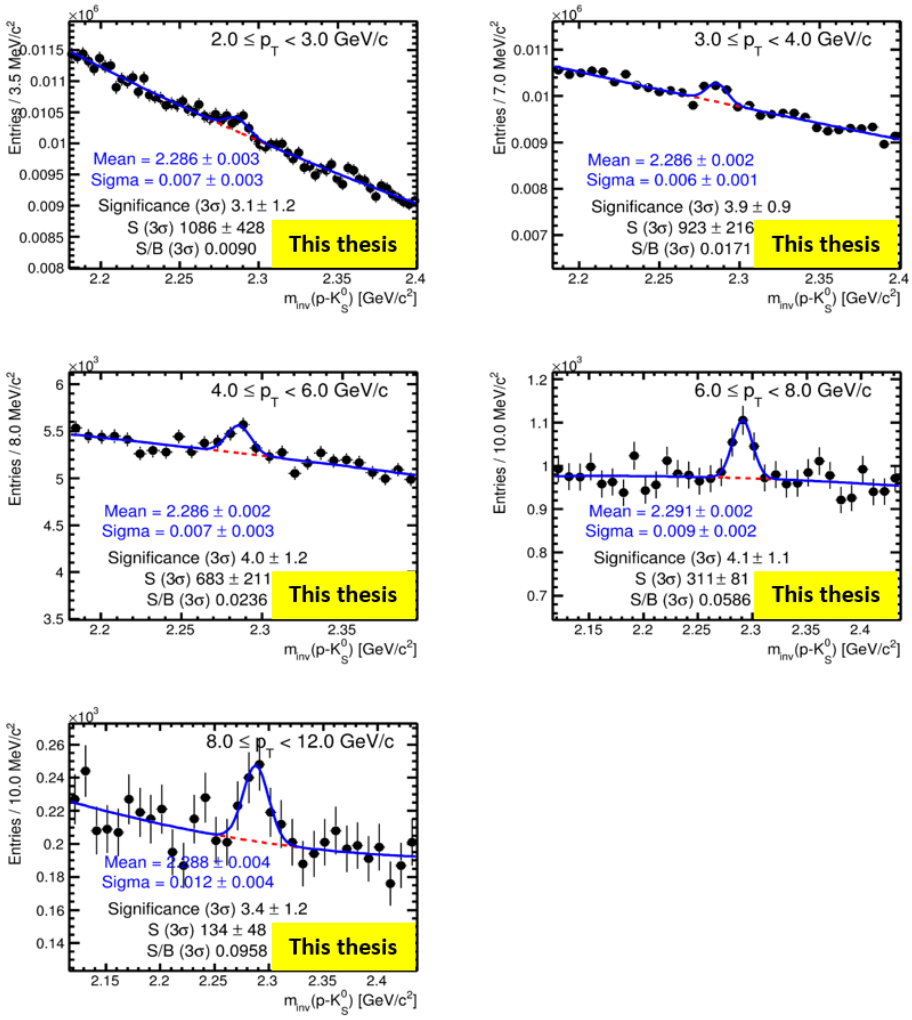

FIGURE 6.2: Raw yield extraction in five different p_{T} bins in [2;12[GeV/c in p-Pb collisions at $\sqrt{s_{NN}}$= 5.02 TeV.

As a cross-check and to try to recover more statistics, since this factor only depends on kinematical factor, we also estimated it with a toy model (macro *$ALICE_PHYSICS/ PWGHF/ vertexingHF/ macros/ ComputeAcceptance.C*). The result is shown in Fig. 6.7, where it is compared also with the results on minimum bias MC productions.

Then, in the following we will use the acceptance estimated with the toy model for Λ_{c} prompt and by b-hadron decay.

6.2.1 Efficiency

For the estimates of the efficiencies (for b and c generated Λ_{c}) we used the c/b-enriched LHC10f7a, LHC11b2 and LHC13d3 production. The efficiency is defined as the ratio between the Λ_{c} survived to the cut selection and the Λ_{c} generated in the fiducial acceptance. The results are shown in Fig. 6.8 and 6.9 for pp collisions, 6.10 for p-Pb collisions . Additionally we show in the same figures the ratios of the various selection steps with respect to the

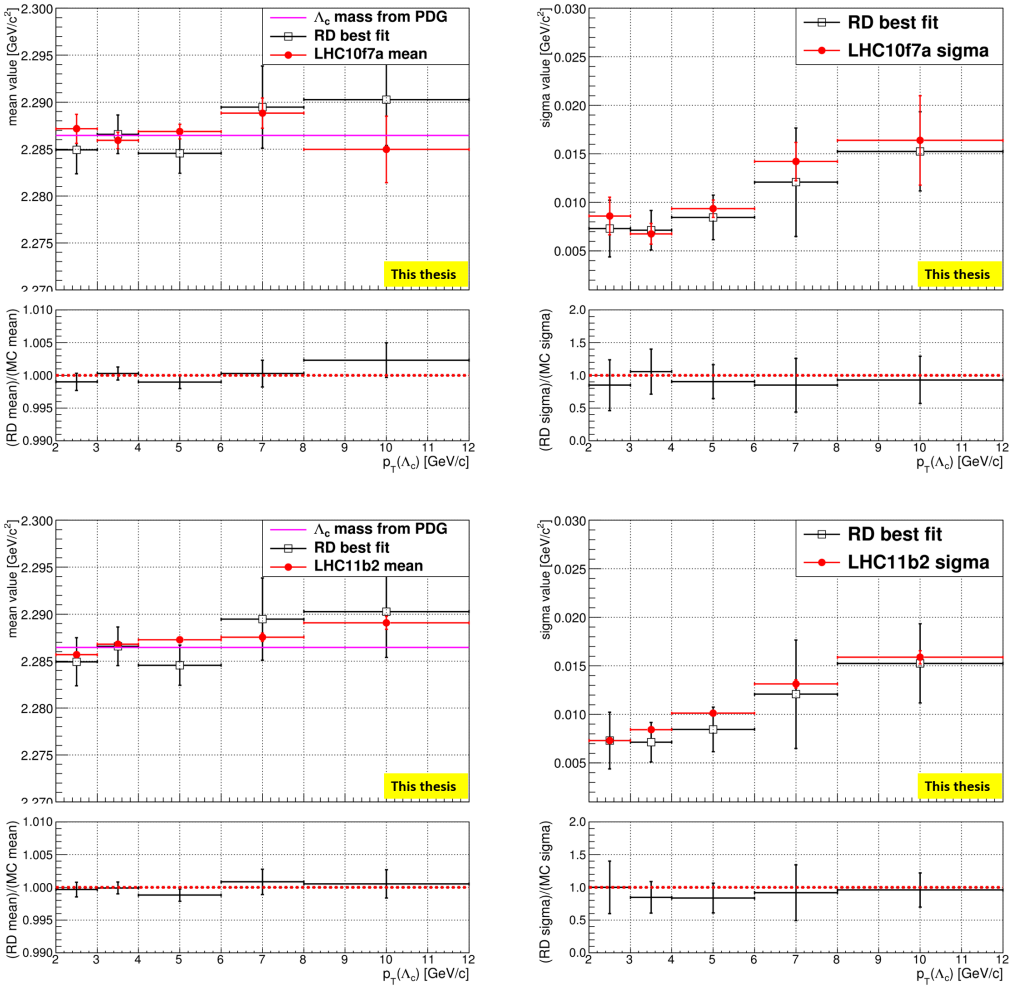

FIGURE 6.3: Mean, on the left, and width, on the right, values compared to the MC ones. On the top, comparison with LHC10f7a; on the bottom, comparison with LHC11b2.

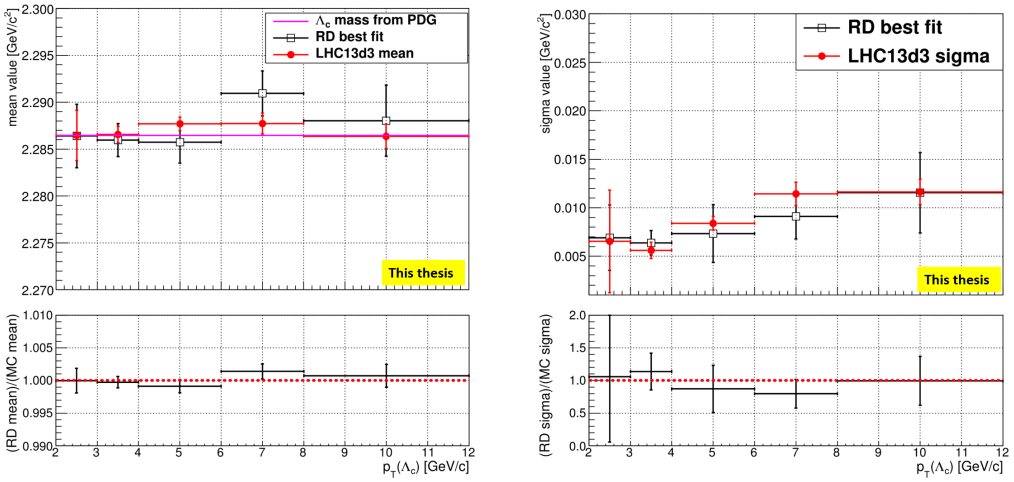

FIGURE 6.4: Mean, on the left, and width, on the right, values compared to the LHC13d3 production.

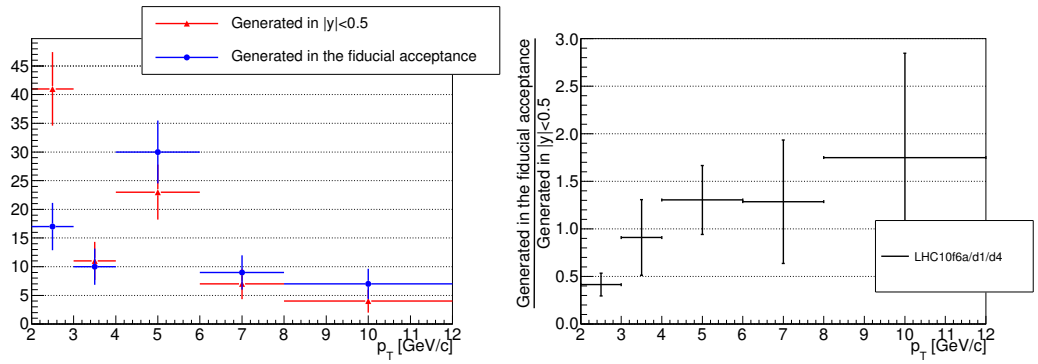

FIGURE 6.5: Λ_c from b: on the left, acceptance numerator (blue) and denominator (red); on the right, acceptance.

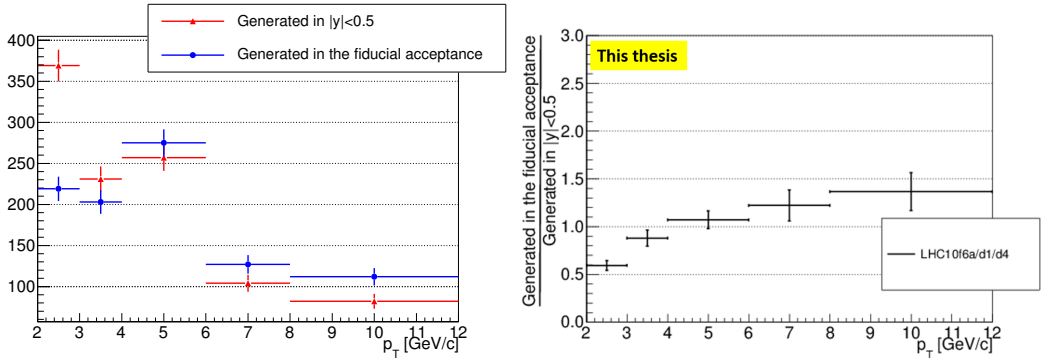

FIGURE 6.6: Λ_c from c: on the left, acceptance numerator (blue) and denominator (red); on the right, acceptance.

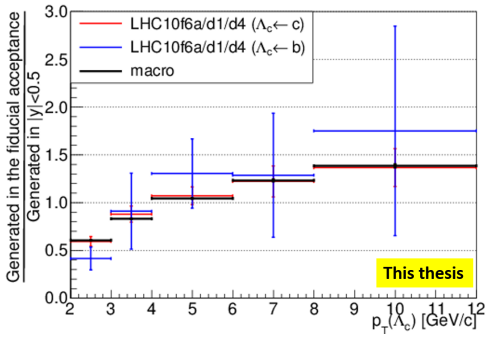

FIGURE 6.7: Acceptance estimated with the toy model, in black. Superimposed in red and blue colors, the results on minimum bias MC productions, for comparison.

Λ_c generated in the fiducial acceptance. This shows the impact of the selection cuts and bachelor identification separately.

A first comment is about the PID efficiency. With respect to other analyses (e.g D mesons) above 1 GeV/c momenta the PID efficiency is the convolution of the TOF matching efficiency ($\approx$ 60-70%, see Fig. 6.13 and 6.14) and the pure PID efficiency (applying a 3 or 2 σ cut). The TOF matching is strictly required, as described. This is the reason of the relatively 'low' PID efficiency shown in Fig. 6.11 for the pp case with respect to the bachelor momentum and in Fig. 6.12 with respect to the Λ_c momentum.

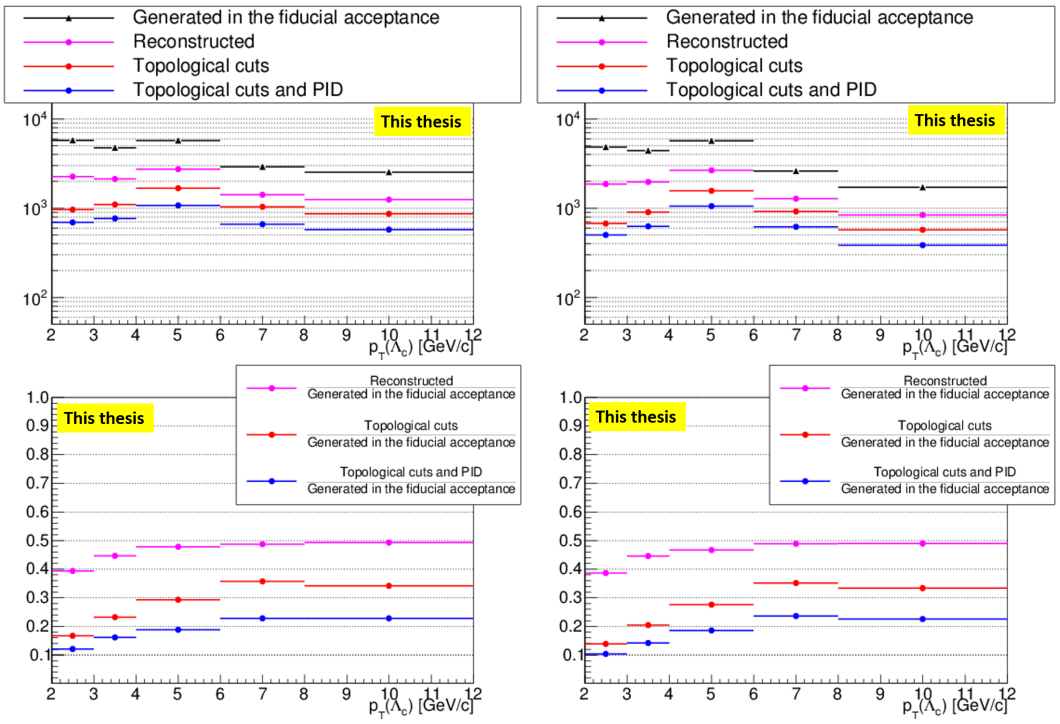

FIGURE 6.8: LHC11b2 production: on the top, $\Lambda_c \rightarrow pK^0_S$ generated in the acceptance (black), reconstructed in the acceptance (magenta), selected according to the cut optimization (red) and bachelor PID (blue); on the bottom: ratios with respect to the $\Lambda_c \rightarrow pK^0_S$ generated in the acceptance. On the left, prompt Λ_c and on the right b-induced Λ_c . The efficiency is the blue fraction on the bottom.

A second comment is about the slight difference in the efficiency estimate for $\Lambda_c \leftarrow$c and $\Lambda_c \leftarrow$b: they are not exactly the same, as shown in Fig. 6.15 for pp and 6.16 for p-Pb . The cut on transverse impact parameters of bachelor and V0 can explain the observed difference; in Figs. 6.17 and 6.18, the transverse impact parameter distributions of bachelor and V0 respectively are shown for $\Lambda_c \leftarrow$c and $\Lambda_c \leftarrow$b in all p_T (Λ_c) bins: superimposed, the cut values used in this analysis (see values in the Tab. 5.9). The $d_0(bachelor)$ and $d_0(V0)$ distributions look different for $\Lambda_c \leftarrow$c and $\Lambda_c \leftarrow$b and this can answer for the observed difference in the efficiency for $\Lambda_c \leftarrow$c and $\Lambda_c \leftarrow$b.

6.3 Feed down corrections

In the absence of a measured beauty hadron production cross section at central rapidity, we use perturbative QCD calculations for the production of beauty hadron and detailed Monte Carlo simulations to estimate the fraction of Λ_c stemming from the decay of $beauty-$hadrons in $\Lambda_c + X$ in our raw yields. Let us define $f_{prompt}(p_T)$, the fraction of prompt Λ_c in each p_T bin. We consider the following method to estimate this fraction:
the N_b method uses the FONLL calculation for the b-hadron production cross section multiplied by the fragmentation function of b quark in b-hadrons and

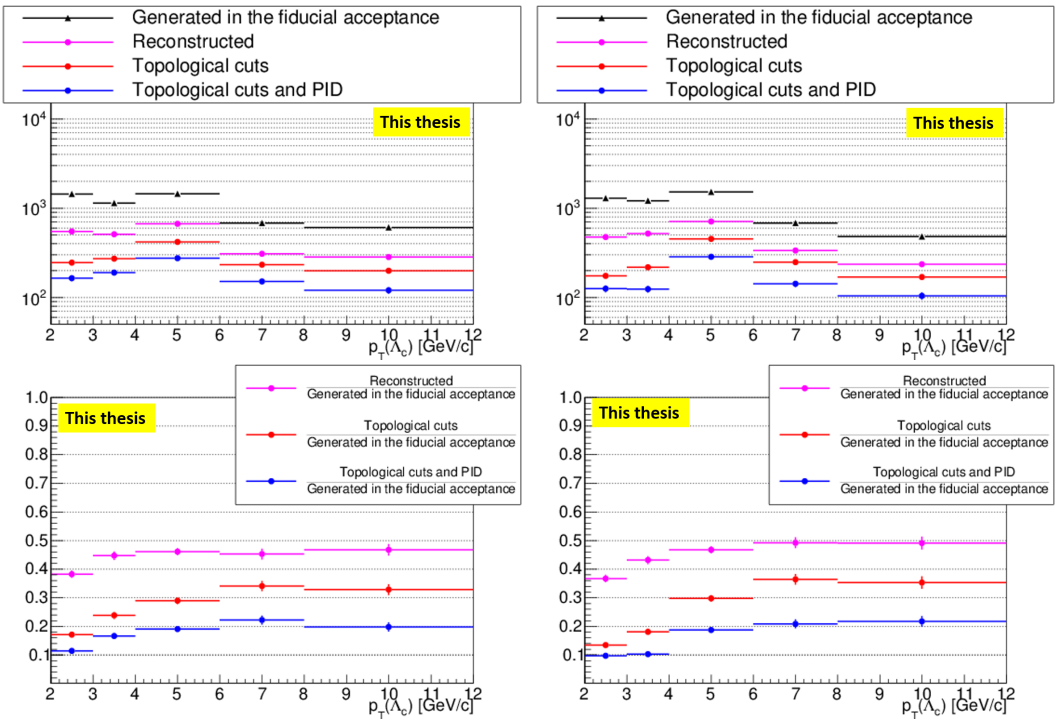

FIGURE 6.9: LHC10f7a production: on the top, $\Lambda_c \rightarrow pK^0_S$ generated in the acceptance (black), reconstructed in the acceptance (magenta), selected according to the cut optimization (red) and bachelor PID (blue); on the bottom: ratios with respect to the $\Lambda_c \rightarrow pK^0_S$ generated in the acceptance. On the left, prompt Λ_c and on the right b-induced Λ_c . The efficiency is the blue fraction on the bottom.

the branching ratio of b-hadrons in Λ_c , BR_b, the correction factors for acceptance and reconstruction efficiency of non-prompt Λ_c , $\epsilon_{\Lambda_c \leftarrow b}$, and the integrated luminosity, L_{int}:

$$f_{prompt} = 1 - \frac{1}{N^{\Lambda_c}_{raw}} \cdot L_{int} \cdot BR_b \cdot \epsilon_{\Lambda_c \leftarrow b} \cdot \int_{\Delta y \Delta p_T} \frac{d^2\sigma^b_{FONLL}}{dydp_T} dydp_T \tag{6.1}$$

There is another method to estimate the feed-down contribution, called f_c method, in which the relative fraction f_{prompt} is entirely based on calculated cross sections for prompt and non-prompt production of Λ_c within the FONLL framework [1]:

$$f_{prompt} = 1 \Big/ \left(\frac{BR_b}{BR_c} \cdot \frac{\epsilon_{\Lambda_c \leftarrow b}}{\epsilon_{\Lambda_c \leftarrow c}} \cdot \frac{\int_{\Delta y \Delta p_T} \frac{d^2\sigma^b_{FONLL}}{dydp_T} dydp_T}{\int_{\Delta y \Delta p_T} \frac{d^2\sigma^c_{FONLL}}{dydp_T} dydp_T} \right) \tag{6.2}$$

where BR_c, is the fragmentation function of c quark in Λ_c and $\epsilon_{\Lambda_c \leftarrow c}$ is the acceptance and reconstruction efficiency of prompt Λ_c .

Actually, the f_c method is dropped for new D measurements, since measured prompt D production is well described by FONLL.

[1] The FONLL pQCD calculations were used to estimate the expected Λ_b production cross section, while the EvtGen generator were used to estimate $\Lambda_b \rightarrow \Lambda_c$ decays.

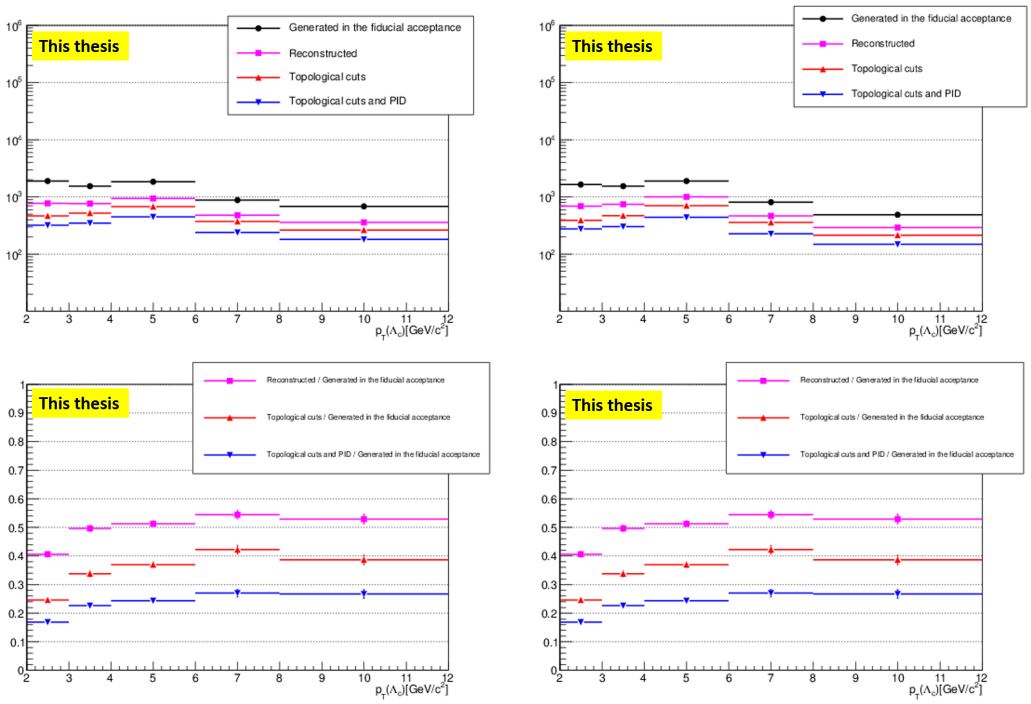

FIGURE 6.10: LHC13d3 production: on the top, $\Lambda_c \rightarrow pK^0_S$ generated in the acceptance (black), reconstructed in the acceptance (magenta), selected according to the cut optimization (red) and bachelor PID (blue); on the bottom: ratios with respect to the $\Lambda_c \rightarrow pK^0_S$ generated in the acceptance. On the left, prompt Λ_c and on the right b-induced Λ_c . The efficiency is the blue fraction on the bottom.

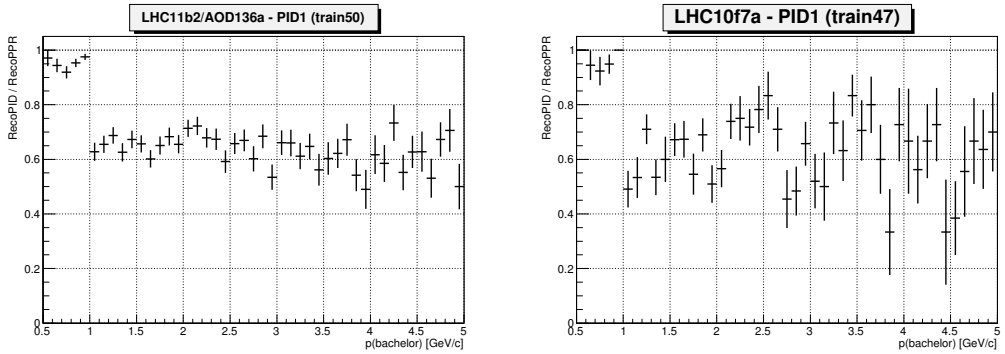

FIGURE 6.11: Bachelor identification efficiency vs p of the bachelor in pp collisions.

6.3.1 Λ_c cross section estimate and comparison with measured D^0 cross section

The cross-section has been initially evaluated using the following formula, not making distinction about prompt and no-prompt Λ_c

$$\left.\frac{d\sigma}{dp_T}\right|_{|y|<0.5} = \frac{1}{2}\cdot\frac{\sigma_{VZERO}}{N_{ev}\Delta p_T}\cdot\frac{N_{raw}(p_T)|_{|y|<y_{fiducial}}}{BR(\Lambda_c^+ \rightarrow p\bar{K^0})AW(\bar{K^0} \rightarrow K_S^0)BR(K_S^0 \rightarrow \pi^+\pi^-)}\cdot\frac{1}{(Acc\times\epsilon)_{prompt}(p_T)} \quad (6.3)$$

where N_{ev} is the total number of events analyzed, σ_{VZERO} the VZERO detector

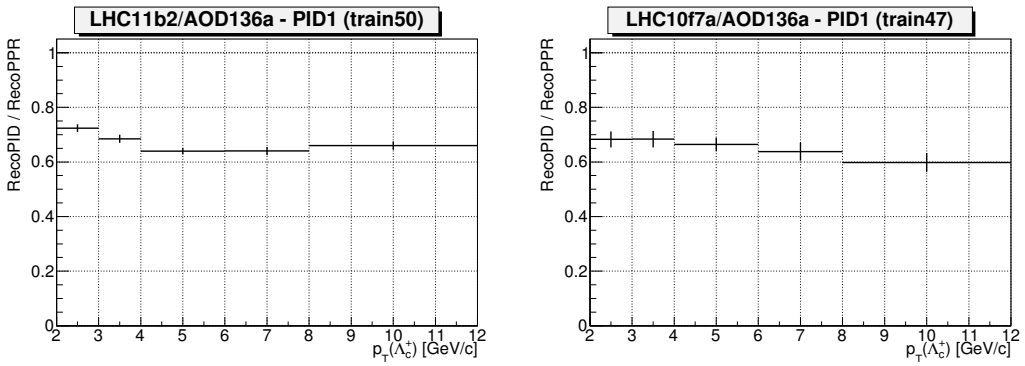

FIGURE 6.12: Bachelor identification efficiency vs p_T of Λ_c in pp collisions.

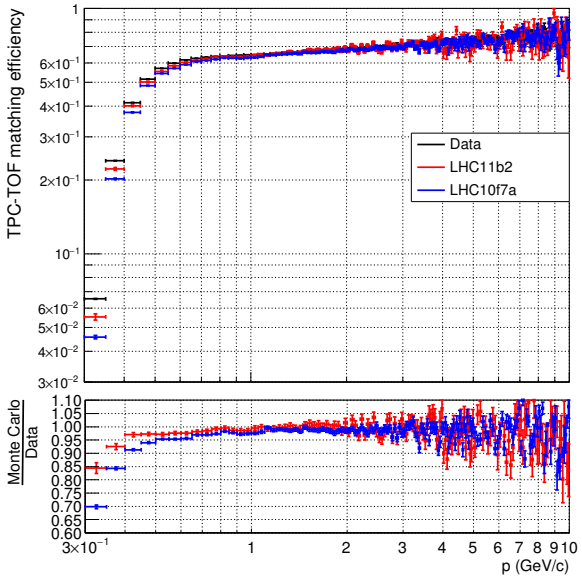

FIGURE 6.13: TPC-TOF matching efficiency. On the top, the comparison between the value in function of the trasverse momentum, for the two Monte Carlo productions LHC10f7a (in blue) and LHC11b2 (in red) and data (in black); on the bottom, the ratios LHC11b2/Data (in red) and LHC10f7a/Data (in blued) matching efficiency vs p are shown.

normalization minimum-bias cross section, $N_{raw}(p_{\rm T})|_{|y|<y_{fiducial}}$, and $(Acc{\times}\epsilon)_{prompt}(p_{\rm T})$ are, respectively, the raw yields and acceprtance×efficiencies extracted or computed in each Λ_c $p_{\rm T}$ bin. The factor 2 takes into account the charged conjugates reactions. BR($\Lambda_c^+ \to p\bar{K^0}$) and BR($K_S^0 \to \pi^+\pi^-$) are the branching ratios for the defined decays and $AW(\bar{K^0} \to K_S^0)$ is the amplitude of K_S^0 in the wave-function of the initially produced $\bar{K^0}$.

If the treatment of the feed down is taken into account in a similar way as done for D mesons, the cross-section is evaluated via:

$$\left.\frac{d\sigma}{dp_{\rm T}}\right|_{|y|<0.5} = \frac{1}{2}\cdot\frac{\sigma_{VZERO}}{N_{ev}}\cdot\frac{1}{\Delta p_{\rm T}}\cdot\frac{f_{prompt}(p_{\rm T})\cdot N_{raw}(p_{\rm T})|_{|y|<y_{fiducial}}}{BR(\Lambda_c^+\to p\bar{K^0})AW(\bar{K^0}\to K_S^0)BR(K_S^0\to\pi^+\pi^-)}\cdot\frac{1}{(Acc\times\epsilon)_{prompt}(p_{\rm T})}. \quad (6.4)$$

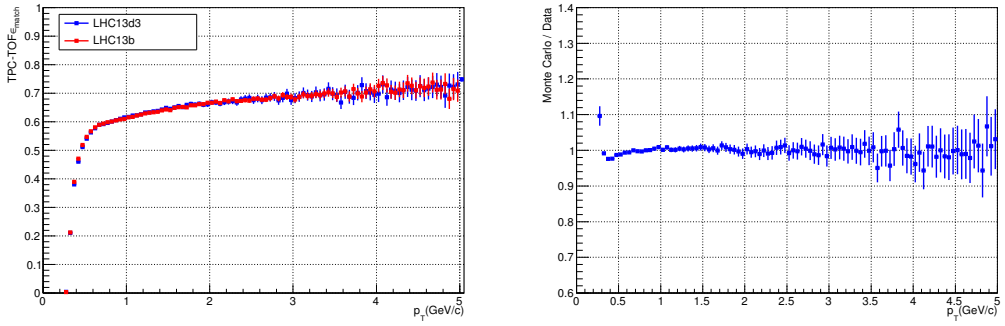

FIGURE 6.14: TPC-TOF matching efficiency: on the left, the comparison between the value in function of the trasverse momentum, for the Monte Carlo production LHC13d3 (in blue) and data (in red); on the right, the ratio LHC13d3/Data (in blue) matching efficiency vs p_{T} is shown.

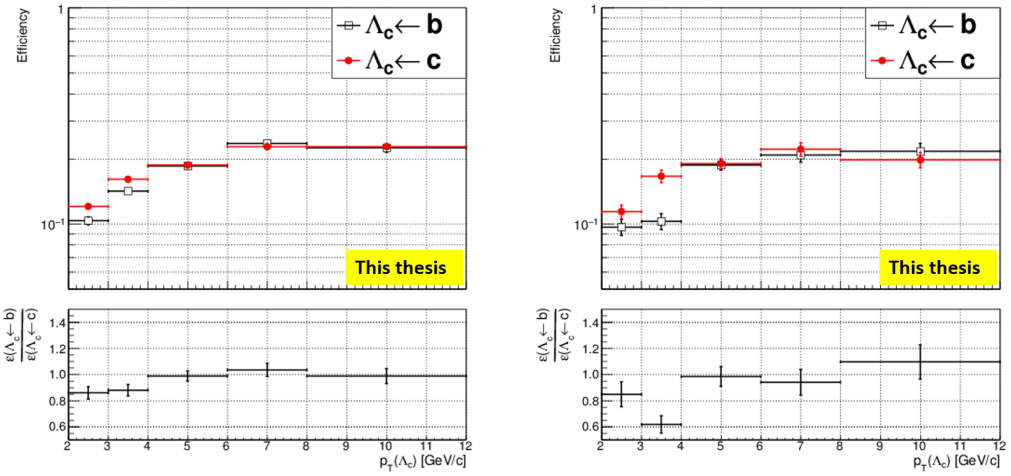

FIGURE 6.15: On the top: blue curves in Figs. 6.8 and 6.9; on the bottom their ratios. On the left, LHC11b2 results; on the right, LHC10f7a ones.

In Fig. 6.19, on the top, the Λ_c cross section results in pp and p-Pb collisions are shown as found before and after feed down subtraction with the Nb method. The two measurements without and with feed-down corrections, are in agreement, for both data samples. On the bottom, the ratios between the cross sections estimated with feed-down correction and the one estimated without feed-down correction are also shown. These results are in agreement with the f_{prompt} shown in Fig. 6.38.

We also compared our results with the ones obtained for D^0 mesons on the same data set [166] [2]. In the Figs. 6.20 and 6.21 we report this comparison. In particular, in Fig. 6.20 we report also the comparison between theoretical expectations (FONLL [71])and measurements. Currently, FONLL predictions for Λ_c in p-Pb collisions are not available.

In case of Λ_c the measurement refers to the one obtained with feed-down correction estimated with N_b method.

[2]The branching ratio for $D_0 \rightarrow K^-\pi^+$ changed with respect the one used in [166] and [167]. As a consequence, the published D^0 measurement has been scaled according to the new branching ratio value: the old one was $(3.88 \pm 0.05)\%$ [168], the new one is $(3.93 \pm 0.04)\%$ [169].

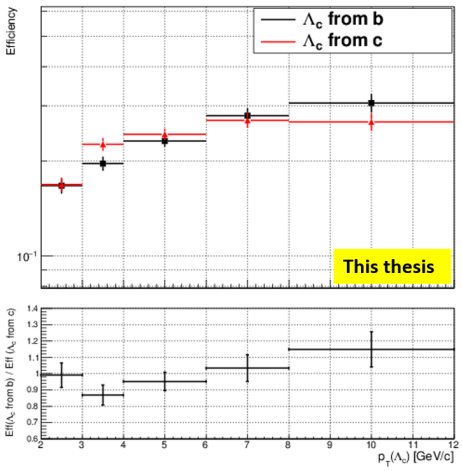

FIGURE 6.16: On the top: blue curves in Fig. 6.10, for LHC13d3 production; on the bottom their ratio.

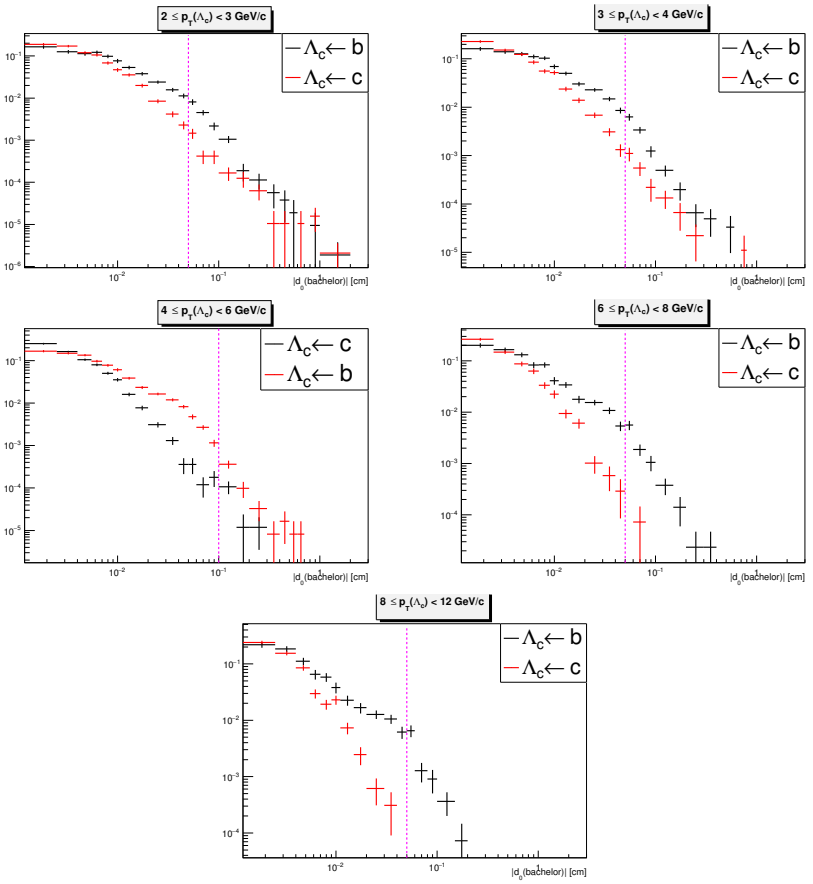

FIGURE 6.17: $d_0(bachelor)$ distributions for true Λ_c candidates in the five p_T bins: in black the prompt ones and in red the ones coming from beauty hadrons decay.

6.4 Systematic uncertainties

Several sources of systematics were taken into account and listed below:

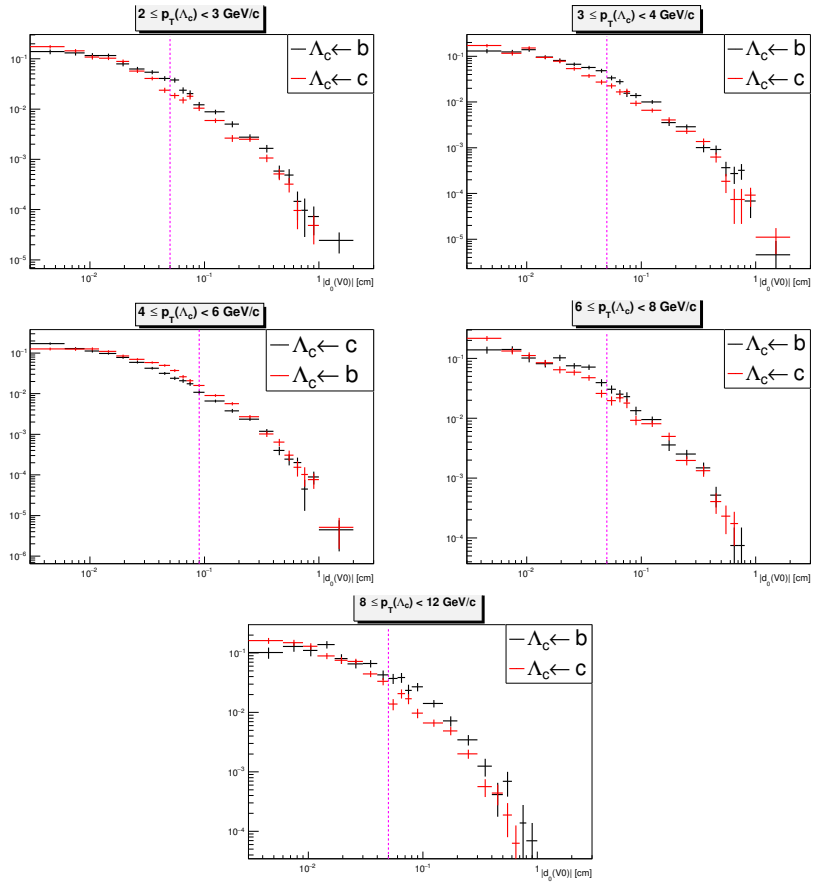

FIGURE 6.18: $d_0(K^0_S)$ distributions for true Λ_c candidates in the five p_T bins: in black the prompt ones and in red the ones coming from beauty hadrons decay.

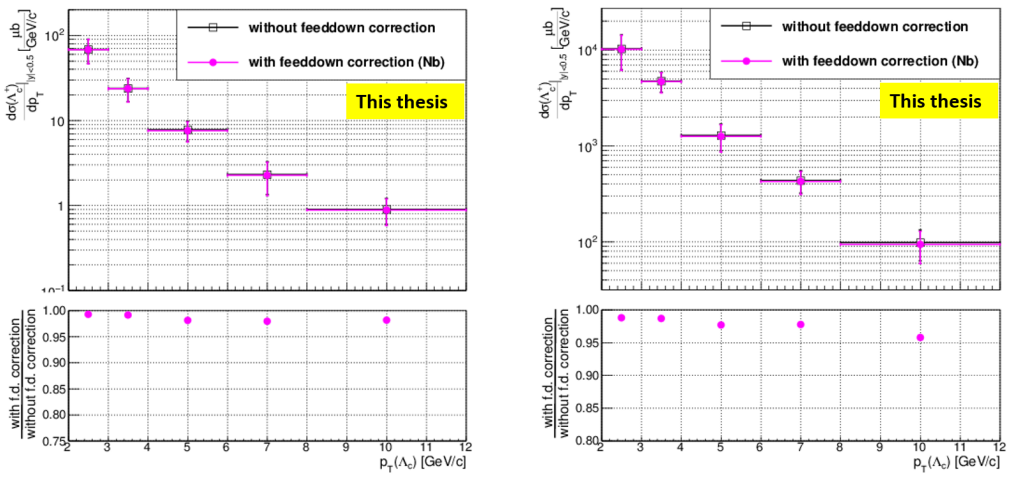

FIGURE 6.19: Λ_c cross sections without feddown correction, in black, and with N_b feed down correction, in magenta. Left: pp case; Right: p-Pb case.

- raw yield extraction: fit procedure could depend on the chosen values for the fit parameters (binning, range, background function),
- cut variation: the cut variables could not be perfectly described in simulation,

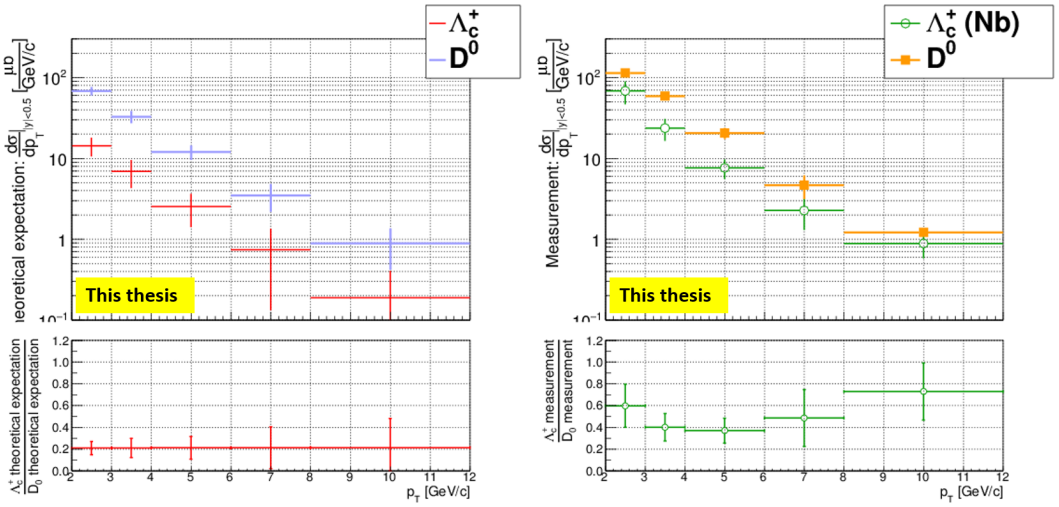

FIGURE 6.20: D^0 and Λ_c cross sections in pp collisions. On the left: theoretical expectations; on the right: measurements.

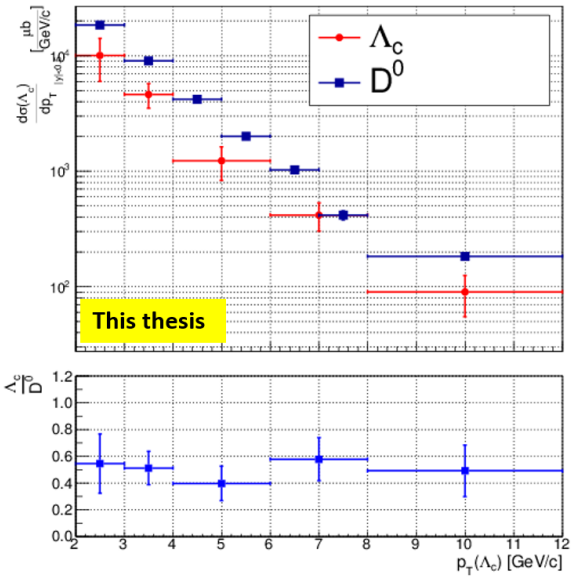

FIGURE 6.21: D^0 and Λ_c cross sections in p-Pb collisions.

- particle identification: the PID response could not be perfectly described in simulation,
- tracking efficiency: single track parameters (number of TPC crossed rows, number of TPC clusters, ITS-TPC matching efficiency, etc.) could not be perfectly described in simulation,
- Λ_c simulated p_T shape: the final result could depend on the assumed Λ_c simulated p_T shape,
- multiplicity dependence: only for the p-Pb data sample, the multiplicity distribution in the data is not described very well in simulation and this could affect the reconstruction efficiency,

- subtraction of feed-down Λ_c baryons from B decays: the final result could depend on the model parameters used to estimate the fraction of no-prompt Λ_c ,
- global systematic uncertainties due the branching ratio and integrated luminosity.

A summary of all the contributions is given in Tabs. 6.3 and 6.4 and inf Fig. 6.22, for the considered p_T intervals.

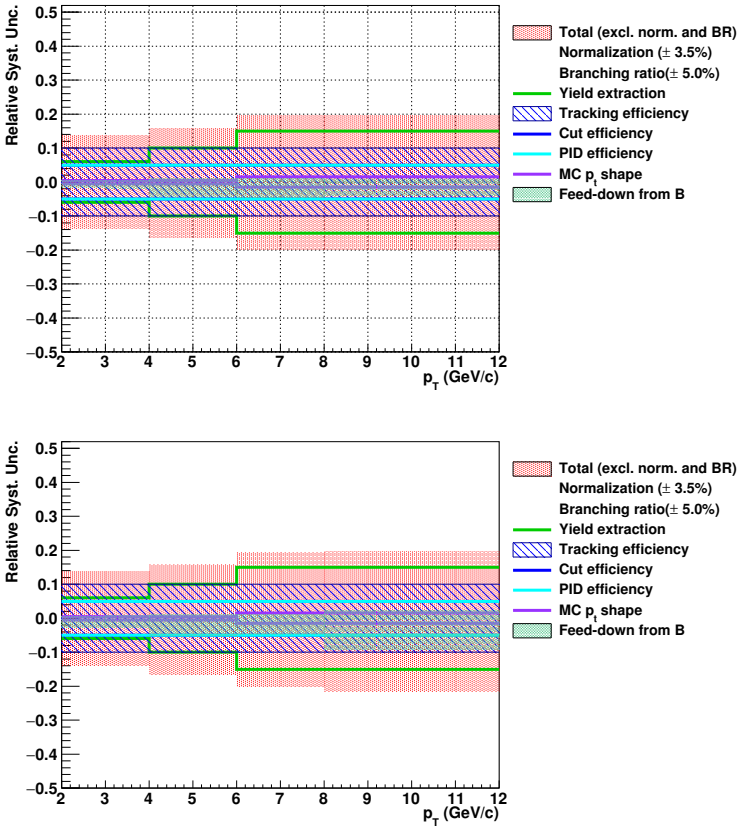

FIGURE 6.22: Summary of the systematics values.
Top: values for the analysis in pp collisions; bottom: values for the analysis in p-Pb collisions.

	p_{T} (Λ_{c}) $[GeV/c]$				
	2-3	3-4	4-6	6-8	8-12
Raw yield extraction	6%	6%	10%	15%	15%
Cut variation	5%	5%	5%	5%	5%
PID	5%	5%	5%	5%	5%
Tracking efficiency	10%	10%	10%	10%	10%
Λ_{c} simulated p_{T} shape	0.5%	0.5%	0.5%	1.5%	1.5%
Feed-down subtraction	+0.44% -1.7%	+0.50% -2.0%	+1.0% -4.9%	+1.0% -4.5%	+1.0% -3.9%
Branching ratio			5%		
Integrated luminosity			3.5%		

TABLE 6.3: Summary of the systematics values for Λ_{c} analysis in pp collisions.

	p_{T} (Λ_{c}) $[GeV/c]$				
	2-3	3-4	4-6	6-8	8-12
Raw yield extraction	10%	10%	10%	10%	10%
Cut variation	5%	5%	5%	5%	9%
PID	6%	6%	6%	6%	6%
Tracking efficiency	7%	7%	7%	7%	7%
Λ_{c} simulated p_{T} shape	1%	2%	2%	3%	3%
Multiplicity dependence	2%	2%	2%	6%	6%
Feed-down subtraction	+0.70% -0.76%	+0.79% -0.72%	+1.4% -1.2%	+1.3% -1.1%	+2.4% -2.2%
Branching ratio			5%		
Integrated luminosity			3.7%		

TABLE 6.4: Summary of the systematics values for the Λ_{c} analysis in p-Pb collisions.

6.4.1 Raw Yield extraction

The systematics uncertainties on the raw yield extraction was determined by repeating the Λ_c invariant mass fit changing the mass range, the function used to describe the background, the rebin factor and the first bin used to rebin the invariant mass histograms, and via a method based on bin counting. In particular the latter estimates the signal counting the entries of the invariant mass histograms after the subtraction of the background fit. The resulting deviations from the standard method are shown in Figs. 6.23 and 6.24, for what concerns the multi-trial method; the superimposed red lines refer to the extracted raw yield used as central value, the solid line, and the extracted raw yield plus/minus the statistical uncertainty, the dashed lines. As you can see, for what concerns the [4;6[Λ_c p_T bin in the pp case, and [4;6[and [6;8[Λ_c p_T bins in p-Pb , the central value and the mean of the multi-trial distribution have a clear discrepancy: for this reason only in this case we estimate the systematic uncertainty assuming a flat distribution instead of a gaussian one as done for all the other Λ_c p_T bins.

In Fig. 6.25, we show the deviation in the raw yield extraction by using the bin counting method.

The maximum between the two methods is assigned as systematic error for the raw yield extraction; the values are reported in Tabs. 6.5 and 6.6.

	p_T (Λ_c) $[GeV/c]$				
	2-3	3-4	4-6	6-8	8-12
Multi-trial (A)	5%	5%	11%	5%	8%
Bin counting (B)	7%	3%	9%	17%	15%
Maximum(A,B)	7%	5%	11%	17%	15%
smoothing	6%	6%	10%	15%	15%

TABLE 6.5: Summary of the systematics values for the raw yield extraction for Λ_c analysis in pp collisions.

	p_T (Λ_c) $[GeV/c]$				
	2-3	3-4	4-6	6-8	8-12
Multi-trial (A)	4%	4%	6%	8%	6%
Bin counting (B)	15%	10%	2%	2%	15%
Maximum(A,B)	15%	10%	6%	8%	15%
Final systematic error	10%	10%	10%	10%	10%

TABLE 6.6: Summary of the systematics values for the raw yield extraction for Λ_c analysis in p-Pb collisions.

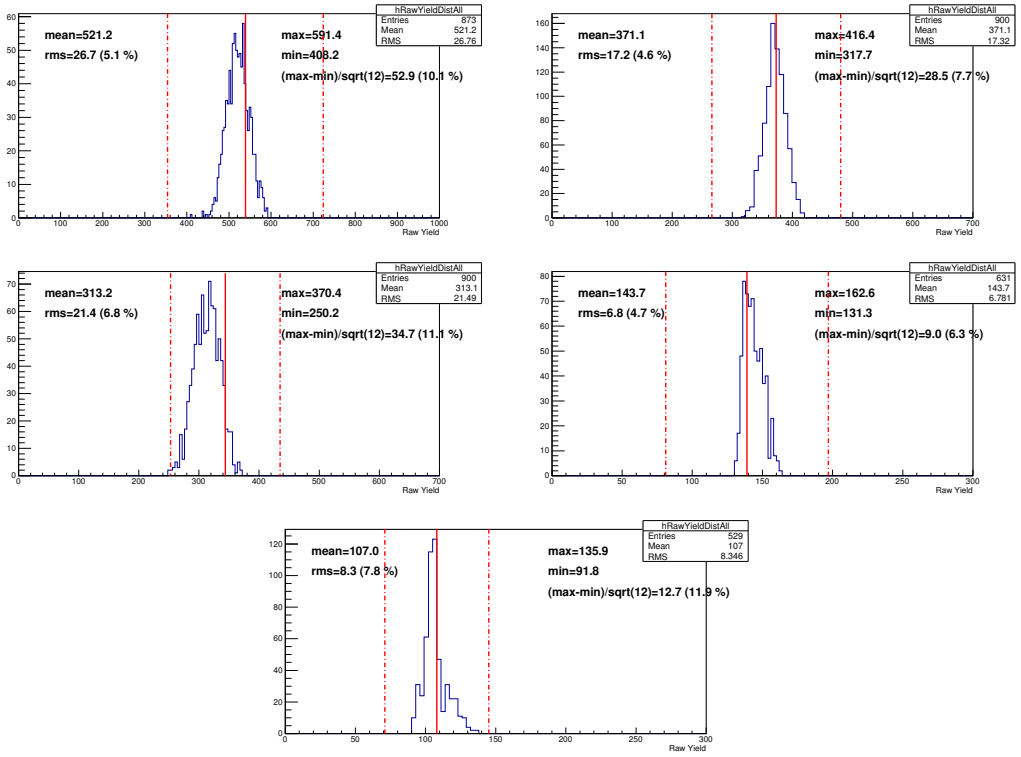

FIGURE 6.23: pp analysis: Deviations from the standard method by varying the fit parameters (multi-trial approach).

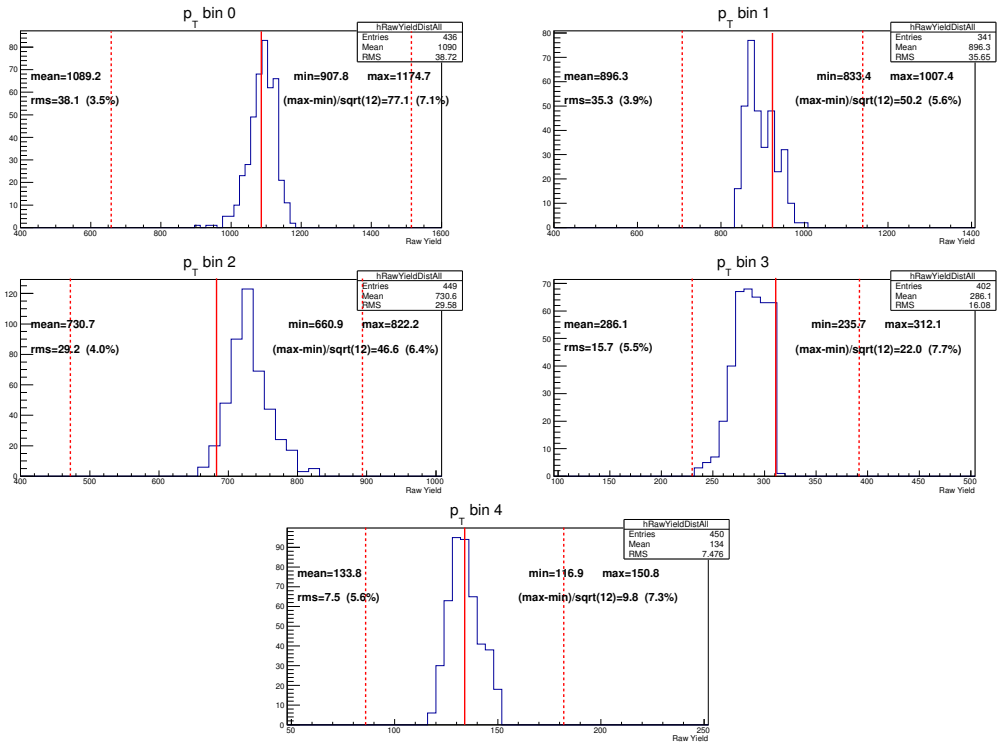

FIGURE 6.24: p-Pb analysis: deviations from the standard method by varying the fit parameters (multi-trial approach).

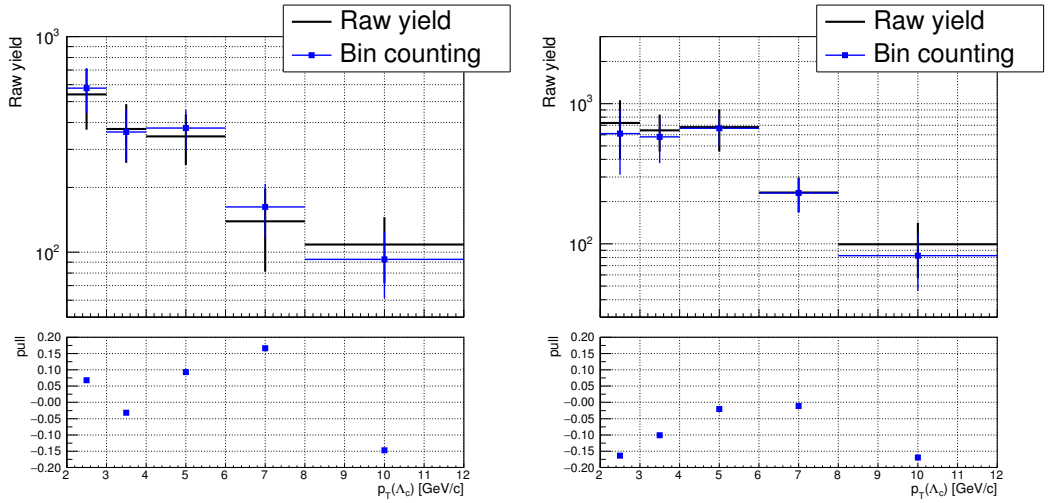

FIGURE 6.25: Deviations from the standard method by using the bin counting. Top: Λ_c analysis in pp ; Bottom: analysis in p-Pb .

6.4.2 Cut variation

A source of systematic uncertainty comes from the residual discrepancy between data and Monte Carlo simulations for all the variables used to select Λ_c candidates. This contribution was estimated by repeating the analysis with different, tighter and looser, sets of cuts. Each of the selection variables has been plotted, leaving unchanged the other ones, in order to find new cut values. The plots have been performed both on data and on MC, where it is possible to discriminate between signal and background. Starting form these plots, several trials to optimize cuts on these parameters have been done extracting raw yield from $p - K^0_S$ invariant mass spectra in the five $p_{\rm T}$ bins mentioned in the section 5.5. For some variables, like $e^+ - e^-$ invariant mass, similar results with tighter and looser cuts have been obtained. For some bins, small variation implied that significance goes under 3. A non-automatic procedure has been adopted for the cut variation. We focused on $p_{\rm T}$ for each prong, $p_{\rm T}$ (bachelor), $p_{\rm T}$ (V0-daughters), $p_{\rm T}$ ($K^0_{\rm S}$), and on $m_{inv}(\pi^+, \pi^-)$, $m_{inv}(e^+, e^-)$, $m_{inv}(p, \pi^-)$ and $m_{inv}(\pi^+, \bar{p})$. The guidelines for loose and tight choice have been the following: small changes in values from one to another set (dominated by statistical fluctuations); from central to tight- reduction of signal and background but increase in their ratio; from central to loose -increase of signal and background. Since, as already said, small variations in the cuts values implied different and often not even more good signal extraction, we decided to change cut values for only one variable per time, keeping unchanged all the other variables. Cut values that did not vary the efficiency of signal extraction with respect to the central values in all the $p_{\rm T}$ intervals were not taken into account. We selected only sets of cuts that provided a good Λ_c signal extraction, with reasonable fit parameters and we did not take into account sets of cuts for which the efficiencies were unchanged with respect to the central ones. The systematics uncertainty was evaluated considering for each set of cuts the relative difference of the $p_{\rm T}$ -differential cross sections from that estimated on the central set. In order to reduce as much as possible the contribution from statistical fluctuations, we took into account the raw yield extracted fixing mean and/or sigma to the values found for the central set of cuts. In order to have more statistics available (still to try to disentangle the statistical fluctuation from the systematic one), we estimated also the systematic values in the three merged $p_{\rm T}$ intervals 2-4, 4-6 and 6-12 GeV/c, and compared these values with the ones estimated on five $p_{\rm T}$ intervals. The relative ratios for the cross section in five $p_{\rm T}$ intervals are shown in Fig. 6.26 and 6.28; the results obtained considering three $p_{\rm T}$ intervals are instead in Figs. 6.27 and 6.29. The resulting variation of the cross section was found to be less than 10% in all the considered $p_{\rm T}$ intervals, and the results in three and five $p_{\rm T}$ bins were found to be in very good agreement with each other. We decided to take as final value for the systematic uncertainty on cut variation what obtained fixing the signal-width values. In the Tabs. 6.7 and 6.8 we report the values obtained for each trial.

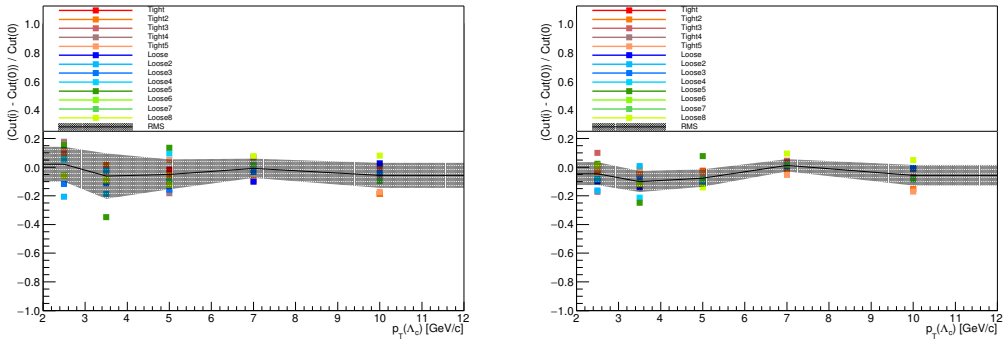

FIGURE 6.26: Systematics on cut variation in pp . Relative discrepancy of the p_{T} -differential cross section in five p_{T} intervals estimated for each set of cuts with respect to that one estimated on the central cuts set. In the left plot, the signal extraction was performed without any restriction on the fit parameter. In the right plot, sigmas are fixed to the values obtained from signal extraction on the central set of cuts.

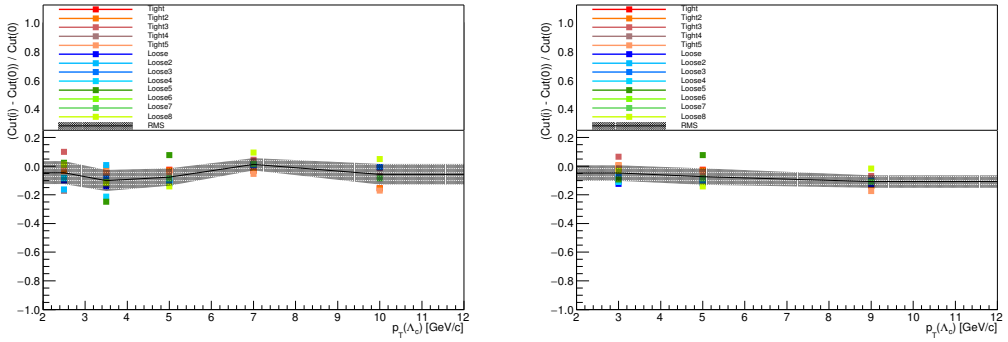

FIGURE 6.27: pp analsysis: Relative discrepancy of the p_{T} - differential cross section in five, on the left, and three, on the right,p_{T} intervals estimated for each set of cuts with respect to that one estimated on the central cuts set. Sigmas are fixed to the values obtained from signal extraction on the central set of cuts.

	p_{T} (Λ_c) $[GeV/c]$				
	2-3	3-4	4-6	6-8	8-12
Free	12%	16%	10%	7%	9%
Fixed (5bins)	8%	7%	6%	4%	7%
Fixed (3 bins)	5%		6%		4%
smoothing	5%	5%	5%	5%	5%

TABLE 6.7: Summary of the systematics values on the cut variation in pp collisions. The values in the first row refer to the case where the fit parameters, in particular the signal width is left free. The values in the other rows refer to the case where the signal width is fixed to the value obtained when the central set of cuts is used.

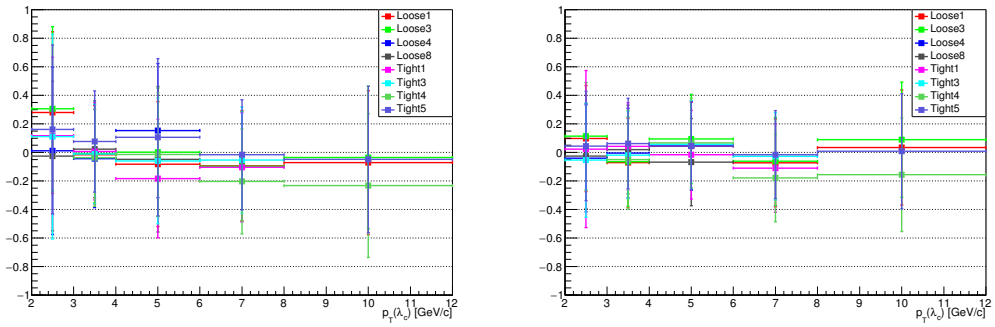

FIGURE 6.28: Systematics on cut variation in p-Pb . Relative discrepancy of the p_{T} -differential cross section in five p_{T} intervals estimated for each set of cuts with respect to that one estimated on the central cuts set. In the left plot, the signal extraction was performed without any restriction on the fit parameter. In the right plot, mean and sigma are fixed to the values obtained from signal extraction on the central set of cuts.

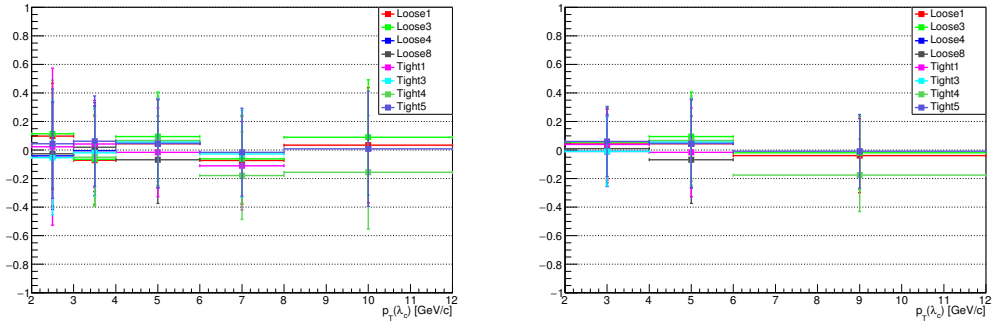

FIGURE 6.29: p-Pb analsysis: Relative discrepancy of the p_{T} -differential cross section in five, on the left, and three, on the right, p_{T} intervals estimated for each set of cuts with respect to that one estimated on the central cuts set. Mean and sigma are fixed to the values obtained from signal extraction on the central set of cuts.

	p_{T} (Λ_{c}) $[GeV/c]$				
	2-3	3-4	4-6	6-8	8-12
Free	12%	16%	10%	7%	9%
Fixed (5bins)	8%	7%	6%	4%	7%
Fixed (3 bins)	5%		6%		4%
smoothing	5%	5%	5%	5%	5%

TABLE 6.8: Summary of the systematics values on the cut variation in p-Pb collisions. The values in the first row refer to the case where the fit parameters, in particular the signal width is left free. The values in the other rows refer to the case where the signal width is fixed to the value obtained when the central set of cuts is used.

6.4.3 PID efficiency

The systematic uncertainty induced by a different efficiency for particle identification in data and Monte Carlo simulations was evaluated by comparing the p_T -differential cross section estimated with the PID strategy defined in section 5.5, with the ones obtained using different PID approaches, without changing the topological cuts. We first tried to change the number-of-sigma cuts on TPC and TOF, and then the cut values on the proton p_T . We also tried to use the combined probability PID, using TPC and TOF. PID strategies that did not vary the efficiency of signal extraction with respect to the central PID strategy in all the p_T intervals were not taken into account.

As done for the cut variation efficiency, also in this case we tried to fix the mean and/or the sigma to the values coming from the signal extraction on the central set of cuts: results are showed in Figs. 6.30 and 6.32. It is evident in this figure that the statistical fluctuations affect the signal extrapolation. So, to disentangle the statistical fluctuations from the systematics on the PID variation, we merged bins and we compared results in five and three p_T intervals, as shown in Figs. 6.31 and 6.33. The resulting variation of the cross section was found to be less than 10% in all the p_T intervals considered. The results in three and five p_T bins are not in a good agreement with each other: the measured systematics decreases when we took into account the merged p_T bins $2-4$ and $6-12$ GeV/c (instead of $2-3$, $3-4$, $6-8$ and $8-12$), and compared results. In Tabs. 6.9 and 6.10we report the values obtained for each trial.

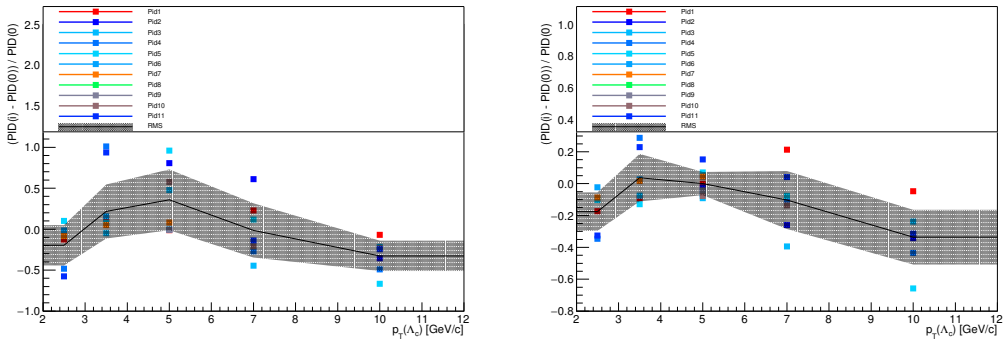

FIGURE 6.30: Systematics on PID variation for pp . Relative discrepancy of the p_T -differential cross section in five p_T intervals estimated with different PID strategies with respect to that one estimated on the central cuts set. In the left plot, the signal extraction was performed without any restriction on the fit parameter. In the right plot, sigmas are fixed to the values obtained from signal extraction on the central set of cuts.

Proton/anti-proton from $\Lambda/\bar{\Lambda}$ decay

To definitely disentangle statistical fluctuation from systematics uncertainties on the PID variation for the analysis in pp , we performed a cross-check on the protons/anti-protons coming from $\Lambda/\bar{\Lambda}$ decay. In particular, we took into account the $\Lambda/\bar{\Lambda}$ V0 candidates. We applied our bachelor PID strategy on the protons/anti-protons coming from $\Lambda/\bar{\Lambda}$ decay. We estimated the PID efficiency as the fraction of the identified $p/\bar{p}$ coming from $\Lambda/\bar{\Lambda}$ decay. Comparing the efficiencies estimated respectively on

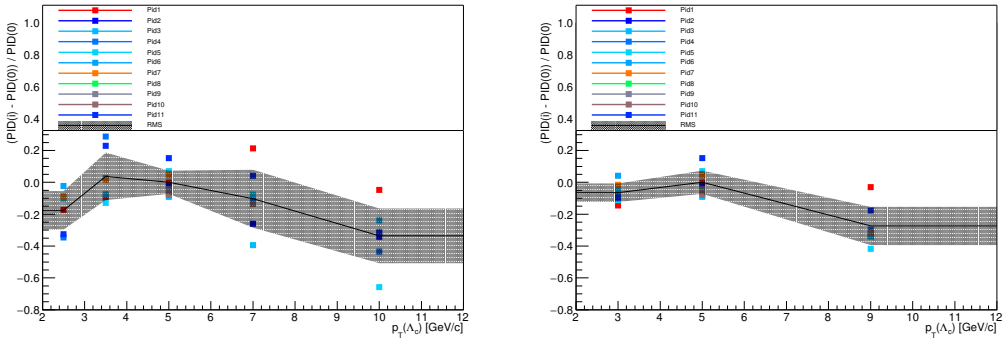

FIGURE 6.31: Relative discrepancy of the p_{T} -differential cross section in five, on the left, and three, on the right, p_{T} intervals in pp , estimated with different PID strategies with respect to that one estimated on the central one. Sigmas are fixed to the values obtained from signal extraction on the central PID.

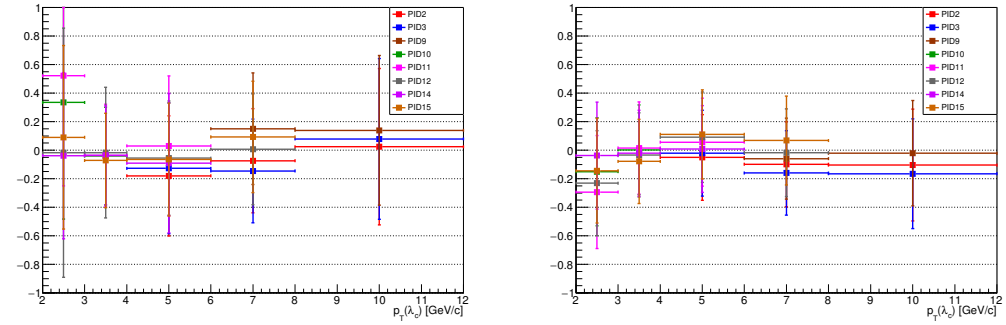

FIGURE 6.32: Systematics on PID variation in p-Pb . Relative discrepancy of the p_{T} -differential cross section in five p_{T} intervals estimated with different PID strategies with respect to that one estimated on the central cuts set. In the left plot, the signal extraction was performed without any restriction on the fit parameter. In the right plot, mean and sigma are fixed to the values obtained from signal extraction on the central set of cuts.

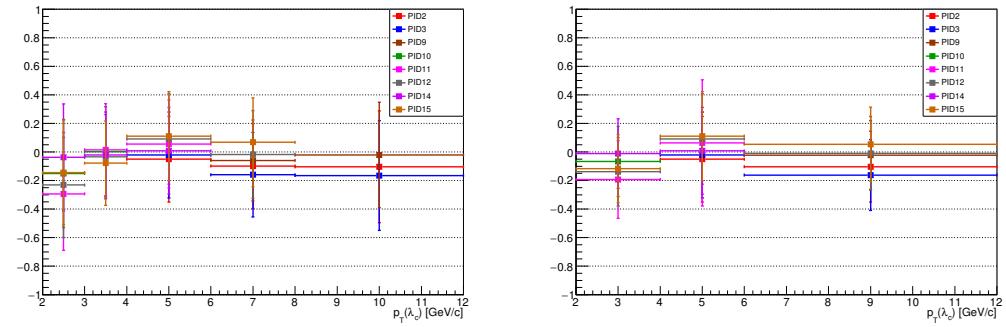

FIGURE 6.33: Relative discrepancy of the p_{T} -differential cross section in three p_{T} intervals estimated with different PID strategies with respect to that one estimated on the central cuts set in p-Pb . In the left plot, the signal extraction was performed without any restriction on the fit parameter. In the right plot, mean and sigma are fixed to the values obtained from signal extraction on the central set of cuts.

	p_T (Λ_c) $[GeV/c]$				
	2-3	3-4	4-6	6-8	8-12
Free	25%	33%	37%	33%	18%
Fixed (5bins)	12%	15%	7%	18%	17%
Fixed (3 bins)	6%		7%		12%

TABLE 6.9: Summary of the PID systematics values for the pp data sample. The values in the first row refer to the case where the fit parameters, in particular the signal width is left free. The values in the other rows refer to the case where the signal width is fixed to the value obtained when the central PID strategy is used.

	p_T (Λ_c) $[GeV/c]$				
	2-3	3-4	4-6	6-8	8-12
Free	25%	33%	37%	33%	18%
Fixed (5bins)	12%	15%	7%	18%	17%
Fixed (3 bins)	6%		7%		12%

TABLE 6.10: Summary of the PID systematics values for the p-Pb data sample. The values in the first row refer to the case where the fit parameters, in particular the signal width is left free. The values in the other rows refer to the case where the signal width is fixed to the value obtained when the central PID strategy is used.

data and Monte Carlo, we have an independent estimate of the systematics on the PID.

On the same data sample and MC used for our analysis, we used the tool developed for the preparation of the paper on the Bayesian particle identification approach [170], i.e. *$ALICE_PHYSICS/ PWGpp/ pid/ AliAnalysisTaskLambdaBayes.h/cxx* class.

The efficiencies estimated on data and MC are shown in Fig. 6.34, as well as their ratio in Fig. 6.35, in function of the transverse momentum of proton/anti-proton. This ratio is lower that 5% until $4\ GeV/c$ of transverse momenta for the proton/anti-proton. for higher p_T values, the ratio goes down quickly, since the statistical fluctuations become higher, as it happens in Λ_c case.

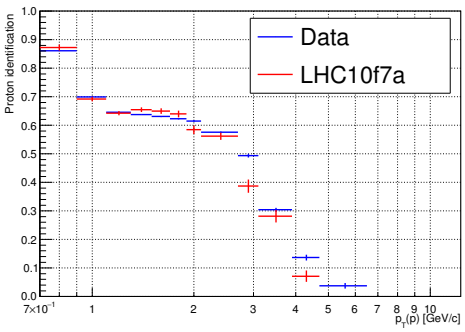

FIGURE 6.34: Proton/anti-proton identification efficiency as estimated on $\Lambda/\bar{\Lambda}$ V0 candidates. The blue points are related to data and the red ones to the MC.

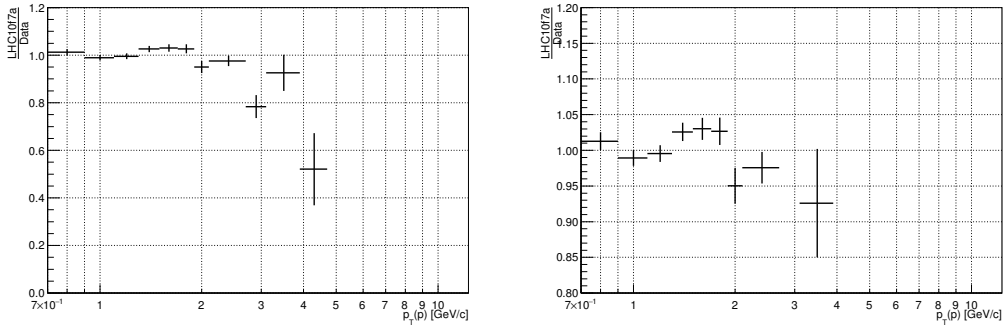

FIGURE 6.35: The ratio of the proton identification in data and in MC is shown. On the right a zoom is shown.

Then, according to this result, we took 5% as the final value for the systematics on the PID variation for all the p_{T} (Λ_{c}) intervals.

6.4.4 MC p_T shape

The effect on the efficiency due to the shape of the Λ_c p_T spectrum used in the simulation was also estimated, looking at the relative difference between the Monte Carlo efficiencies obtained using different p_T shapes, namely those used in PYTHIA, in FONLL calculation and also a flat p_T -shape. The resulting contribution to the systematic uncertainty was found to be not more than few% in all p_T bins, as shown in Fig. 6.36.

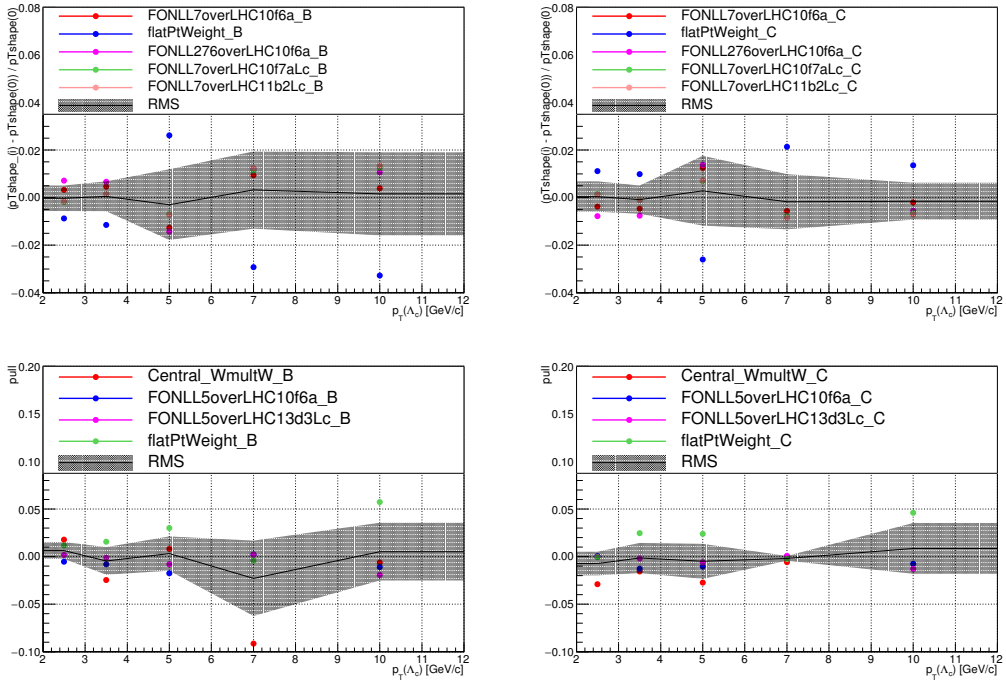

FIGURE 6.36: Relative discrepancy of the efficiency estimated with different MC p_T -shapes with respect to that one used in our analysis. On the left, for Λ_c from b; on the right the prompt ones. Top: pp analysis; Bottom: p-Pb analysis.

MC multiplicity dependence

The production LHC13d3 doesn't describe very well the multiplicity distribution in the data, so the reconstruction efficiency depends on the particle multiplicity and in particular decrease at higher multiplicity. This effect was already evaluated in the analysis of D mesons in the same p-Pb data, and it was found very small, since it's important only at very low multiplicity. In our case, the effect on the efficiency due to the reweight of the MC events using different multiplicity weights was also estimated, looking again at the relative difference between the Monte Carlo efficiencies obtained. Similarly to what was done for the D mesons, we checked three different weights:

- *hNtrUnCorrEvWithD*: all events with a D in the D0 invariant mass window
- *hNtrUnCorrEvWithCand*: all events with a D meson candidate
- *hNtrUnCorrEvSel*: all events used for analysis

We found a very small contribution to the systematics uncertainty, not greater than 3%, for the first three p_{T} intervals, and about 6% for the last two ones, as shown in Fig. 6.37.

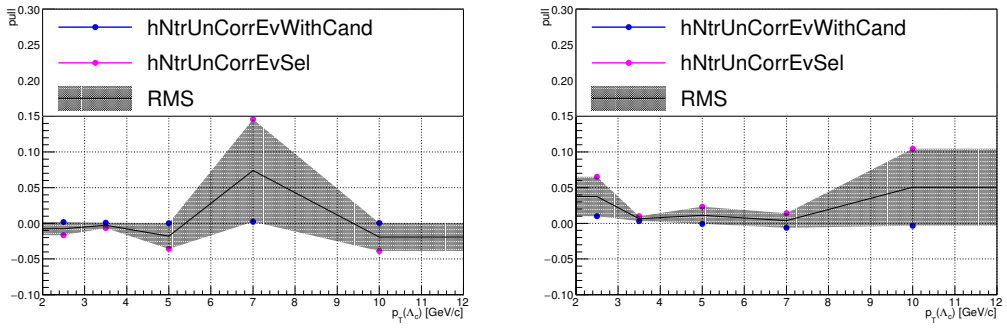

FIGURE 6.37: Relative discrepancy of the efficiency estimated with different multiplicity weights with respect to that one used in our analysis. On the left, for Λ_c from b; on the right the prompt ones.

6.4.5 Track reconstruction efficiency

This systematic uncertainty includes the effects arising from track finding in the TPC for what concerns all our three prongs, and track propagation from the TPC to the ITS (ITS-TPC matching efficiency), only for what concerns our bachelor, that is primary and for which we require at least one point in the ITS detector. We assigned a value of 4% to the bachelor for pp and 3% for pPb, according to what already done for the other analysis in pp collisions at 7 TeV and p-Pb collisions at 5 TeV. For what concerns the two charged pions coming from the K^0_S decay, we we considered the following terms:

- the crossed-over-findable TPC clusters (variable as a function of p_T (K^0_S),
- the TPC crossed rows,
- the material budget;

and we expressed them as a function of p_T (Λ_c). In Tabs. 6.11 and 6.12 we reported the final estimate. The found values are lower than the expected by assuming primaries all three prongs (i.e. 12% for pp , 9% for p-Pb); this is expected since one of the main contributes to the tracking uncertainty comes from the TPC-ITS matching requirement and, as explained, in our case this is true only for one of our three prongs.

	p_T (Λ_c) $[GeV/c]$				
	2-3	3-4	4-6	6-8	8-12
bachelor (A)	4%	4%	4%	4%	4%
V0 (B)	5%	5%	5%	6%	6%
A+B	9%	9%	9%	10%	10%
smoothing	10%	10%	10%	10%	10%

TABLE 6.11: Summary of the systematics values for the prong tracking for the pp data sample.

	p_T (Λ_c) $[GeV/c]$				
	2-3	3-4	4-6	6-8	8-12
bachelor (A)	3%	3%	3%	3%	3%
V0 (B)	4%	4%	4%	4%	4%
A+B	7%	7%	7%	7%	7%

TABLE 6.12: Summary of the systematics values for the prong tracking for the p-Pb data sample.

6.4.6 Feed-down from B

The cross section was computed using N_b method described in Sec. 6.3. The systematic uncertainty on the estimation of feed-down correction from $beauty$-hadrons is performed by varying the parameters used for the FONLL B predictions. More than 95% of no-prompt Λ_c comes from Λ_b; the remaining 5% comes from B_0 and B^+, according to recent studied. Concerning the Λ_b cross section, LHCb measurements [171] are in agreement with FONLL predictions with respect to the shape, but

a rescaling is needed. Since the discrepancy is within a factor 2, we scaled the Λ_b cross section by a factor 2, as a safety margin, and to evaluate the systematic uncertainty due to the feed-down subtraction we took the envelope of the uncertainty bands from the two methods: with and without the rescaling. The resulting uncertainty is reported in Fig. 6.38, The systematic errors on the value for f_{prompt} are reported in Tabs. 6.13 and 6.14.

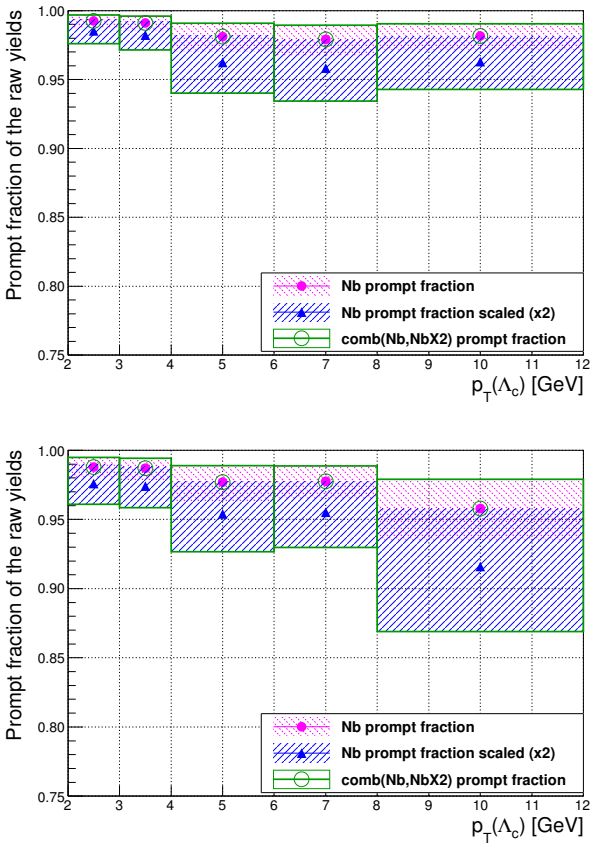

FIGURE 6.38: Relative fraction of Λ_c in the raw yield using N_b method no rescaling (magenta) and rescaling (blue) by a factor of 2 the Λ_b production cross section. Superimposed in green the combination of the 2 estimates. Left: pp analysis; Right: p-Pb analysis.

	p_T (Λ_c) $[GeV/c]$				
	2-3	3-4	4-6	6-8	8-12
Feed-down subtraction	+0.44%	+0.50%	+1.0%	+1.0%	+1.0%
	-1.7%	-2.0%	-4.9%	-4.5%	-3.9%

TABLE 6.13: Systematic uncertainty on feed-down from B for Λ_c analysis for the pp data sample.

6.4.7 Branching ratio

Finally, the results have a global systematic uncertainty due to the branching ratio of the Λ_c decay channel taken into account in this analysis. Its value is not dependent from p_T (Λ_c) bin and it is 5% according to the last accepted PDG value [169].

	p_T (Λ_c) $[GeV/c]$				
	2-3	3-4	4-6	6-8	8-12
Feed-down subtraction	+0.70%	+0.79%	+1.4%	+1.3%	+2.4%
	-0.76%	-0.72%	-1.2%	-1.1%	-2.2%

TABLE 6.14: Systematic uncertainty on feeddown from B for Λ_c analysis for the p-Pb data sample.

6.5 Final cross section measurement

In Figs. 6.39 and 6.40 the final result are shown: the Λ_c cross section estimated using the scaled Nb method is shown including statistical and systematic uncertainties.

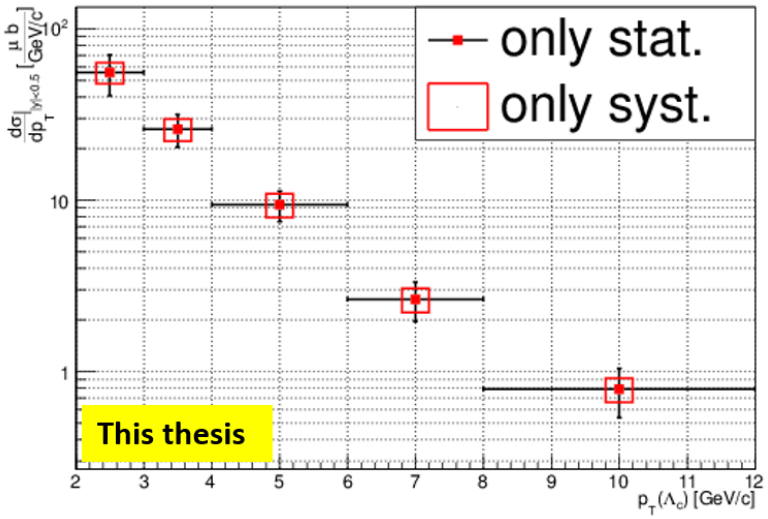

FIGURE 6.39: Cross-section production for Λ_c analysis in pp collisions, considering Nb feed down correction. Statistical and systematic uncertainties are shown.

6.6 Comparison with the other Λ_c measurements

The measurement of Λ_c production has been performed in ALICE by reconstructing three decay modes, $\Lambda_c^+ \rightarrow pK^-\pi^+$(with branching ratio, BR, of (6.35 $\pm$ 0.33)%), $\Lambda_c^+ \rightarrow pK_S^0$(BR of (1.58 $\pm$ 0.08)%), with $K_S^0 \rightarrow \pi^+\pi^-$(BR of (69.20 $\pm$ 0.05)%), and $\Lambda_c^+ \rightarrow e^+\nu_e\Lambda$(BR of (3.6 $\pm$ 0.4)%), with $\Lambda \rightarrow p\pi^-$(BR of (63.9 $\pm$ 0.5)%), together with their charge conjugates [168]. Each of the analysis strategies for the extraction of the Λ_c signals from the large combinatorial background due to uncorrelated tracks is based on the reconstruction of charged tracks in the ALICE central barrel, on the V0 topology decay reconstruction, on kinematical and geometrical selection, and on the use of Particle Identification (PID). For some of the results presented here, MultiVariate Analysis techniques (MVA) are additionally adopted. Finally, an invariant mass analysis is used to extract the signal yield. In Tab. 6.15 the summary of the analysis approaches used (among them also the analysis subject of this thesis) for Λ_c studies is shown.

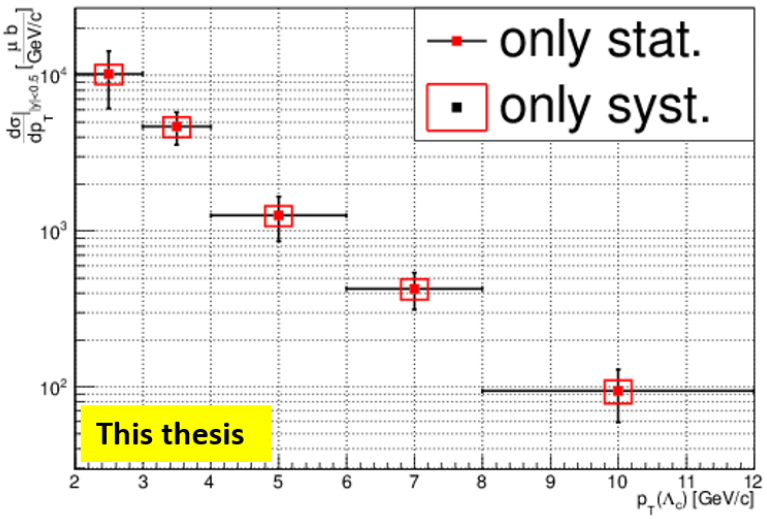

FIGURE 6.40: Cross-section production for Λ_c analysis in p-Pb collisions, considering Nb feed down correction. Statistical and systematic uncertainties are shown.

Decay channel	Collision system ($\sqrt{s_{NN}}$[TeV])	strategy	
		Method	PID
$\Lambda_c^+ \to pK^-\pi^+$	pp (7) and p-Pb (5.02)	Topological cuts	Bayes
$\Lambda_c^+ \to pK_S^0$	pp (7) and p-Pb (5.02)	Topological cuts	nσ
$\Lambda_c^+ \to e^+\nu_e\Lambda$	pp (7)	Rigth/wrong sign	nσ
$\Lambda_c^+ \to pK^-\pi^+$	p-Pb (5.02)	MVA (BDT)	Bayes
$\Lambda_c^+ \to pK_S^0$	p-Pb (5.02)	MVA (BDT)	Bayes

TABLE 6.15: Summary of the different Λ_c analyses performed with ALICE.

The analysis is performed in the moderate and high momentum range of the Λ_c ($2 < p_T$ (Λ_c) < 16 Gev/c). The lower limit is imposed by the small decay length of the Λ_c ($c\tau$= 59.9 μ m) and the current impact parameter resolution of the ALICE detector which is of the order of $\sim$ 65 μ m at 1 Gev/c, rapidly deteriorating at lower p_T . The upper limit is a consequence of the statistical limitation of the analysis.

6.6.1 Multivariate analysis techinque (MVA)

In this analysis technique, a multivariate selection is used to separate the combinatorial background from the signal, based on Boosted Decision Trees (BDT) [172]. Training Λ_c samples are used, in which the type of each event (signal or background) is known, to determine a mapping function optimized to maximize signal/background separation. This learned mapping function is then applied to a real data sample, and a cut on this function aims to reject background candidates while keeping signal candidates. Before the BDT selection, a first loose topological selection and PID using TOF and TPC information is applied.

6.6.2 Semileptonic decay $\Lambda_c^+ \rightarrow e^+\nu_e\Lambda$

Λ baryons are reconstructed using the decay $\Lambda \rightarrow p\pi$, detecting protons and pions in the ALICE central barrel. Λ baryon have a long lifetime of $c\tau\sim$ 7.89 cm and they can be identified using their V-shaped decay topology. $e\Lambda$ pairs satisfying a cut on their opening angle and on their invariant mass (expected closed to the Λ_c mass) are selected and used for this analysis.
Due to the missing neutrino (which can't be detected), the invariant $e\Lambda$ mass distributions don't show a peak, and the the background subtraction procedure used by the other Λ_c analyses cannot be used. In this case, the background contributions are estimated using *wrong sign pairs* $e^-\Lambda$, while Λ_c^+ decay only into *right-sign* $e^+\Lambda$ pairs. After subtracting this background, the Λ_c spectra are corrected for the Λ_b^0 contribution, the $\Xi_c^{0,+}$ ($\Xi_c^{0,+} \rightarrow e^+\Xi^{-,0}\nu \rightarrow e^+\Lambda\pi^{-,0}\nu$) contribution to right-sign pairs, missing momenta of neutrino. reconstruction and selection efficiency.

6.6.3 Comparison of all the Λ_c production cross sections

The p_T -differential cross sections for Λ_c production are shown in Fig. 6.41. The cross sections in pp collisions in the decay channels $\Lambda_c^+ \rightarrow pK_S^0$, $\Lambda_c^+ \rightarrow pK^-\pi^+$and $\Lambda_c^+ \rightarrow e^+\nu_e\Lambda$are shown in the left plot, while the cross sections in p-Pb collisions in the decay channels $\Lambda_c^+ \rightarrow pK_S^0$and $\Lambda_c^+ \rightarrow pK^-\pi^+$in the plot on the right.

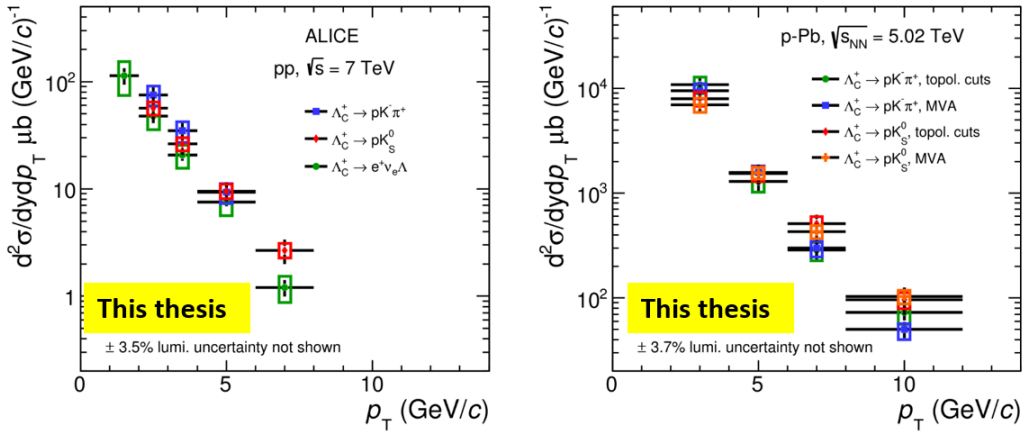

FIGURE 6.41: p_T -differential Λ_c cross sections measurements in pp and p-Pb collisions. Left plot: Λ_c cross sections in pp collisions at $\sqrt{s}$ = 7 TeV, in the p_T range 1 < p_T < 12 GeV/c, in the decay channels $\Lambda_c^+ \rightarrow pK_S^0$, $\Lambda_c^+ \rightarrow pK^-\pi^+$and $\Lambda_c^+ \rightarrow e^+\nu_e\Lambda$: Right plot: Λ_c cross sections in p-Pb collisions at $\sqrt{s_{NN}}$= 5.02 TeV in the p_T range 2 < p_T < 12 GeV/c, in the decay channels $\Lambda_c^+ \rightarrow pK_S^0$and $\Lambda_c^+ \rightarrow pK^-\pi^+$.

A good agreement, within the statistical and systematic uncertainties can be observed for a wide Λ_c p_T range, in both collisions systems. To be consistent with the other performed measurements, the results in pp collisions are shown only up to 8 GeV/c. The results in the p_T interval 2-4 GeV/c for p-Pb collisions, for which the agreement between the measurements is not good, are currently under investigation.

6.6.4 Λ_c /D^0

From the measured cross sections is possible to derive the ratio Λ_c /D^0, allowing to explore hadronization mechanisms in the charm sector for what concerns the baryon/meson ratio. In Fig. 6.42 the comparison between all the ratios Λ_c /Dzero is shown, again for pp collisions on the left and for p-Pb collisions on the right. There is a good agreement within uncertainties between all the analyses in the two decay different channels with a ratio between 0.3 and 0.8, except for first p_T range 2-4 GeV/c.
In Fig.6.43 the average of all the resutls for the Λ_c /D^0ratio is shown, respectively for the pp and p-Pb data samples.

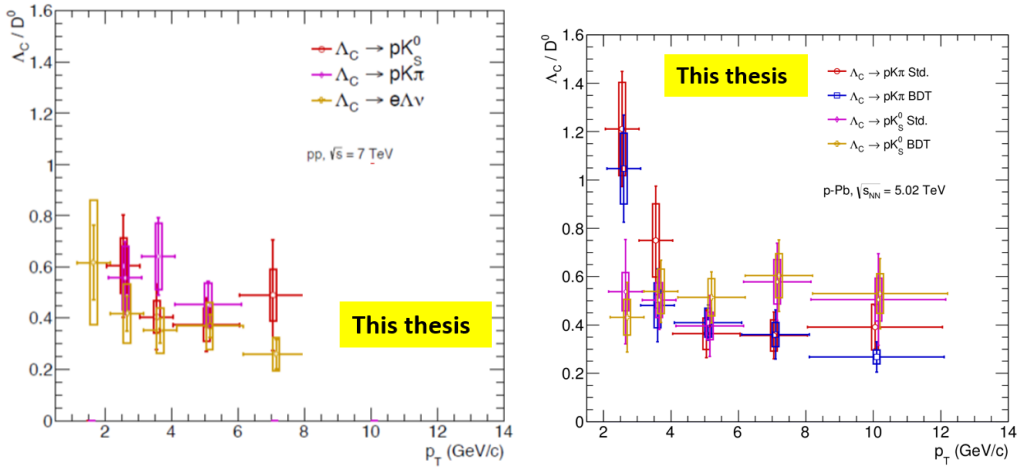

FIGURE 6.42: Comparison between all the Λ_c /D^0ratios in pp collisions (Left plot) and p-Pb collisions (Right plot).

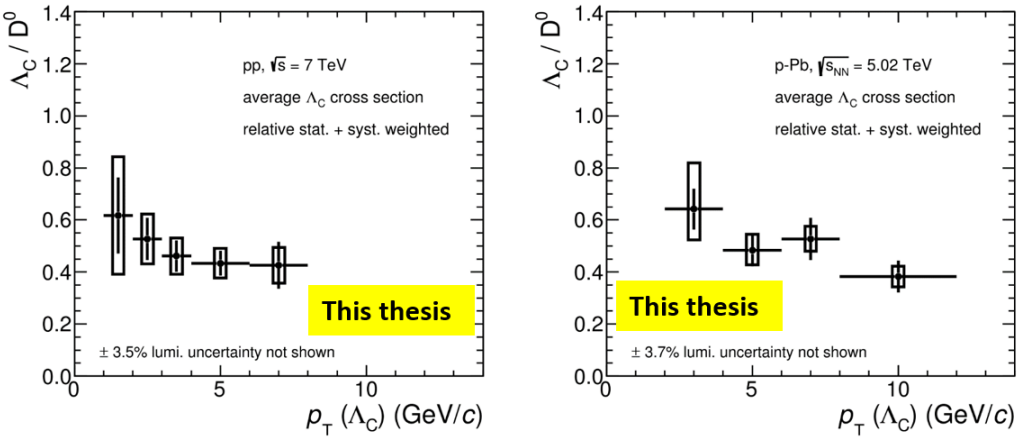

FIGURE 6.43: Average of all Λ_c /D^0ratios, in pp collisions (Left plot) and p-Pb collisions (Right plot).

Fig. 6.44 shows in pp and p-Pb the Λ_c /D^0ratio with data taken, for the D^0, from ALICE measurements compared, for pp , with PYTHIA8 Monash tune and several other tunes [173]. The enhanced color reconnection mechanisms enabled in PYTHIA8 increase, as expected, the baryon meson ratio also in the charm sector,

describing qualitatively better the data. of the Λ_c D^0ratio, as measured in different collision systems (taken from [174] with the addition of the two ALICE points, obtained averaging over all p_T bins.

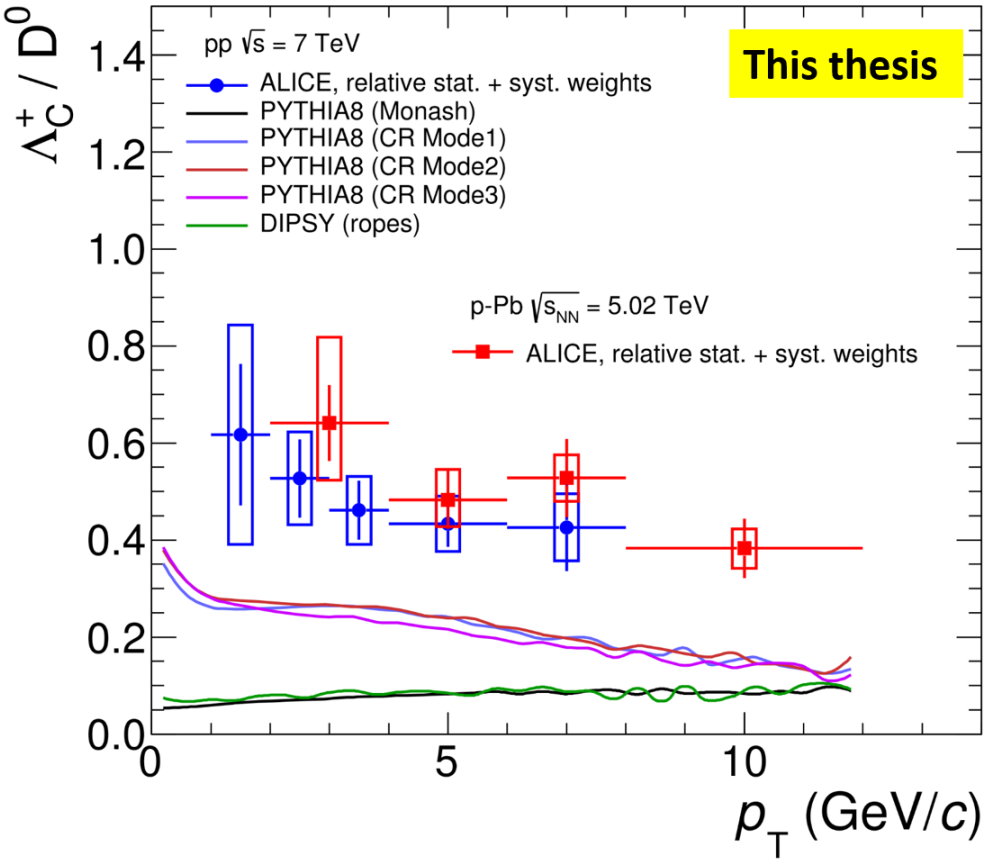

FIGURE 6.44: The Λ_c /D^0ratio as measured in pp and p-Pb collisions by ALICE, compared with different models.

The comparison of our result with the one reported by the LHCb Collaboration [11] at the same center-of-mass energy is not straightforward, given the different rapidity region covered by the two experiments.
In Fig. 6.45 (Left) the Λ_c /D^0measurements performed with the ALICE experiment in both collision systems are compared with the results obtained by LHCb [11] in pp collisions at 7 $\sqrt{s}$= 7 TeV. ALICE measurements, as a function of p_T , are systematically higher than the ones by LHCb, performed in a completely rapidity range, giving a hint of a enhanced charmed baryon production in the central region. In the right plot of Fig. 6.45 we show as a function of rapidity how the Λ_c /D^0ALICE result compare with the LHCb measurement. LHCb points published in [11] have been shifted to take into account of the updated branching ratio value [169]. As a function of rapidity they are compatible when compared with the largest rapidity points measured by LHCb. At the same time the LHCb points as a fucntion of rapidity show an unexpected trend.

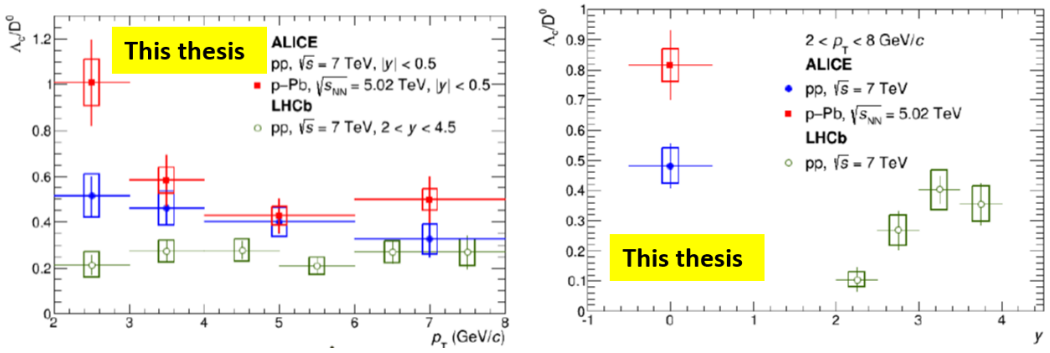

FIGURE 6.45: Comparison between the Λ_c /D^0ratios measured by ALICE and LHCb experiments, as function of p_T (Left) and rapidity (Right).

The measurements performed by ALICE are referred to two data sample, pp collisions at $\sqrt{s}$= 7 TeV and p-Pb collisions at $\sqrt{s_{NN}}$= 5.02 TeV, at mid-rapidity. The LHCb measurement was performed only in pp collisions and in a different rapidity range, 2 < y < 4.

Conclusions

In this thesis work, the analysis of the Λ_c production in pp collisions at $\sqrt{s}$= 7 TeV and p-Pb collisions at $\sqrt{s_{NN}}$= 5.02 TeV has been performed, through the reconstruction of the decay channel $\Lambda_c^+ \rightarrow pK_S^0$.
This study could give an insight in the baryon and meson production mechanisms in hard hadronic processes, measuring the Λ_c /D^0ratio. The Λ_c production measurement in pp collisions is the needed baseline reference for studies in heavy ions collisions. Λ_c studies in p-Pb collisions allow for the study of CNM effects. Moreover, previous Λ_c measurements are old and performed in extremily different energy and experimental conditions.
This particular analysis is performed using the detectors of the ALICE central barrel and, in partucular, exploits the very good PID capability of ALICE (using TPC and TOF information)
After a brief description on the ALICE experiment, the focus has been on the Time-Of-Flight system. The aspects of TOF data quality control have been discussed in detail, while illustrating the excellent and very stable performance of the system in different collision environments at the LHC. It has been shown that TOF PID allows a 2σ separation between pions, kaons and protons up to $\sim$ 4.0 GeV/c. This is a fundamental feature for the identification of protons for the Λ_c analsis.
The analysis strategy has been finally described in its stages. The signal is extracted via an invariant mass analysis. The high combinatorial background is subtracted using a strong topological selection and using the PID to identify protons. After applying acceptance and efficiency corrections, and removing contribution from Λ_c coming from beauty hadrons decays (*feed-down*), the Λ_c cross section is finally measured in a wide Λ_c p_T range, in both collisions systems, pp at $\sqrt{s}$= 7 TeV and p-Pb at $\sqrt{s_{NN}}$= 5.02 TeV. The Λ_c /D^0ratio is also estimated.
Our results are compared with other Λ_c measurements performed with ALICE using the same data samples but different decay channels and different analysis techniques. The aim is to combine all these Λ_c measurements and give the first measurement of Λ_c production in pp and p-Pb collisions with the ALICE experiment at the LHC. We are waiting for the theoreticians to have a theoretical expectation to be compared with our analysis results. Last developments of the analysis are planned, towards the final merging of all the Λ_c measurement in a publication (the paper writing is in progress).

Appendix A

Check on possible contaminations from D mesons

We checked if the m_{inv}(p,$K^0_{\rm S}$) distributions could be contaminated by $D^+ \to \pi^+ K^0_{\rm S}$ or $D_s^+ \to K^+ K^0_{\rm S}$ and c.c. because of a not well kaon-proton or pion-proton separation at high momenta. Since in the available MB MC productions we did not have enough statistics to study possible contaminations from D meson reflections and other $\Lambda_{\rm c}$ decay modes, we created and used a toy model to check it.

As already done to check $\Lambda_{\rm c}$ reconstruction efficiency, we took into account a statistically significant sample of $D^+ \to \pi^+ K^0_{\rm S}$, $D_s^+ \to K^+ K^0_{\rm S}$ and $\Lambda_{\rm c}^+ \to$p$K^0_{\rm S}$ (in the right ratios) with all prongs in the ALICE reconstruction pseudorapidity region (i.e. $|\eta| < 0.9$).

Then, to each D^+ (D_s^+) we applied pion (kaon) and $K^0_{\rm S}$ reconstruction efficiencies and the pion (kaon) as proton misidentification probability according to the PID strategy used in our analysis. In Figs. A.1 and A.2 we shown the m_{inv}(p,$K^0_{\rm S}$) plots, respectively without and with PID applied to the bachelor for $\Lambda_{\rm c}^+$ (black), D^+ (blue) and D_s^+ (red) - and c.c.- candidates.

From the results obtained, it seems that the correlated background coming from D^+ and/or D_s^+ mesons does not affect significantly the $\Lambda_{\rm c}$ signal extraction.

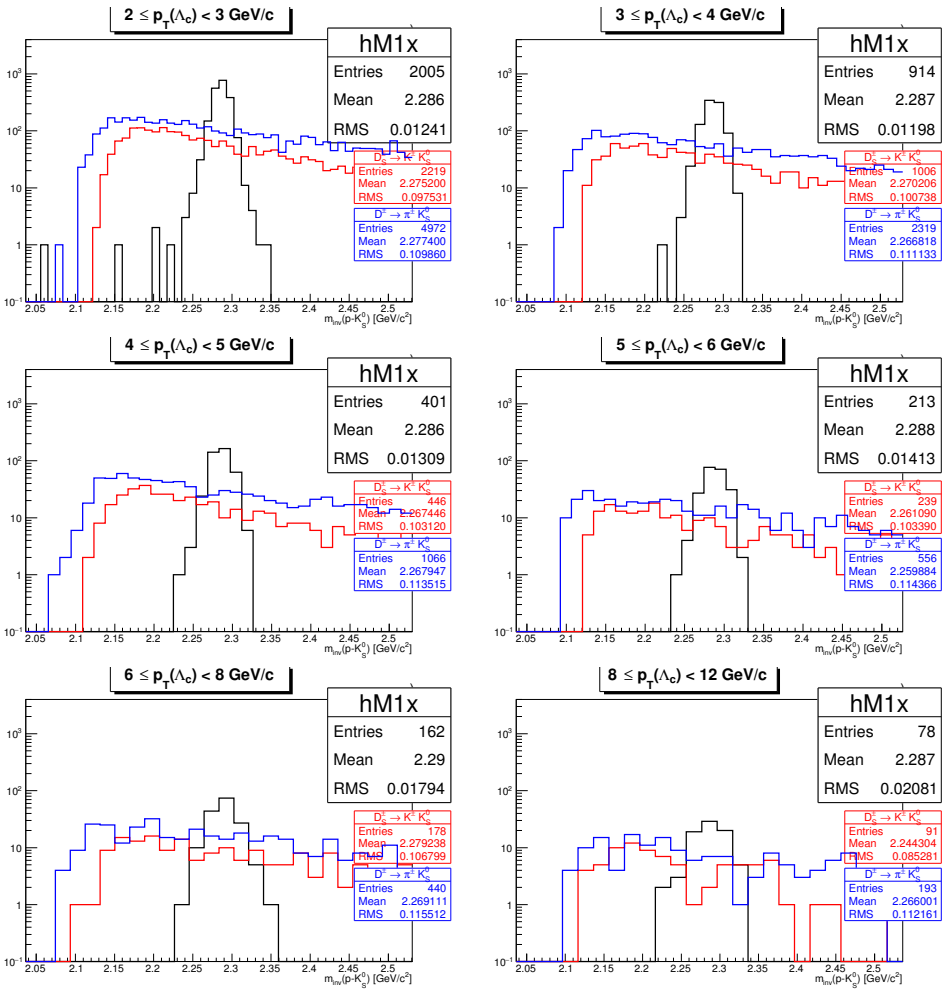

FIGURE A.1: m_{inv}(p,K^0_S) distributions for true reconstructed Λ_c^+ (black), D^+ (blue) and D_s^+ (red) in six different p_T bins.

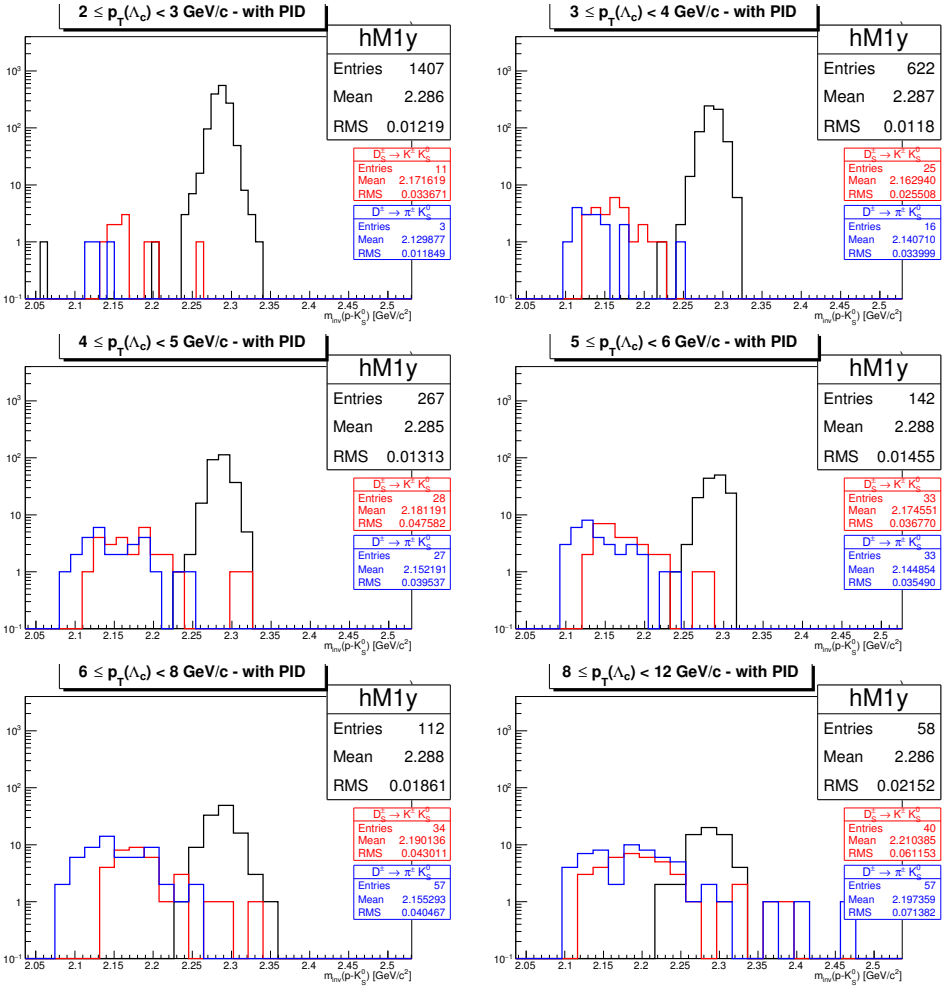

FIGURE A.2: m_{inv}(p,K^0_S) for true reconstructed Λ_c^+ (black), D^+ (blue) and D_s^+ (red) in six different p_T bins. Particle (mis)identification has been taken into account here

Bibliography

[1] S. Yasui et al. "Lambda(c) enhancement from strongly coupled QGP". In: *Indian J. Phys.* 85 (2011), pp. 1043–1046. DOI: 10.1007/s12648-011-0142-3.

[2] B. Abelev et al. *Technical Design Report for the Upgrade of the ALICE Inner Tracking System*. Tech. rep. CERN-LHCC-2013-024. ALICE-TDR-017. 2013. URL: https://cds.cern.ch/record/1625842.

[3] B. Aubert et al. "Measurements of Λ_c^+ branching fractions of Cabibbo-suppressed decay modes involving Λ and Σ^0". In: *Phys. Rev. D* 75 (5 2007), p. 052002. DOI: 10.1103/PhysRevD.75.052002. URL: http://link.aps.org/doi/10.1103/PhysRevD.75.052002.

[4] P. Avery et al. "Observation of Lambda(c)+ decays to Lambda pi+ pi0, Sigma0 pi+, Sigma0 pi+ pi0, and Sigma0 pi- pi+ pi+". In: *Phys. Lett.* B325 (1994), pp. 257–262. DOI: 10.1016/0370-2693(94)90100-7.

[5] H. Albrecht et al. "A Measurement of asymmetry in the decay lambda(c)+ —> lambda pi+". In: *Phys. Lett.* B274 (1992), pp. 239–245. DOI: 10.1016/0370-2693(92)90529-D.

[6] H. Abramowicz et al. "Measurement of D^+ and Λ_c^+ production in deep inelastic scattering at HERA". In: *JHEP* 11 (2010), p. 009. DOI: 10.1007/JHEP11(2010)009. arXiv: 1007.1945 [hep-ex].

[7] G. Anzivino et al. "Intrinsic charm in pp and γp interactions". In: *Il Nuovo Cimento A (1965-1970)* 107.6 (1994), pp. 955–988. ISSN: 1826-9869. DOI: 10.1007/BF02731107. URL: http://dx.doi.org/10.1007/BF02731107.

[8] D. Acosta et al. "Measurement of Prompt Charm Meson Production Cross Sections in $p\bar{p}$ Collisions at $\sqrt{s} = 1.96$ TeV". In: *Phys. Rev. Lett.* 91 (24 2003), p. 241804. DOI: 10.1103/PhysRevLett.91.241804. URL: http://link.aps.org/doi/10.1103/PhysRevLett.91.241804.

[9] D. Acosta et al. "Measurement of Prompt Charm Meson Production Cross Sections in $p\bar{p}$ Collisions at $\sqrt{s} = 1.96$ TeV". In: *Phys. Rev. Lett.* 91 (24 2003), p. 241804. DOI: 10.1103/PhysRevLett.91.241804. URL: http://link.aps.org/doi/10.1103/PhysRevLett.91.241804.

[10] J. M. Link et al. "Search for $\Lambda_c^+ \to pK^+\pi^-$ and $D_s^+ \to K^+K^+\pi^-$ Using Genetic Programming Event Selection". In: *Phys. Lett.* B624 (2005), pp. 166–172. eprint: hep-ex/0507103.

[11] R Aaij et al. "Prompt charm production in pp collisions at $\sqrt{(}s)$=7 TeV". In: *Nucl. Phys.* B871 (2013), pp. 1–20. DOI: 10.1016/j.nuclphysb.2013.02.010. arXiv: 1302.2864 [hep-ex].

[12] Michele Arneodo. "Nuclear effects in structure functions". In: *Physics Reports* 240.5 (1994), pp. 301 –393. ISSN: 0370-1573. DOI: http://dx.doi.org/10.1016/0370-1573(94)90048-5. URL: http://www.sciencedirect.com/science/article/pii/0370157394900485.

[13] Simona Malace et al. "The Challenge of the EMC Effect: existing data and future directions". In: *Int. J. Mod. Phys.* E23.08 (2014), p. 1430013. DOI: 10.1142/S0218301314300136. arXiv: 1405.1270 [nucl-ex].

[14] Francois Gelis et al. "The Color Glass Condensate". In: *Ann. Rev. Nucl. Part. Sci.* 60 (2010), pp. 463–489. DOI: 10.1146/annurev.nucl.010909.083629. arXiv: 1002.0333 [hep-ph].

[15] Ivan Vitev. "Non-Abelian energy loss in cold nuclear matter". In: *Phys. Rev. C* 75 (6 2007), p. 064906. DOI: 10.1103/PhysRevC.75.064906. URL: http://link.aps.org/doi/10.1103/PhysRevC.75.064906.

[16] M. Lev and B. Petersson. "Nuclear effects at large transverse momentum in a QCD parton model". In: *Zeitschrift für Physik C Particles and Fields* 21.1 (1983), pp. 155–161. ISSN: 1431-5858. DOI: 10.1007/BF01648792. URL: http://dx.doi.org/10.1007/BF01648792.

[17] Betty Abelev et al. "Long-range angular correlations on the near and away side in p-Pb collisions at $\sqrt{s_{NN}} = 5.02$ TeV". In: *Phys. Lett.* B719 (2013), pp. 29–41. DOI: 10.1016/j.physletb.2013.01.012. arXiv: 1212.2001 [nucl-ex].

[18] Betty Bezverkhny Abelev et al. "Long-range angular correlations of π, K and p in p-Pb collisions at $\sqrt{s_{\rm NN}}$ = 5.02 TeV". In: *Phys. Lett.* B726 (2013), pp. 164–177. DOI: 10.1016/j.physletb.2013.08.024. arXiv: 1307.3237 [nucl-ex].

[19] Betty Bezverkhny Abelev et al. "Multiplicity Dependence of Pion, Kaon, Proton and Lambda Production in p-Pb Collisions at $\sqrt{s_{NN}}$ = 5.02 TeV". In: *Phys. Lett.* B728 (2014), pp. 25–38. DOI: 10.1016/j.physletb.2013.11.020. arXiv: 1307.6796 [nucl-ex].

[20] Betty Bezverkhny Abelev et al. "Suppression of ψ(2S) production in p-Pb collisions at $\sqrt{s_{\rm NN}}$ = 5.02 TeV". In: *JHEP* 12 (2014), p. 073. DOI: 10.1007/JHEP12(2014)073. arXiv: 1405.3796 [nucl-ex].

[21] R. P. Feynman. *QED: The Strange Theory of Light and Matter*. Princeton University Press, 1985.

[22] D. J. Griffiths. *Introduction to Quantum Mechanics*. New York: John Wiley & Sons, 1995.

[23] K. Yagi, T. Hatsuda, and Y. Miyake. *Quark-Gluon Plasma*. Cambridge University Press., 2005.

[24] J. Beringer et al. "Review of Particle Physics (RPP)". In: *Phys. Rev.* D86 (2012), p. 010001. DOI: 10.1103/PhysRevD.86.010001.

[25] M. Knecht. "Une introduction à la symétrie chirale". Lecture. Maubuisson, (France), du 7-12 septembre 1998 : 17ème session, Sept. 1998. URL: https://cel.archives-ouvertes.fr/cel-00652926.

[26] Edward V. Shuryak. "Quark-Gluon Plasma and Hadronic Production of Leptons, Photons and Psions". In: *Phys. Lett.* B78 (1978). [Yad. Fiz.28,796(1978)], p. 150. DOI: 10.1016/0370-2693(78)90370-2.

[27] R. Hagedorn. "Statistical thermodynamics of strong interactions at high-energies". In: *Nuovo Cim. Suppl.* 3 (1965), pp. 147–186.

[28] H. David Politzer. "Reliable Perturbative Results for Strong Interactions?" In: *Phys. Rev. Lett.* 30 (26 1973), pp. 1346–1349. DOI: 10.1103/PhysRevLett.30.1346. URL: http://link.aps.org/doi/10.1103/PhysRevLett.30.1346.

[29] David J. Gross and Frank Wilczek. "Ultraviolet Behavior of Non-Abelian Gauge Theories". In: *Phys. Rev. Lett.* 30 (26 1973), pp. 1343–1346. DOI: 10.1103/PhysRevLett.30.1343. URL: http://link.aps.org/doi/10.1103/PhysRevLett.30.1343.

[30] N. Cabibbo and G. Parisi. "Exponential hadronic spectrum and quark liberation". In: *Physics Letters, Section B: Nuclear, Elementary Particle and High-Energy Physics* 59.1 (Oct. 1975), pp. 67–69. ISSN: 0370-2693. DOI: 10.1016/0370-2693(75)90158-6.

[31] Olaf Kaczmarek and Felix Zantow. "Static quark-antiquark interactions in zero and finite temperature QCD: I. Heavy quark free energies, running coupling, and quarkonium binding". In: *Phys. Rev. D* 71 (11 2005), p. 114510. DOI: 10.1103/PhysRevD.71.114510. URL: https://link.aps.org/doi/10.1103/PhysRevD.71.114510.

[32] Kenneth G. Wilson. "Confinement of quarks". In: *Phys. Rev. D* 10 (8 1974), pp. 2445–2459. DOI: 10.1103/PhysRevD.10.2445. URL: https://link.aps.org/doi/10.1103/PhysRevD.10.2445.

[33] F. Karsch. "Lattice QCD at high temperature and density". In: *Lect. Notes Phys.* 583 (2002), pp. 209–249. DOI: 10.1007/3-540-45792-5_6. arXiv: hep-lat/0106019 [hep-lat].

[34] Robert D. Pisarski and Frank Wilczek. "Remarks on the chiral phase transition in chromodynamics". In: *Phys. Rev. D* 29 (2 1984), pp. 338–341. DOI: 10.1103/PhysRevD.29.338. URL: https://link.aps.org/doi/10.1103/PhysRevD.29.338.

[35] Owe Philipsen. "Lattice QCD at finite temperature and density". In: *Eur. Phys. J. ST* 152 (2007), pp. 29–60. DOI: 10.1140/epjst/e2007-00376-3. arXiv: 0708.1293 [hep-lat].

[36] A. Monnai. *Relativistic Dissipative Hydrodynamic Description of the Quark-Gluon Plasma*. New York: RIKEN BNL Research Center, 2014.

[37] J. Letessier and J. Rafelski. *Hadrons and Quark–Gluon Plasma (Vol.18)*. Cambridge University Press, 2002.

[38] D. Keane et al. "Results from the EOS Time Projection chamber at the Bevalac". In: *Hot and Dense Nuclear Matter*. Ed. by Walter Greiner, Horst Stöcker, and André Gallmann. Boston, MA: Springer US, 1994, pp. 559–568. ISBN: 978-1-4615-2516-5. DOI: 10.1007/978-1-4615-2516-5_49. URL: http://dx.doi.org/10.1007/978-1-4615-2516-5_49.

[39] K. Adcox et al. "Formation of dense partonic matter in relativistic nucleus–nucleus collisions at RHIC: Experimental evaluation by the {PHENIX} Collaboration". In: *Nuclear Physics A* 757.1–2 (2005). First Three Years of Operation of {RHIC}, pp. 184 –283. ISSN: 0375-9474. DOI: http://dx.doi.org/10.1016/j.nuclphysa.2005.03.086. URL: http://www.sciencedirect.com/science/article/pii/S0375947405005300.

[40] J. Adams et al. "Experimental and theoretical challenges in the search for the quark–gluon plasma: The {STAR} Collaboration's critical assessment of the evidence from {RHIC} collisions". In: *Nuclear Physics A* 757.1–2 (2005). First Three Years of Operation of {RHIC}, pp. 102 –183. ISSN: 0375-9474. DOI: http://dx.doi.org/10.1016/j.nuclphysa.2005.03.085. URL: http://www.sciencedirect.com/science/article/pii/S0375947405005294.

[41] B.B. Back et al. "The {PHOBOS} perspective on discoveries at {RHIC}". In: *Nuclear Physics A* 757.1–2 (2005). First Three Years of Operation of {RHIC}, pp. 28 –101. ISSN: 0375-9474. DOI: http://dx.doi.org/10.1016/j.nuclphysa.2005.03.084. URL: http://www.sciencedirect.com/science/article/pii/S0375947405005282.

[42] "Editorial Board". In: *Nuclear Physics A* 757.1–2 (2005). First Three Years of Operation of {RHIC}, CO2 –. ISSN: 0375-9474. DOI: http://dx.doi.org/10.1016/S0375-9474(05)00916-4. URL: http://www.sciencedirect.com/science/article/pii/S0375947405009164.

[43] S. S. Adler et al. "Elliptic flow of identified hadrons in Au+Au collisions at s(NN)**(1/2) = 200-GeV". In: *Phys. Rev. Lett.* 91 (2003), p. 182301. DOI: 10.1103/PhysRevLett.91.182301. arXiv: nucl-ex/0305013 [nucl-ex].

[44] J. Adams et al. "Particle-Type Dependence of Azimuthal Anisotropy and Nuclear Modification of Particle Production in $\mathrm{Au} + \mathrm{Au}$ Collisions at $\sqrt{s_{NN}} = 200\ \mathrm{GeV}$". In: *Phys. Rev. Lett.* 92 (5 2004), p. 052302. DOI: 10.1103/PhysRevLett.92.052302. URL: http://link.aps.org/doi/10.1103/PhysRevLett.92.052302.

[45] S. Y. Lo. *Geometrical Pictures in Hadronic Collisions*. Singapore: World Scientific, 1987.

[46] G. X. Peng, X. J. Wen, and Y. D. Chen. "New solutions for the color-flavor locked strangelets". In: *Phys. Lett.* B633 (2006), pp. 314–318. DOI: 10.1016/j.physletb.2005.11.081. arXiv: hep-ph/0512112 [hep-ph].

[47] Nancy M. Mar et al. "Improved search for elementary particles with fractional electric charge". In: *Phys. Rev. D* 53 (11 1996), pp. 6017–6032. DOI: 10.1103/PhysRevD.53.6017. URL: http://link.aps.org/doi/10.1103/PhysRevD.53.6017.

[48] Sergei G. Matinyan and G. K. Savvidy. "Vacuum Polarization Induced by the Intense Gauge Field". In: *Nucl. Phys.* B134 (1978), pp. 539–545. DOI: 10.1016/0550-3213(78)90463-7.

[49] S. Sarkar, H. Satz, and B. Sinha. *The Physics of the Quark-Gluon Plasma: Introductory Lectures*. Lect. Notes Phys. 785 (Springer, Berlin Heidelberg 2010), 2010.

[50] A. Adare et al. "Enhanced Production of Direct Photons in $\mathrm{Au}+\mathrm{Au}$ Collisions at $\sqrt{s_{NN}} = 200\ \mathrm{GeV}$ and Implications for the Initial Temperature". In: *Phys. Rev. Lett.* 104 (13 2010), p. 132301. DOI: 10.1103/PhysRevLett.104.132301. URL: http://link.aps.org/doi/10.1103/PhysRevLett.104.132301.

[51] Martin Wilde. "Measurement of Direct Photons in pp and Pb-Pb Collisions with ALICE". In: *Nucl. Phys.* A904-905 (2013), pp. 573c–576c. DOI: 10.1016/j.nuclphysa.2013.02.079. arXiv: 1210.5958 [hep-ex].

[52] A. Adare et al. "Observation of Direct-Photon Collective Flow in $\mathrm{Au} + \mathrm{Au}$ Collisions at $\sqrt{s_{NN}} = 200$ GeV". In: *Phys. Rev. Lett.* 109 (12 2012), p. 122302. DOI: 10.1103/PhysRevLett.109.122302. URL: http://link.aps.org/doi/10.1103/PhysRevLett.109.122302.

[53] S. Chatrchyan et al. "Study of Z Boson Production in PbPb Collisions at $\sqrt{s_{NN}} = 2.76$ TeV". In: *Phys. Rev. Lett.* 106 (21 2011), p. 212301. DOI: 10.1103/PhysRevLett.106.212301. URL: http://link.aps.org/doi/10.1103/PhysRevLett.106.212301.

[54] Serguei Chatrchyan et al. "Study of W boson production in PbPb and pp collisions at $\sqrt{s_{NN}} = 2.76$ TeV". In: *Phys. Lett.* B715 (2012), pp. 66–87. DOI: 10.1016/j.physletb.2012.07.025. arXiv: 1205.6334 [nucl-ex].

[55] J. Adams and others. "Evidence from $d + \mathrm{Au}$ Measurements for Final-State Suppression of High-p_T Hadrons in $\mathrm{Au} + \mathrm{Au}$ Collisions at RHIC". In: *Phys. Rev. Lett.* 91 (7 2003), p. 072304. DOI: 10.1103/PhysRevLett.91.072304. URL: http://link.aps.org/doi/10.1103/PhysRevLett.91.072304.

[56] C. Adler et al. "Disappearance of Back-To-Back High-p_T Hadron Correlations in Central $\mathrm{Au} + \mathrm{Au}$ Collisions at $\sqrt{s_{NN}} = 200$ GeV". In: *Phys. Rev. Lett.* 90 (8 2003), p. 082302. DOI: 10.1103/PhysRevLett.90.082302. URL: http://link.aps.org/doi/10.1103/PhysRevLett.90.082302.

[57] T. Matsui and H. Satz. "J/ψ Suppression by Quark-Gluon Plasma Formation". In: *Phys. Lett.* B178 (1986), pp. 416–422. DOI: 10.1016/0370-2693(86)91404-8.

[58] S. Chatrchyan et al. "Observation of Sequential Υ Suppression in PbPb Collisions". In: *Phys. Rev. Lett.* 109 (22 2012), p. 222301. DOI: 10.1103/PhysRevLett.109.222301. URL: http://link.aps.org/doi/10.1103/PhysRevLett.109.222301.

[59] Takao Sakaguchi. "PHENIX Highlights". In: *Nucl. Phys.* A904-905 (2013), pp. 11c–18c. DOI: 10.1016/j.nuclphysa.2013.01.039. arXiv: 1211.0324 [nucl-ex].

[60] A. Andronic et al. "Heavy-flavour and quarkonium production in the LHC era: from proton–proton to heavy-ion collisions". In: *Eur. Phys. J.* C76.3 (2016), p. 107. DOI: 10.1140/epjc/s10052-015-3819-5. arXiv: 1506.03981 [nucl-ex].

[61] Partha Bagchi and Ajit M. Srivastava. "Quarkonia disintegration due to time dependence of the $q\bar{q}$ potential in relativistic heavy-ion collisions". In: *Mod. Phys. Lett.* A30.32 (2015), p. 1550162. DOI: 10.1142/S021773231550162X. arXiv: 1411.5596 [hep-ph].

[62] R. L. Thews. "Quarkonium production via recombination". In: *Nucl. Phys.* A783 (2007), pp. 301–308. DOI: 10.1016/j.nuclphysa.2006.11.084. arXiv: hep-ph/0609121 [hep-ph].

[63] K. J. Eskola, H. Paukkunen, and C. A. Salgado. "EPS09: A New Generation of NLO and LO Nuclear Parton Distribution Functions". In: *JHEP* 04 (2009), p. 065. DOI: 10.1088/1126-6708/2009/04/065. arXiv: 0902.4154 [hep-ph].

[64] D. de Florian and R. Sassot. "Nuclear parton distributions at next to leading order". In: *Phys. Rev. D* 69 (7 2004), p. 074028. DOI: 10.1103/PhysRevD.69.074028. URL: http://link.aps.org/doi/10.1103/PhysRevD.69.074028.

[65] Ivan Vitev. "Non-Abelian energy loss in cold nuclear matter". In: *Phys. Rev. C* 75 (6 2007), p. 064906. DOI: 10.1103/PhysRevC.75.064906. URL: http://link.aps.org/doi/10.1103/PhysRevC.75.064906.

[66] A. Adare et al. "Measurement of High-p_T Single Electrons from Heavy-Flavor Decays in $p+p$ Collisions at $\sqrt{s} = 200$ GeV". In: *Phys. Rev. Lett.* 97 (25 2006), p. 252002. DOI: 10.1103/PhysRevLett.97.252002. URL: http://link.aps.org/doi/10.1103/PhysRevLett.97.252002.

[67] H. Agakishiev et al. "High p_T non-photonic electron production in $p+p$ collisions at $\sqrt{s} = 200$ GeV". In: *Phys. Rev.* D83 (2011), p. 052006. DOI: 10.1103/PhysRevD.83.052006. arXiv: 1102.2611 [nucl-ex].

[68] Georges Aad et al. "Measurements of the electron and muon inclusive cross-sections in proton-proton collisions at $\sqrt{s} = 7$ TeV with the ATLAS detector". In: *Phys. Lett.* B707 (2012), pp. 438–458. DOI: 10.1016/j.physletb.2011.12.054. arXiv: 1109.0525 [hep-ex].

[69] Betty Abelev et al. "Measurement of electrons from semileptonic heavy-flavour hadron decays in pp collisions at $\sqrt{s}$ = 7 TeV". In: *Phys. Rev.* D86 (2012), p. 112007. DOI: 10.1103/PhysRevD.86.112007. arXiv: 1205.5423 [hep-ex].

[70] Jaroslav Adam et al. "Measurement of electrons from heavy-flavour hadron decays in p-Pb collisions at $\sqrt{s_{\rm NN}} = 5.02$ TeV". In: *Phys. Lett.* B754 (2016), pp. 81–93. DOI: 10.1016/j.physletb.2015.12.067. arXiv: 1509.07491 [nucl-ex].

[71] Matteo Cacciari et al. "Theoretical predictions for charm and bottom production at the LHC". In: *JHEP* 10 (2012), p. 137. DOI: 10.1007/JHEP10(2012)137. arXiv: 1205.6344 [hep-ph].

[72] Georges Aad et al. "Measurement of event shapes at large momentum transfer with the ATLAS detector in pp collisions at $\sqrt{s} = 7$ TeV". In: *Eur. Phys. J.* C72 (2012), p. 2211. DOI: 10.1140/epjc/s10052-012-2211-y. arXiv: 1206.2135 [hep-ex].

[73] Bernd A. Kniehl et al. "Inclusive charmed-meson production at the CERN LHC". In: *The European Physical Journal C* 72.7 (2012), p. 2082. ISSN: 1434-6052. DOI: 10.1140/epjc/s10052-012-2082-2. URL: http://dx.doi.org/10.1140/epjc/s10052-012-2082-2.

[74] L. Adamczyk et al. "Measurements of D^0 and D^* production in p+p collisions at $\sqrt{s}$=200 GeV". In: *Phys. Rev. D* 86 (7 2012), p. 072013. DOI: 10.1103/PhysRevD.86.072013. URL: http://link.aps.org/doi/10.1103/PhysRevD.86.072013.

[75] Betty Abelev et al. "D_s^+ meson production at central rapidity in proton–proton collisions at $\sqrt{s} = 7$ TeV". In: *Phys. Lett.* B718 (2012), pp. 279–294. DOI: 10.1016/j.physletb.2012.10.049. arXiv: 1208.1948 [hep-ex].

[76] Betty Abelev et al. "Measurement of charm production at central rapidity in proton-proton collisions at $\sqrt{s} = 2.76$ TeV". In: *JHEP* 07 (2012), p. 191. DOI: 10.1007/JHEP07(2012)191. arXiv: 1205.4007 [hep-ex].

[77] J. Adam and others. "D-meson production in p-Pb collisions at $\sqrt{s_{NN}} = 5.02$ TeV and in pp collisions at $\sqrt{s} = 7$ TeV". In: *Phys. Rev. C* 94 (5 2016), p. 054908. DOI: 10.1103/PhysRevC.94.054908. URL: http://link.aps.org/doi/10.1103/PhysRevC.94.054908.

[78] Michael Andreas Winn. "Inclusive J/ψ production at mid-rapidity in p-Pb collisions at $\sqrt{^sNN}$=5.02 TeV". PhD thesis. Heidelberg U., 2016-02-15. URL: https://inspirehep.net/record/1503875/files/CERN-THESIS-2016-031.pdf.

[79] J. Adam et al. "Measurement of D-meson production versus multiplicity in p-Pb collisions at $\sqrt{s_{NN}} = 5.02$ TeV". In: *JHEP* 08 (2016), p. 078. DOI: 10.1007/JHEP08(2016)078. arXiv: 1602.07240 [nucl-ex].

[80] E. G. Ferreiro and C. Pajares. "High multiplicity pp events and J/ψ production at energies available at the CERN Large Hadron Collider". In: *Phys. Rev. C* 86 (3 2012), p. 034903. DOI: 10.1103/PhysRevC.86.034903. URL: http://link.aps.org/doi/10.1103/PhysRevC.86.034903.

[81] E. G. Ferreiro and C. Pajares. "Open charm production in high multiplicity proton-proton events at the LHC". In: (2015). arXiv: 1501.03381 [hep-ph].

[82] K. Werner et al. "Analyzing radial flow features in p-Pb and p-p collisions at several TeV by studying identified-particle production with the event generator EPOS3". In: *Phys. Rev. C* 89 (6 2014), p. 064903. DOI: 10.1103/PhysRevC.89.064903. URL: http://link.aps.org/doi/10.1103/PhysRevC.89.064903.

[83] Torbjorn Sjostrand, Stephen Mrenna, and Peter Z. Skands. "A Brief Introduction to PYTHIA 8.1". In: *Comput. Phys. Commun.* 178 (2008), pp. 852–867. DOI: 10.1016/j.cpc.2008.01.036. arXiv: 0710.3820 [hep-ph].

[84] T. Aaltonen et al. "Measurement of the Λ_b^0 Lifetime in $\Lambda_b^0 \to \Lambda_c^+\pi^-$ Decays in $p\bar{p}$ Collisions at $\sqrt{s} = 1.96$ TeV". In: *Phys. Rev. Lett.* 104 (10 2010), p. 102002. DOI: 10.1103/PhysRevLett.104.102002. URL: http://link.aps.org/doi/10.1103/PhysRevLett.104.102002.

[85] Timo Antero Aaltonen et al. "Evidence for a bottom baryon resonance Λ_b^{*0} in CDF data". In: *Phys. Rev.* D88.7 (2013), p. 071101. DOI: 10.1103/PhysRevD.88.071101. arXiv: 1308.1760 [hep-ex].

[86] B. A. Kniehl et al. "Inclusive D*+- production in p anti-p collisions with massive charm quarks". In: *Phys. Rev.* D71 (2005), p. 014018. DOI: 10.1103/PhysRevD.71.014018. arXiv: hep-ph/0410289 [hep-ph].

[87] B. A. Kniehl et al. "Collinear subtractions in hadroproduction of heavy quarks". In: *Eur. Phys. J.* C41 (2005), pp. 199–212. DOI: 10.1140/epjc/s2005-02200-7. arXiv: hep-ph/0502194 [hep-ph].

[88] Roel Aaij et al. "Measurement of the $\eta_c(1S)$ production cross-section in proton-proton collisions via the decay $\eta_c(1S) \to p\bar{p}$". In: *Eur. Phys. J.* C75.7 (2015), p. 311. DOI: 10.1140/epjc/s10052-015-3502-x. arXiv: 1409.3612 [hep-ex].

[89] Georges Aad et al. "Measurement of the production cross-section of $\psi(2S) \to J/\psi(\to \mu^+\mu^-)\pi^+\pi^-$ in pp collisions at $\sqrt{s}$ = 7 TeV at ATLAS". In: *JHEP* 09 (2014), p. 079. DOI: 10.1007/JHEP09(2014)079. arXiv: 1407.5532 [hep-ex].

[90] Georges Aad et al. "Measurement of χ_{c1} and χ_{c2} production with $\sqrt{s}$ = 7 TeV pp collisions at ATLAS". In: *JHEP* 07 (2014), p. 154. DOI: 10.1007/JHEP07(2014)154. arXiv: 1404.7035 [hep-ex].

[91] Serguei Chatrchyan et al. "Inclusive b-jet production in pp collisions at $\sqrt{s} = 7$ TeV". In: *JHEP* 04 (2012), p. 084. DOI: 10.1007/JHEP04(2012)084. arXiv: 1202.4617 [hep-ex].

[92] Konrad Tywoniuk. "Is there jet quenching in pPb?" In: *Nuclear Physics A* 926 (2014). {IS2013International} Conference on the Initial Stages in High-Energy Nuclear CollisionsInternational Conference on the Initial Stages in High-Energy Nuclear Collisions, pp. 85 –91. ISSN: 0375-9474. DOI: http://dx.doi.org/10.1016/j.nuclphysa.2014.04.023. URL: http://www.sciencedirect.com/science/article/pii/S0375947414001055.

[93] Michael L. Miller et al. "Glauber modeling in high energy nuclear collisions". In: *Ann. Rev. Nucl. Part. Sci.* 57 (2007), pp. 205–243. DOI: 10.1146/annurev.nucl.57.090506.123020. arXiv: nucl-ex/0701025 [nucl-ex].

[94] A. Adare et al. "Cold-Nuclear-Matter Effects on Heavy-Quark Production at Forward and Backward Rapidity in d+Au Collisions at $\sqrt{s_{NN}} = 200$GeV". In: *Phys. Rev. Lett.* 112.25 (2014), p. 252301. DOI: 10.1103/PhysRevLett.112.252301. arXiv: 1310.1005 [nucl-ex].

[95] Shuang Li. "Measurements of the heavy-flavour nuclear modification factor in p–Pb collisions at $\sqrt{s_{\rm NN}}$ = 5.02 TeV with ALICE at the LHC". In: *Nucl. Phys.* A931 (2014), pp. 546–551. DOI: 10.1016/j.nuclphysa.2014.08.067. arXiv: 1408.1915 [hep-ex].

[96] Betty Bezverkhny Abelev et al. "Measurement of prompt D-meson production in $p-Pb$ collisions at $\sqrt{s_{NN}}$ = 5.02 TeV". In: *Phys. Rev. Lett.* 113.23 (2014), p. 232301. DOI: 10.1103/PhysRevLett.113.232301. arXiv: 1405.3452 [nucl-ex].

[97] Javier L. Albacete et al. "CGC predictions for p + Pb collisions at the LHC". In: *Nucl. Phys.* A897 (2013), pp. 1–27. DOI: 10.1016/j.nuclphysa.2012.09.012. arXiv: 1209.2001 [hep-ph].

[98] Michelangelo L. Mangano, Paolo Nason, and Giovanni Ridolfi. "Heavy quark correlations in hadron collisions at next-to-leading order". In: *Nucl. Phys.* B373 (1992), pp. 295–345. DOI: 10.1016/0550-3213(92)90435-E.

[99] Rishi Sharma, Ivan Vitev, and Ben-Wei Zhang. "Light-cone wave function approach to open heavy flavor dynamics in QCD matter". In: *Phys. Rev. C* 80 (5 2009), p. 054902. DOI: 10.1103/PhysRevC.80.054902. URL: http://link.aps.org/doi/10.1103/PhysRevC.80.054902.

[100] Andrea Beraudo et al. "Heavy-flavour production in high-energy d-Au and p-Pb collisions". In: *Journal of High Energy Physics* 2016.3 (2016), p. 123. ISSN: 1029-8479. DOI: 10.1007/JHEP03(2016)123. URL: http://dx.doi.org/10.1007/JHEP03(2016)123.

[101] R Aaij et al. "Study of J/ψ production and cold nuclear matter effects in pPb collisions at $\sqrt{s_{NN}} = 5$ TeV". In: *JHEP* 02 (2014), p. 072. DOI: 10.1007/JHEP02(2014)072. arXiv: 1308.6729 [nucl-ex].

[102] CMS Collaboration. "Measurements of the B^+, B^0 and $B_{\rm s}^0$ production cross sections in pPb collisions at $\sqrt{s_{\rm NN}}$ = 5.02 TeV". In: (2014).

[103] J. L. Albacete et al. "Predictions for p+Pb Collisions at $\sqrt{s_{NN}} = 5.02$ TeV TeV". In: *Int. J. Mod. Phys.* E22 (2013), p. 1330007. DOI: 10.1142/S0218301313300075. arXiv: 1301.3395 [hep-ph].

[104] B. Abelev et al. "Transverse Momentum and Centrality Dependence of High-p_T Nonphotonic Electron Suppression in Au + Au Collisions at $\sqrt{s_{\rm NN}} = 200$ GeV". In: *Phys. Rev. Lett.* 98 (19 2007), p. 192301. DOI: 10.1103/PhysRevLett.98.192301. URL: http://link.aps.org/doi/10.1103/PhysRevLett.98.192301.

[105] A. Adare et al. "Energy Loss and Flow of Heavy Quarks in Au+Au Collisions at s(NN)**(1/2) = 200-GeV". In: *Phys. Rev. Lett.* 98 (2007), p. 172301. DOI: 10.1103/PhysRevLett.98.172301. arXiv: nucl-ex/0611018 [nucl-ex].

[106] S. S. Adler et al. "Nuclear modification of electron spectra and implications for heavy quark energy loss in Au+Au collisions at s(NN)**(1/2) - 200-GeV". In: *Phys. Rev. Lett.* 96 (2006), p. 032301. DOI: 10.1103/PhysRevLett.96.032301. arXiv: nucl-ex/0510047 [nucl-ex].

[107] A. Adare et al. "Heavy Quark Production in $p+p$ and Energy Loss and Flow of Heavy Quarks in Au+Au Collisions at $\sqrt{s_{NN}} = 200$ GeV". In: *Phys. Rev.* C84 (2011), p. 044905. DOI: 10.1103/PhysRevC.84.044905. arXiv: 1005.1627 [nucl-ex].

[108] A. Adare et al. "Cold-nuclear-matter effects on heavy-quark production in d+Au collisions at $\sqrt{s_{NN}} = 200$ GeV". In: *Phys. Rev. Lett.* 109.24 (2012), p. 242301. DOI: 10.1103/PhysRevLett.109.242301. arXiv: 1208.1293 [nucl-ex].

[109] A. Adare et al. "System-size dependence of open-heavy-flavor production in nucleus-nucleus collisions at $\sqrt{s_{NN}}$=200 GeV". In: *Phys. Rev.* C90.3 (2014), p. 034903. DOI: 10.1103/PhysRevC.90.034903. arXiv: 1310.8286 [nucl-ex].

[110] Betty Abelev et al. "Production of muons from heavy flavour decays at forward rapidity in pp and Pb-Pb collisions at $\sqrt{s_{NN}}$ = 2.76 TeV". In: *Phys. Rev. Lett.* 109 (2012), p. 112301. DOI: 10.1103/PhysRevLett.109.112301. arXiv: 1205.6443 [hep-ex].

[111] Shingo Sakai. "Measurement of RAA and v2 of electrons from heavy-flavour decays in Pb–Pb collisions at sNN=2.76 TeV with ALICE". In: *Nuclear Physics A* 904 (2013), pp. 661c –664c. ISSN: 0375-9474. DOI: http://dx.doi.org/10.1016/j.nuclphysa.2013.02.102. URL: http://www.sciencedirect.com/science/article/pii/S0375947413002285.

[112] "Measurement of the centrality dependence of open heavy flavour production in lead-lead collisions at sqrts = 2.76 TeV with the ATLAS detector". In: (2012).

[113] L. Adamczyk et al. "Observation of D^0 Meson Nuclear Modifications in Au+Au Collisions at $\sqrt{s_{NN}} = 200$GeV". In: *Phys. Rev. Lett.* 113.14 (2014), p. 142301. DOI: 10.1103/PhysRevLett.113.142301. arXiv: 1404.6185 [nucl-ex].

[114] Betty Abelev et al. "Suppression of high transverse momentum D mesons in central Pb-Pb collisions at $\sqrt{s_{NN}} = 2.76$ TeV". In: *JHEP* 09 (2012), p. 112. DOI: 10.1007/JHEP09(2012)112. arXiv: 1203.2160 [nucl-ex].

[115] Alessandro Grelli. "D meson nuclear modification factors in Pb-Pb collisions at $\sqrt{s_{NN}} = 2.76$ TeV with the ALICE detector". In: *Nucl. Phys.* A904-905 (2013), pp. 635c–638c. DOI: 10.1016/j.nuclphysa.2013.02.096. arXiv: 1210.7332 [hep-ex].

[116] Gian Michele Innocenti. "D_s^+ production at central rapidity in Pb Pb collisions at $\sqrt{s_{NN}} = 2.76$ TeV with the ALICE detector". In: *Nucl. Phys.* A904-905 (2013), pp. 433c–436c. DOI: 10.1016/j.nuclphysa.2013.02.042. arXiv: 1210.6388 [nucl-ex].

[117] Min He, Rainer J. Fries, and Ralf Rapp. "Heavy-Quark Diffusion and Hadronization in Quark-Gluon Plasma". In: *Phys. Rev.* C86 (2012), p. 014903. DOI: 10.1103/PhysRevC.86.014903. arXiv: 1106.6006 [nucl-th].

[118] Min He, Rainer J. Fries, and Ralf Rapp. "Heavy Flavor at the Large Hadron Collider in a Strong Coupling Approach". In: *Phys. Lett.* B735 (2014), pp. 445–450. DOI: 10.1016/j.physletb.2014.05.050. arXiv: 1401.3817 [nucl-th].

[119] Andrea Festanti. "Heavy-flavour production and nuclear modification factor in Pb-Pb collisions at $\sqrt{s_{\mathrm{NN}}}$=2.76 TeV with ALICE". In: *Nucl. Phys.* A931 (2014), pp. 514–519. DOI: 10.1016/j.nuclphysa.2014.07.044. arXiv: 1407.6541 [nucl-ex].

[120] Serguei Chatrchyan et al. "Suppression of non-prompt J/ψ, prompt J/ψ, and Y(1S) in PbPb collisions at $\sqrt{s_{NN}} = 2.76$ TeV". In: *JHEP* 05 (2012), p. 063. DOI: 10.1007/JHEP05(2012)063. arXiv: 1201.5069 [nucl-ex].

[121] Jaroslav Adam et al. "Inclusive, prompt and non-prompt J/ψ production at mid-rapidity in Pb-Pb collisions at $\sqrt{s_{\mathrm{NN}}}$ = 2.76 TeV". In: *JHEP* 07 (2015), p. 051. DOI: 10.1007/JHEP07(2015)051. arXiv: 1504.07151 [nucl-ex].

[122] Jaroslav Adam et al. "Centrality dependence of high-p$_T$ D meson suppression in Pb-Pb collisions at $\sqrt{s_{\mathrm{NN}}} = 2.76$ TeV". In: *JHEP* 11 (2015), p. 205. DOI: 10.1007/JHEP11(2015)205. arXiv: 1506.06604 [nucl-ex].

[123] Vardan Khachatryan et al. "Suppression and azimuthal anisotropy of prompt and nonprompt J/ψ production in PbPb collisions at $\sqrt{s_{NN}}$ = 2.76 TeV". In: *Submitted to: Eur. Phys. J. C* (2016). arXiv: 1610.00613 [nucl-ex].

[124] Magdalena Djordjevic and Marko Djordjevic. "LHC jet suppression of light and heavy flavor observables". In: *Phys. Lett.* B734 (2014), pp. 286–289. DOI: 10.1016/j.physletb.2014.05.053. arXiv: 1307.4098 [hep-ph].

[125] Jaroslav Adam et al. "Transverse momentum dependence of D-meson production in Pb-Pb collisions at $\sqrt{\mathrm{s_{NN}}} = 2.76$ TeV". In: *JHEP* 03 (2016), p. 081. DOI: 10.1007/JHEP03(2016)081. arXiv: 1509.06888 [nucl-ex].

[126] Arthur M. Poskanzer and S. A. Voloshin. "Methods for analyzing anisotropic flow in relativistic nuclear collisions". In: *Phys. Rev.* C58 (1998), pp. 1671–1678. DOI: 10.1103/PhysRevC.58.1671. arXiv: nucl-ex/9805001 [nucl-ex].

[127] C. Adler et al. "Elliptic flow from two and four particle correlations in Au+Au collisions at s(NN)**(1/2) = 130-GeV". In: *Phys. Rev.* C66 (2002), p. 034904. DOI: 10.1103/PhysRevC.66.034904. arXiv: nucl-ex/0206001 [nucl-ex].

[128] Ante Bilandzic, Raimond Snellings, and Sergei Voloshin. "Flow analysis with cumulants: Direct calculations". In: *Phys. Rev.* C83 (2011), p. 044913. DOI: 10.1103/PhysRevC.83.044913. arXiv: 1010.0233 [nucl-ex].

[129] A. Adare et al. "Heavy-quark production in p + p and energy loss and flow of heavy quarks in Au + Au collisions at $\sqrt{s_{NN}} = 200$ GeV". In: *Phys. Rev. C* 84 (4 2011), p. 044905. DOI: 10.1103/PhysRevC.84.044905. URL: http://link.aps.org/doi/10.1103/PhysRevC.84.044905.

[130] L. Adamczyk et al. "Elliptic flow of non-photonic electrons in Au+Au collisions at $\sqrt{s_{\mathrm{NN}}} = 200$, 62.4 and 39 GeV". In: (2014). arXiv: 1405.6348 [hep-ex].

[131] B. Abelev et al. "D meson elliptic flow in non-central Pb-Pb collisions at $\sqrt{s_{\mathrm{NN}}}$ = 2.76TeV". In: *Phys. Rev. Lett.* 111 (2013), p. 102301. DOI: 10.1103/PhysRevLett.111.102301. arXiv: 1305.2707 [nucl-ex].

[132] B. Abelev et al. "D Meson Elliptic Flow in Noncentral Pb-Pb Collisions at $\sqrt{s_{NN}} = 2.76$ TeV". In: *Phys. Rev. Lett.* 111 (10 2013), p. 102301. DOI: 10.1103/PhysRevLett.111.102301. URL: http://link.aps.org/doi/10.1103/PhysRevLett.111.102301.

[133] B. Abelev et al. "Azimuthal anisotropy of D-meson production in Pb-Pb collisions at $\sqrt{s_{NN}} = 2.76$ TeV". In: *Phys. Rev. C* 90 (3 2014), p. 034904. DOI: 10.1103/PhysRevC.90.034904. URL: http://link.aps.org/doi/10.1103/PhysRevC.90.034904.

[134] Betty Bezverkhny Abelev et al. "Azimuthal anisotropy of D meson production in Pb-Pb collisions at $\sqrt{s_{\mathrm{NN}}} = 2.76$ TeV". In: *Phys. Rev.* C90.3 (2014), p. 034904. DOI: 10.1103/PhysRevC.90.034904. arXiv: 1405.2001 [nucl-ex].

[135] Lyndon Evans and Philip Bryant. "LHC Machine". In: *Journal of Instrumentation* 3.08 (2008), S08001. URL: http://stacks.iop.org/1748-0221/3/i=08/a=S08001.

[136] W. de Boer. "Precision Experiments at LEP". In: *Adv. Ser. Direct. High Energy Phys.* 23 (2015), pp. 107–136. DOI: 10.1142/9789814644150_0005. arXiv: 1509.06050 [hep-ex].

[137] C. Carli. *LHC Design Report - The Injector Chain - LEIR*. Ed. by K. Schindl. CERN. Dec. 2004. Chap. 35. URL: https://edms.cern.ch/file/445804/4/Vol3_Chap35_v4.pdf.

[138] Betty Bezverkhny Abelev et al. "Performance of the ALICE Experiment at the CERN LHC". In: *Int. J. Mod. Phys.* A29 (2014), p. 1430044. DOI: 10.1142/S0217751X14300440. arXiv: 1402.4476 [nucl-ex].

[139] Gerardo Herrera Corral. "A new detector array for diffractive physics in ALICE at the LHC". In: *AIP Conf. Proc.* 1350 (2011), pp. 176–179. URL: https://cds.cern.ch/record/1478382.

[140] J Allen et al. *ALICE DCal: An Addendum to the EMCal Technical Design Report Di-Jet and Hadron-Jet correlation measurements in ALICE*. Tech. rep. CERN-LHCC-2010-011. ALICE-TDR-14-add-1. 2010. URL: https://cds.cern.ch/record/1272952.

[141] G. Dellacasa et al. "ALICE: Technical design report of the time projection chamber". In: (2000).

[142] E. Abbas et al. "Performance of the ALICE VZERO system". In: *JINST* 8 (2013), P10016. DOI: 10.1088/1748-0221/8/10/P10016. arXiv: 1306.3130 [nucl-ex].

[143] K. Aamodt and others. "Centrality Dependence of the Charged-Particle Multiplicity Density at Midrapidity in Pb-Pb Collisions at $\sqrt{s_{\mathrm{NN}}} = 2.76$ TeV". In: *Phys. Rev. Lett.* 106 (3 2011), p. 032301. DOI: 10.1103/PhysRevLett.106.032301. URL: http://link.aps.org/doi/10.1103/PhysRevLett.106.032301.

[144] S. Beole et al. "The forward muon spectrometer of ALICE". In: (1996).

[145] Sylvain Chapeland et al. "Experiences and evolutions of the ALICE DAQ Detector Algorithms framework". In: *Journal of Physics: Conference Series* 396.1 (2012), p. 012012. URL: http://stacks.iop.org/1742-6596/396/i=1/a=012012.

[146] S Chapeland et al. "Online processing in the ALICE DAQ The detector algorithms". In: *Journal of Physics: Conference Series* 219.2 (2010), p. 022004. URL: http://stacks.iop.org/1742-6596/219/i=2/a=022004.

[147] Imre Nagi. *Data Quality Monitoring: Automatic MOnitoRing Environment (AMORE) Web Administration Tool in ALICE Experiment*. Tech. rep. 2013.

[148] Barthélémy von Haller et al. "The ALICE Data Quality Monitoring: qualitative and quantitative review of three years of operations". In: *Journal of Physics: Conference Series*. Vol. 513. 1. IOP Publishing. 2014, p. 012038.

[149] "ALICE technical design report of the computing". In: (2005).

[150] *The ALICE Off-line Project*. http://aliweb.cern.ch/Offline/.

[151] *ROOT Data Analysis Framework*. https://root.cern.ch/.

[152] *Alien - ALICE Environment Grid framework*. http://alien.web.cern.ch.

[153] R. Fruhwirth. "Application of Kalman filtering to track and vertex fitting". In: *Nucl. Instrum. Meth.* A262 (1987), pp. 444–450. DOI: 10.1016/0168-9002(87)90887-4.

[154] *ALICE Quality Assurance offline*. http://aliweb.cern.ch/Offline/Activities/QA.html.

[155] G. Dellacasa et al. "ALICE technical design report of the time-of-flight system (TOF)". In: (2000).

[156] A. Akindinov et al. "Performance of the ALICE Time-Of-Flight detector at the LHC". In: *The European Physical Journal Plus* 128.4 (2013), p. 44. ISSN: 2190-5444. DOI: 10.1140/epjp/i2013-13044-x. URL: http://dx.doi.org/10.1140/epjp/i2013-13044-x.

[157] The ALICE Collaboration, K Aamodt, et al. "The ALICE experiment at the CERN LHC". In: *Journal of Instrumentation* 3.08 (2008), S08002. URL: http://stacks.iop.org/1748-0221/3/i=08/a=S08002.

[158] ALICE Collaboration et al. "ALICE: Physics Performance Report, Volume II". In: *Journal of Physics G: Nuclear and Particle Physics* 32.10 (2006), p. 1295. URL: http://stacks.iop.org/0954-3899/32/i=10/a=001.

[159] A Akindinov et al. "The multigap resistive plate chamber as a time-of-flight detector". In: *Nuclear Instruments and Methods in Physics Research Section A: Accelerators, Spectrometers, Detectors and Associated Equipment* 456.1–2 (2000). Proceedings of the 5th Int. Workshop on Resistive Plate Chambers and Related Detectors, pp. 16 –22. ISSN: 0168-9002. DOI: http://dx.doi.org/10.1016/S0168-9002(00)00954-2. URL: http://www.sciencedirect.com/science/article/pii/S0168900200009542.

[160] A.V. Akindinov et al. "Results from a large sample of MRPC-strip prototypes for the {ALICE} {TOF} detector". In: *Nuclear Instruments and Methods in Physics Research Section A: Accelerators, Spectrometers, Detectors and Associated Equipment* 532.3 (2004), pp. 611 –621. ISSN: 0168-9002. DOI: http://dx.doi.org/10.1016/j.nima.2004.05.125. URL: http://www.sciencedirect.com/science/article/pii/S0168900204013506.

[161] A. Akindinov et al. "Final test of the MRPC production for the ALICE TOF detector". In: *Nucl. Instrum. Meth.* A602 (2009), pp. 709–712. DOI: 10.1016/j.nima.2008.12.095.

[162] A. Akindinov et al. "A study of the multigap RPC at the gamma irradiation facility at CERN". In: *Nucl. Instrum. Meth.* A490 (2002), pp. 58–70. DOI: 10.1016/S0168-9002(02)00918-X.

[163] F. Anghinolfi et al. "NINO: an ultra-fast and low-power front-end amplifier/discriminator {ASIC} designed for the multigap resistive plate chamber". In: *Nuclear Instruments and Methods in Physics Research Section A: Accelerators, Spectrometers, Detectors and Associated Equipment* 533.1–2 (2004). Proceedings of the Seventh International Workshop on Resistive Plate Chambers and Related Detectors, pp. 183 –187. ISSN: 0168-9002. DOI: http://dx.doi.org/10.1016/j.nima.2004.07.024. URL: http://www.sciencedirect.com/science/article/pii/S0168900204014299.

[164] A. Akindinov et al. "A topological trigger based on the Time-of-Flight detector for the ALICE experiment". In: *Nucl. Instrum. Meth.* A602 (2009), pp. 372–376. DOI: 10.1016/j.nima.2008.12.016.

[165] B. Abelev and etal. "Measurement of charm production at central rapidity in proton-proton collisions at $ \sqrt{s} = 7{}TeV$". In: *Journal of High Energy Physics* 2012.1 (2012), p. 128. ISSN: 1029-8479. DOI: 10.1007/JHEP01(2012)128. URL: http://dx.doi.org/10.1007/JHEP01(2012)128.

[166] B. Abelev et al. "Measurement of charm production at central rapidity in proton-proton collisions at $\sqrt{s} = 7$ TeV". In: *JHEP* 01 (2012), p. 128. DOI: 10.1007/JHEP01(2012)128. arXiv: 1111.1553 [hep-ex].

[167] B. Abelev et al. "Measurement of Prompt D-Meson Production in $p-\mathrm{Pb}$ Collisions at $\sqrt{s_{NN}} = 5.02$ TeV". In: *Phys. Rev. Lett.* 113 (23 2014), p. 232301. DOI: 10.1103/PhysRevLett.113.232301. URL: http://link.aps.org/doi/10.1103/PhysRevLett.113.232301.

[168] K. A. Olive et al. "Review of Particle Physics". In: *Chin. Phys.* C38 (2014), p. 090001. DOI: 10.1088/1674-1137/38/9/090001.

[169] C. Patrignani and Particle Data Group. "Review of Particle Physics". In: *Chinese Physics C* 40.10 (2016), p. 100001. URL: http://stacks.iop.org/1674-1137/40/i=10/a=100001.

[170] Jaroslav Adam et al. "Particle identification in ALICE: a Bayesian approach". In: *Eur. Phys. J. Plus* 131.5 (2016), p. 168. DOI: 10.1140/epjp/i2016-16168-5. arXiv: 1602.01392 [physics.data-an].

[171] R Aaij et al. "Measurement of B meson production cross-sections in proton-proton collisions at $\sqrt{s}$ = 7 TeV". In: *JHEP* 08 (2013), p. 117. DOI: 10.1007/JHEP08(2013)117. arXiv: 1306.3663 [hep-ex].

[172] Andreas Hoecker et al. "TMVA: Toolkit for Multivariate Data Analysis". In: *PoS* ACAT (2007), p. 040. arXiv: physics/0703039.

[173] Jesper R. Christiansen and Peter Z. Skands. "String Formation Beyond Leading Colour". In: *JHEP* 08 (2015), p. 003. DOI: 10.1007/JHEP08(2015)003. arXiv: 1505.01681 [hep-ph].

[174] Mykhailo Lisovyi, Andrii Verbytskyi, and Oleksandr Zenaiev. "Combined analysis of charm-quark fragmentation-fraction measurements". In: *Eur.Phys.J.C* 76 (2016), p. 397. DOI: 10.1140/epjc/s10052-016-4246-y.